

Sensitivity to atmospheric tau-neutrino appearance
and all-flavour search for neutrinos from the
Fermi Bubbles with the deep-sea telescopes
KM3NeT/ORCA and ANTARES

Sensitivitätsstudien zur Messung von atmosphärischen
Tau-Neutrinos und Suche nach Neutrinos von den
Fermi Bubbles mit den Tiefsee-Teleskopen
KM3NeT/ORCA und ANTARES

Der Naturwissenschaftlichen Fakultät
der Friedrich-Alexander-Universität
Erlangen-Nürnberg
zur

Erlangung des Doktorgrades Dr. rer. nat.

vorgelegt von

Steffen Hallmann

Als Dissertation genehmigt
von der Naturwissenschaftlichen Fakultät
der Friedrich-Alexander-Universität Erlangen-Nürnberg

Tag der mündlichen Prüfung:

25.01.2021

Vorsitzender des Promotionsorgans:

Prof. Dr. Wolfgang Achtziger

Gutachter:

Prof. Dr. Gisela Anton
Assoc. Prof. Dr. Revaz Shanidze

Acknowledgements

I am truly grateful for all the support I have received over the last years, without which this thesis would still not be finished.

◇ Gisela und Uli, eurer Unterstützung und der so freien Entfaltungsmöglichkeit im Bezug auf meine Arbeit konnte ich mir die ganzen Jahre am ECAP über immer gewiss sein. Vielen lieben Dank dafür! ◇ Thomas, danke Dir für deine allzeit guten Ratschläge und Beistand bei Analysen und Konferenzbeiträgen, und Kay dafür, dass ich die letzte Zeit über bei den EU-Projekten mitarbeiten durfte. ◇ Tom, auf deine schnelle Hilfe bei Computingfragen kann man immer bauen. Jannik, dein tiefes Wissen über Neutrinophysik war bei den vielen Diskussionen stets unglaublich hilfreich. ◇ Michael, Nicole, Stefan und Thomas, dass ihr in unserem Büro eine gemütliche und schöne Atmosphäre geschaffen habt (die ausgedörrten Pflanzen ausgenommen) ◇ Danke an alle, die mir mit Ratschlägen und nützlichen Hinweisen beim Korrekurlesen weitergeholfen haben! ◇ All the other colleagues at ECAP and also the entire KM3NeT and ANTARES collaborations. Since my Bachelor project I have had countless fruitful discussions, wonderful meetings and conferences – sometimes even followed by exciting trips. An exhaustive list of individual names would be too long here ◇ Anna and Rodrigo, I am still looking back to all our joint activities during your extended stays at ECAP and my visits. I hope we meet again soon! ◇ Rezo, thank you for writing my Zweitgutachten without a glimpse of hesitation. ◇ Eva, danke, dass du mir in diesen letzten Monaten immer den nötigen Raum zum Schreiben gegeben hast und mir jeden Tag zu einem so viel schöneren machst. ◇ Meiner Familie ein riesen Dankeschön, dass ihr mich schon immer so bedingungslos unterstützt habt und allzeit lieb willkommen heißt, selbst wenn die Besuche zu Hause mitunter kurz und vollgepackt ausfallen. ◇ All the other friends and colleagues I did not mention here explicitly. Thank you all for your support along this journey.

** *****

Contents

Overview of the contents and main results	ix
Inhalt und wesentliche Ergebnisse im Überblick	xiii
Statement on the author’s personal contributions	xvii
I Neutrinos – from generation to detection	0
1 A short overview on neutrino physics and neutrino astronomy	2
1.1 The neutrino, a special particle	2
1.2 Very-large-volume neutrino detectors	3
1.3 Neutrino interactions in the Standard Model	5
2 Generation of neutrinos	7
2.1 Sources of neutrinos	7
2.2 Atmospheric neutrinos	8
2.3 Cosmic neutrinos as astrophysical messenger	12
3 Propagation	14
3.1 Flux attenuation	14
3.2 Neutrino oscillation	15
3.2.1 Discovery of neutrino oscillation	15
3.2.2 Neutrino oscillation in vacuum	15
3.2.3 Neutrino oscillation in matter	18
4 Interaction	22
4.1 Observables in neutrino interactions	22
4.2 Interaction cross sections	23
4.3 Differences between ν and $\bar{\nu}$	24
5 Neutrino detection in the GeV to PeV energy region	26
5.1 Cherenkov radiation	27
5.2 Water properties	27
5.3 Optical sensors	28

5.4	Background sources	28
5.4.1	Optical background noise	28
5.4.2	Atmospheric muons	30
5.5	Detection in very-large-volume Cherenkov detectors	31
5.5.1	Event signatures	31
5.5.2	Neutrino effective volumes of ANTARES and KM3NeT	32
II	Tau-neutrino appearance with KM3NeT/ORCA	36
6	Tau-neutrino appearance	38
6.1	Status of neutrino oscillations and unitarity	38
6.2	Kinematics and signatures of $\bar{\nu}_\tau$ interactions	41
6.2.1	Interaction of $\bar{\nu}_\tau$	42
6.2.2	Tau decay	43
6.3	Existing and future $\bar{\nu}_\tau$ appearance measurements	45
6.3.1	Direct $\bar{\nu}_\tau$ detection in beam dumps	46
6.3.2	Long baseline neutrino beams	47
6.3.3	Indirect detection in atmospheric oscillation experiments	48
6.4	Oscillation analysis with ORCA: A roadmap towards the $\bar{\nu}_\tau$ appearance study	50
7	The KM3NeT detector design	52
7.1	The Digital Optical Module (DOM)	52
7.2	The Detection Unit (DU)	53
7.3	The ORCA Detector	54
7.4	Signal digitisation and data transmission	54
7.4.1	L0 hits	54
7.4.2	L1 and L2 hits for the trigger	55
8	Monte Carlo simulations for ORCA	56
8.1	Simulation chain up to trigger-level	57
8.2	Monte Carlo mass productions for realistic detector setups	58
9	Triggering in ORCA	61
9.1	Description of the triggers used in ORCA	61
9.1.1	Triggers based on L2 hits	61
9.1.2	Low-energy trigger MXShower	63
9.2	Trigger optimisation	63
9.2.1	Trigger optimisation for the 3DTrack and 3DShower triggers	64
9.2.2	Trigger optimisation for the MXShower trigger	64
9.3	Evaluation of trigger performance	68

9.3.1	Performance of MXShower compared to the 3D triggers	68
9.3.2	Trigger comparison with the idealised setup	68
9.4	Impact of data-taking conditions on the trigger performance	71
9.4.1	Bioluminescence bursts and high rate veto	71
9.4.2	Missing channels	74
9.4.3	Consequences for neutrino analyses	75
9.5	In situ verification of trigger rates for a small sub-detector	77
9.6	Triggering for higher instrumentation density	78
10	Event reconstruction and pre-selection of analysis event sample	80
10.1	Reconstruction of track- and shower-like event signatures	80
10.1.1	Shower reconstruction algorithm Dusj	80
10.1.2	Track reconstruction algorithm JGandalf	81
10.2	Event pre-selection	82
10.2.1	Event pre-selection for the track reconstruction	82
10.2.2	Event pre-selection for the shower reconstruction	83
10.2.3	Pre-selected event sample	84
11	Event type identification in ORCA	88
11.1	Machine learning in ORCA and ANTARES	88
11.2	Random Decision Forest technique	90
11.2.1	RDF architecture and training settings	91
11.2.2	Cross validation	92
11.2.3	Training features	92
11.2.4	Additional hit distribution based features	93
11.3	Background reduction	93
11.3.1	Training and analysis of the background classifier	94
11.3.2	Atmospheric muon classifier	95
11.3.3	Pure noise classifier	96
11.3.4	Conclusions from the background rejection outputs	96
11.4	Event type identification	97
11.4.1	Separation between tracks and showers	97
11.4.2	Dependence on instrumentation density and input features	99
11.5	Classification of the event sample	100
11.6	Detector resolutions for the pre-selected and classified event sample	103
12	Sensitivity of ORCA to $\overleftrightarrow{\nu}_\tau$ appearance	107
12.1	Measurement principle and sensitive region	107
12.1.1	Region of interest for the $\overleftrightarrow{\nu}_\tau$ appearance measurement	108
12.2	Oscillation fit using ParamNMH	110
12.2.1	Oscillation analysis frameworks for ORCA	110

12.2.2	Implementation of detector response in ParamNMH	111
12.2.3	Event distribution histograms	112
12.2.4	Fit statistic	113
12.2.5	Statistical likelihood	115
12.2.6	Nuisance parameters with Gaussian priors	115
12.2.7	Nuisance parameters accounted for in the $\bar{\nu}_\tau$ appearance fit	115
12.3	Sensitivity study to $\bar{\nu}_\tau$ appearance with ORCA	116
12.3.1	Resulting sensitivities for the full ORCA detector	117
12.3.2	Non-unitary mixing: the $n_\tau < 1$ scenario	117
12.3.3	CC-only vs. combined CC+NC scaling	120
12.3.4	Influence of nuisance parameters	122
12.4	Tau-neutrino appearance with an early stage sub-array	125
13	Conclusion on Part II and outlook for measuring $\bar{\nu}_\tau$ appearance in-situ	127
III Search for neutrinos from the Fermi Bubbles with ANTARES		130
14	The Fermi Bubbles – giant lobes of γ -rays and neutrinos?	132
14.1	Possible origins of the Fermi Bubbles	132
14.2	Gamma-ray emission measured by Fermi-LAT	133
15	Analysis method and expected neutrino flux	135
15.1	Analysis method	135
15.2	Assumed neutrino flux and energy spectrum	135
16	Recorded ANTARES data	139
16.1	The ANTARES detector	139
16.2	Event reconstruction	140
16.2.1	AAFit for the track analysis	140
16.2.2	TANTRA for the shower analysis	141
16.3	ANTARES dataset recorded between 2008 and 2015	142
16.3.1	Evolution of neutrino detection efficiency	143
16.3.2	Run-by-run Monte Carlo simulations	145
16.3.3	Run selection for analysis	146
17	All-flavour search for neutrinos from the Fermi Bubbles at high Galactic latitudes	149
17.1	General analysis procedure	149
17.2	Track analysis of the 2014/15 dataset	152
17.2.1	Data pre-selection of the track analysis	152
17.2.2	Test for possible re-optimisation of analysis cuts	154

17.2.3 Data – Monte Carlo agreement	156
17.2.4 Observed track events and track-only flux upper limits	158
17.3 Search for shower-like signatures	159
17.3.1 Data pre-selection of the shower analysis	159
17.3.2 Analysis cut optimisation	163
17.3.3 Data – Monte Carlo agreement	164
17.3.4 Observed shower events	167
17.4 All-flavour result and combined flux upper limits	168
18 Prospects for detecting low-latitude emission with ANTARES	170
19 Conclusion on Part III and prospects for observing a Fermi Bubble neutrino flux	173
Appendix	175
List of Abbreviations	175
List of Figures	175
List of Tables	179
Bibliography	181

Overview of the contents and main results

The neutrino detectors KM3NeT and ANTARES

Neutrinos are fundamental leptonic particles that have very small masses, do not carry electric charge, and hence interact barely with matter via the weak force. Indirect detection of neutrinos is possible by inferring their energy and origin from the charged interaction products which induce emission of Cherenkov light in a transparent dielectric medium. This light can be registered using optical sensors.

This thesis is devoted to the detection of neutrinos with two different large-volume neutrino detectors 2.5 km below sea level in the clear sea water off-shore Toulon in the south of France. The first is the ANTARES neutrino telescope, taking data in its final configuration since spring 2008. ANTARES is optimised for neutrino astronomy with an optimal view of the central region of the Milky Way. The second, KM3NeT/ORCA (short ORCA), is part of the KM3NeT research infrastructure, which is hosting the next generation neutrino facilities in the Mediterranean Sea. ORCA is optimised for the study of neutrino properties by measuring flavour oscillations of neutrinos produced in the Earth's atmosphere. Currently, the instrument is taking data with a small fraction of the planned sensors and already now capable of reconstructing and identifying neutrino candidates.

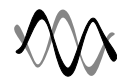
Part I: Neutrinos – from generation to detection



The first part of the thesis is to set the scientific context, with a recapitulation of the neutrino properties and sources currently known and remaining to be determined. The general ingredients needed for the analysis and interpretation of neutrino data are explained whilst accompanying neutrinos on their journey. This journey starts with the generation in hadronic interactions, continues with their flavour oscillations during propagation, and ends with the interaction and the detection principle of deep-sea neutrino detectors.

More detail that is relevant only for the particular studies with the individual detectors is given in the remaining two parts. The subsequent paragraphs provide a framework for the contents of Parts II and III.

Part II: Tau-neutrino appearance with KM3NeT/ORCA



There are three light and active types of neutrinos, named flavours: the electron neutrino, ν_e , the muon neutrino, ν_μ , and the tau neutrino, ν_τ . Meanwhile all three of them have been observed in direct detection experiments. It was also shown that neutrinos change flavour while they travel, a phenomenon called neutrino oscillation. Since the oscillation requires neutrinos to carry mass, it was necessary to extend the Standard Model of Particle Physics, where originally neutrinos were assumed massless.

In the now commonly accepted picture, the three – and only three – neutrino flavours undergo oscillation amongst each other. If this picture is complete, their mixing can be described by a unitary 3×3 mixing matrix, called the PMNS matrix. Unitarity implies that the total sum of $\bar{\nu}_e$, $\bar{\nu}_\mu$, and $\bar{\nu}_\tau$ remains constant¹. Confirmation or rejection of the unitarity assumption requires precise knowledge of the elements of the PMNS matrix. The third row of the matrix currently has the largest uncertainty and is linked to the appearance of $\bar{\nu}_\tau$, i.e. the oscillation from other flavours into the $\bar{\nu}_\tau$ channel. In the measurement of tau-neutrino appearance ($\bar{\nu}_\tau$ appearance) the normalisation of the $\bar{\nu}_\tau$ event rate in the detector is determined with respect to the expectation in case of unitary mixing. This normalisation measurement represents a model independent test for new physics.

While $\bar{\nu}_\tau$ appearance has meanwhile been detected directly by the long-baseline neutrino beam experiment OPERA, and observed indirectly also in the atmospheric neutrino oscillation experiments Super Kamiokande and IceCube/DeepCore, constraints on the normalisation of the signal are currently still poor. With a multi-megaton instrumented mass and a few-GeV energy threshold, ORCA will collect more than 3000 $\bar{\nu}_\tau$ events per year. They originate from $\bar{\nu}_\mu \rightarrow \bar{\nu}_\tau$ oscillation in the atmospheric flux which has a broad maximum with almost complete conversion at ~ 25 GeV. Muons, μ^\pm , as produced in charged current interactions of $\bar{\nu}_\mu$, leave distinct track-like (light emission along a line) signatures in the detector. On the other hand, neutrino interactions without μ^\pm in the final state appear shower-like (light emission at a single point), which is the case for most $\bar{\nu}_\tau$. The oscillation probabilities depend on the distance travelled and on energy. Therefore, ORCA can observe $\bar{\nu}_\tau$ appearance on a statistical basis by measuring the zenith and energy dependent distribution of events with shower-like signatures.

The sensitivity study for $\bar{\nu}_\tau$ appearance presented in this part of the thesis finds that ORCA is able to rule out non-appearance, i.e. a normalisation of zero, at the 5σ confidence level (CL) already with one month of recorded data. After one year of operation, the normalisation of the $\bar{\nu}_\tau$ flux can be constrained within $\pm 30\%$ at 3σ CL. It is shown, that the stated sensitivity does not depend on a prior knowledge of the true neutrino mass ordering, a yet not conclusively determined parameter and the main physics goal of ORCA.

These results motivated to study the sensitivity to $\bar{\nu}_\tau$ appearance also for a small sub-array of ORCA, with 6% of sensors installed. It turns out that a first appearance confirmation is already feasible after six months of data-taking with the studied sub-array. The measurement of $\bar{\nu}_\tau$ appearance will therefore be one of the first physics results of ORCA and is competitive with current best limits.

Preceding and in addition to the $\bar{\nu}_\tau$ appearance analysis, two major contributions of general use for sensitivity studies with ORCA have been made.

First, a new trigger algorithm developed by the collaboration has been optimised for a realistic detector setup. With the found optimal settings, the detection threshold is lowered by $\sim 30\%$ in energy, yielding a factor 2 (1.4) more events at 3 (6) GeV. The trigger is expected to allow stable data-taking if sensors with high optical background are vetoed. The efficiency loss induced by this veto is studied and turns out to be small for $\bar{\nu}_\tau$ appearance. However, close to the threshold, a veto-induced efficiency reduction of up to 25% at 3 GeV (10% at 7 GeV) can be estimated for the complete ORCA detector. This should be accounted for in future sensitivity studies. This is particularly relevant when the analysed signal is near the detection threshold

¹The notation $\bar{\nu}$ refers to both neutrinos ν and their anti-particle partners $\bar{\nu}$.

of the instrument.

Second, classification models have been trained using the Random Decision Forest (RDF) approach. The RDF models trained to distinguish between neutrinos and background allow individual and efficient rejection of the atmospheric muon and pure noise components to below $\sim 3\%$ in the analysis sample. The remaining neutrino candidates can be separated into several event type classes using a third classification model. In analyses, the separation is done based on a score variable indicating how track-like the events appear. For $\bar{\nu}_\tau$ appearance and other recent sensitivity studies three event classes (tracks, showers, middle) are now used instead of only two in earlier studies. The provided RDF models use additional training features which compare the distributions of detected photon signals in the detector with the expectation for a track ($\bar{\nu}_\mu$) or shower ($\bar{\nu}_e$) hypothesis. Including these lowers the turn-on energy, above which track–shower separation is possible, by 25%, from 7.3 GeV to 5.5 GeV.

Part III: Search for neutrino emission from the Fermi Bubbles with ANTARES



Because neutrinos do not carry electric charge, they are not deflected in magnetic fields during propagation. In addition, their small interaction cross section allows them to escape and traverse dense media. These properties make neutrinos ideal messengers to look for sources of hadronic acceleration. In hadronic interactions neutrinos are produced (mainly) in the decays of π^\pm mesons alongside γ -rays from π^0 . On the other side, neutrinos are absent in the case of leptonic emission scenarios. The satellite based Fermi-LAT instrument has observed giant lobes of γ -ray emission from the region above and below the Galactic Centre, dubbed the ‘Fermi Bubbles’. While their origin is still under debate, the measurement or exclusion of an associated neutrino flux could constrain the range of possible models.

ANTARES data recorded between 2008 and 2015 are used to search for such high energy neutrino emission from the Fermi Bubbles. The background expected in the signal region is determined in a data-driven approach in off-zones. The presented analysis is an all-flavour search combining two exclusive searches for track- and shower-like neutrino events. While for tracks, a previous six-year analysis is only extended by two additional years, 2014 and 2015, the presented 2008–2015 shower analysis is the first search for shower-like signatures from the Fermi Bubbles.

Both observe a small but non-significant excess (tracks: 1.5σ , showers: 0.6σ) in the signal region.

To derive an expected neutrino flux from the Fermi Bubbles, the measured Fermi-LAT γ -ray flux needs to be extrapolated to higher energies. The assumed model flux per neutrino flavour is

$$\frac{d\Phi_{\text{model}}}{dE} = (1.8 - 3.6) \times 10^{-7} \text{GeV}^{-1} \text{cm}^{-2} \text{s}^{-1} \text{sr}^{-1} \times (E/\text{GeV})^{-2.18} \times \exp(-E/E_{\text{cutoff},\nu})$$

and represents a power-law with an exponential cut-off in energy evaluated down to $E_{\text{cutoff},\nu}^{\text{min}} = 50 \text{ TeV}$. As a consequence of the found excess, the derived combined 90% flux upper limits are one order of magnitude above the model flux.

A more recent analysis of the Fermi Bubbles in the Galactic disc revealed a bright emission region with hard energy spectrum, close to E^{-2} but ~ 40 times smaller in size. The analysis procedure is used without re-optimisation to estimate the sensitivity of ANTARES in this

central zone. ANTARES is found sensitive to constrain a possible neutrino emission from this region for cut-off energies higher than $\sim 200\text{--}500$ TeV. This study motivates a future analysis of the low-latitude Fermi Bubbles region, where the sensitivity can be improved with an optimised event selection and by adding additional years of data.

Inhalt und wesentliche Ergebnisse im Überblick

Die Neutrino-Detektoren KM3NeT and ANTARES

Neutrinos sind fundamentale Elementarteilchen. Sie zählen zu den Leptonen und besitzen nur sehr kleine Ruhemassen und keine elektrische Ladung. Lediglich über die schwache Wechselwirkung interagieren sie daher nur sehr wenig mit Materie. In der Wechselwirkung werden relativistische geladene Teilchen produziert, welche in einem transparenten dielektrischen Medium, wie Wasser, Emission von Cherenkov Licht induzieren. Der indirekte Neutrinonachweis gelingt, indem man das Cherenkov-Signal in Photosensoren nachweist und daraus Energie und Richtung der Neutrinos ableitet.

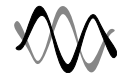
Diese Arbeit befasst sich mit dem Neutrinonachweis mit zwei großvolumigen Detektoren, die sich in 2,5 km Tiefe im klaren Meereswasser bei Toulon (Südfrankreich) befinden. Bei dem ersten handelt es sich um das ANTARES Neutrino-Teleskop, welches im Jahr 2008 fertiggestellt wurde und seither Daten nimmt. ANTARES ist optimiert um Astronomie zu betreiben und hat einen hervorragenden Blick auf die Region um das Zentrum der Milchstraße. Der zweite, KM3NeT/ORCA (kurz ORCA), ist Teil der KM3NeT Forschungsinfrastruktur. ORCA ist dafür optimiert fundamentale Neutrinoeigenschaften mittels Oszillationen zwischen den unterschiedlichen Neutrinentypen, auch Flavours genannt, zu untersuchen. Als Quelle dienen hierfür Neutrinos, die in der Erdatmosphäre produziert werden und den Weg zum Detektor finden. Ein kleiner Teil der Sensoren von ORCA nimmt bereits Daten und ist schon jetzt in der Lage Neutrinokandidaten zu rekonstruieren und gegenüber Untergrundereignissen zu filtern.

Teil I: Neutrinos – ihre Reise von der Erzeugung zur Detektion



Der erste Teil dieser Arbeit hat den Zweck, den wissenschaftlichen Rahmen abzustecken. Dies geschieht durch eine Rekapitulation der fundamentalen Eigenschaften von Neutrinos, den derzeit bekannten Quellen und denen, die erst noch identifiziert werden müssen. Die wissenschaftlichen Hintergründe, die für die Analyse und Interpretation von Neutrinodaten notwendig sind, werden erklärt, während Neutrinos auf ihrer Reise begleitet werden. Diese Reise beginnt mit deren Erzeugung in hadronischen Wechselwirkungen, setzt sich fort mit den Flavour-Oszillationen während der Propagation, und endet mit der Wechselwirkung und dem Detektionsprinzip von Neutrinodetektoren in der Tiefsee.

Darüber hinausgehende Details, die nur für eine der durchgeführten Studien mit ORCA oder ANTARES relevant sind, werden direkt im jeweiligen Teil geliefert. Die nachfolgenden Absätze geben einen Überblick über die Inhalte der Teile II und III.



Teil II: Bestimmung des Tau-Neutrino Flusses mit KM3NeT/ORCA

Es gibt drei Arten von leichten, aktiven Neutrinos, auch Flavours genannt: Das Elektron-Neutrino, ν_e , das Muon-Neutrino ν_μ , und das Tau-Neutrino ν_τ . Mittlerweile konnten alle drei Flavours in Experimenten direkt nachgewiesen werden. Es hat sich auch herausgestellt, dass Neutrinos während ihrer Ausbreitung den Flavour wechseln. Dieses Phänomen bezeichnet man als Neutrino-Oszillation. Eine Voraussetzung für die Oszillation ist, dass Neutrinos Masse tragen müssen. Als Folge musste das Standardmodell der Teilchenphysik, in dem Neutrinos ursprünglich als masselos angenommen wurden, erweitert werden.

In der derzeit gemeinhin akzeptierten Vorstellung oszillieren die drei – und nur genau drei – Neutrino Flavours untereinander. Falls diese Vorstellung vollständig ist, so kann ihre Oszillation durch die unitäre 3×3 Mischungsmatrix, die PMNS Matrix, beschrieben werden. Unitarität impliziert, dass die Summe aus $\bar{\nu}_e$, $\bar{\nu}_\mu$ und $\bar{\nu}_\tau$ durch die Oszillation unverändert bleibt.² Damit die Unitaritätsannahme getestet werden kann, müssen alle Elemente der PMNS Matrix präzise bestimmt sein. Die dritte Zeile dieser Matrix steht in Verbindung mit der Erscheinung von $\bar{\nu}_\tau$, das heißt der Oszillation von anderen Flavours in den $\bar{\nu}_\tau$ Kanal. Die Messung der Normalisierung dieser oszillierten Tau-Neutrino Komponente, im Folgenden als $\bar{\nu}_\tau$ -Appearance (dt.: $\bar{\nu}_\tau$ -Erscheinung) bezeichnet, stellt daher einen modellunabhängigen Test für Physik jenseits des Standardmodells dar.

Zwar ist $\bar{\nu}_\tau$ -Appearance mittlerweile schon direkt im künstlich erzeugten Neutrino-Strahl mit dem OPERA Detektor nachgewiesen worden. Auch der indirekte Nachweis in den Detektoren ‘Super Kamiokande’ und ‘IceCube/DeepCore’, die den atmosphärischen Neutrino-Fluss vermessen, ist gelungen. Jedoch ist die Unsicherheit auf die Normalisierung der $\bar{\nu}_\tau$ Komponente groß. Mit seiner instrumentierten Masse von mehreren Megatonnen (10^9 kg) und der Energieschwelle im GeV-Bereich wird ORCA über eine Statistik von über 3000 $\bar{\nu}_\tau$ Ereignissen pro Jahr verfügen. Diese stammen aus der Oszillation von $\bar{\nu}_\mu \rightarrow \bar{\nu}_\tau$ im atmosphärischen Fluss, welcher ein breites Maximum mit fast kompletter Flavour-Konversion bei ~ 25 GeV aufweist. Myonen, μ^\pm , wie sie in den geladenen Strom Wechselwirkungen von $\bar{\nu}_\mu$ entstehen, hinterlassen im Detektor eindeutige spurartige Signaturen. Neutrinowechselwirkungen ohne μ^\pm im Endzustand, wie die meisten $\bar{\nu}_\tau$, zeigen eher punktförmige Lichtemission – sie erscheinen schauerartig. Da die Oszillationswahrscheinlichkeiten von der zurückgelegten Strecke und der Energie abhängen, weist ORCA daher $\bar{\nu}_\tau$ -Appearance durch die Messung der Ereignisverteilung in Abhängigkeit von Zenitwinkel und Energie auf statistischer Basis nach.

Die Sensitivitätsstudie zur $\bar{\nu}_\tau$ -Appearance, die in diesem Teil der Arbeit präsentiert wird, stellt fest, dass ORCA eine Nicht-Erscheinung (d.h. eine $\bar{\nu}_\tau$ Normalisierung von null) bereits mit einem Monat Datennahme mit einem Konfidenzlevel von 5σ ausschließen kann. Nach einem Jahr Datennahme kann der $\bar{\nu}_\tau$ Fluss auf $\pm 30\%$ auf dem 3σ -Level eingegrenzt werden. Es wird gezeigt, dass die genannte Sensitivität auch erreicht wird, wenn die Anordnung der Neutrino Masseneigenzustände – einem wichtigen Physikziel von ORCA – weiter unbestimmt bleibt.

Die genannten Resultate legen nahe, die Sensitivitätsstudie für einen ORCA Detektor in einem frühen Aufbaustadium (entsprechend den derzeitig aufgebauten 6% des finalen Ausbaus) zu wiederholen. Es zeigt sich, dass eine erste Bestätigung der $\bar{\nu}_\tau$ -Appearance mit 6 Monaten Daten mit der untersuchten kleinen Detektorkonfiguration möglich ist. Die Messung der $\bar{\nu}_\tau$ -

²Die Notation $\bar{\nu}$ bezieht sich sowohl auf Neutrinos ν als auch deren Partner Anti-Teilchen $\bar{\nu}$.

Appearance wird damit eines der ersten Physikergebnisse von ORCA sein und ist kompetitiv mit den momentan publizierten besten Ausschlussgrenzen auf die $\bar{\nu}_\tau$ Normalisierung.

Dem vorausgehend wurden zwei wesentliche Beiträge geleistet, die nicht nur für die $\bar{\nu}_\tau$ Appearance Analyse, sondern für alle ORCA Sensitivitätsstudien von Nutzen sind.

Erstens: Ein neuer, von der Kollaboration entwickelter, Trigger-Algorithmus wurde für ein realistisches Detektorsetup optimiert und analysiert. Mit den resultierenden besten Trigger-einstellungen wird die Detektionsschwelle in der Energie um 30% verbessert, was einer um den Faktor 2 (1.4) höheren Signalausbeute bei 3 (6) GeV entspricht. Mit einem vorübergehenden Veto für Sensoren, die hohe optische Untergrundraten aufweisen, ist stabile Datennahme mit dem kompletten ORCA Detektor zu erwarten. Der Effizienzverlust aufgrund des Vetos wurde analysiert und erweist sich als klein für die $\bar{\nu}_\tau$ -Appearance Analyse. Nahe an der Detektionsschwelle wird über die Zeit gemittelt eine um bis zu 25% bei 3 GeV (10% bei 7 GeV) verringerte getriggerte Neutrinorate abgeschätzt. Das Ergebnis legt nahe, diesen Verlust in zukünftigen Sensitivitäten zu berücksichtigen. Dies gilt insbesondere, falls das analysierte Signal nahe der Nachweisschwelle liegt.

Zweitens: Modelle für die Ereignisklassifikation wurden unter Verwendung eines sogenannten Random Decision Forest (RDF) entwickelt. Die trainierten RDF Modelle erlauben es, die dominanten Untergrundkomponenten – atmosphärische Myonen und reinen optischen Untergrund – separat und effizient auf unter 3% im finalen Datensatz zu unterdrücken. Die zurückbleibenden Neutrino-Kandidaten können mit einem weiteren Klassifikationsmodell in mehrere Analyseklassen aufgeteilt werden. Dies geschieht mittels einer Bewertungsvariable, die abschätzt, wie spurartig die Ereignisse sind. Für $\bar{\nu}_\tau$ -Appearance und andere neuere Sensitivitätsstudien werden nun drei (spurartig, schauerartig, und dazu eine mittlere Klasse) anstelle der vormals zwei Klassen verwendet. Die zur Verfügung gestellten RDF Modelle nutzen zusätzliche Trainingsvariablen aus. Diese vergleichen die Verteilungen der registrierten Signale im Detektor mit der Erwartung für hypothetische Spuren ($\bar{\nu}_\mu$) und Schauer ($\bar{\nu}_e$). Damit reduziert sich die Neutrinoenergie, ab der eine effiziente Klassifikation möglich ist, um 25% von 7,3 GeV auf 5,5 GeV.

Teil III: Suche nach Neutrinos von den Fermi Bubbles mit ANTARES



Da Neutrinos keine elektrische Ladung tragen, werden sie auch nicht auf ihrem Weg von Magnetfeldern abgelenkt. Zusätzlich erlaubt der geringe Wechselwirkungsquerschnitt, dass sie aus dichten Quellen entweichen und ungehindert weite Strecken zurücklegen. Diese Eigenschaften machen Neutrinos zu idealen Botenteilchen, wenn es um die Suche nach hadronischen Beschleunigungsquellen geht. In hadronischen Wechselwirkungen werden Neutrinos (in erster Linie) durch den Zerfall von geladenen Pionen (π^\pm) erzeugt und von einem entsprechenden γ -Fluss aus π^0 begleitet. In leptonischen Emissionsszenarien hingegen fehlt eine entsprechende Neutrino-Komponente.

Das satellitenbasierte Fermi-LAT Instrument hat gigantische blasenförmige Strukturen von γ -Strahlen in den Regionen ober- und unterhalb des Galaktischen Zentrums entdeckt, die als „Fermi Bubbles“ bezeichnet werden. Da deren Ursprung noch nicht abschließend geklärt ist, würde eine Messung oder ein Ausschluss eines zugehörigen Neutrinoflusses die Anzahl möglicher Emissionsmodelle einschränken.

ANTARES Daten, die zwischen 2008 und 2015 aufgezeichnet wurden, werden für die Su-

che nach solch einer Neutrino-Emission genutzt. Der zu erwartende Untergrund in der Signalregion wird in einem datengestützten Ansatz in Kontrollregionen bestimmt. Bei der präsentierten Analyse werden Neutrinos aller Ereignistypen analysiert indem das Ergebnis aus zwei sich gegenseitig ausschließenden Suchen nach spur- und schauerartigen Neutrinosignaturen kombiniert werden. Bei der Spur-Suche handelt es sich um eine Erweiterung einer bestehenden Analyse, die sechs Jahre Daten umfasst, um zwei weitere Jahre, 2014 und 2015. Die vorgestellte Schauer-Analyse umfasst den Datensatz der Jahre 2008 bis 2014 und ist die erste Suche nach schauerartigen Ereignissen aus der Fermi Bubble Region.

Beide Einzelanalysen für sich genommen sehen einen kleinen, jedoch nicht signifikanten Überschuss in der Signalregion (nur spurartig: 1.5σ , nur schauerartig: 0.6σ).

Um eine Erwartung für den Neutrinofluss von den Fermi Bubbles abzuleiten, muss der gemessene Fermi-LAT γ -Fluss zu höheren Energien extrapoliert werden. Der Modellfluss je Flavour nimmt ein Potenzgesetz mit exponentiellem Abfall oberhalb einer maximalen Neutrino-Energie an,

$$\frac{d\Phi_{\text{model}}}{dE} = (1.8 - 3.6) \times 10^{-7} \text{GeV}^{-1} \text{cm}^{-2} \text{s}^{-1} \text{sr}^{-1} \times (E/\text{GeV})^{-2.18} \times \exp(-E/E_{\text{cutoff},\nu}).$$

Die Modellflussannahme wird für unterschiedliche maximale Neutrino-Energien oberhalb von $E_{\text{cutoff},\nu}^{\text{min}} = 50 \text{ TeV}$ ausgewertet. In Folge des gefundenen Überschusses in der Signalregion gegenüber dem erwarteten Untergrund, liegen die kombinierten oberen Ausschlussgrenzen (90% Konfidenzlevel) eine Größenordnung oberhalb des Modellflusses.

Neuere Suchen mit Fermi-LAT nach γ -Strahlung aus den Fermi Bubbles im Bereich um das galaktische Zentrum zeigen eine helle Emissionsregion auf. Diese besitzt ein hartes Energiespektrum, kompatibel mit E^{-2} , und hat keinen sichtbaren Abbruch bei höheren Energien. Hingegen ist die Fläche der Region um ein vielfaches kleiner. Die Analysestrategie der Fermi Bubbles wird ohne Modifikation verwendet, um simulationsbasiert die Sensitivität von ANTARES für einen Neutrinofluss aus dieser zentralen Region abzuschätzen. Es zeigt sich, dass ANTARES sensitiv genug ist, eine mögliche Neutrinoemission aus dieser Region oberhalb von $E_{\text{cutoff},\nu} \approx 200 - 500 \text{ TeV}$ zu begrenzen. Diese Vorstudie legt nahe, die zentrale Region in einer zukünftigen separaten ANTARES Analyse zu untersuchen. Die Sensitivität von ANTARES lässt sich dabei noch steigern, indem die Jahre nach 2015 zur Analyse hinzugenommen werden und die Analyse auf den anderen Modellfluss optimiert wird.

Statement on the author's personal contributions

The construction and operation of neutrino telescopes in the deep sea is a major collaborative effort. The same applies also for the simulation and reconstruction chains. Here, the work of many people has to interlock to produce the final analysis results. Hence, I cannot claim full credit for all the ingredients necessary to arrive at the results presented within this thesis. To avoid a detailed outline at the beginning of each chapter, I state my own contributions and achievements for KM3NeT/ORCA ([Part II](#)), ORCA in the following, and ANTARES ([Part III](#)) here in a summarised form.

In [Part II](#) my work on ORCA is presented. My PhD work on ORCA started after the simulations and sensitivity studies for the 'Letter of Intent for KM3NeT 2.0' [1], short LoI, had been finalised. The ORCA part of the LoI studied primarily the sensitivity to the neutrino mass ordering, using a model detector with similar size but regular spacing of the sensor modules.

A paper draft [2] for an update of the ORCA sensitivity to the neutrino mass ordering and other oscillation parameters with respect to the LoI is currently being reviewed by the publication committee of KM3NeT. Corresponding authors besides myself are J. Hofestädt, M. Perrin-Terrin. The study now features a more realistic detector simulation which meets all constraints for deployment. In addition, a new low-energy trigger is included to lower the detection threshold of the instrument, event classification is improved, the oscillation parameter fit has been upgraded and new systematics are included. As part of this draft, the sensitivity to $\bar{\nu}_\tau$ appearance – not yet analysed for the LoI – is presented. My efforts for ORCA were centred around these improvements.

For the corresponding chapters, I would like to outline my own contributions and emphasise the added value achieved compared to the LoI.

1) Trigger studies including the new low-energy MXShower trigger in [Sec. 9](#).

- For the post-LoI Monte Carlo simulations, I performed an optimisation of all trigger parameters in [Sec. 9.2](#). The MXShower trigger has been implemented by the Collaboration (M. de Jong) and is available within the JPP [3] software framework. I have optimised ([Sec. 9.2.2](#)) and evaluated ([Sec. 9.3](#)) the performance of this trigger in detail for the first time in Monte Carlo mass productions. The optimised parameters are now also used for the first 6% of the detector already installed and taking physics data in the deep sea.
- The MXShower trigger lowers the detection threshold of the instrument, thus increasing the impact of pure noise in the analysis chain. To study this impact in detail, I generated a complete simulation set of pure noise simulations (the same constant background

of single and multiple coincident photon hits was assumed for all photomultiplier tubes (PMTs) from trigger to analysis stage, except for the track reconstruction, which was run by L. Quinn. With this, I could show, that reconstructed pure noise can be rejected efficiently using Random Decision Forest classifiers in [Sec. 11.3](#), and thus do not significantly impact neutrino analyses.

- The stability of the trigger rates against bioluminescence bursts thanks to a high-rate veto is verified in [Sec. 9.4](#). For this, the bioluminescence burst simulation tool tuned on rate distributions measured in ANTARES developed by J. Hofestädt [4] is used to obtain predicted distributions for the background rates of PMTs. I have used the trigger software of the Collaboration and modified it to simulate individual PMT backgrounds with the rates provided by this tool.
- In [Sec. 9.4.3](#) I study the expected efficiency loss of the instrument due to high background rates and broken channels. Results suggest, that the loss is negligible for $\bar{\nu}_\tau$ appearance, but should be accounted for in the future at lower energies, such as e.g. the sensitivity to the neutrino mass ordering.
- In [Sec. 9.6](#), I have optimised the MXShower for several denser versions of ORCA, named SuperORCA. As input for the trigger software, I used SuperORCA simulation files generated by J. Hofestädt. With the resulting optimal settings I have produced triggered output files which have been further processed and used in SuperORCA studies for the ‘Letter of Interest for a Neutrino Beam from Protvino to KM3NeT/ORCA’ [5] and in Ref. [6].

2) Event type identification using Random Decision Forests in [Sec. 11](#):

- The C⁺⁺ implementation of the Random Decision Forest (RDF) classifier in Ref. [7] used previously in ANTARES and also for the LoI is used for continuity.
- To be able to train classification models, I have merged the output from the different reconstruction algorithms. After extracting the best-fit result parameters and adding additional variables, I generated flat summary files, which are straightforward to use at analysis level. For convenience, I implemented a python wrapper around the RDF classifier.
- The hit-based features, which boost performance of the classifier ([Sec. 11.2.4](#)) have been developed in collaboration with J. Hofestädt.
- A main change with respect to the LoI is that separate classifiers are trained on each classification task. Like this it is straightforward to reject each of the background components (atm. muons, pure noise) efficiently, and several event classes (shown in [Sec. 11.4.1](#)) can be defined for analysis.
- The detector performance in [Sec. 11.6](#) and the classifier performance in [Sec. 11.3](#) and [Sec. 11.4](#) are part of the above-mentioned paper draft [2]. This is indicated in the captions of plots where applicable.

3) Study of ORCA’s sensitivity to $\bar{\nu}_\tau$ appearance, [Sec. 12.3](#):

- For the sensitivity of $\bar{\nu}_\tau$ appearance the ParamNMH [8] software for neutrino oscillation parameter fits is used. Over the last years it has been mainly developed at CPPM (Marseille) by J. Brunner, L. Quinn and, currently, M. Perrin-Terrin.
- For the fit of $\bar{\nu}_\tau$ normalisation, I implemented a necessary extension which is now part of the main project from the tagged version v5.1 onwards.
- The sensitivity analysis for an 115 DUs ORCA detector in [Sec. 12](#) has been performed entirely by myself.
- Since the analysis for 115 DU suggested that $\bar{\nu}_\tau$ appearance could be studied with competitive sensitivity already with an early phase ORCA during construction, I prepared a full set of MC simulations from trigger-stage onwards. The trained models and simulation files have been used to study the sensitivity to measure the atmospheric oscillation parameters and $\bar{\nu}_\tau$ appearance with results presented in Ref. [9]. The $\bar{\nu}_\tau$ appearance results presented therein were contributed by L. Maderer in the scope of his Master's thesis [10] using the SWIM framework; cross checks with a second framework, MONA, have been prepared by B. Strandberg. To both I have contributed in terms of intense discussions/suggestions and in preparing the classed datasets as input to the analysis codes.

[Part III](#) covers my work on the search for neutrino emission from the Fermi Bubbles with ANTARES. A first search for a neutrino flux from the Fermi Bubbles with ANTARES (corresponding author: V. Kulikovskiy) had been published in Ref. [11] and analysed only four years of track signatures. Thereafter I have continued the analysis. Already in the scope of my Master's thesis, an additional two years of data had been added (presented in [12]).

During the PhD, I continued working on this topic. First, I analysed the full livetime of ANTARES, 2008–2015, for which at the time of the analysis corresponding run-by-run Monte Carlo simulations had been available (presented in [13], cf. [Sec. 17.2](#)), i.e. two additional years were added. Thereafter, the same data-set was analysed for shower-like event signatures (cf. [Sec. 17.3](#)), and combined limits for the all-flavour neutrino flux from the Fermi Bubbles (cf. [Sec. 17.4](#)) were derived (and presented in [12]). Both for the track- and shower-channel, I have performed the analysis and comparisons between data and Monte Carlo simulations entirely myself.

The work is now continued within the collaboration, in a search for a signal from the – meanwhile more promising – central outflow region close to the Galactic Centre. Using the analysed 8–year dataset without further optimisation, a first sensitivity estimate for the central region is provided in [Sec. 18](#).

Part I

Neutrinos – from generation to detection



This part starts with an introduction why neutrinos are both an interesting object to study fundamental particle physics and an outstanding messenger for astronomy in [Sec. 1](#). Then neutrinos are accompanied along their path. The generation of neutrinos ([Sec. 2](#)), their propagation from source to detector ([Sec. 3](#)), and their interactions and event signatures in deep-sea neutrino detectors ([Sec. 4](#)) are described. Finally, the ingredients relevant for their detection are explained in [Sec. 5](#).

This sets the foundation for the other parts of this work, which specialise on tau-neutrino appearance in [Part II](#) and the search for Galactic neutrino emission from the ‘Fermi Bubbles’ in [Part III](#). Hence, this part ends with a motivation why the KM3NeT/ORCA detector, currently under construction, and the ANTARES telescope, which has been collecting data for more than a decade, are the instruments of choice for the respective studies.



All that is gold does not glitter, Not all those who wander are lost; The old that is strong does not wither, Deep roots are not reached by the frost. – J.R.R. Tolkien, The Fellowship of the Ring

Part I: Neutrinos – from generation to detection

1 A short overview on neutrino physics and neutrino astronomy

1.1 | The neutrino, a special particle

In a “desperate” attempt to explain the continuous energy distribution of electrons observed in radioactive beta decay spectra and the seemingly violated conservation of angular momentum, Wolfgang Pauli postulated the neutrino in a letter to the “radioactive” community in 1930 [14]: An electrically neutral particle of spin $\frac{1}{2}$, travelling with “subluminal speed”. In the letter he also asked about the experimental prospects for a detection in case of “similar to tenfold higher attenuation length compared to gamma-rays”.

Today, we know that this guessed attenuation length was overoptimistic. With a cross-section only of order $\sigma/E \approx 10^{-42} \text{ m}^2/\text{GeV}$ [15, Sec. 50], it was not before 1956 that the neutrino was experimentally confirmed by the Cowan–Reines reactor neutrino experiment [16].

Like for the charged fermions – up-type quarks (u, c, t), down-type quarks (d, s, b) and leptons (electron, e , muon, μ , and tau lepton, τ) – three experimentally confirmed neutrino **flavours** – the electron-, muon- and tau-neutrino ($\nu_{e,\mu,\tau}$) – exist and are associated with the charged leptons,

$$\begin{pmatrix} e \\ \nu_e \end{pmatrix}, \begin{pmatrix} \mu \\ \nu_\mu \end{pmatrix}, \begin{pmatrix} \tau \\ \nu_\tau \end{pmatrix}. \quad (1.1)$$

Each fermion comes with its anti-particle partner of opposite charge, where $\bar{\nu}$ is the notation for anti-neutrinos.

Ever since their detection, neutrinos have taken a special role in the Standard Model of particle physics (SM). Being the only spin $\frac{1}{2}$ fermion without electric charge, they only interact via the weak force by the exchange of W^\pm and Z^0 bosons¹. While all other fermions in the SM due to their charge are necessarily Dirac spinors, neutrinos could possibly be of Majorana type implying they could be their own anti-particle. Taking Pauli’s other vague statement – that neutrinos are subluminal – in the literal sense is particularly interesting from today’s point of view. Originally postulated as massless particles in the SM, an extension was necessary to explain the observation of neutrino oscillations through which neutrinos can change their flavour during propagation. In the established picture the three neutrino flavour eigenstates (ν_e, ν_μ, ν_τ) are admixtures of three mass generations (ν_1, ν_2, ν_3). Neutrino oscillation implies that neutrinos must carry small masses and thus propagate with $v \lesssim c$.

The scale of neutrino masses is however at least six orders of magnitude below the electron e as can be seen from Fig. 1.1. While intuitive theories beyond the SM, like the see-saw mechanism (see e.g. [18] for a review), exist that could explain the large mass gap between

¹and of course gravity, which is safely ignored as far as the work of this thesis is concerned...

1. A short overview on neutrino physics and neutrino astronomy

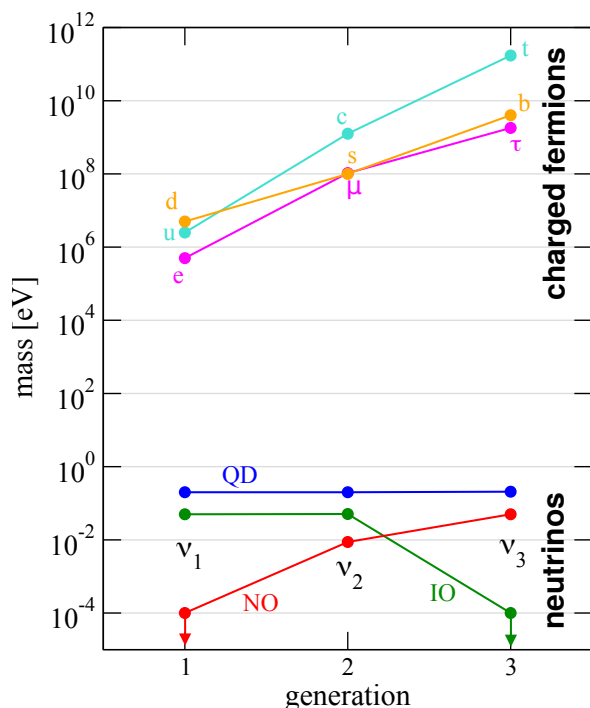


Figure 1.1: Mass spectra of the fermions of the Standard Model. For neutrinos three possible mass spectra are shown: Normal Ordering (NO), Inverted Ordering and a Quasi-Degeneracy (QD). Taken from Ref. [17].

neutrinos and other fermions, the unresolved neutrino mass spectrum still leaves room for surprises: Concerning the neutrino mass ordering (NMO), there is a non-conclusive hint towards normal ordering (NO, i.e. $m_1 < m_2 \ll m_3$) from global fits to oscillation data [19]. Yet, inverted ordering (IO, i.e. $m_3 \ll m_1 < m_2$) would imply a neutrino mass spectrum for the three generations that behaves differently compared to all the charged fermions. The same is true if the mass splittings between generations are small compared to the still unknown absolute neutrino masses, which would result in a quasi degenerate (QD) neutrino mass spectrum.

The small cross-section and missing electric charge make neutrinos an outstanding probe for particle physics at long distances on the one side, and an ideal messenger for astronomy on the other. From a particle physics perspective, neutrinos are an interesting candidate for physics beyond the Standard Model and the currently accepted picture of 3×3 neutrino mixing between mass- and flavour-eigenstates. The work on KM3NeT/ORCA, or short ORCA, in [Part II](#) will focus on this first aspect. On the other hand, unlike other astronomical messengers, neutrinos are not deflected by (inter-) galactic magnetic fields; they escape dense media and can be observed over large distances without significant attenuation of the flux. The work on ANTARES in [Part III](#) will focus on this second aspect. Artists' impressions of the two instruments used in this work are shown in [Fig. 1.2](#).

1.2 | Very-large-volume neutrino detectors

Since KM3NeT/ORCA and ANTARES have already been mentioned, it is useful to briefly summarise their key properties, and the other similar instruments here.

ANTARES The ANTARES (Astronomy with a Neutrino Telescope and Abyss environmental REsearch) neutrino telescope has been taking data since 2008 in its final configuration [21].

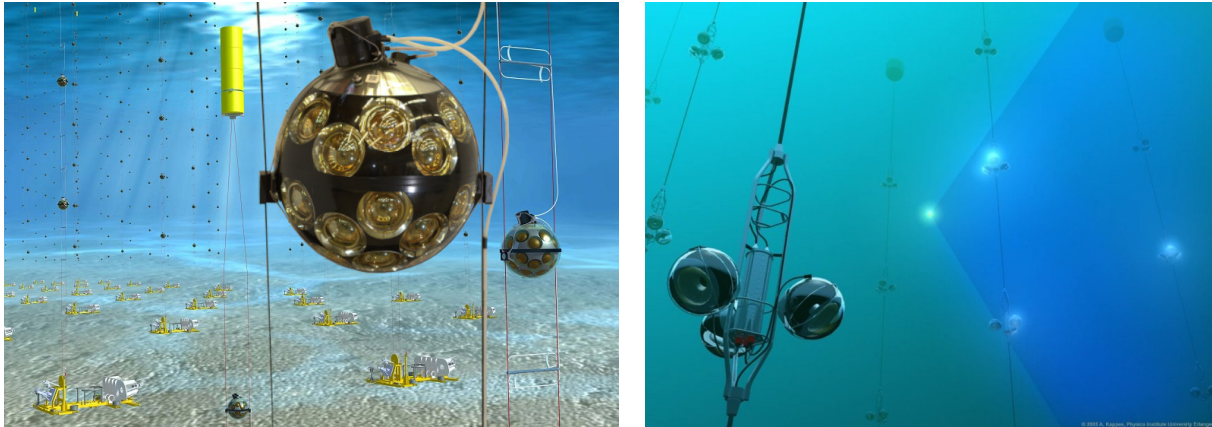


Figure 1.2: Artists' impressions of the KM3NeT (left, graphic by E. Berbee / Nikhef, overlaid with a KM3NeT/DOM from [20]) and ANTARES (right, graphic by A. Kappes / then ECAP) detectors.

ANTARES is installed in a depth of 2.5 km below sea-level around 40 km off-shore Toulon in France. In total, 885 optical sensor modules are distributed over twelve detection lines. The detection lines are about 480 m long, of which ~ 380 m are instrumented (the bottom 100 m hold no sensors) with a spacing of ~ 60 m between lines. The instrumented volume amounts to ~ 0.01 km³. ANTARES has best performance in the energy range of ~ 1 -100 TeV, but is able to study atmospheric neutrinos down to $\mathcal{O}(10$ GeV). The original goal of ANTARES was to demonstrate the feasibility of reliably operating a neutrino telescope and detect neutrinos in the deep sea. ANTARES has fulfilled this goal and even more. Since its construction in 2008 it has continuously delivered data² for more than twelve years now and continues operation beyond the planned dismantling, although with meanwhile only ten detection lines still being operational.

KM3NeT KM3NeT [1] is a research infrastructure under construction in the abysses of the Mediterranean sea. The Collaboration aims at constructing two next-generation deep sea neutrino telescopes with a common technology but optimised for different science goals, ARCA and ORCA (Astroparticle / Oscillation Research with Cosmics in the Abyss).

The different goals can be met by arranging the common sensor modules more densely in ORCA than in ARCA. More precisely, the vertical spacings between sensor modules is 9 m and 36 m between the 18 sensor modules on each detection line. The horizontal spacings between detection lines are 20 m and 90 m.

ARCA is being built off-shore Capo Passero, Sicily, and is optimised for astronomy and with best sensitivity towards Galactic neutrino sources. To this day, two detection lines are installed and have delivered data. However, data-taking is stalled until a reworking of the sea floor infrastructure scheduled for 2021. Currently, 230 detection lines are proposed, which are going to instrument a volume of ~ 1 km³.

ORCA is located close to the ANTARES site. Since end of January 2020, six out of an envisaged total 115 detection lines are taking data. The detector is optimised for neutrino energies between ~ 3 GeV and 100 GeV to study neutrino properties using atmospheric neutrinos. The

²With only few periods of several weeks continuous off-time due to extremely bad environmental conditions during some years in spring and interruptions due to maintenance.

1. A short overview on neutrino physics and neutrino astronomy

Table 1.1: Fundamental particles of the Standard Model. Vector bosons do not couple to the fermions of rows below.

	fermions			vector bosons	scalar bosons
quarks	u	c	t	g	H
	d	s	b	γ	
leptons	e	μ	τ	Z^0, W^\pm	
	ν_e	ν_μ	ν_τ		

prime scientific goal is the determination of the neutrino mass ordering (NMO), one of the remaining unknowns assuming unitary 3×3 neutrino mixing. With 6.7 Mm^3 instrumented volume, ORCA is smaller than ANTARES, but has more than 10-fold higher density of sensors.

Other very-large-volume neutrino experiments The cubic-kilometre (1 km^3) instrumented volume IceCube detector is taking data in the South Pole ice in its final configuration since 2010 and has produced remarkable results by detecting a diffuse astrophysical neutrino flux and by identifying a first point-source candidate for neutrino emission (see [Sec. 2.3](#)). The central region has a higher instrumentation density in order to measure neutrino oscillations down to $\sim 10 \text{ GeV}$.

An additional dense in-fill IceCube Upgrade [22] array is meanwhile funded and scheduled for deployment. As a precursor for a proposed ~ 10 times larger array, IceCube-Gen2 [23], it will test new detector technology. In addition, the analysis of already recorded IceCube data will benefit from the Upgrade's additional calibration measurements and the better determination of the optical properties of the bulk ice.

Furthermore, the construction of the freshwater Cherenkov detector Baikal-GVD in lake Baikal is ongoing. Baikal-GVD is optimised for TeV–PeV energies. It has surpassed ANTARES in instrumented volume and is foreseen to reach 0.4 km^3 in 2021 [24].

1.3 | Neutrino interactions in the Standard Model

The Standard Model of Particle Physics (SM) is an extremely successful theory and comprises the 17 fundamental particles listed in [Tab. 1.1](#). They are twelve spin $\frac{1}{2}$ fermions and five bosons of integer spin. The SM describes the interactions of the particles via the strong, the electromagnetic, and the weak force; the latter two being unified in the electroweak theory. Vector bosons act as mediators for these forces. Particles get their mass through the Higgs field, whose excitation is the scalar Higgs Boson (H). Its experimental discovery [25, 26] has completed the set of SM particles, such that the SM is a self-contained theory.

Neutrinos do not carry colour³ nor electric charge⁴ and can only interact weakly by exchange of W^\pm bosons in charged current (CC) interactions or Z^0 bosons in neutral current

³Neutrinos therefore do not take part in strong interactions mediated by the gluon g . The strong force is e.g. responsible for the formation of bound quark states like protons and neutrons.

⁴As opposed to all the other charged fermions, neutrinos therefore cannot interact electromagnetically by coupling to the photon γ . The electromagnetic force is responsible for electric and magnetic fields, and light.

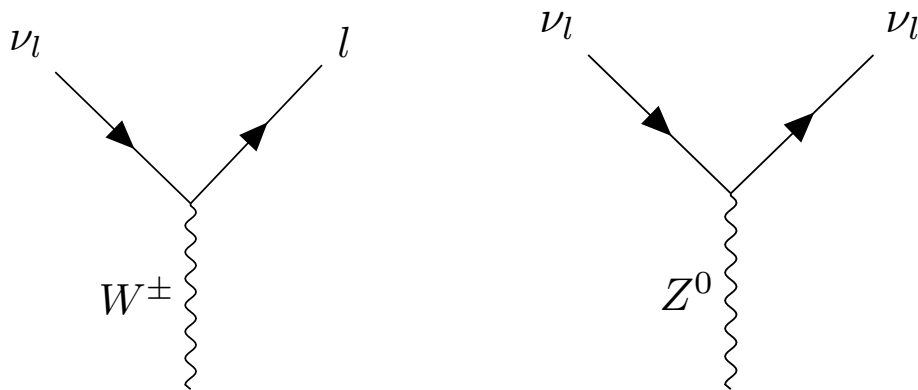


Figure 1.3: Feynman diagrams for the fundamental neutrino charged current (CC; left) and neutral current (NC; right) interaction vertices. For neutrinos with flavour $l \in \{e, \mu, \tau\}$.

(NC) interactions. The fundamental Feynman vertices for the couplings to neutrinos are shown in Fig. 1.3.

Noteworthy properties of the weak interaction are:

- The weak CC vertex can convert between charged lepton and the neutrino of the same flavour. Lepton number is however conserved in weak interactions and no cross-generation couplings are allowed.⁵ This implies, for example, that the leptonic decay of τ^- must involve neutrino and anti-neutrino, $\tau^- \rightarrow \mu^- \bar{\nu}_\mu \nu_\tau$, and $\tau^- \rightarrow \mu^- \gamma$ is forbidden (cf. Sec. 6.2.2).
- Weak interaction violates CP-symmetry – the product of charge conjugation and parity.⁶ CP violation has been observed in the quark sector, but its size is too small to explain the matter-antimatter symmetry in the universe. CP violation in the lepton sector might be large (cf. Sec. 6.1), but is not strongly constrained by current experiments.
- The weak force depends on chirality – or, handedness – of particles. At the energies relevant for this work ($E_\nu \gg m_\nu$), handedness becomes equivalent to helicity $h = \frac{\mathbf{p}}{|\mathbf{p}|} \cdot \mathbf{s}$, the projection of the spin vector \mathbf{s} on the momentum \mathbf{p} axis. Particles are called righthanded (lefthanded) when spin and momentum point in same (opposite) direction. The weak interaction only couples to left-handed ν and right-handed $\bar{\nu}$.⁷

⁵This is different for quarks, where cross-generation couplings are possible via the CKM mixing.

⁶Simply put, under CP symmetry the exchange of particles by their anti-particle partners was assumed to be the equivalent to the space-time mirrored process.

⁷Since neutrinos only interact weakly, right-handed ν do not couple to any SM interaction and are therefore referred to as ‘sterile neutrinos’.

2 Generation of neutrinos

2.1 | Sources of neutrinos

After the photon, the neutrino is the second-most abundant particle in the universe. The flux of neutrinos in our environment extends over many orders of magnitude falling off steeply in energy with the main contributors summarised in Fig. 2.1.

The neutrino fluxes for which an event-based detection has been possible are flanked by cosmological neutrinos at the lower end and by cosmogenic neutrinos at the upper end of the energy scale. **Cosmological neutrinos** are relics from the freeze-out shortly after the Big Bang and play an important role in the understanding of the cosmological evolution [28]. While they are abundant, there is no straightforward path for event-based detection due to their small energy and thus cross-section. **Cosmogenic neutrinos** [29] are generated in the interactions of ultra-high energy cosmic rays with photons of the cosmic microwave background on the other end of the energy scale. Owing to the small flux only future radio-detection telescopes [30] will reach effective volumes large enough such that statistically significant detection can come within reach.

There are several other neutrino sources below the detection threshold of very large volume Cherenkov telescopes like ANTARES and KM3NeT:

Solar ν : The Sun is a source of ν_e with the main contribution coming from the proton-proton fusion reaction to a deuteron ($p + p \rightarrow d + e^+ + \nu_e$).

Terrestrial anti- ν Radioactive decays in the Earth's interior are a source of $\bar{\nu}_e$.

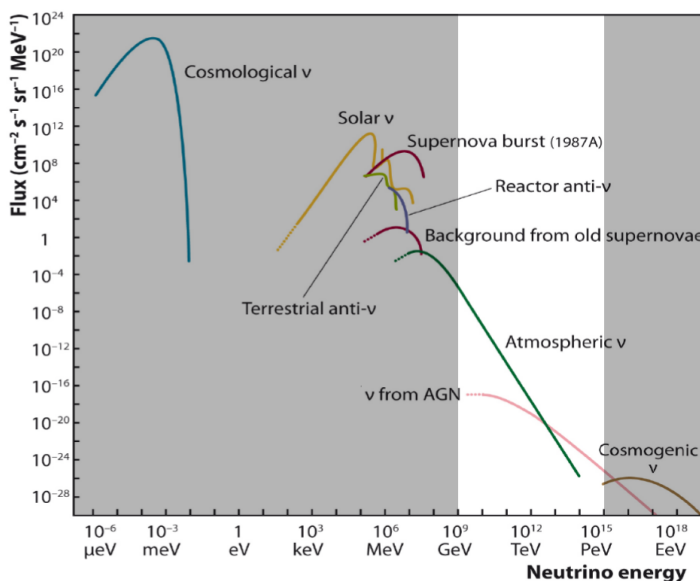


Figure 2.1: Neutrino flux across energy scales. Taken from [27]. Gray bands were added to emphasise the energy region of interest for KM3NeT and ANTARES region between 1 GeV and 1 PeV.

Reactor anti- ν Nuclear reactors generate $\bar{\nu}_e$ in radioactive decays.

In addition, **supernova (SN) bursts** generate an enormous flux of neutrinos. Depending on the SN distance, these may generate a detectable rate of sub-threshold neutrino events in neutrino telescopes. If the instrument's optical background is low enough, as it is the case for the IceCube telescope in Antarctica [31], SN bursts can be identified by an increase in the background baseline rate. Otherwise, and this is the approach pursued by KM3NeT, the time-series of multi-photon time-coincidences on the sensors can be used to search for SN bursts [32].

The white area in Fig. 2.1 highlights the region from GeV to PeV at which very large volume Cherenkov telescopes are sensitive. At GeV energies, neutrinos produced in the atmosphere dominate the flux. Since ORCA is mainly interested in these **atmospheric neutrinos** and their oscillations, they are discussed in more detail below, in Sec. 2.2. Neutrinos from outside the solar system start to outnumber the atmospheric flux beyond the TeV-scale. This flux is usually referred to as the **cosmic (or astrophysical) neutrino flux** (and is represented by ' ν from active galactic nuclei' in Fig. 2.1). While the diffuse cosmic flux has first been observed by the IceCube experiment [33] in 2013, identifying the individual source contributions still remains a central goal of neutrino astronomy. This branch is summarised in Sec. 2.3. The expected flux for the Fermi Bubbles, a potential source within our Galaxy analysed with ANTARES will be derived in more detail later in Part III.

2.2 | Atmospheric neutrinos

High energy cosmic rays (CRs) from outer space constantly impinge on the Earth's upper atmosphere. They are predominantly composed of protons (95%) with the remaining part consisting of helium (4%) and heavier nuclei up to iron (1%).

Upon interaction with air nuclei, CRs produce cascades of secondary particles. At the beginning of the cascade, where the available energy per particle is high, resonances with large invariant masses and hadrons with c -quark content (like D -mesons) can be produced. In their decays they give rise to the high energy tail of the atmospheric neutrino flux. This is commonly referred to as the 'prompt' component in the atmospheric flux. In the further evolution of the cascades, kaons and pions start to dominate the particle content. In the decay of neutral pions, $\pi^0 \rightarrow \gamma\gamma$, electromagnetic sub-showers are initiated. The atmospheric neutrino flux generated at this stage is referred to as the 'conventional' flux and it is mainly produced in the decays of kaons and charged pions.

The decays of charged kaons¹

$$\begin{aligned} K^+ &\longrightarrow \mu^+ \nu_\mu \quad (\text{leptonic, } 64\%) \\ K^+ &\longrightarrow \pi^+ \pi^0, \pi^+ \pi^+ \pi^-, \pi^+ \pi^0 \pi^0 \quad (\text{hadronic, } 28\%) \\ K^+ &\longrightarrow \pi^0 e^+ \nu_e, \pi^0 \mu^+ \nu_\mu \quad (\text{semileptonic, } 8\%) \end{aligned} \tag{2.1}$$

¹and analogous for the charge conjugate K^-

2. Generation of neutrinos

and neutral kaons

$$\begin{aligned}
 K_S^0 &\longrightarrow \pi^0 \pi^0 \quad (31\%) & K_L^0 &\longrightarrow \pi^\pm e^\mp \bar{\nu}_e \quad (41\%) \\
 K_S^0 &\longrightarrow \pi^+ \pi^- \quad (69\%) & K_L^0 &\longrightarrow \pi^\pm \mu^\mp \bar{\nu}_\mu \quad (27\%) \\
 & & K_L^0 &\longrightarrow 3\pi^0 \quad (20\%) \\
 & & K_L^0 &\longrightarrow \pi^0 \pi^+ \pi^- \quad (13\%)
 \end{aligned} \tag{2.2}$$

contribute to the atmospheric neutrino flux in their (semi-)leptonic decay modes directly. The hadronic modes and the semileptonic K_L^0 produce additional pions.

Charged pions decay via

$$\pi^+ \longrightarrow \nu_\mu \mu^+ \longrightarrow \nu_\mu \bar{\nu}_\mu \nu_e e^+, \tag{2.3}$$

where the decay for the negatively-charged π^- is again the charge conjugate.

From the final state particles in Eq. 2.3 a ratio $\bar{\nu}_\mu/\bar{\nu}_e \simeq 2$ is expected. While this is true at low energies, the ratio increases towards higher energies and towards the nadir/zenith. That is because an increasing fraction of muons do not decay in air, but reach the ground. There, they are stopped and only yield low energy neutrinos. These in turn are not detected in large volume neutrino telescopes. At higher energies also the contribution from kaon decays becomes more and more relevant. This can be seen in Fig. 2.2, which shows the individual contributions of different components to the total atmospheric flux for the three neutrino flavours.²

In particular, $\bar{\nu}_\tau$ neutrinos are produced exclusively in the prompt component in the decays of τ -leptons, with a $< 10\%$ contribution from D_s and D mesons [35], but not in the conventional component. As can be seen in the overall flux ratios to $\bar{\nu}_\mu$ in Fig. 2.3, the non-oscillated atmospheric neutrino flux is hence essentially free of $\bar{\nu}_\tau$ neutrinos below 10 TeV.

Isotropy in the primary cosmic ray flux leads to an approximate upward–downward symmetry of the generated neutrino flux in zenith, as well as isotropy in azimuth. This argument does not hold exactly, especially not below few-GeV energy, since [41]:

1. The geomagnetic field cuts off the proton flux at low energies. Low energy protons are trapped by the field lines and can enter the atmosphere only close to the poles. Geomagnetism also introduces east–west effects in the neutrino flux.
2. The solar wind varies over the solar cycle. Contrary to the naive assumption, the low-energy neutrino flux is suppressed during the maximum of solar activity. As the geomagnetic field lines are more compressed, the proton cut-off is shifted to higher energies.
3. Changes in temperature, or equivalently density, in the atmosphere induce seasonal variations.

All these effects are accounted for in detailed 3D simulations of the atmospheric neutrino flux carried out by the HKKM³ group [41] and are publicly available (see [40] for the flux tables

²Note that Fig. 2.2 shows the contributions from the immediate parents. In particular the $\bar{\nu}_e$ from the π^\pm decay in Eq. 2.3 will appear as μ -decay neutrinos.

³The efforts are led by M. Honda. Hence, the flux is sometimes also referred to as ‘Honda flux’. The remaining initials are contributed by Kajita, Kasahara and Midorikawa.

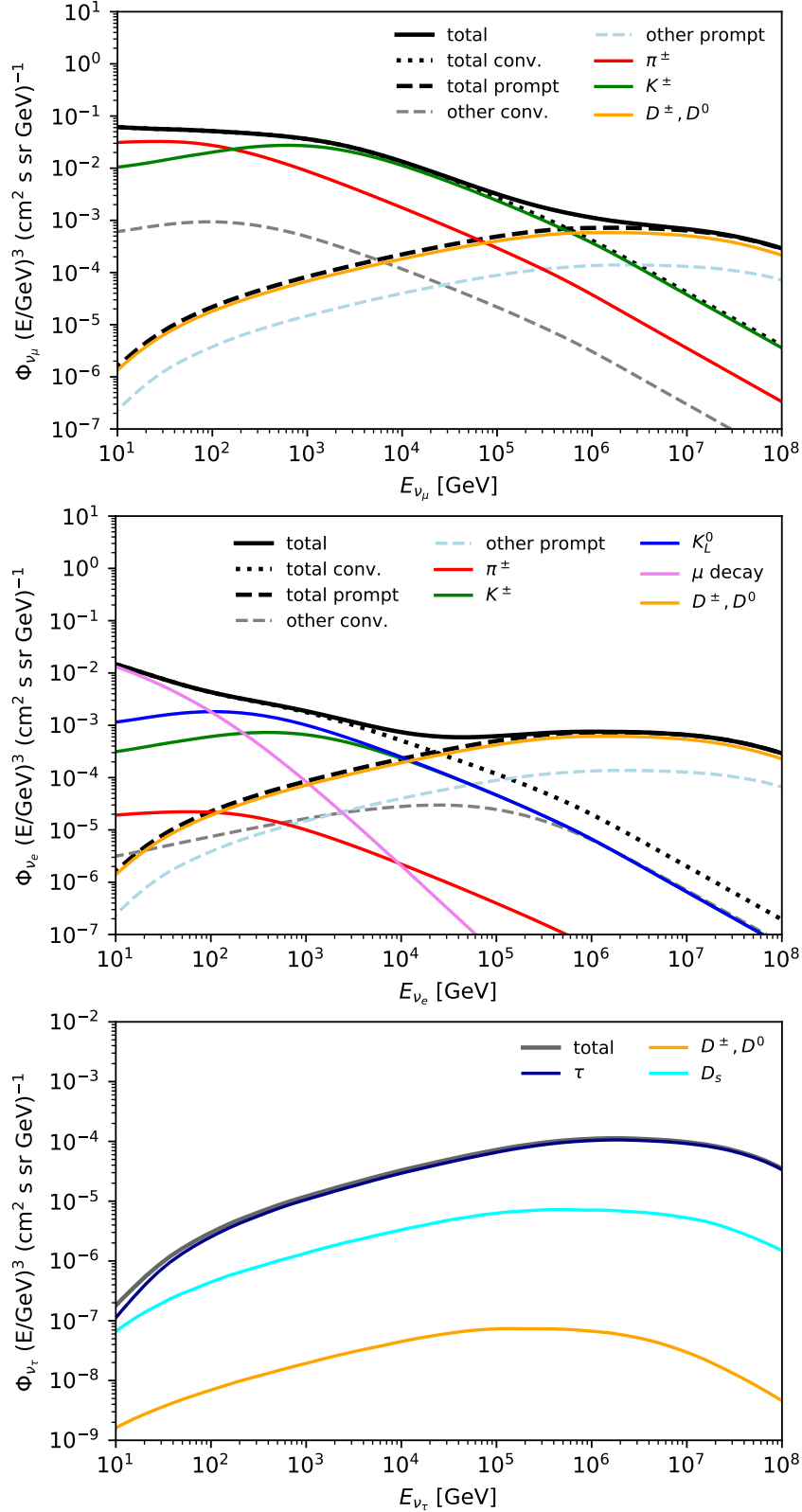


Figure 2.2: Individual parent contributions to the fluxes of $\vec{\nu}_e$, $\vec{\nu}_\mu$, and $\vec{\nu}_\tau$ arriving from 30° above horizon. Generated using example code in [34], and essentially identical to [35, Fig. 9] but using interaction model SIBYLL 2.3c [36].

2. Generation of neutrinos

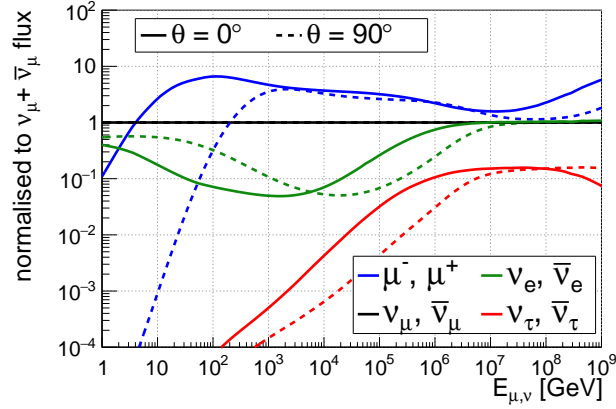


Figure 2.3: Flavour ratios of leptons at the surface normalised to the $\bar{\nu}_{\mu}$ flux. Figure as in [35, Fig. 10] but extended to lower energies using the flux calculation code MCEq [37]. Ratios are presented for the vertically downward-going (solid) and horizontal (dashed) lepton fluxes. Atmospheric model for the ORCA site from Ref. [38], the cH4a primary flux [39] and interaction model SIBYLL 2.3c [36] have been used to prepare the figure.

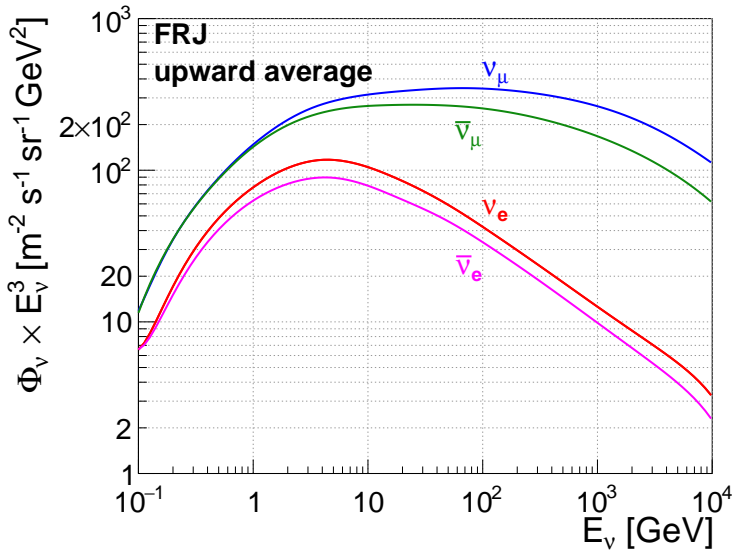


Figure 2.4: HKKM neutrino flux prediction averaged over upward-going directions as a function of energy for the Fréjus site. Data obtained from [40]. Plot analogous to those for other locations in Ref. [41].

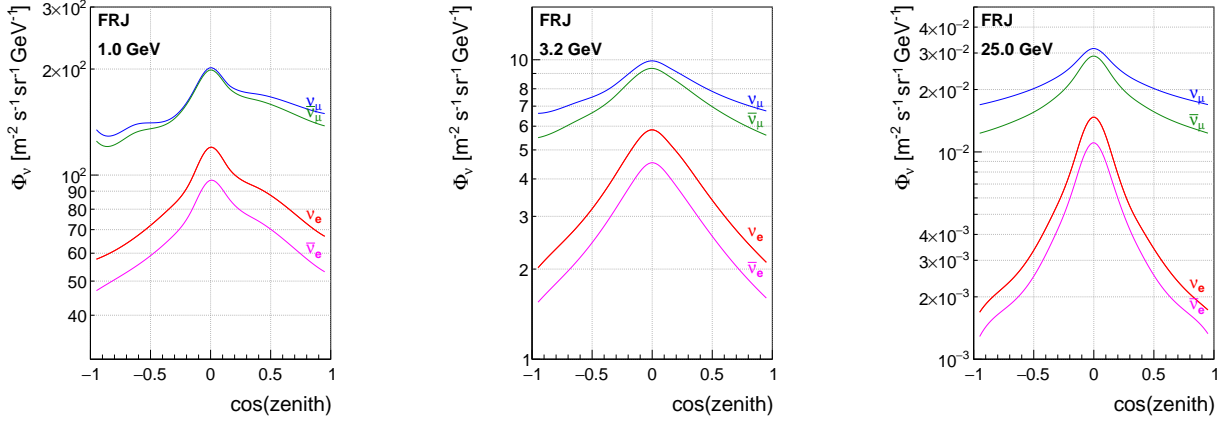


Figure 2.5: HKKM neutrino flux prediction as a function of zenith angle for the Fréjus site. Data obtained from [40]. Plots analogous to those for other locations in Ref. [41].

used throughout this work) for various detector sites. For ORCA, the azimuth averaged fluxes for the close-by⁴ Fréjus site can be used. The flux distributions at Fréjus as a function of energy and cosine of the zenith angle are shown in Fig. 2.4 and Fig. 2.5, respectively. The amplitude of the neutrino flux peaks at the horizon, where the traversed distance in the atmosphere is largest, and consequently the time for particles to decay during air shower evolution. The approximate upward–downward symmetry in the neutrino flux is broken at the few-GeV energy threshold of ORCA (cf. Fig. 2.5, left and middle panel). For ANTARES, the prompt component from Ref. [42] is added to the HKKM flux prediction at high energies.

2.3 | Cosmic neutrinos as astrophysical messenger

The cosmic (or astrophysical) neutrino flux also has its origin in hadronic interactions, just as the atmospheric flux. The most natural scenario is the π^\pm decay scenario, that is expected when ultra-high-energy protons interact with the material surrounding their source. In these interactions, π^\pm are produced and give rise to a neutrino flux in their decays. From Eq. 2.3, a flavour ratio of $(\bar{\nu}_e : \bar{\nu}_\mu : \bar{\nu}_\tau) = (1 : 2 : 0)$ is then expected at the source. Other source flavour ratios are in principle possible (see e.g. [43]). Besides more exotic scenarios, the flavour ratios $(\bar{\nu}_e : \bar{\nu}_\mu : \bar{\nu}_\tau) = (0 : 1 : 0)$ in case muons are damped in very dense environments before they are able to decay, and $(\bar{\nu}_e : \bar{\nu}_\mu : \bar{\nu}_\tau) = (1 : 0 : 0)$ in case of neutron decay, $n \rightarrow pe^- \bar{\nu}_e$, are rather straightforward to motivate.

For the detection of any astrophysical flux one needs to exclude that the neutrino flux originates from within the solar system. For violent sources with proton acceleration up to PeV energies, a spectral index in the proton flux of E^{-2} can be motivated from the Fermi acceleration mechanism [44, 45], and the produced neutrino flux will follow a similar energy spectrum. If the spectral index of emerging neutrinos is harder than that of the atmospheric flux, the astrophysical signal might be detectable at high neutrino energies. This procedure is viable for detecting neutrino fluxes from extended regions (e.g. the Fermi Bubbles in Part III) or a diffuse flux spread over the entire sky.

⁴ORCA location: 42°48' N, 6°10' E; Fréjus location: 43°26' N, 6°44' E

2. Generation of neutrinos

In 2013, the IceCube detector, a cubic-kilometre sized neutrino telescope at the South Pole, has been able to identify the diffuse astrophysical neutrino flux [33]. The IceCube data is up to now consistent with an isotropic emission and shows no clear indication that a significant portion of the measured diffuse flux originates from within our Galaxy.

For point source emission, the restriction to small regions in space or/and time in the analysis helps in suppressing the atmospheric background. The first – and up to now only – identified candidate for extra-galactic neutrino emission from a point source is the blazar TXS 0506+056 detected by IceCube in 2017 and together with the coincident observation of a flaring activity of TXS 0506+056 in other experiments heralded the era of multimessenger astronomy [46, 47].

3 Propagation

3.1 | Flux attenuation

Thanks to their small cross section, neutrinos propagate practically unattenuated over extreme distance through space, even from extragalactic sources. However, since neutrino telescopes typically look for neutrinos coming from below the horizon to suppress atmospheric muons, Earth absorption starts to play a role above $\sim 10^3$ GeV. At higher energies¹ the transmission probability is exponentially suppressed and can be written as

$$P_{\text{Earth}}(E_\nu, \theta_\nu) = e^{-N_A \rho_{\text{eff}}(\theta_\nu) \times \sigma_\nu(E_\nu)}, \quad (3.1)$$

where N_A is the Avogadro number, $\sigma_\nu(E_\nu)$ is the interaction cross section with matter, and ρ_{eff} the effective matter traversed by a neutrino incident under zenith angle θ_ν . The right hand side involves an integration along the matter density profile of the Earth according to the PREM model [48], which is shown in Fig. 3.1. At the abrupt step from the Earth's mantle to the outer core, the matter density almost doubles and corresponds to a neutrino origin from $\cos(\theta_\nu) \approx -0.83$, or $\theta_\nu = 146^\circ$ ².

For neutrinos traversing the entire Earth, half of the flux is suppressed at ~ 30 TeV [49], such that Earth absorption needs to be accounted for only in ANTARES, but not for oscillation measurements with ORCA below ~ 50 GeV.

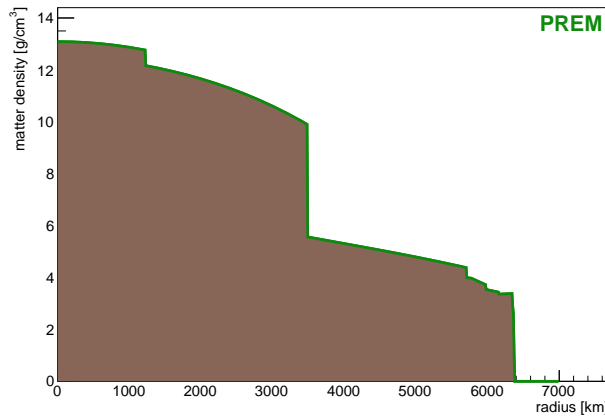


Figure 3.1: The Earth's matter density profile according to the Preliminary Reference Earth Model (PREM) [48].

¹For high energies $\sigma(E_\nu) \propto E_\nu$, as will be motivated in Sec. 4.

²In the used convention, $\theta_\nu = 180^\circ$ corresponds to a particle reaching the detector from straight below.

3.2 | Neutrino oscillation

Neutrino oscillation on the other side affects both atmospheric neutrino fluxes in ORCA and Galactic neutrino fluxes in ANTARES. Since neutrino oscillation studies are the first and foremost goal of ORCA, this phenomenon is described on a theoretical basis in detail in this section. The direct effects for the oscillation studies in ORCA and Galactic searches in ANTARES are then summarised in a more visual way thereafter.

3.2.1 | Discovery of neutrino oscillation

Two decades ago the precise measurement of the invisible Z^0 decay width at the e^+e^- collider LEP [50] at CERN has shown that in analogy to the known three flavour generations of charged leptons (e^\pm, μ^\pm, τ^\pm) there are also three corresponding light generations of leptons without electric charge, the three neutrino flavours ν_e, ν_μ and ν_τ . In the SM neutrinos were originally assumed to be massless. However, neutrinos were observed to oscillate, i.e. they change their flavour during propagation, which implies that they carry mass [51, 52, 53]. Today, the small extension to the standard model that the three flavour eigenstates (ν_e, ν_μ, ν_τ) are admixtures of three mass eigenstates (ν_1, ν_2, ν_3) is well established and as of today there are no experimental results that put this model of 3×3 neutrino mixing under serious pressure.

3.2.2 | Neutrino oscillation in vacuum

This commonly accepted picture is assumed during the explanation of neutrino oscillation here³; uncertainties, unknowns and a possible incompleteness of the presumed 3×3 mixing are detailed later in [Part II](#).

Theoretical framework In the generally accepted picture, neutrinos interact as flavour eigenstates ν_α ($\alpha = e, \mu, \tau$) in weak interactions. During free particle evolution on the other hand, they propagate as mass eigenstates ν_i ($i = 1, 2, 3$). In the following, Greek letters are used for flavour, Latin letters for mass eigenstates. The flavour eigenstates can be expressed as a linear combination of the mass eigenstates using the neutrino mixing matrix \mathcal{U} , named PMNS matrix⁴,

$$\begin{pmatrix} \nu_e \\ \nu_\mu \\ \nu_\tau \end{pmatrix} = \mathcal{U} \times \begin{pmatrix} \nu_1 \\ \nu_2 \\ \nu_3 \end{pmatrix} = \begin{pmatrix} \mathcal{U}_{e1} & \mathcal{U}_{e2} & \mathcal{U}_{e3} \\ \mathcal{U}_{\mu1} & \mathcal{U}_{\mu2} & \mathcal{U}_{\mu3} \\ \mathcal{U}_{\tau1} & \mathcal{U}_{\tau2} & \mathcal{U}_{\tau3} \end{pmatrix} \times \begin{pmatrix} \nu_1 \\ \nu_2 \\ \nu_3 \end{pmatrix}. \quad (3.2)$$

In case that the three flavour and mass eigenstates each form complete eigenbases, \mathcal{U} is a unitary matrix, $\mathcal{U}^* \mathcal{U} = \mathbb{1}_3$. As a direct consequence of unitarity, the overall normalisation is conserved. In simple terms, neutrinos disappearing from one flavour through oscillation need to appear as another flavour such that the total number of neutrinos stays constant.

³The formulae for neutrino oscillation in vacuum and matter follow Refs. [54], [55] and [15, c. 14]. The reasoning is similar to my earlier work in Ref. [56].

⁴which are the initials of Pontecorvo, Maki, Nakagawa, and Sakata who pioneered the concept of neutrino oscillation [57, 58]

Unitary assumed, the PMNS matrix can therefore be expressed in terms of rotational components⁵,

$$\mathcal{U} = \begin{pmatrix} 1 & 0 & 0 \\ 0 & \cos\theta_{23} & \sin\theta_{23} \\ 0 & -\sin\theta_{23} & \cos\theta_{23} \end{pmatrix} \begin{pmatrix} \cos\theta_{13} & 0 & \sin\theta_{13}e^{-i\delta_{\text{CP}}} \\ 0 & 1 & 0 \\ -\sin\theta_{13}e^{-i\delta_{\text{CP}}} & 0 & \cos\theta_{13} \end{pmatrix} \begin{pmatrix} \cos\theta_{12} & \sin\theta_{12} & 0 \\ -\sin\theta_{12} & \cos\theta_{12} & 0 \\ 0 & 0 & 1 \end{pmatrix}. \quad (3.3)$$

In addition to the three mixing angles ($\theta_{12}, \theta_{13}, \theta_{23}$), there is one additional complex parameter for the charge parity (CP) violating phase, δ_{CP} .

In the notation given in Eq. 3.3, two additional but currently undetermined Majorana phases are omitted, since they do not affect neutrino oscillation. They can however be non-zero if neutrinos turn out to be Majorana type particles.

The time evolution in the mass basis and likewise in the flavour basis can be expressed by the Schrödinger Equation:

$$i\frac{\partial}{\partial t} \begin{pmatrix} \nu_1(t) \\ \nu_2(t) \\ \nu_3(t) \end{pmatrix} = \mathcal{H}_0 \begin{pmatrix} \nu_1(t) \\ \nu_2(t) \\ \nu_3(t) \end{pmatrix}, \quad i\frac{\partial}{\partial t} \begin{pmatrix} \nu_e(t) \\ \nu_\mu(t) \\ \nu_\tau(t) \end{pmatrix} = \mathcal{H}_0^f \begin{pmatrix} \nu_e(t) \\ \nu_\mu(t) \\ \nu_\tau(t) \end{pmatrix}. \quad (3.4)$$

In vacuum the Hamiltonian \mathcal{H}_0 in the mass basis is diagonal

$$\mathcal{H}_0 = \begin{pmatrix} E_1 & 0 & 0 \\ 0 & E_2 & 0 \\ 0 & 0 & E_3 \end{pmatrix}, \quad E_i = \sqrt{m_i^2 + \mathbf{p}^2}, \quad (3.5)$$

with the usual notation for total energy E , mass m and momentum \mathbf{p} . With this, Eq. 3.4 is solved by plane waves and the propagation of the mass eigenstates becomes

$$|\nu_k(t)\rangle = e^{-i\mathcal{H}_0 t} |\nu_k(0)\rangle \quad (3.6)$$

in vacuum. Switching to the flavour basis using \mathcal{U} , the evolution of a flavour eigenstate in vacuum can then be written as a unitary transformation U_f as follows:

$$\begin{pmatrix} \nu_e(t) \\ \nu_\mu(t) \\ \nu_\tau(t) \end{pmatrix} = U_f \begin{pmatrix} \nu_e(0) \\ \nu_\mu(0) \\ \nu_\tau(0) \end{pmatrix} = \mathcal{U} e^{-i\mathcal{H}_0 t} \mathcal{U}^* \begin{pmatrix} \nu_e(0) \\ \nu_\mu(0) \\ \nu_\tau(0) \end{pmatrix}. \quad (3.7)$$

In the calculation of transition probabilities in vacuum, for ultra-relativistic neutrinos one can substitute

$$E_i \approx E_\nu + \frac{m_i^2}{2E_\nu}, \quad \mathbf{p} \approx E_\nu, \quad t \approx L, \quad (3.8)$$

such that Eq. 3.6 reduces to

$$|\nu_k(t)\rangle = e^{-i\frac{m_k^2 L}{2E_\nu}} |\nu_k(0)\rangle. \quad (3.9)$$

⁵The decomposition into the three matrices in Eq. 3.3, is often used also for illustrative reasons, since it stakes out the playgrounds for experiments being sensitive to different neutrino sources, namely and following Eq. 3.3 by their order: atmospheric ν , reactor ν , and solar ν .

3. Propagation

The transition probabilities between two flavours – which are measured by neutrino oscillation experiments – are then just the square of the transition amplitudes $\psi_{\alpha\beta}(t)$ from flavour state ν_α to ν_β evaluated at time t :

$$P_{\nu_\alpha \rightarrow \nu_\beta}(t) = |\psi_{\alpha\beta}(t)|^2 = |\langle \nu_\beta | \nu_\alpha(t) \rangle|^2 \quad (3.10)$$

For completeness, the transition probability in vacuum can be written as,

$$\begin{aligned} P_{\nu_\alpha \rightarrow \nu_\beta}(L) = & \delta_{\alpha\beta} - 4 \cdot \sum_{j>k} \Re(\mathcal{U}_{\alpha j}^* \mathcal{U}_{\beta j} \mathcal{U}_{\alpha k} \mathcal{U}_{\beta k}^*) \sin^2 \left(\frac{\Delta m_{jk}^2 L}{4E_\nu} \right) \\ & \pm 2 \cdot \sum_{j>k} \Im(\mathcal{U}_{\alpha j}^* \mathcal{U}_{\beta j} \mathcal{U}_{\alpha k} \mathcal{U}_{\beta k}^*) \sin^2 \left(\frac{\Delta m_{jk}^2 L}{2E_\nu} \right) \end{aligned} \quad (3.11)$$

subdivided to its real \Re , and imaginary \Im parts, where the latter is only present for CP-violating values of δ_{CP} .

In addition to the three mixing angles and δ_{CP} in the PMNS mixing matrix (see Eq. 3.3), the exponentials from Eq. 3.9 result in additional oscillatory terms depending on L/E_ν , with L being the distance from source to detector and E_ν the neutrino energy⁶, and on the squared mass differences between the mass eigenstates $\Delta m_{ij}^2 = m_i^2 - m_j^2$. Oscillation however does not reveal their absolute mass scale and – due to the sin squared – in vacuum not even the sign of the splitting.

Effects for ORCA and ANTARES To visualise the influence of vacuum oscillation on the analyses in Part II and Part III, the oscillation between ν_μ and ν_τ is considered. To first order this can be seen here as a two flavour oscillation, with consequently only one mass splitting $\Delta m_{2\nu}^2$ and angle $\theta_{2\nu}$.

$$\begin{aligned} P_{\nu_\mu \rightarrow \nu_\tau}^{2\nu}(L, E_\nu) = & \sin^2(2\theta_{2\nu}) \sin^2 \left(\frac{\Delta m_{2\nu}^2 \cdot L}{4E_\nu} \right) \\ \approx & \sin^2(2\theta_{23}) \sin^2 \left(1.27 \cdot \frac{\Delta m_{23}^2 [\text{eV}^2] \cdot L [\text{km}]}{E_\nu [\text{GeV}]} \right) \end{aligned} \quad (3.12)$$

is the two flavour oscillation formula, and the oscillation parameters may be set to the best-fit θ_{23} , Δm_{23}^2 [59]. The oscillation is plotted in Fig. 3.2 in units of the Earth diameter divided by 25 GeV, corresponding to the oscillation maximum of $\overline{\nu}_\tau$ neutrinos relevant for ORCA, on the lower axis. Keeping the L/E_ν ratio constant, the position of the oscillation maximum consequently shifts to lower energies for neutrinos not traversing the Earth's core. The second maximum is reached only for neutrinos with $\lesssim 9$ GeV at most, where ORCA is still in the efficiency turn-on for detecting $\overline{\nu}_\tau$ (cf. Sec. 9, Sec. 11.4).

For atmospheric neutrinos at TeV energies and beyond, $P_{\nu_\mu \rightarrow \nu_\tau}^{2\nu} \rightarrow 0$, such that neutrino oscillation can be safely ignored in the atmospheric flux background in ANTARES affecting

⁶The appropriate L/E_ν may be an experimental choice, although with more or less tight constraints set by the used source and its distance from the detector. Atmospheric neutrinos offer a wide range of both different pathlengths (zenith angles) and energy.

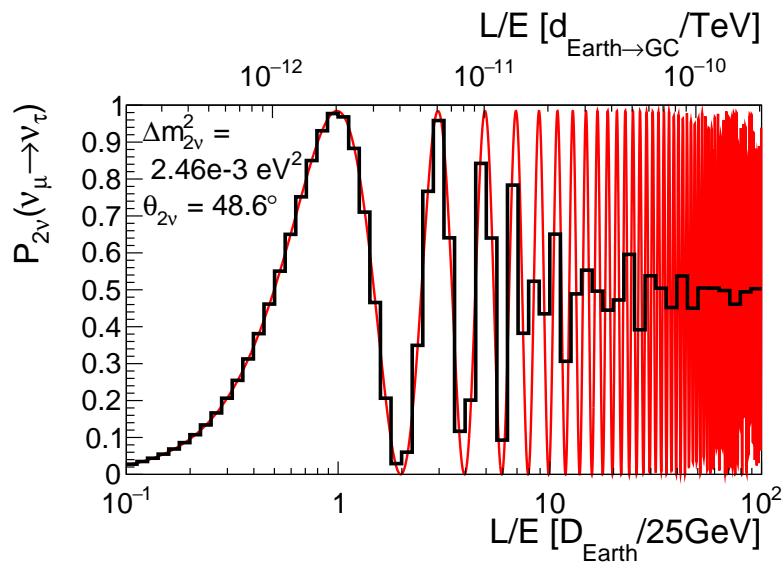


Figure 3.2: Two-flavour formula for $\nu_\mu \rightarrow \nu_\tau$ oscillation in units corresponding to the search scale for atmospheric neutrino analyses with ORCA and Galactic searches with ANTARES. Average oscillation probability is shown in black.

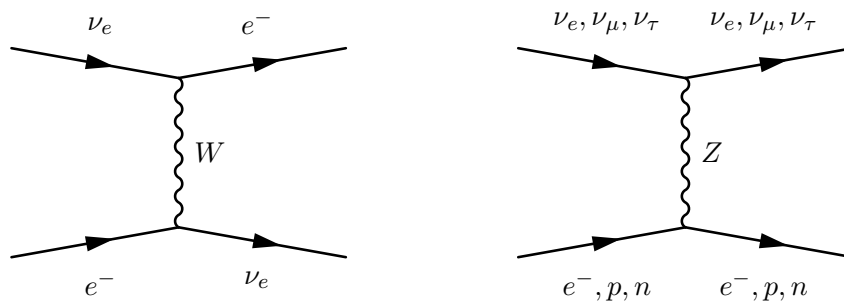


Figure 3.3: Feynman graphs for the coherent forward scattering of neutrinos.

searches for high-energy signal fluxes. The additional top axis in Fig. 3.2 sets the scale corresponding to the typical units relevant for Galactic distances. Even ~ 10 orders of magnitude below the relevant scale, the oscillation has averaged out (cf. black line) to an average transition probability of 50% for the close to maximum θ_{23} . In the standard π^\pm emission scenario in Sec. 2.3 (flavour ratio 1:2:0 at source) this redistribution results in an averaged equal portion of all three neutrino flavours (1:1:1) expected at the detector.

3.2.3 | Neutrino oscillation in matter

Theoretical framework The calculations above assume neutrinos that propagate through vacuum. In matter, neutrinos undergo coherent forward scattering as illustrated by the diagrams in Fig. 3.3. The neutral current (NC) identically couples to all flavours, and only introduces an overall phase shift. Due to the electrons in matter however, additional elastic charged current (CC) interactions exist for $\bar{\nu}_e$ only. The diagram for ν_e is shown in Fig. 3.3

3. Propagation

(left), the one for $\bar{\nu}_e$ is obtained by rotation of this diagram by 90° . As a consequence, $\bar{\nu}_e$ feel an additional matter potential,

$$V_{CC, \bar{\nu}_e} = \pm \sqrt{2} G_F n_e, \quad (3.13)$$

with electron number density $n_e \approx \rho N_A/2$ for an isoscalar target, and Fermi coupling constant G_F . Opposite $+$ ($-$) sign applies for (anti-)neutrinos, respectively.

The complete derivation in the three neutrino framework goes beyond the scope of this work. Instead only a rough motivation on the ingredients needed to calculate oscillation probabilities in matter is given in the following. For propagation through Earth, neutrino probabilities in matter are calculated numerically and the effects on $\bar{\nu}_\tau$ oscillation probabilities are shown below.

The main consequence of the additional matter potential is that the complete Hamiltonian is diagonal neither in the mass- nor in the flavour-basis. In the mass basis, it can be written as

$$\mathcal{H}_m = \mathcal{H}_0 + \mathcal{U}^* \begin{pmatrix} V_{CC, \bar{\nu}_e} & 0 & 0 \\ 0 & 0 & 0 \\ 0 & 0 & 0 \end{pmatrix} \mathcal{U}. \quad (3.14)$$

It is possible to diagonalise this Hamiltonian and the solution leads to effective quantities for the squared mass differences and mixing angles. Here, it shall be sufficient to motivate this by looking at the effective mixing angle derived for two-flavour mixing, where

$$\tan(2\theta_M) = \frac{\tan(2\theta)}{1 - \frac{2E_\nu V_{CC}}{\Delta m^2 \cos(2\theta)}}. \quad (3.15)$$

Mikheyev, Smirnov and Wolfenstein found [60, 61] that this can lead to a resonant enhancement of the oscillation for either neutrinos or anti-neutrinos (different sign in V_{CC}) depending on the sign of Δm^2 , named the MSW effect. Note that the vacuum case is recovered for $N_e \rightarrow 0$. For the electron density in the Earth's core (mantle), the resonance energy that can be calculated from the denominator in Eq. 3.15 is 3 (7) GeV.

In addition to this MSW resonance, the oscillation is enhanced for specific energy and zenith angle combinations. Due to the abrupt change in the matter density profile between mantle and core, the Earth's matter density can be seen as a 'castle-wall' profile. If the oscillation lengths in the core and mantle are matched with the traversed distance, this can lead to so-called 'parametric enhancement' effects in the transition probability.

Numerical calculation of matter oscillation The transition probabilities between ν_e , ν_μ , and ν_τ (and $\bar{\nu}$) in matter can be calculated using the OscProb [62] package. OscProb approximates the matter density profile with layers of constant densities.⁷ For a given neutrino zenith angle θ_z , the traversed layers and associated pathlengths can be calculated. A set of differential equations is then solved to calculate the transition probability between generated and detected flavour. The KM3NeT Collaboration meanwhile uses OscProb by default as it yields consistent results with other well-established oscillation codes⁸, with acceptable computing times and convenient usability with changing pathlengths and energies.

⁷In the default tables shipped with OscProb the PREM profile given in Fig. 3.1 is approximated by either 44 or 425 layers of constant densities.

⁸such as GLoBES [63] developed for long-baseline experiments

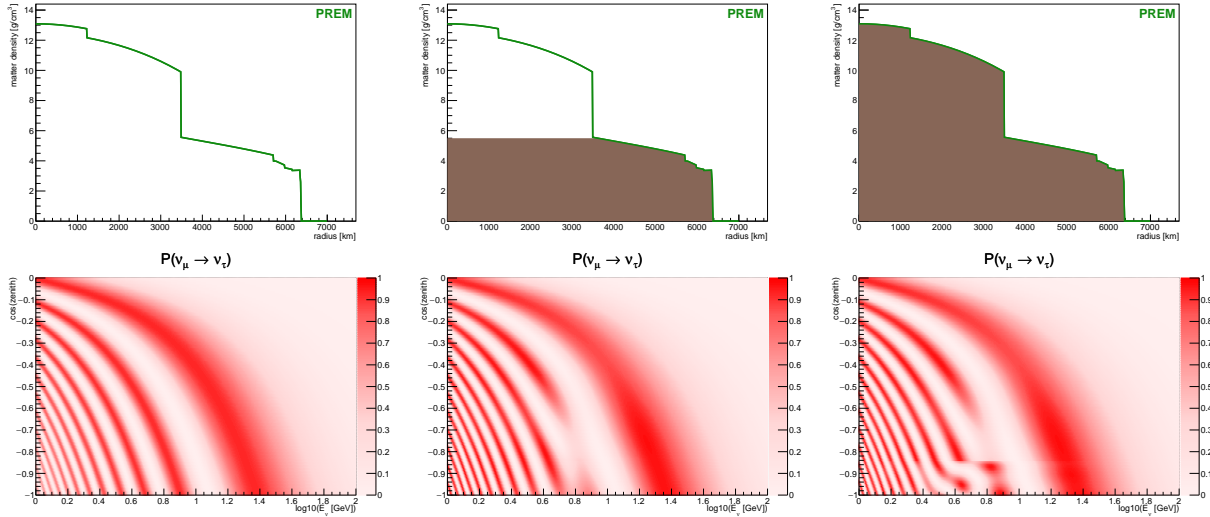


Figure 3.4: Effects of the Earth's matter density profile on the $\nu_\mu \rightarrow \nu_\tau$ oscillation probability. Calculated using OscProb [62].

Effects for ORCA The influence of matter on the oscillation probability from $\nu_\mu \rightarrow \nu_\tau$ in the three-neutrino framework is visible in Fig. 3.4 in energy and $\cos(\theta_z)$ dependent oscillograms. Oscillation probabilities can be compared for vacuum oscillation (left) with the oscillation in matter (right) depending on the density seen under different zenith angles. An intermediate model, where the core density is not higher than in the mantle is given to illustrate the change in the oscillation for $\cos(\theta_z) \lesssim -0.83$. The most prominent difference to the vacuum case is the dip around 7 GeV, for neutrinos traversing the mantle. Here the matter resonance leads to sizeable probability for $\nu_\mu \rightarrow \nu_e$ transition.

The large oscillation maximum at 25 GeV which is most relevant for $\bar{\nu}_\tau$ appearance is almost unaffected by matter effects. At lower energies resonant enhancement becomes evident for $4 \text{ GeV} \lesssim E_\nu \lesssim 10 \text{ GeV}$ when traversing the core ($\cos(\theta_z) \lesssim -0.83$). Since the matter resonance affects only ν but not $\bar{\nu}$ for NO (vice versa for IO), only one of the two oscillograms shows the distortion induced by the matter profile (see Fig. 3.5).

In summary, mostly $E_\nu \lesssim 10 \text{ GeV}$ are sensitive to the sign of the large mass splitting Δm_{13}^2 . This matter effect is exploited for the determination of the NMO. However, which NMO assumption is true has barely any effect on the measurement of $\bar{\nu}_\tau$ appearance in ORCA, as will be shown later.

3. Propagation

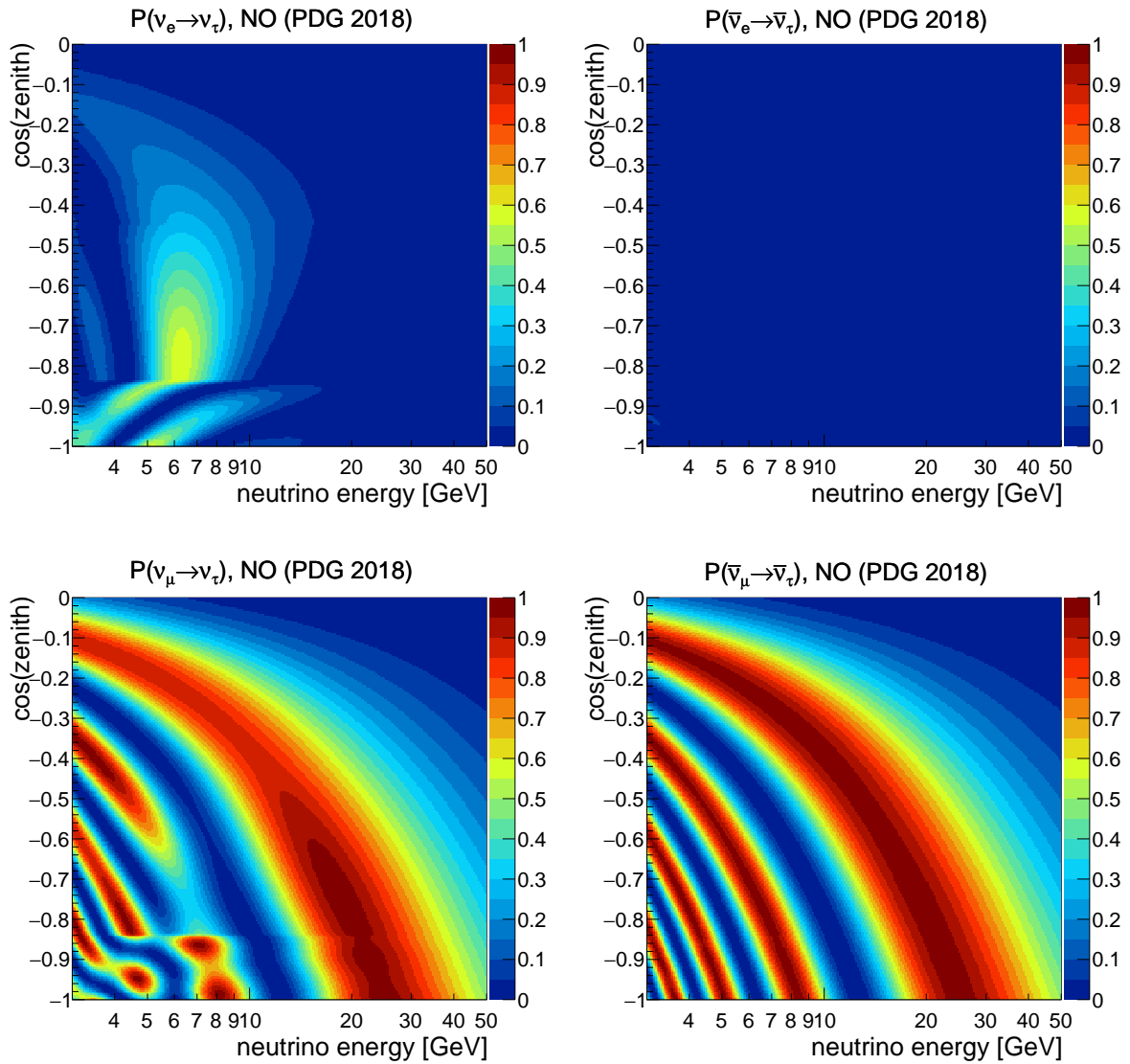


Figure 3.5: Oscillation probabilities for $\bar{\nu}_e$ and $\bar{\nu}_\mu$ to $\bar{\nu}_\tau$ calculated with OscProb. Here, normal mass ordering is assumed and oscillation parameters are set to the best fit values from the global analysis in Ref. [15]. The $\cos(\theta_z)$ ranges from horizontal (0) to straight upward travelling (-1) in the detector.

4 Interaction

4.1 | Observables in neutrino interactions

In the charged current interaction of an (anti-)neutrino $\bar{\nu}_l$ with a nucleon, a lepton $l^{-(+)}$ of the same generation and a hadronic final state H are produced,

$$\bar{\nu}_l + \text{nucleon} \rightarrow l^{-(+)} + H. \quad (4.1)$$

The most relevant observables in neutrino detectors are the energy E_l and the direction of the produced lepton. In the high energy regime the lepton is forward boosted and the mean scattering angle between $\bar{\nu}_l$ and l^\pm lepton is approximately [64]

$$\langle \theta_{\nu l} \rangle \approx \frac{0.6^\circ}{\sqrt{E_\nu [\text{TeV}]} }. \quad (4.2)$$

The reconstructed l^\pm direction serves as a good proxy for the neutrino direction.

In the few-GeV energy region relevant for ORCA, the median scattering angles $\theta_{\nu l}$ are shown separately for ν and $\bar{\nu}$ in Fig. 4.1. They are significantly larger for ν than $\bar{\nu}$ ¹ and lead to an intrinsic resolution of the instrument on the neutrino direction, when the final state lepton is reconstructed.

The neutrino energy is split between the produced lepton and the hadronic final state, $E_\nu = E_l + E_H$. Observation of only E_l therefore yields a lower limit for the energy of the interacting neutrino.

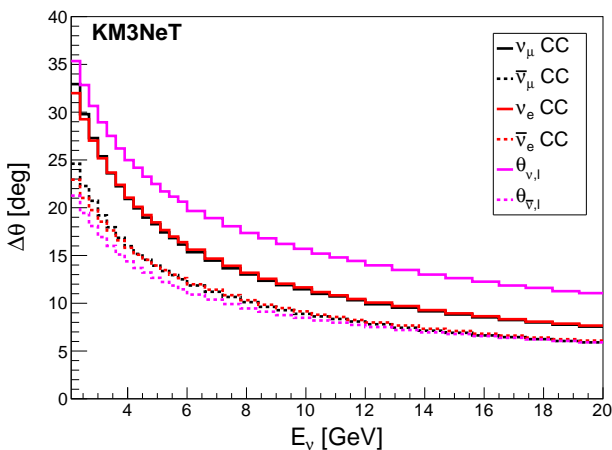
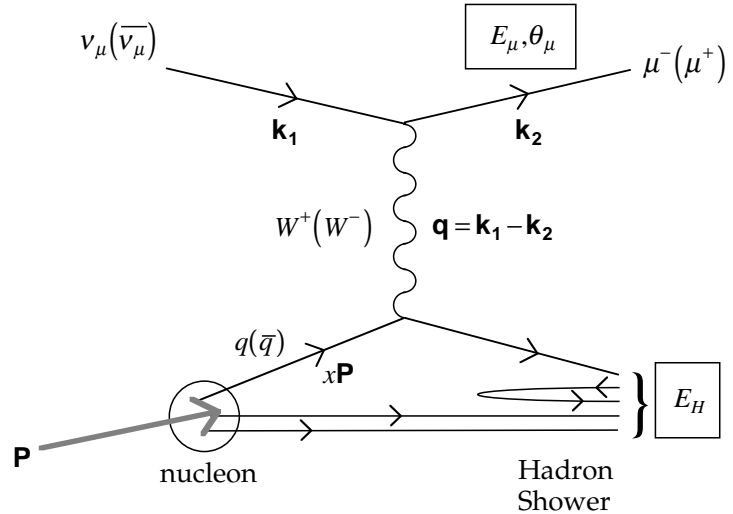


Figure 4.1: 68% quantiles for the scattering angle between (anti-)neutrino and produced lepton $\theta_{\nu l}$ (pink). In addition the 68% quantiles for the resolution on the neutrino direction for $\bar{\nu}_e^{\text{CC}}$ and $\bar{\nu}_\mu^{\text{CC}}$ are shown. The reason for ν_μ^{CC} and ν_e^{CC} being better than $\theta_{\nu l}$ basically comes from the signal of the hadronic component. Figure taken from Ref. [65], where a more detailed explanation can be found.

¹The reason for this is explained below, in Sec. 4.3.

4. Interaction

Figure 4.2: First order Feynman-like diagram for deep inelastic neutrino–nucleon scattering. The labels $k_{1,2}$ (P) indicate the neutrino (proton) four-momenta. Interaction takes place with a quark carrying a momentum fraction x of the proton. $-q^2$ is the four-momentum transfer. Figure taken from Ref. [66]



Sometimes the energy transferred into the hadronic final state might be determined in addition.² Then, the energies can be used to define the inelasticity y , or the Bjorken y , as

$$y = 1 - \frac{E_l}{E_\nu} = \frac{E_H}{E_\nu} \quad (4.3)$$

which corresponds to the fraction of the neutrino energy transferred into to the hadronic system.

4.2 | Interaction cross sections

The key kinematic features of the neutrino deep-inelastic interaction with a nucleon are depicted in the Feynman-like diagram in Fig. 4.2.³ Here the parameters in boxes highlight the observables for the produced lepton and hadron component just mentioned above.

During interaction the nucleon is disrupted and generates a set of final state hadronic particles (denoted H in Eq. 4.2). This process is known as hadronisation and a consequence of the confinement in the strong interaction.

The total neutrino–nucleon cross sections are of order $\sigma_{\nu N}/E \approx 10^{-42} \text{ m}^2/\text{GeV}$. In Fig. 4.3 they are shown in the energy region where processes in addition to deep-inelastic scattering become relevant. Due to the lower accessible energies at few GeV, no hadronisation takes place, such that instead of a complex system H only few final state hadrons are produced.

Quasi-elastic scattering alludes to the according NC elastic scattering process where initial and final particles remain the same. In quasi-elastic scattering the nucleon is converted ($n \leftrightarrow p$) and a charged lepton is produced.

In the resonance region the nucleon is converted to resonant state, most importantly $\Lambda(1232)$. The resonance then can produce a set of one or several π or K during decay.⁴

²In principle one might determine also its direction to some extent. However, current reconstruction algorithms in ORCA and ANTARES only reconstruct one particle.

³More precisely, $\bar{\nu}_\mu^{\text{CC}}$ is shown, but the flavour is arbitrary. A similar NC process is possible by replacing W^\pm by Z^0 and μ^\mp by $\bar{\nu}_\mu$.

⁴In Cherenkov detectors like ORCA, where individual particles are not reconstructable, differences between

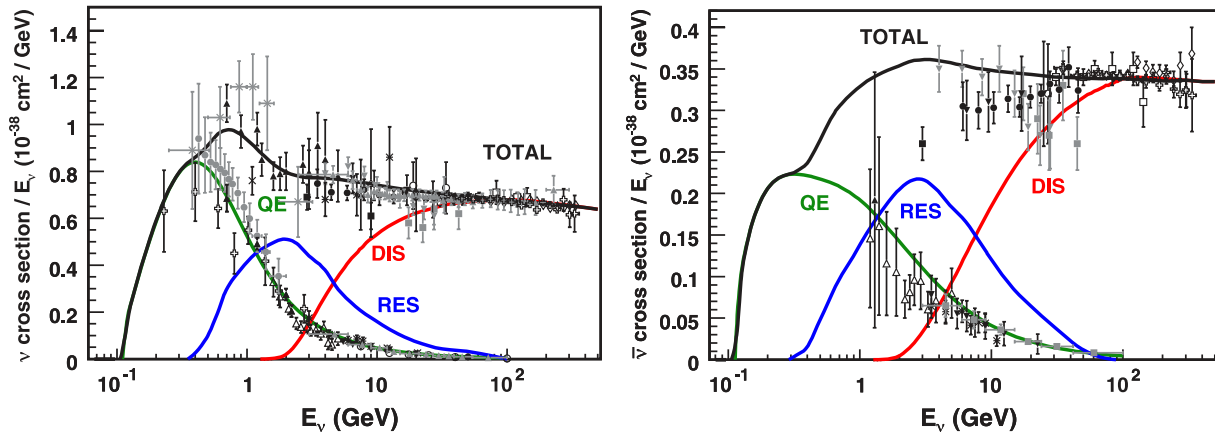


Figure 4.3: Total CC cross sections per nucleon for an isoscalar target for ν_μ and $\bar{\nu}_\mu$. Figure taken from Ref. [67].

4.3 | Differences between ν and $\bar{\nu}$

In the previous paragraphs, two differences between neutrinos and anti-neutrinos were pointed out: The (anti-)neutrino cross sections differ by a factor $\sigma_{\text{CC}}(\nu N)/\sigma_{\text{CC}}(\bar{\nu} N) \approx 2$ and even more at few GeV. In addition, the average neutrino–lepton scattering angle $\theta_{\nu l}$ is larger for neutrinos than anti-neutrinos.

The reason behind this can be understood solely from helicity considerations of pure neutrino–fermion interactions of the type

$$\bar{\nu}_l + f \rightarrow l^{+(-)} + f' \quad (l \neq f). \quad (4.4)$$

The weak interaction couples only to left-handed neutrinos and right-handed anti-neutrinos, and, in the relativistic limit chirality becomes equivalent to helicity (as mentioned previously, in Sec. 1.3). Anti-neutrinos consequently carry a net angular momentum along the axis of interaction and its conservation leads to a preference for forward scattering with cross section:

$$\begin{aligned} \frac{d\sigma_{\text{CC}}(\nu f)}{dy} &= \frac{G_F^2 s}{\pi} \\ \frac{d\sigma_{\text{CC}}(\bar{\nu} f)}{dy} &= \frac{G_F^2 s}{\pi} \times \left(\frac{1 + \cos(\theta_{\nu l})}{2} \right)^2 = \frac{G_F^2 s}{\pi} \times (1 - y)^2, \end{aligned} \quad (4.5)$$

where the Fermi coupling constant G_F is a measure for the coupling strength, and \sqrt{s} is the centre-of-mass energy. The latter equality in Eq. 4.5 is because in the centre-of-mass frame, the inelasticity y and the neutrino–lepton scattering angle $\theta_{\nu l}$ are related by $y = (1 - \cos(\theta_{\nu l}))/2$. Integration over y in Eq. 4.5 leads to a ratio of the pure neutrino–fermion CC cross section $\sigma_{\text{CC}}(\nu f)/\sigma_{\text{CC}}(\bar{\nu} f) = 3$.

The consequences for neutrino–nucleon scattering are:

sets of final state particles obviously become a large systematic.

4. Interaction

- The cross section increases linearly with E_ν , since $s \sim E_\nu$.⁵
- The CC cross section per nucleon is larger for ν than $\bar{\nu}$. The overall ratio however is reduced to ≈ 2 due to the increasing $q\bar{q}$ sea quark content in the struck nucleons at high energies.
- The y , or $\theta_{\nu l}$, dependence on average leads to smaller scattering angles $\theta_{\nu l}$ and higher energy transfer onto (smaller y) the outgoing lepton for anti-neutrinos compared to neutrinos.

The neutral current Z^0 couples to both the left- and right-handed components although with different coupling strengths depending on the Weinberg angle θ_W [15]. For the following parts of this work it is important to recall that the NC cross section is about three times smaller than for CC. In addition, the produced neutrino in NC interactions escapes the detector unseen, which lowers the chance to be observed and reconstructed energy.

⁵More precisely, $s = 2m_f(m_f + E_\nu)$. And since for quarks interaction takes place with an effective mass fraction x of the nucleon, $\sigma_{CC}(\nu e)/\sigma_{CC}(\nu N) \sim 10^{-3}$. Neutrino–nucleon scattering is therefore the dominant process, and the contribution from scattering off electrons is small.

5 Neutrino detection in the GeV to PeV energy region

energy region

When neutrinos interact they produce a set of relativistic secondary particles. Relativistic charged particles may induce the emission of a characteristic light pattern via the Cherenkov effect. In a transparent medium, like sea water, the light can propagate and be registered by optical sensors of neutrino detectors. Since neutrinos only interact weakly with matter, large detector volumes are needed to collect an adequate rate of neutrino events.

This chapter covers the light emission, propagation through the sea water to the optical sensors, and the sources of background present in the deep sea. Finally, the event signatures in large scale Cherenkov detectors are introduced and the efficiency of the instruments used in this work in registering neutrino interactions is compared.

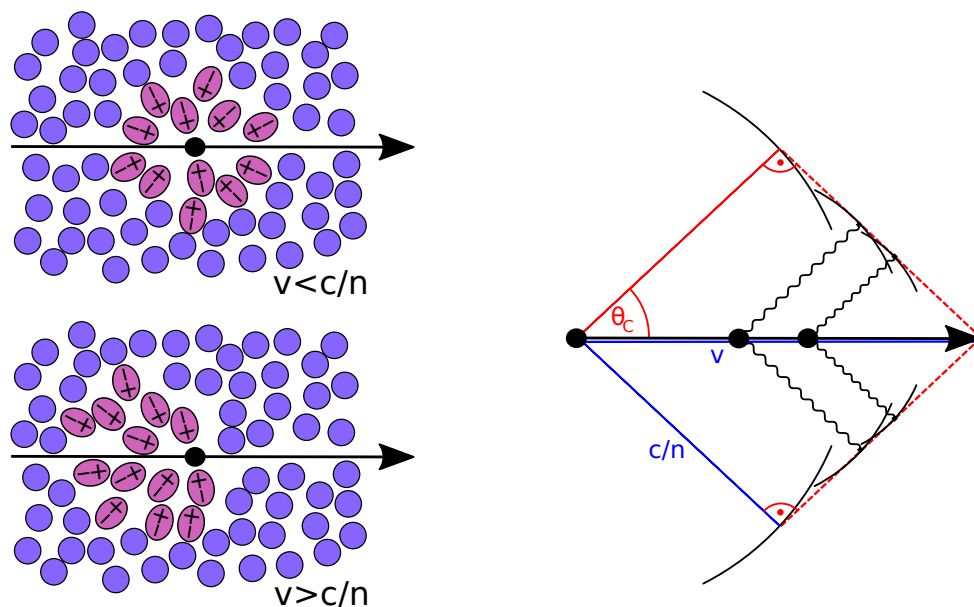


Figure 5.1: Polarisation of a dielectric medium (left) and geometric illustration of the Cherenkov angle θ_C (right). Illustrations following Refs. [68, 69].

5.1 | Cherenkov radiation

A charged particle placed in a dielectric medium polarises the material in its vicinity. During motion, this results in a time dependent dipole field along the particle's trajectory. For particle speeds exceeding the phase velocity of light in the medium, the resulting polarisation is asymmetric along the trajectory and emission of Cherenkov radiation [70] is induced. This is illustrated in Fig. 5.1 (left). The light is emitted under the characteristic Cherenkov angle θ_C with respect to the trajectory forming a conic light front. The angle is

$$\cos \theta_C = \frac{1}{\beta n}, \quad (5.1)$$

where β is the particle's speed normalised by the speed of light and n the index of refraction of the medium. A 2D projection of this conic light front is shown in Fig. 5.1 (right).

For deep sea water, the average index of refraction is $n_{\text{water}} = 1.35$. The secondary particles from neutrino interactions are typically ultra-relativistic ($\beta \approx 1$), such that Cherenkov light is detected under an angle $\theta_C = 42^\circ$ and independent of energy.

Light is emitted only if the particle is above Cherenkov threshold, $\beta > 1/n$. The corresponding threshold kinetic energy T_{thres} for particles with rest mass m_0 is

$$T_{\text{thres}} = E_{\text{thres}} - m_0 c^2 = \left(\frac{1}{\sqrt{1 - n^{-2}}} - 1 \right) \cdot m_0 c^2. \quad (5.2)$$

That is, in sea water, the threshold kinetic energy for Cherenkov light emission is $\approx 49\%$ of the particle's rest mass.

The emitted Cherenkov spectrum falls off with $dN/d\lambda \propto 1/\lambda^2$. For an ultra-relativistic particle ($\beta = 1$) of unit charge $1e$, the number of Cherenkov photons emitted per unit path length dl in a wavelength window $[\lambda_{\text{min}}, \lambda_{\text{max}}]$ is approximately [15, eq. 33.44]

$$\frac{dN_C[\lambda_{\text{min}}, \lambda_{\text{max}}]}{dl} = 2\pi\alpha (1 - n^{-2}) \frac{\lambda_{\text{max}} - \lambda_{\text{min}}}{\lambda_{\text{min}} \lambda_{\text{max}}}, \quad (5.3)$$

with $\alpha \approx 1/137$ the fine-structure constant.

Sea water is transparent in the ultraviolet to visible band from 300 nm to 600 nm. Following Eq. 5.3, the number of emitted Cherenkov photons in this band is $dN_C/dl|_{\text{water}} \approx 340/\text{cm}$.

5.2 | Water properties

When Cherenkov photons propagate through sea water, they are affected by absorption and scattering. Absorption reduces the total number of detectable photons exponentially. The absorption length l_{abs} is defined as the distance after which the number of photons is reduced to $1/e$. For optically pure sea water, the absorption lengths reach a maximum of 70 m at a wavelength of ≈ 440 nm [71]. Measurements in the deep Mediterranean sea [72, 73] show only modestly reduced maximum absorption lengths $l_{\text{abs}} \approx 60$ m and are given as a function of wavelength in Fig. 5.2. Long-term studies of the absorption length with the ANTARES detector [74] indicate a better agreement of data with the 'NEMO' measurement off-shore

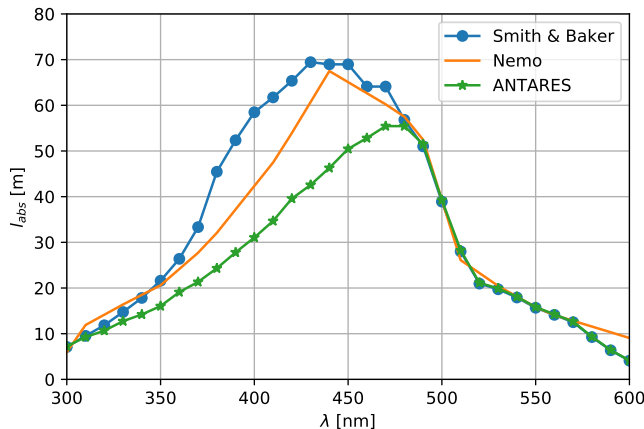


Figure 5.2: Absorption lengths for pure sea water (Smith & Baker) [71] and measurements at the NEMO (off-shore Capo Passero, Sicily) [72] and ANTARES [73] sites.

Sicily, such that for both KM3NeT detector locations (close to ANTARES in France and off-shore Sicily) this measurement is currently accepted as the reference.

Scattering of light in sea water is dominated by the scattering off small dust grains. A scattering length $l_{\text{scat}} \approx 55$ m at 470 nm has been measured at the ANTARES site [73] even though the scattering is mostly forward-peaked¹. Scattering leads to a blurring of the Cherenkov signature in angle and time at large distances [75].

5.3 | Optical sensors

Photomultiplier tubes (PMTs) are used as sensors to detect Cherenkov light. They consist of a photo-cathode which converts Cherenkov photons to electrons by the photoelectric effect. The probability for this conversion is called quantum efficiency (QE). Over several stages, the initial photo-electrons are then multiplied and form an electrical pulse, which can be read out. If the pulse surpasses a pre-defined threshold, it is digitised. Digitised signals are referred to as a *hit*. PMTs achieve nanosecond timing resolution and high QEs of $\sim 25\%$ in the relevant wavelength band.

In the deep sea telescopes, the PMTs are integrated in pressure resistant glass spheres. An optical gel is used as glue to optically link the glass sphere with the PMT surface. Both the glass and the optical gel have a high transmittance for the Cherenkov photons arriving at the sensors. This is visualised in Fig. 5.3. The transmittance is constant above $\gtrsim 350$ nm with the glass becoming opaque for ultra-violet light of shorter wavelengths.

5.4 | Background sources

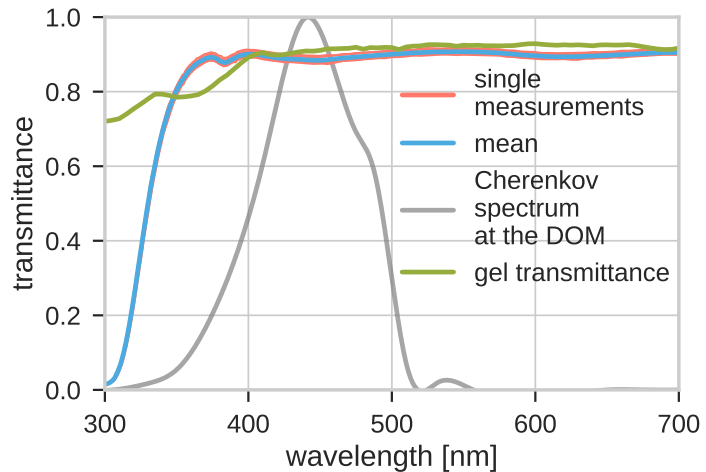
5.4.1 | Optical background noise

The PMTs in ORCA on average record photon hits with a rate of ~ 7 kHz. This rate is dominated by optical background noise. The three sources that contribute to this noise hit level are

¹referred to as ‘Mie scattering’

5. Neutrino detection in the GeV to PeV energy region

Figure 5.3: Transmittance of the KM3NeT glass spheres (red/blue) and of 1 cm optical gel. The normalised Cherenkov spectrum at 100 m from the source is shown for comparison. Taken from [76, Fig. 7.2].



(a) the PMTs' dark count rate in addition to the predominant actual photon hits originating from (b) natural radioactivity in sea water and from (c) bioluminescence activity.

(a) Dark counts

The dark count rate refers to the rate of hits registered by the photo-sensors without presence of an external source of light. This type of noise is steady and thermally generated within the dynode structure of the PMTs. In addition, also the radioactive background (mainly ^{40}K) from within the glass and gel that holds the photo-sensors is typically considered as dark counts. The dark count contribution to the overall noise level is usually small compared to that of ^{40}K in the surrounding sea water. Otherwise tuning of the PMT threshold can reduce thermal noise.

(b) Decays of ^{40}K in sea water

A small amount of the isotope ^{40}K is naturally present in sea water ($\sim 0.04\%$) and is the dominant source of radioactive background. It can disintegrate via β -decay



and electron capture (EC)



In the case of β -decay, the electrons ($E_{e^-} \leq 1.31 \text{ MeV}$) are above the Cherenkov threshold. During EC, the 1.46 MeV photon released by the excited state $^{40}\text{Ar}^*$ can transfer energy to electrons via Compton scattering, which then in turn emit Cherenkov light.

(c) Bioluminescence

Even deep down in the abyss, where no sunlight penetrates, the deep sea is populated with living organisms. Many of them produce light in chemical reactions consisting of two basic ingredients: the oxidation of a light emitting molecule, the luciferin, and an enzyme, the luciferase, controlling the reaction rate of the luciferin [77]. The chemical

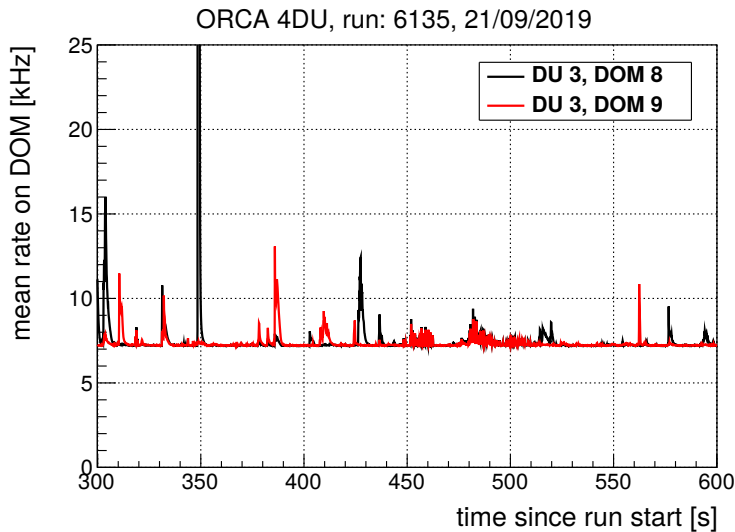


Figure 5.4: Optical background rates averaged over the 31 PMTs contained in a KM3NeT Digital Optical Module (DOM). The distance between the two adjacent DOMs shown is 8.7 m.

nature of the generation implies that the light emission of bioluminescence is not time-correlated on a nano-second basis. Diffuse bioluminescent emission by microscopic organisms can extend over large parts of the detector and adds a slowly time-varying contribution to the constant noise level of ^{40}K . In addition, bright bioluminescence bursts significantly increase the optical background rates locally. They typically last up to several seconds.

A time series of the optical background rates in two neighbouring KM3NeT sensor modules is shown in Fig. 5.4. Some of the bright bursts above the ~ 7 kHz baseline are seen on both modules.

Bioluminescence is often mechanically triggered in turbulences downstream of the detector structures or upon direct impact on them, and hence both baseline rate and the frequency of bursts correlate with the sea current velocity [4]. Since bioluminescence light serves as a means of communication and to satisfy one of the four basic F's of evolutionary biology (fighting, fleeing, feeding and reproduction), it is natural that most of the species emit light at wavelengths where the absorption length in water is maximal [78]. Due to the overlap with the Cherenkov signal, reduction by optical filters is therefore not possible. However, PMTs can be vetoed by the trigger and reconstruction algorithms if the baseline rate is too high. The impact of bioluminescence for data analysis in ORCA is studied in detail in Sec. 9.4.1.

5.4.2 | Atmospheric muons

In cosmic-ray air showers, muons are produced alongside neutrinos. They originate mainly from the decays of π^\pm (Eq. 2.3) and, to a lesser extent, directly from the leptonic decay of K^\pm (Eq. 2.1). The contribution of K^\pm increases with energy from only $\sim 5\%$ to $\sim 27\%$ beyond $E_\mu \gtrsim 1$ TeV [79]. With reference to their origin these muons are called atmospheric muons.

Most atmospheric muons are absorbed before reaching ORCA and ANTARES. Nevertheless, muons with energies exceeding ~ 1 TeV can reach the detectors from above despite an $\gtrsim 2$ km overburden of sea water. The remaining atmospheric muon rate at detector level outnumbers detected neutrinos still by $\sim 10^4$.

5. Neutrino detection in the GeV to PeV energy region

Since only neutrinos can reach the detectors from below, neutrino analyses suppress the atmospheric muon background by a cut on the reconstructed direction. But sometimes atmospheric muons are mis-reconstructed as upward travelling. This happens predominantly at the detector edges when only the upward oriented part of the Cherenkov light front is seen, leading to a mis-reconstruction by twice the Cherenkov angle. These atmospheric muons are particularly challenging to reject, since they can resemble upward-travelling muons from $\bar{\nu}_\mu^{\text{CC}}$ interactions.

To reach an acceptable neutrino purity in analyses, further selection cuts are needed. Atmospheric muon rejection for ORCA consists of a direction, position and quality pre-selection in combination with a machine-learning based anti-muon classifier implemented in [Sec. 11.3.2](#). The classifier is needed, since ORCA analyses the neutrino signal close to the threshold, and faint clusters of hits from atmospheric muons are sometimes mistakenly accepted as upward-reconstructed event. Since neutrino analyses in ANTARES – at least the search in this work – target high energies and not faint near-threshold events, this source of background is reduced. Consequently, stringent de-selection cuts are used in ANTARES only to achieve an acceptable background level (cf. [Sec. 17.2.2](#)).

5.5 | Detection in very-large-volume Cherenkov detectors

Cherenkov detectors with very large instrumented volumes (VLV) at the megaton to gigaton scale can be realised only in naturally occurring transparent media such as water or ice. While the focus of this section lies on the differences between the Cherenkov detectors ANTARES and KM3NeT in the Mediterranean Sea, other experiments with comparable technology, but built in ice or freshwater are currently being operated or planned.

5.5.1 | Event signatures

In all neutrino interactions, a hadronic shower is produced at the interaction vertex, carrying the inelasticity fraction y of the neutrino energy. For NC events the produced neutrino escapes unseen. The particles in hadronic showers have small interaction and/or decay lengths, such that their longitudinal extension is short, typically below $\lesssim 10$ m for energies targeted by large volume neutrino detectors (see e.g. [\[64, Fig. 12\]](#)). The light signature of hadronic interactions therefore resembles the emission from single point; it is said to be *shower-like* in VLV neutrino detectors.

For CC interactions, a lepton is produced in addition to the hadronic shower at the neutrino interaction vertex, and unless $y \simeq 1$ the signature in the detector might be different depending on the lepton flavour:

- The e^\pm radiation length is only 36 cm in water [\[15\]](#) before an electromagnetic shower of e^\pm s and γ s initiated. Electromagnetic cascades only have an extension of few metres, with smaller event-to-event fluctuations than for hadronic showers, especially in the few-GeV energy region. Their signature is also shower-like with the emitted light more peaked around the Cherenkov angle and the light-yield per energy is up to $\sim 20\%$ larger in the few-GeV range compared to hadronic showers [\[4\]](#). Hence $\bar{\nu}_e^{\text{CC}}$ interactions are shower-like.

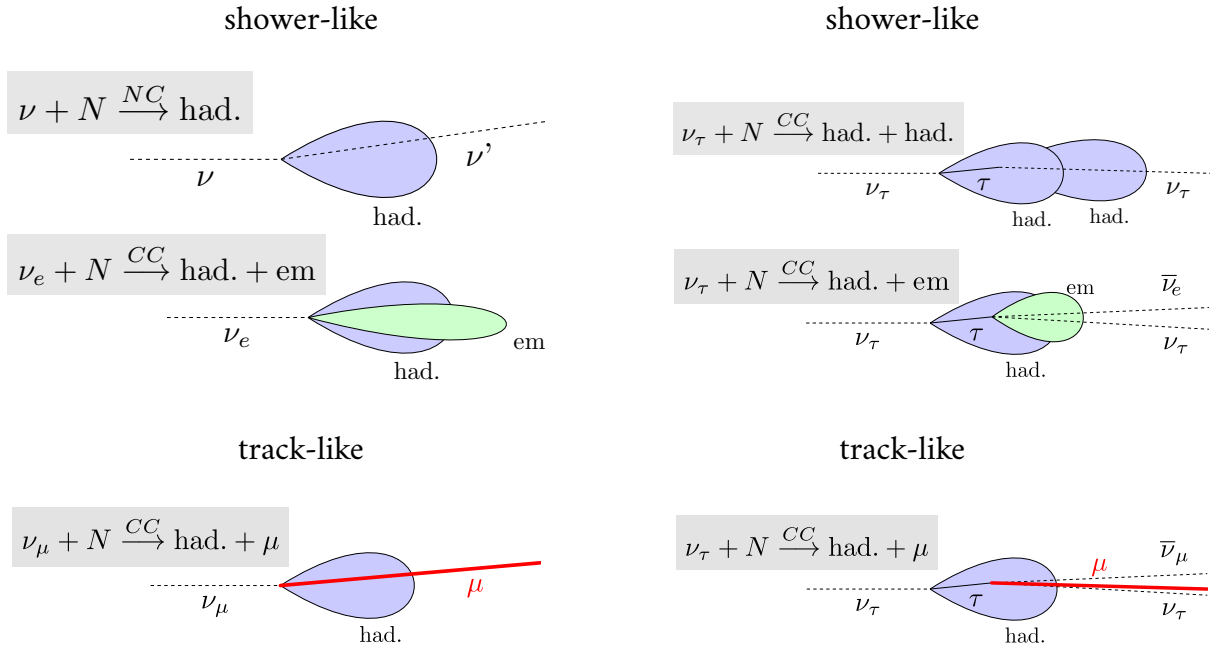


Figure 5.5: Schematic illustrations of the different neutrino event topologies, for ν^{NC} , ν_e^{CC} , ν_μ^{CC} on the left, and the ν_τ^{CC} with signatures corresponding to the hadronic and the leptonic decay channels to e and μ , respectively.

- Only μ^\pm traverse significant distances in matter travelling with almost constant dE/dx energy loss below ~ 100 GeV before radiate losses become dominant. This produces a distinct *track-like* signature in the detector. Atmospheric muons and $\bar{\nu}_\mu^{\text{CC}}$ events appear predominantly track-like.
- The τ^\pm , due to its short lifetime of $\sim 2.9 \times 10^{-13}$ s, will decay essentially instantaneous for VLV detectors below PeV energies. Only in 17% of the decays the leptonic decay to μ^\pm may produce a track-like signature. In the other cases, an additional hadronic (65%) or electromagnetic cascade (17%) produce shower-like signatures in the detector. Therefore, $\bar{\nu}_\tau^{\text{CC}}$ interactions are predominantly shower-like. The $\bar{\nu}_\tau^{\text{CC}}$ interaction is discussed in more detail later, in [Sec. 6.2.1](#).

In [Fig. 5.5](#), the possible event signatures for $\bar{\nu}_e^{\text{CC}}$ and $\bar{\nu}_\mu^{\text{CC}}$ and NC (left) and the possibilities $\bar{\nu}_\tau^{\text{CC}}$ (right) are sketched.

5.5.2 | Neutrino effective volumes of ANTARES and KM3NeT

The primary physics goal of the experiment specifies the required photocathode density. This is because the number of generated Cherenkov photons increases with deposited energy, and the number of collected photons is proportional to the photocathode area. Sparser instrumentation density therefore increases the volume of the detector and with it the collectable statistics of neutrino interactions. On the other hand, the sparser instrumentation also raises the instrument's detection threshold.

5. Neutrino detection in the GeV to PeV energy region

A useful measure to compare different detectors according to their effective size and detection threshold is the effective volume V_{eff} . It is defined as

$$V_{\text{eff},X}(E_\nu) = \frac{N_X(E_\nu)}{N_{\text{int}}(E_\nu)} V_{\text{int}}, \quad (5.6)$$

where $N_{\text{int}}/V_{\text{int}}$ is the number of interacting events per reference volume, i.e. the interacting event density, and $N_X(E)$ symbolises the number of events passing a requirement X chosen, and could be a placeholder for ‘registered events passing the trigger condition’ or ‘events passing the final selection stage for a specific physics analysis’. In addition to the energy dependence, the effective volume may depend also on the zenith angle and interacting flavour.

At the point where the detector is fully efficient, the effective volume will reach a plateau value close to the instrumented volume. The instrumented volume can even be larger, if events interacting outside the instrumented volume are detected and pass requirement X . At the lower end of the energy scale, a turn on can be defined as the point where 50% of the plateau value is reached.

When using simulated data, the $N_{\text{int}}/V_{\text{int}}$ are equivalent to the simulated event density.

A conversion from an effective volume an effective area is possible by multiplying the effective volume with the neutrino-nucleon cross section $\sigma_{\nu N}$ and the nucleon density ρN_A ,

$$A_{\text{eff}}(E) = V_{\text{eff}}(E) \cdot \rho N_A \cdot \sigma_{\nu N}(E) \cdot P_{\text{Earth}}(E). \quad (5.7)$$

Depending on the energy, Earth absorption ($P_{\text{Earth}}(E)$, see [Sec. 3.1](#)) might need to be included in the calculation. The effective area, when multiplied by the incident neutrino flux directly yields the detected event rate.²

In [Fig. 5.6](#), the effective volumes at the trigger level are compiled for ANTARES, ARCA, and ORCA. They have been calculated, by taking Monte Carlo simulations triggered with the default trigger setups for each instrument. More precisely, for ANTARES run-by-run Monte Carlo simulations have been used which match the in-situ data-taking conditions of 100 physics runs taken in 2008. For ARCA and ORCA simulation files have been processed with the forseen trigger settings provided in Ref. [1] and derived in [Tab. 9.1](#) (for 23 m), respectively.

The effective volumes being larger for $\bar{\nu}_\mu^{\text{CC}}$ than for $\bar{\nu}_e^{\text{CC}}$ at the ends of the energy scale results from the length of the μ^\pm tracks. At high energies these can reach the detector from outside. The effective volume for $\bar{\nu}_\mu^{\text{CC}}$ consequently increases beyond the plateau value near the instrumented volume. At low energies, they can be detected more easily when travelling past neighbouring sensors, as is the case for upward-travelling μ^\pm close to a detection line. At the low threshold of ORCA muon tracks are too short to produce the same effect. For neutral current events, the turn-on behaviour is similar to the one of $\bar{\nu}_e^{\text{CC}}$ for the instruments, but shifted to higher energies by $\sim 0.3 - 0.4$ in $\log_{10}(E_\nu)$.

The division of the successor experiments into the low- and high-energy branches is evident from [Fig. 5.6](#). While ARCA will have an instrumented volume surpassing ANTARES by one order of magnitude for one building block (same number of sensors as the full ORCA detector), ORCA will lower the detection threshold by roughly one order of magnitude, and, with an energy turn on at ~ 3 GeV plateau is reached at 10 GeV for $\bar{\nu}_e$ and $\bar{\nu}_\mu$. ORCA is

²It is therefore often the preferred quantity to straightforwardly evaluate astrophysical emission models.

therefore the instrument of choice to carry out precise oscillation measurements, as done in the following [Part II](#), where the sensitivity to the $\bar{\nu}_\tau$ component in the atmospheric neutrino flux peaking below 25 GeV is one of the main goals. While ANTARES is able to successfully analyse the disappearance of $\bar{\nu}_\mu$ [80], reconstructing and selecting shower-like signatures right at the threshold is significantly harder. And since the turn-on is higher than for $\bar{\nu}_e^{CC}$ a measurement of $\bar{\nu}_\tau$ appearance is hence not promising. The good visibility towards the Galactic Centre and long integrated livetime on the other side makes ANTARES most sensitive for the search for a neutrino signal from the ‘Fermi Bubbles’ in [Part III](#).

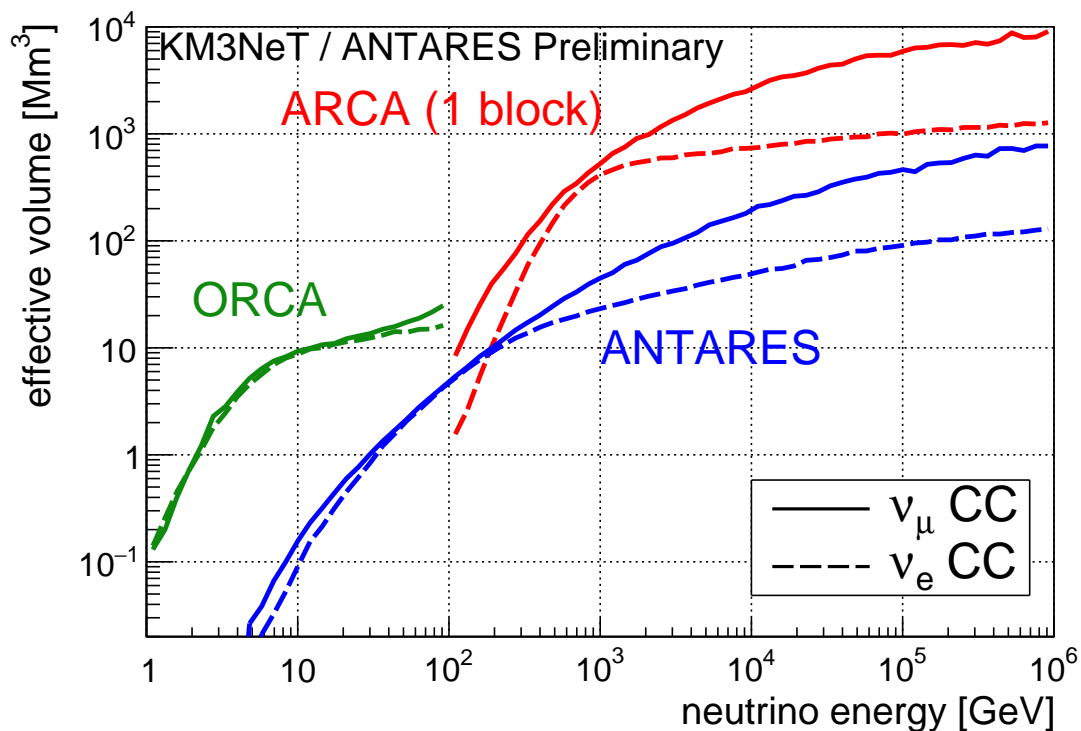


Figure 5.6: Trigger effective volumes for the standard physics triggers of ANTARES (blue) and the KM3NeT detectors, ORCA (green) and ARCA (red). The provided effective volume for ARCA corresponds to one building block (115 detection lines), i.e. half of what is planned in KM3NeT 2.0.

5. *Neutrino detection in the GeV to PeV energy region*

Part II

Sensitivity to tau-neutrino appearance with a realistic KM3NeT/ORCA detector



In this part, ORCA and in particular its sensitivity to the appearance of $\bar{\nu}_\tau$ in the atmospheric flux through neutrino oscillations are covered. An overview of the current experimental status and the signature of the $\bar{\nu}_\tau$ signal is given in [Sec. 6](#). Then, in [Sec. 7](#), the ORCA detector and the associated chain to produce simulated data are described. Since the first performance study with ORCA was published in the ‘Letter of Intent for KM3NeT 2.0’ (LoI, [1]), the detector used in simulation has been upgraded to meet all requirements for deployment in the deep sea. At the same time several steps in the simulation and reconstruction chain (summarised in [Sec. 8](#)) have been further developed. Two crucial ingredients in this chain have been contributed as part of this thesis: The optimisation and analysis of a new low-energy trigger discussed in [Sec. 9](#), and the development of event type identifiers using Random Decision Forests given in [Sec. 11](#). The description of the event reconstruction and selection ([Sec. 10](#)) bridges the gap between trigger output and event type identification. The classified event sample is the starting point for physics analyses. The sensitivity analysis for $\bar{\nu}_\tau$ appearance with ORCA at the end of this part ([Sec. 12](#)) extends the science case of ORCA with respect to what has already been published in the LoI. [Section 13](#) concludes on the results of this part.



Ich bin kein Gipfelsüchtiger, ich bin horizonsüchtig, will wissen, was dahinter ist. – Reinhold Messner

6 Neutrino oscillations and the $\bar{\nu}_\tau$ signal in ORCA

6.1 | Status of neutrino oscillations and unitarity

Direct evidence for neutrino oscillations was first observed in the zenith-angle distribution of muon-tracks from atmospheric neutrinos by Super-Kamiokande [51] and the result in Fig. 6.1 was presented at the International Cosmic Ray Conference in 1998. Whilst expecting an upward-downward symmetry in the measured flux, a deficit of muon-tracks reaching the detector from below was observed. The ν_e event rates expected at Earth from the fusion processes in the Sun had been predicted in nuclear models. A long-standing problem was however, that less ν_e^{CC} events seemed to arrive at Earth than predicted by these models [82]. In the measurement of both ν_e^{CC} and ν_e^{NC} event rates in the solar neutrino flux by SNO [52] in 2001, a deficit was seen only for ν_e^{CC} events, but not for NC events. The observed deficit has shown, that ν_e^{CC} indeed have oscillated away, since the NC rate, being a sum of all flavours, is not affected by oscillations.

These two experimental results have proven that neutrinos do oscillate and thus are required to have non-zero masses. The discoveries resulted in the Nobel Prize in Physics awarded to Arthur B. McDonald and Takaaki Kajita in 2015.

Known parameters... Now, two decades after the first observation, neutrino oscillation experiments have entered an era of precision measurements: All three mixing angles of the unitary PMNS mixing matrix (in Eq. 3.3) have been determined to reasonable precision. Also, the value of the small mass splitting and the absolute value of the large mass splitting are determined from solar¹ and atmospheric neutrino oscillation experiments, respectively.

In contrast to the CKM mixing matrix in the quark sector, where the off-diagonal elements are small, significant mixing occurs through the PMNS matrix for neutrinos. This is visualised

¹The Sun is a source of ν_e but not $\bar{\nu}_e$. Since the MSW resonance was observed, the sign is known to be "+", cf. Sec. 3.2.3.

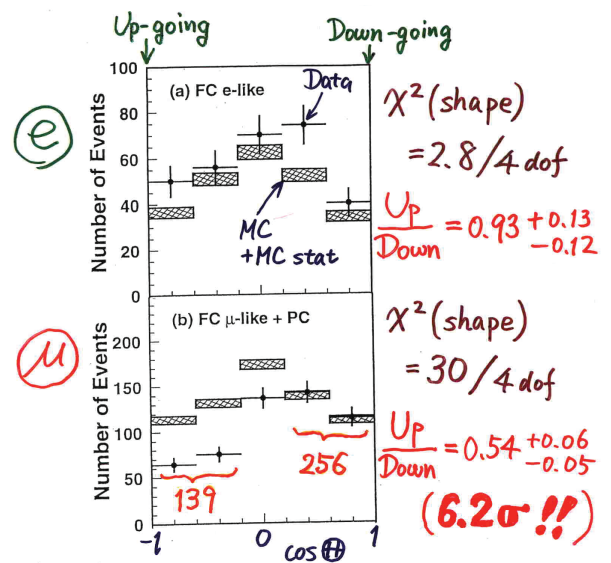


Figure 6.1: First observation of atmospheric neutrino oscillations presented by the Super Kamiokande Collaboration during the International Cosmic Ray Conference 1998. Figure from Ref. [81].

6. Tau-neutrino appearance

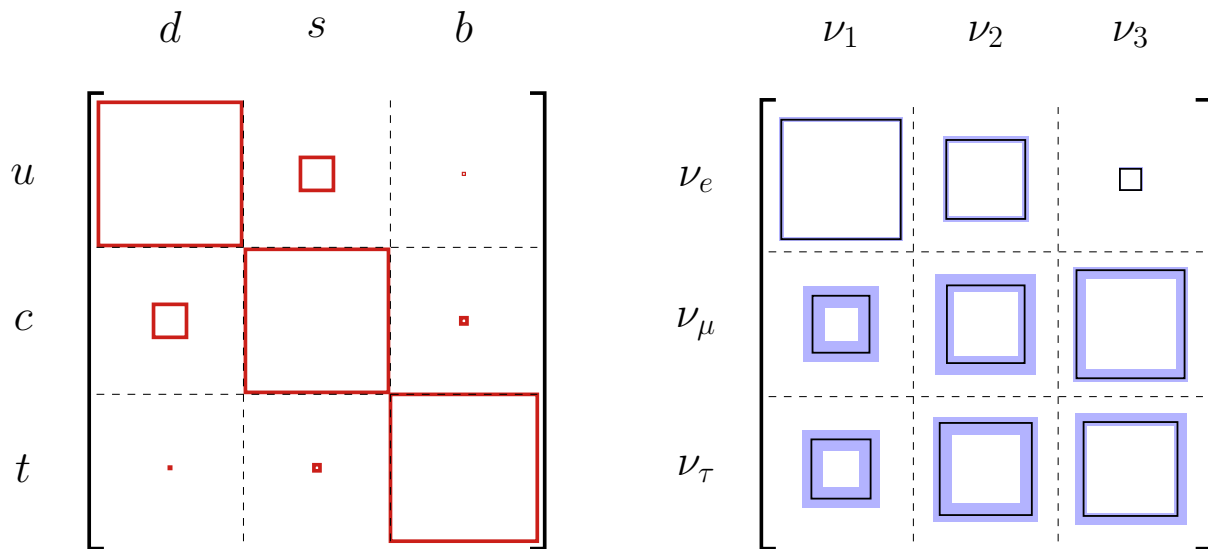


Figure 6.2: Graphical representation of the absolute size of the entries in the unitary oscillation matrices of quarks (CKM mixing matrix, *left*) and neutrinos (PMNS mixing matrix, *right*). The sides of the boxes are proportional to the absolute value of the respective entry. The blue band in the PMNS mixing matrix represents the $\pm 3\sigma$ uncertainty range. The graphic has been generated using the values given in Ref. [15].

in Fig. 6.2, where the lengths of the sides of the squares represent the absolute values of the entries in the mixing matrices, $|V_{ab}^{\text{CKM}}|$ and $|U_{\alpha i}^{\text{PMNS}}|$, respectively. The blue bands in Fig. 6.2 (*right*) depict recent 3σ uncertainty ranges on the values. It is apparent, that the uncertainty in the lower two rows are still sizeable. Since these entries contain the atmospheric mixing parameter θ_{23} , atmospheric neutrino experiments can help in reducing the uncertainty ranges on these entries.

Known unknowns... There are however three known unknown parameters that remain to be determined from oscillation experiments, namely

- (1) the octant of the close-to-maximal atmospheric mixing angle θ_{23} – Is it smaller (first octant), larger (second octant) or in fact exactly 45° corresponding to maximal mixing?
- (2) the ordering of the neutrino masses, i.e. $m_1 < m_2 \ll m_3$ (NO) or $m_3 \ll m_1 < m_2$ (IO), and
- (3) the value of the CP violating phase, δ_{CP} .

While $\theta_{23} \equiv 45^\circ$ would be a suspicious coincidence, the discovery of a relatively large θ_{13} [83, 84, 85] has spurred the interest in determining the latter two points, since it opened up the possibility to study NMO with atmospheric neutrino detectors [86] and – since the entries in the mixing matrix only appear in terms $\propto \sin(\theta_{13})e^{-i\delta_{\text{CP}}}$ – this is a pre-requirement to translate a large δ_{CP} to a sizeable asymmetry between matter and anti-matter in the lepton sector during leptogenesis shortly after the Big Bang.

Current global neutrino fits [59, 87, 88] indicate a preference for NO, second octant for θ_{23} , and close-to-maximum CP-violation, $\delta_{\text{CP}} \approx \frac{3}{2}\pi$. However, most recently the significance for NO from the global fit has reduced to below 3σ and the CP-conserving $\delta_{\text{CP}} = 180^\circ$ is only 0.6σ from the best-fit value [19].

Unknown unknowns... It is still possible, that the picture of 3×3 neutrino mixing within the Standard Model framework is incomplete. A range of new physics phenomena might be visible in the detected neutrino flux over long baselines, such as [89, c. 3.8]

- non-standard interactions,
- violation of Lorentz invariance or CPT,
- sterile neutrinos mixing with the active neutrino states,
- additional states predicted in string theory models mixing with the active neutrino states.

The most frequently tested of this (incomplete) list of possible phenomena is the (3+1) extension of neutrino mixing by one additional sterile neutrino, i.e. four neutrino mixing involving one additional sterile state and the three active neutrinos. In that case the PMNS matrix is not unitary any more, but only a sub-set of a larger unitary matrix,

$$U_{3+1} = \begin{pmatrix} \mathcal{U}_{e1} & \mathcal{U}_{e2} & \mathcal{U}_{e3} & ? \\ \mathcal{U}_{\mu1} & \mathcal{U}_{\mu2} & \mathcal{U}_{\mu3} & ? \\ \mathcal{U}_{\tau1} & \mathcal{U}_{\tau2} & \mathcal{U}_{\tau3} & ? \\ ? & ? & ? & ? \end{pmatrix}. \quad (6.1)$$

Unitarity imposes summation rules on the rows and columns of the 3×3 matrix,

$$\sum_i |\mathcal{U}_{\alpha i}|^2 \equiv 1 \quad \alpha = \{e, \mu, \tau\} \quad \text{and} \quad \sum_\alpha |\mathcal{U}_{\alpha i}|^2 \equiv 1 \quad i = \{1, 2, 3\}. \quad (6.2)$$

The potential deviations of the row/column sums from unity have been tested [90] using a range of current measurement results. This has provided the result given in Fig. 6.3. The potential deviation from the unitarity condition in the τ row is almost one order of magnitude larger than from e and μ .

Since global fits generally assume unitarity, the allowed 3σ ranges of the oscillation parameters also increase when removing this constraint. The resulting mixing matrix elements in case of non-unitarity are extracted from Ref. [90] and depicted in Fig. 6.4.

The additional freedom on the oscillation parameters manifests itself mainly in the third row of the mixing matrix. This is due to the lack of stringent experimental constraints in the matrix elements involving $\bar{\nu}_\tau$, whose cross section at energies available to most experiments is significantly suppressed owed to the large τ^\pm rest-mass.

The most general model independent test for the validity of the PMNS mixing is therefore to measure the overall normalisation of the $\bar{\nu}_\tau$ flux, n_τ , after oscillation. This measurement is what is commonly referred to as $\bar{\nu}_\tau$ appearance measurement.

6. Tau-neutrino appearance

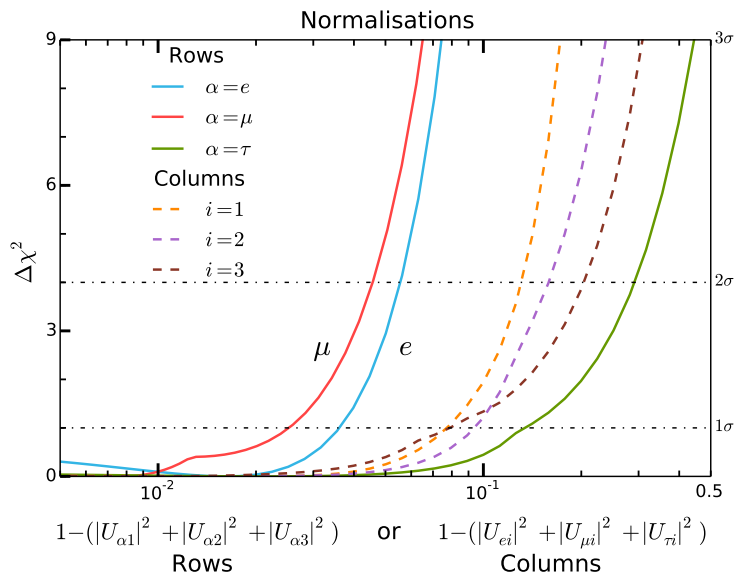


Figure 6.3: One-dimensional $\Delta\chi^2$ for deviations in the unitarity in specific rows / columns in the mixing matrix. Fitted with spectral and normalisation data assuming non-unitarity. More analysis details can be found in Ref. [90], where this figure is taken from.

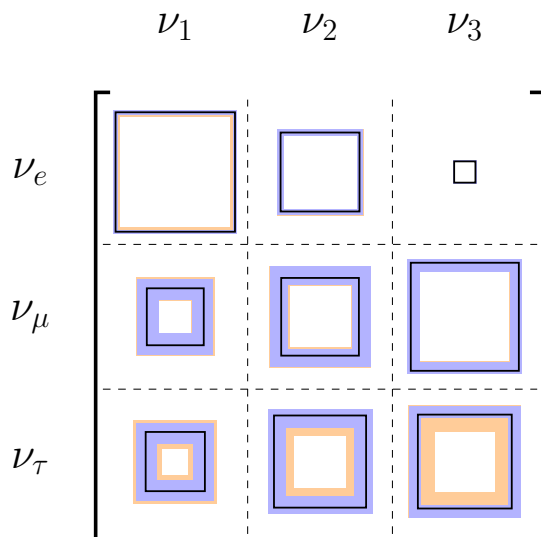


Figure 6.4: Same as in Fig. 6.2, right. The orange bands represent the 3σ precision range on $|U_{\alpha i}|$ without unitarity constraint.

6.2 | Kinematics and signatures of $\overleftrightarrow{\nu}_\tau$ interactions

The key difference of the $\overleftrightarrow{\nu}_\tau^{\text{CC}}$ interaction compared to $\overleftrightarrow{\nu}_e^{\text{CC}}$ and $\overleftrightarrow{\nu}_\mu^{\text{CC}}$, is the large invariant mass and the short lifetime of the τ lepton associated with it, $m_\tau = 1.777 \text{ GeV}/c^2$ and $\tau_\tau = 2.9 \times 10^{-13} \text{ s}$. The former affects primarily the interaction of $\overleftrightarrow{\nu}_\tau$, while the latter leads to a rapid decay of the produced τ^\pm . Both ingredients are discussed in the following. These details on the kinematics of $\overleftrightarrow{\nu}_\tau^{\text{CC}}$ interactions will explain why the τ channel is so much harder to probe experimentally than e and μ . This sets the foundation for the discussion on the current status of $\overleftrightarrow{\nu}_\tau$ experiments and define a strategy to measure $\overleftrightarrow{\nu}_\tau$ appearance in ORCA in Sec. 6.3.

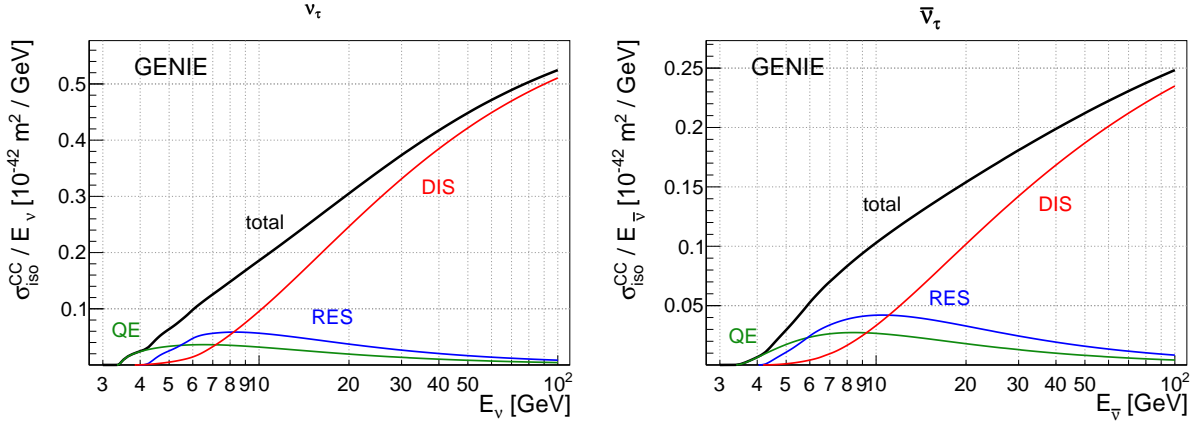


Figure 6.5: Cross section per nucleon predicted by the GENIE [91] event generator for ν_τ and $\bar{\nu}_\tau$ on an isoscalar target. Contributions from deep-inelastic scattering (DIS), resonance production (RES) and quasi-elastic scattering (QE) are shown individually.

6.2.1 | Interaction of $\bar{\nu}_\tau$

For quasi-elastic $\bar{\nu}_\tau$ scattering on a nucleon N (proton p or neutron n),

$$\nu_\tau n \rightarrow \tau^- p \quad \text{and} \quad \bar{\nu}_\tau p \rightarrow \tau^+ n, \quad (6.3)$$

the kinematics of the reactions require a minimum threshold energy of

$$E_{\text{thres}} = m_\tau \left(1 + \frac{m_\tau}{2 \cdot m_N} \right) = 3.46 \text{ GeV}, \quad (6.4)$$

due to the invariant mass of the τ^\pm , $m_\tau = 1.777 \text{ GeV}/c^2$. Above the high threshold both the overall cross section and the inelasticity distribution y are affected by the τ mass.

Cross section: Similar to the $\bar{\nu}_\mu^{\text{CC}}$ neutrino–nucleon cross sections in Fig. 4.3, the $\bar{\nu}_\tau^{\text{CC}}$ cross sections are given for quasi-elastic, resonance, and deep inelastic scattering in Fig. 6.5.

Above the production threshold, $\sigma_{\text{CC}}(\bar{\nu}_\tau N)$ gradually increases but is still only 30% (50%) of the other flavours at 10 (25) GeV. The cross section ratio with respect to $\bar{\nu}_\mu^{\text{CC}}$ in Fig. 6.6 shows this suppression as a function of energy.

To date, the $\bar{\nu}_\tau$ cross sections with nucleons and nuclei are poorly constrained experimentally. Theoretically, they can be calculated in the SM for deep-inelastic, resonance and quasi-elastic scattering and combined in a similar manner than for the other flavours [92, 93]. Due to the large τ mass compared to e/μ , however, the relative importance of several ingredients changes: In the deep-inelastic regime, additional form factors F_4 and F_5 in the cross section²

²For completeness [94, eq. 3.4.]:

$$\begin{aligned} \frac{d^2 \sigma_{\text{DIS}}^{\bar{\nu}_\tau^{\text{CC}}}}{dx dy} &= \frac{G_F^2 M E_\nu}{\pi (1 + Q^2/M_W^2)^2} \left(\left(y^2 x + \frac{m_\tau^2 y}{2E_\nu M} \right) F_1 + \left[\left(1 - \frac{m_\tau^2}{4E_\nu^2} \right) - \left(1 + \frac{Mx}{2E_\nu} \right) y \right] F_2 \right. \\ &\quad \left. \pm \left[xy \left(1 - \frac{y}{2} \right) - \frac{m_\tau^2 y}{4E_\nu M} \right] F_3 + \frac{m_\tau^2 (m_\tau^2 + Q^2)}{4E_\nu^2 M^2 x} F_4 - \frac{m_\tau^2}{E_\nu M} F_5 \right). \end{aligned}$$

6. Tau-neutrino appearance

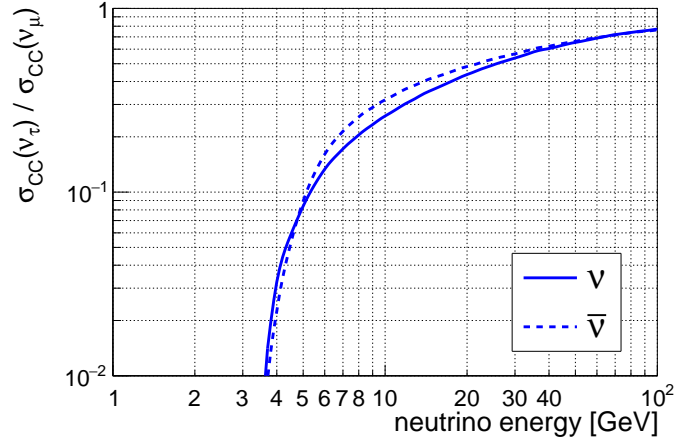


Figure 6.6: Ratio of the $\bar{\nu}_\tau$ to $\bar{\nu}_\mu$ total neutrino–nucleon cross section. The cross sections used for this work are taken from the GENIE event generator code [91]. The cross section ratio to $\bar{\nu}_e$ is similar.

have sizeable impact [95]. Theoretical SM calculations exist up to next-to-leading order QCD, and the uncertainties on the cross section above ~ 10 GeV are estimated $\lesssim 7\%$ [92] in the deep-inelastic scattering region. At low energies, the effects of the nucleus, and the polarisation of the τ^\pm have up to now not been followed up on a theoretical level extensively due to the currently low experimental precision. Consequently, the uncertainties in this region are larger [96].

Inelasticity of ν_τ and $\bar{\nu}_\tau$: At energies up to few tens of GeV relevant for $\bar{\nu}_\tau$ appearance, valence quarks dominate the quark content of the target nucleons and the contribution of sea quarks is small. Following the discussion of the ν and $\bar{\nu}$ interaction with free fermions in Eq. 4.5, the neutrino–nucleon cross section is approximately flat in inelasticity y (or Bjorken y ; defined in Eq. 4.3). In contrast, the antineutrino–nucleon cross section falls off with $(1 - y)^2$. The differential cross section shown in Fig. 6.7 shows this behaviour for $\bar{\nu}_\mu^{\text{CC}}$. The suppression at low y results from the required minimum invariant mass of the hadronic final state.

For $\bar{\nu}_\tau^{\text{CC}}$, the Bjorken y distribution is kinematically limited due to the rest mass of the produced τ^\pm ,

$$y_{\text{max}} = 1 - \frac{m_\tau}{E_\nu}. \quad (6.5)$$

This suppresses the high y region for $\bar{\nu}_\tau$ and the difference between neutrino and anti-neutrino is smaller compared to $\bar{\nu}_e/\bar{\nu}_\mu$. This will become evident in the next chapters.

6.2.2 | Tau decay

The τ lepton has a short lifetime of $\tau_\tau = 2.9 \times 10^{-13}$ s [15]. At energies typical for $\bar{\nu}_\tau$ -appearance, τ leptons will therefore decay within one millimetre and less from the point of

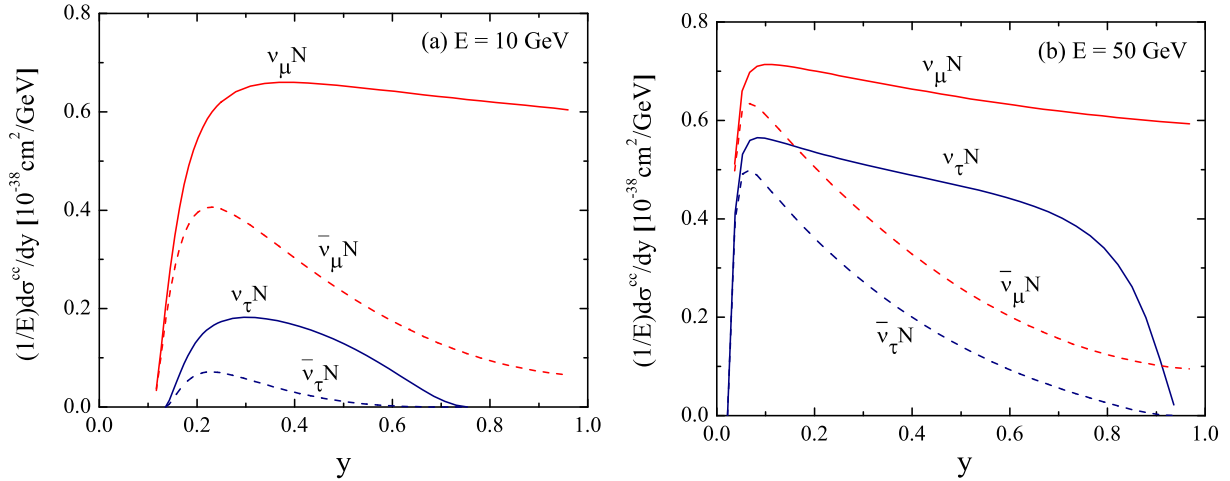


Figure 6.7: Differential cross section $d\sigma/dy/E$ for deep-inelastic CC scattering on an isoscalar target for (a) 10 GeV and (b) 50 GeV. The value $W_{\min} = 1.4 \text{ GeV}/c^2$ was used for the minimum invariant mass. Figure taken from Ref. [92, Fig. 3].

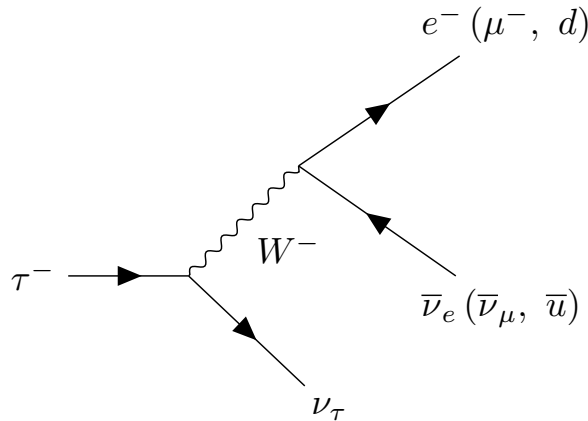


Figure 6.8: Feynman diagram for leading order τ decays

production ($\langle d \rangle = (p/mc) \times 87 \mu\text{m}$). For water/ice Cherenkov detectors the decay appears instantaneous. A separation between the final state particles of the τ -decay and the hadronic shower at the $\bar{\nu}_\tau$ vertex is not possible.

Figure 6.8 visualises the simplest possible Feynman diagram for the τ lepton decay. Irrespective of the final state, a $\bar{\nu}_\tau$ is always produced for conservation of lepton number. In addition, if the decay is leptonic, a second neutrino is produced alongside the final state charged lepton. In the more probable hadronic decays (65%), the final state typically involves one or more pions in addition to the $\bar{\nu}_\tau$.

The main τ decay modes and the corresponding branching fractions are [15]:

6. Tau-neutrino appearance

$$\begin{array}{l}
 \tau^- \rightarrow e^- \bar{\nu}_e \nu_\tau \quad (17.8\%) \\
 \tau^- \rightarrow \mu^- \bar{\nu}_\mu \nu_\tau \quad (17.4\%) \\
 \tau^- \rightarrow \pi^- \pi^0 \nu_\tau \quad (25.5\%) \\
 \tau^- \rightarrow \pi^- \nu_\tau \quad (10.8\%) \\
 \tau^- \rightarrow \pi^- \pi^0 \pi^0 \nu_\tau \quad (9.3\%) \\
 \tau^- \rightarrow \pi^- \pi^- \pi^+ \nu_\tau \quad (9.0\%) \\
 \tau^- \rightarrow \pi^- (> 2\pi) \nu_\tau \quad (9.0\%)
 \end{array}
 \left. \begin{array}{l} \\ \\ \\ \\ \\ \\ \\ \end{array} \right\} \begin{array}{l} \text{leptonic (35.2\%)} \\ \\ \\ \text{hadronic (64.8\%)} \end{array}$$

and the respective charge conjugated decays for τ^+ . Only 17.4% of decays are leptonic with a μ^\pm in the final state and may appear track-like in the detector provided sufficient energy is transferred to the μ^\pm . The majority of events will have a shower-like event signature. In addition, the invisible energy carried by the neutrinos produced in the τ -decay lowers both the overall light yield of $\bar{\nu}_\tau^{\text{CC}}$ events and the light output of the τ -decay daughters with respect to the vertex shower.

6.3 | Existing and future $\bar{\nu}_\tau$ appearance measurements

In the previous section, three main points have been outlined that complicate the measurement of $\bar{\nu}_\tau$:

- The τ^\pm decays fast, requiring sub millimetre precision for direct detection of its track.
- The cross section is suppressed with respect to other flavours and has a 3.46 GeV energy threshold.
- Energy is carried away by neutrinos in the τ decay, reducing the visible energy of the events.

Facing these challenges, the experimental status of $\bar{\nu}_\tau$ measurements is summarised in this section.

One possibility to study $\bar{\nu}_\tau$ is using artificial beams of neutrinos. Artificial neutrino beams are generated by directing a beam of accelerated protons onto a massive target. This procedure is commonly referred to as a ‘beam dump’ experiment. The ‘protons on target’ (POT) is a useful measure for the neutrino fluence (or, equivalently, the time-integrated flux) delivered by the beam dump. If the primary neutrino beam is already rich in $\bar{\nu}_\tau$, which are produced in the decays of heavy mesons³, detectors can be placed directly downstream of the beam dump. Otherwise long baseline experiments can detect the oscillated $\bar{\nu}_\tau$ flux, primarily from $\bar{\nu}_\mu \rightarrow \bar{\nu}_\tau$ transition (as was depicted in Fig. 3.5). For detection using artificial neutrino beams right behind the beam dump and after oscillation, the corresponding experiments and results are discussed in Sec. 6.3.1 and Sec. 6.3.2.

The experiments that fall into this category typically try to identify $\bar{\nu}_\tau^{\text{CC}}$ interactions directly. Unambiguous identification is possible by resolving both the primary interaction and

³ primarily $D_s^\pm \rightarrow \tau^\pm \bar{\nu}_\tau$, from similar processes as the prompt production of $\bar{\nu}_\tau$ in the atmospheric neutrino flux in Fig. 2.2.

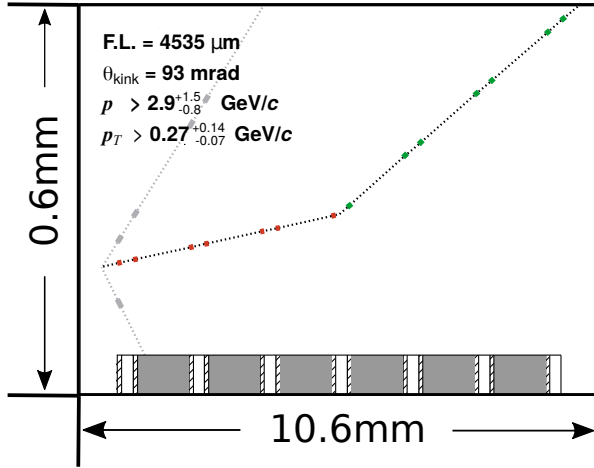


Figure 6.9: DONUT ν_τ CC candidate event, with $\tau \rightarrow e \bar{\nu}_e \nu_\tau$ decay after ~ 4.5 mm. Target materials are indicated in the bottom: steel (grey), emulsion (hatched) and plastic (white). Taken from Ref. [97].

the subsequent decay of the τ lepton. Only densely instrumented detectors reach the required (sub-)millimetre vertex precision for this direct identification. Since high instrumentation density implies a small instrumented volume, all currently completed $\bar{\nu}_\tau$ beam experiments are statistically limited.

The second group of experiments are discussed in Sec. 6.3.3. These try to avoid the problem of small event statistics by using the naturally produced atmospheric neutrino flux in combination with large scale ($\sim 10^5 - 10^7$ tons instrumented mass) neutrino detectors. Directly resolving the short τ track for these detectors is impossible. Instead the analysis is based on observing $\bar{\nu}_\tau$ on a statistical basis. This latter approach is also pursued by ORCA.

6.3.1 | Direct $\bar{\nu}_\tau$ detection in beam dumps

The tau neutrino was first directly observed in the year 2001 by the DONUT experiment [97, 98]. DONUT was located 36 m behind the beam dump of the 800 GeV proton beam at Fermilab's Tevatron. In total, DONUT reported nine CC interactions of $\bar{\nu}_\tau$ with an expected background of 1.5 events in the search for neutrino interaction vertices with a τ^\pm as the only produced lepton. To identify the τ^\pm , the production and the decay vertex were resolved with μm -precision in alternating layers of iron, emulsion plates, and plastic. One of the candidate events reconstructed in DONUT is shown in Fig. 6.9.

Even though the event statistics were limited, DONUT also provided a first measurement for the $\nu_\tau + \bar{\nu}_\tau$ averaged cross section [98], which can be factorised:

$$\sigma_{\nu_l} = \sigma_{\nu_l}^{\text{const.}} \cdot E \cdot K(E) \quad (l = e, \mu, \tau), \quad (6.6)$$

$$\sigma_{\nu_\tau}^{\text{const.}} = (0.72 \pm 0.24^{\text{(stat.)}} \pm 0.36^{\text{(syst.)}}) \times 10^{-42} \text{ m}^2 \text{ GeV}^{-1}. \quad (6.7)$$

Here $K(E)$ is a function for the kinematic suppression due to the τ lepton mass and essentially follows the curve of the $\bar{\nu}_\tau / \bar{\nu}_\mu$ cross section ratio in Fig. 6.6. For e and μ , $K(E) \equiv 1$ is a good approximation.

The result is consistent with the Standard Model expectation, however the sizes of both the statistical and the systematic error do not currently allow to experimentally constrain the theoretical $\bar{\nu}_\tau^{\text{CC}}$ cross sections presented in Sec. 6.2.1.

6. Tau-neutrino appearance

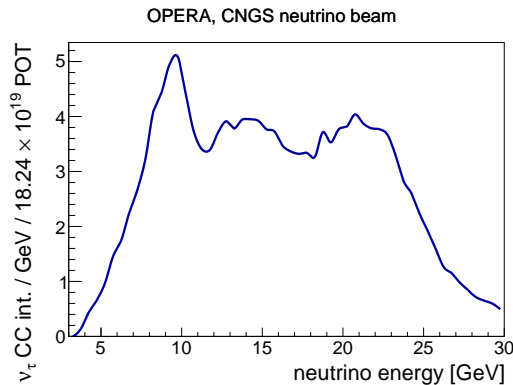


Figure 6.10: ν_τ CC interactions per GeV in OPERA for the integrated CNGS POT. Neutrino fluence taken from [101]. The OscProb package [62] has been used to calculate oscillation probabilities, GENIE [91] interaction cross sections have been used.

A significant improvement on the cross section measurement is only expected to be provided from the planned SHiP experiment. SHiP is foreseen downstream of CERN’s SPS beam dump ($E_p = 400$ GeV) and will collect several thousands of $\bar{\nu}_\tau$ events [95]. In addition, the capability to distinguish between τ^- and τ^+ will allow SHiP to measure not only inclusive, but also differential cross sections for ν_τ^{CC} and $\bar{\nu}_\tau^{\text{CC}}$ separately.

6.3.2 | Long baseline neutrino beams

Direct detection is also possible in neutrino beams which are initially free of $\bar{\nu}_\tau$. These experiments search for oscillated $\bar{\nu}_\tau$ at long baselines.

The oscillation $\nu_\mu \rightarrow \nu_\tau$ has been directly observed by OPERA in the 730 km long baseline of the CNGS neutrino beam from CERN to Gran Sasso. The event statistics expected to have interacted in the detector after the total delivered 18.24×10^{19} POT [99] is given as a function of energy in Fig. 6.10.

Similar to direct detection experiments right after the beam dump, the OPERA experiment was able to distinguish ν_τ events from other interaction channels by identifying the small kink between the primary vertex of the neutrino CC interaction ($\nu_\tau + \text{nucleon} \rightarrow \tau^- + \text{hadronic cascade}$) and the second vertex produced by the rapid τ^- decay thanks to the excellent vertex resolution of the instrument. With this approach it was possible to report a detection with 5.1σ significance based on only five ν_τ -like events [100].

Again, low statistics impeded a stringent cross section measurement, even though the flux in this case was free of anti-neutrinos.

In future, the upcoming liquid argon experiment DUNE will be able to collect sizeable statistics in oscillated $\bar{\nu}_\tau$ using the 1,300 km long baseline LBNF neutrino beam [89].

The high intensity beam aims to deliver an annual 1.1×10^{21} POT and is expected to run for seven years (3.5+3.5 in neutrino and anti-neutrino mode) in current plans. The option to produce a higher energy neutrino beam optimised for $\bar{\nu}_\tau$ studies during one of the seven years is under discussion [102].

The energy profile of expected $\bar{\nu}_\tau^{\text{CC}}$ interactions per year in DUNE (obtained from Ref. [103]) is shown in Fig. 6.11. In comparison to the CNGS beam (Fig. 6.10), the interacting $\bar{\nu}_\tau$ on

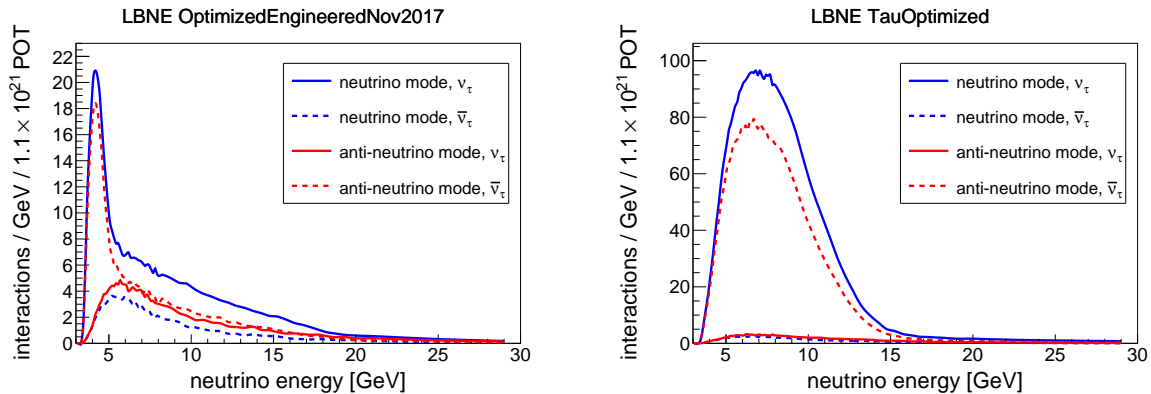


Figure 6.11: $\bar{\nu}_\tau$ CC interactions per GeV in DUNE for the expected annual POT in the LBNE neutrino beam. The OscProb package [62] has been used to calculate oscillation probabilities, GENIE [91] cross sections have been used.

average have lower energies, and statistics are small above ~ 15 GeV neutrino energy even for the $\bar{\nu}_\tau$ optimised beam. Compared to OPERA the main advantages are the much higher event statistics and the possibility to run in neutrino and anti-neutrino mode. The tracking resolution of liquid argon detectors is several millimetres [89] and hence not precise enough for direct detection of the τ^\pm tracks. Yet, the produced hadrons can be reconstructed individually with high accuracy. Like this, DUNE is projected to still obtain a relatively clean sample of $\bar{\nu}_\tau$ with less than 50% contribution from neutral-current backgrounds [102, Fig. 3] despite its 40 kT fiducial mass.

The presented approaches by beam experiments have two common limiting factors which impede the collection of $\bar{\nu}_\tau^{\text{CC}}$ events with high statistics. The detectors strive for precise event reconstruction by detecting the short τ track itself or at least by measuring the produced particles individually with high accuracy. This requires dense instrumentation. But the scaling of the technology to masses at the megaton-scale would be prohibitively expensive. The second limitation is the energy distribution in the neutrino beam. With the $\bar{\nu}_\tau^{\text{CC}}$ threshold at 3.5 GeV and a significantly suppressed cross section at low energies, it is difficult to exploit the produced $\bar{\nu}_\tau$ flux in a high intensity neutrino beam.

6.3.3 | Indirect detection in atmospheric oscillation experiments

A different approach is to measure $\bar{\nu}_\tau$ appearance using the naturally present atmospheric neutrino flux. The flux is essentially free of $\bar{\nu}_\tau$ at production (cf. Sec. 2.2), such that all $\bar{\nu}_\tau$ events observed stem from oscillations during propagation to the detector. Atmospheric neutrino experiments are able to collect high event statistics with sparse instrumentation of photo-sensors to search for the Cherenkov light patterns of neutrino interactions. A drawback from the sparser instrumentation is that $\bar{\nu}_\tau^{\text{CC}}$ interactions can no longer be identified on an event-by-event basis. Instead the additional $\bar{\nu}_\tau$ events will appear as a statistical excess on top of the event distribution that is expected from other flavours without $\bar{\nu}_\tau$. Due to the branching ratios of the τ decay, this excess will appear predominantly in the event distribution with shower-like signature. An identification of the event type as either shower- or track-like is therefore typically used as a proxy for the neutrino flavour in atmospheric neutrino

6. Tau-neutrino appearance

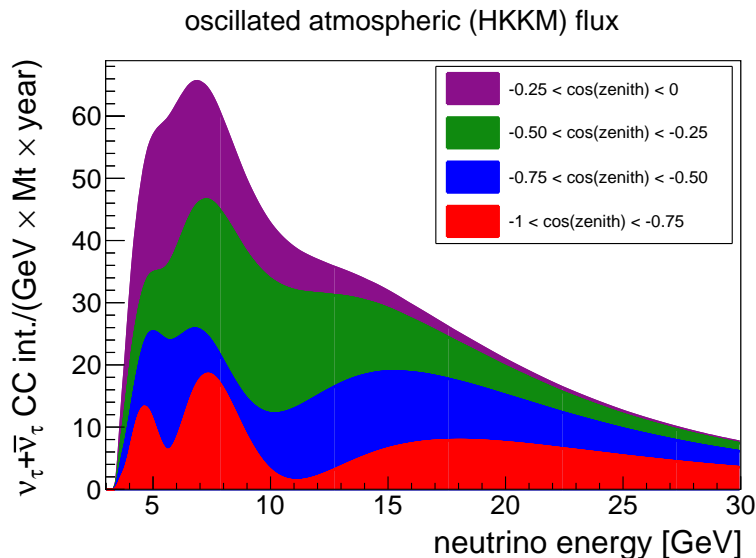


Figure 6.12: Annual $\bar{\nu}_\tau$ CC interactions per GeV and megaton appearing in the atmospheric neutrino flux through oscillation. Different $\cos(\text{zenith})$ ranges are stacked. The OscProb package [62] has been used to calculate oscillation probabilities, GENIE [91] cross sections have been used.

experiments.

The rate of interacting $\bar{\nu}_\tau^{\text{CC}}$ events in the atmospheric flux is shown in Fig. 6.12. The contributions from different cosine zenith ranges are indicated by colour. In contrast to the event distributions for the beam experiments (Fig. 6.10, Fig. 6.11), where the baseline is fixed, the maxima of the interacting event rates in energy change with the observed zenith angle.

The Super Kamiokande detector has been taking data deep underground in the Kamioka mine for more than a decade. Its water tank holds 50 kilo-tons of pure water and has the surrounding walls covered with photomultiplier tubes. Using multivariate techniques to improve the signal significance, Super Kamiokande observes $\bar{\nu}_\tau$ appearance with 4.6σ in the latest update of the analysis. In the analysis sample a $\bar{\nu}_\tau$ contribution of only about 20 events per year is retained [104, 105].

The low-energy extension of the IceCube neutrino observatory, DeepCore, has an energy threshold of ~ 10 GeV. This is also low enough to probe $\bar{\nu}_\tau$ appearance. In an analysis of 1006 days livetime an estimated 1804 $\bar{\nu}_\tau^{\text{CC}}$ and 556 $\bar{\nu}_\tau^{\text{NC}}$ are observed in 6.2×10^4 events. As opposed to OPERA and Super Kamiokande, where the best-fit value was found above one, DeepCore measured a normalisation $n_\tau^{\text{CC}} = 0.57^{+0.41}_{-0.27}$ at 68% CL for the $\bar{\nu}_\tau^{\text{CC}}$ contribution. When scaling both CC and NC contributions, a normalisation $n_\tau^{\text{CC+NC}} = 0.73^{+0.34}_{-0.24}$ is measured [106]. A comparison of the measured flux normalisations mentioned is provided in Fig. 6.13.

The size of the error bands suggests that as of today, it is known that $\bar{\nu}_\tau$ do appear in detectors through neutrino oscillation with a normalisation $n_\tau \approx \mathcal{O}(1)$. The constraint on the precise value of the normalisation is however still low.

Thanks to the better resolution with respect to DeepCore, the proposed dense in-fill IceCube Upgrade array, which is scheduled for deployment at the South Pole will be able to constrain the normalisation of the $\bar{\nu}_\tau$ flux to $\pm 10\%$ (with 1σ CL) within one year of operation [22].

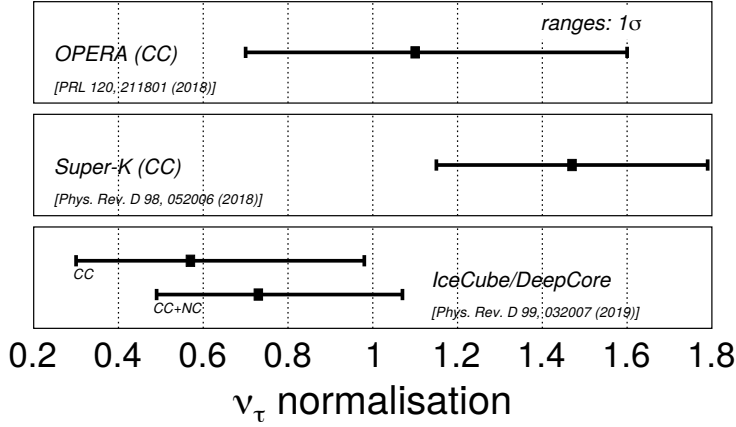


Figure 6.13: Current constraints on $\bar{\nu}_\tau$ appearance from OPERA [107], Super Kamiokande [104], and IceCube/DeepCore [106].

In this work the sensitivity of ORCA to $\bar{\nu}_\tau$ appearance is studied in Sec. 12. It will turn out that due to its multi-megaton instrumented volume and few-GeV energy threshold, ORCA will collect an unprecedented event statistics of >3000 $\bar{\nu}_\tau^{\text{CC}}$ events per year in the analysis sample and be able to measure the $\bar{\nu}_\tau$ appearance with high precision, $\pm 10\%$ ($\pm 30\%$) at 1σ (3σ) CL.

6.4 | Oscillation analysis with ORCA:

A roadmap towards the $\bar{\nu}_\tau$ appearance study

Since neutrino oscillation probabilities depend on L/E and both the neutrino energy and the traversed distance from the point of generation in the atmosphere to detector are not fixed for atmospheric oscillation experiments, a natural choice is to use a two-dimensional parameter-space. In addition, identification of the different event signatures can serve as a proxy for the neutrino flavour.

In ORCA, the analysis is performed in the two-dimensional plane of reconstructed energy and cosine of the reconstructed zenith angle in a set of three different event classes: track-like events, shower-like events, and ambiguous events in a middle class.⁴

In Fig. 6.14, the roadmap for simulated data to arrive at the event distribution in the reconstructed quantities for analysis is summarised. The first part is detector independent. It yields the interaction rate for (anti-)neutrino flavours a per unit volume as a function of energy (E) and zenith angle (θ_z) [1]:

$$R_a = \frac{\rho_{\text{water}}}{m_{\text{nucleon}}} \cdot \sum_b \sigma_a(E) \cdot P_{b \rightarrow a}^{\text{osc}}(E, \theta_z) \cdot \Phi_b^{\text{atm}}(E, \theta_z). \quad (6.8)$$

The ingredients to this calculation have been covered in Part I and are:

- a sum over initial flavours $b = \{\nu_e, \nu_\mu, \bar{\nu}_e, \bar{\nu}_\mu\}$ in the atmospheric neutrino flux Φ_b^{atm} (in Sec. 2)
- the oscillation probabilities between flavours $P_{a \rightarrow b}^{\text{osc}}$ for neutrinos traversing Earth (in Sec. 3)

⁴In earlier studies, e.g. in Ref. [1], only two classes, tracks and showers, had been used.

6. Tau-neutrino appearance

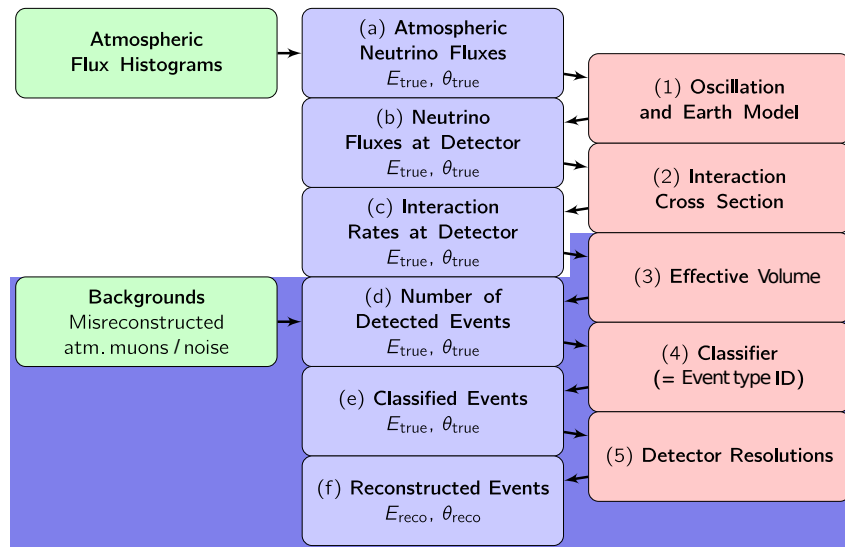


Figure 6.14: Computation scheme for event distributions followed by the analysis frameworks within ORCA. The detector-dependent part is backed with blue colour. Taken from Ref. [1] and slightly updated.

- the neutrino nucleon cross section σ_a (in Sec. 4)

The different R_a calculated for the CC and NC channels of the six different (anti-)neutrino flavours enter the second part of the calculation, which is dependent on the response of the detector (and highlighted with the background colour in Fig. 6.14).

The individual steps (3-5 in Fig. 6.14) of the detector dependent part have been further developed since the publication of the Letter of Intent for KM3NeT 2.0 [1] (LoI).

After the LoI, the Collaboration has started producing simulations with a detector layout that meets all external constraints in order to be deployed in the deep sea. This thesis contributes two of the main pillars in the further development of detector dependent part of the simulation and analysis chain using a realistic ORCA detector, namely the trigger studies in Sec. 9 to maximise the effective volume ((3) in Fig. 6.14) and the classification in Sec. 11 in order to reject background and to distinguish between neutrino event signatures ((4) in Fig. 6.14).

Together with the detector resolutions⁵, these constitute the main steps necessary for all neutrino oscillation sensitivity studies.

The $\bar{\nu}_\tau$ appearance study in Sec. 12 enlarges the physics scope of ORCA beyond the neutrino mass ordering analysis and measurement of the atmospheric oscillation parameters already covered in the LoI.

⁵A summary of the event reconstruction algorithms and event selection is provided in Sec. 10. Resolutions of the classed event samples are evaluated in Sec. 11.6.

7 The KM3NeT detector design

7.1 | The Digital Optical Module (DOM)

The basic detector element in KM3NeT, is a sensor module called the *Digital Optical Module*, or *DOM* for short. **Figure 7.1** (left) shows the picture of a DOM including its support structure. It consists of a 43 cm diameter glass sphere housing 31 photomultiplier tubes (PMTs) of which 19 are contained in the lower and 12 in the upper hemisphere of the module, additional sensors, calibration devices and the associated readout electronics. With respect to the current neutrino telescopes ANTARES, IceCube and Baikal-GVD, which consist of modules with a single large PMT, the novel multi PMT design of KM3NeT offers numerous advantages. The most important of them, in particular in light of their relevance for the studies in this thesis, are [76]:

1. **Increased photocathode area:** One KM3NeT DOM alone has a photocathode area comparable to three ANTARES sensor modules with a single 10-inch PMT (cf. **Sec. 16.1**).
2. **Background suppression:** Local coincidences of registered photons on the same module can be used to reduce the level of background noise.

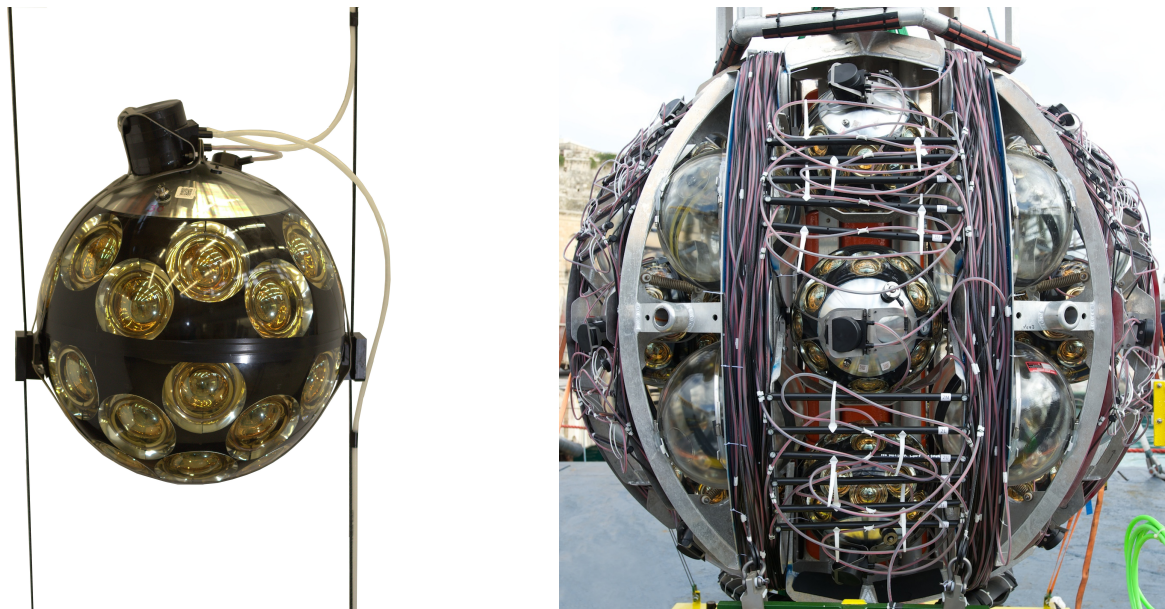


Figure 7.1: KM3NeT Digital Optical Module (DOM) with support structure and a Detection Unit (DU) furling onto a deployment device. Pictures taken from [20].

7. The KM3NeT detector design

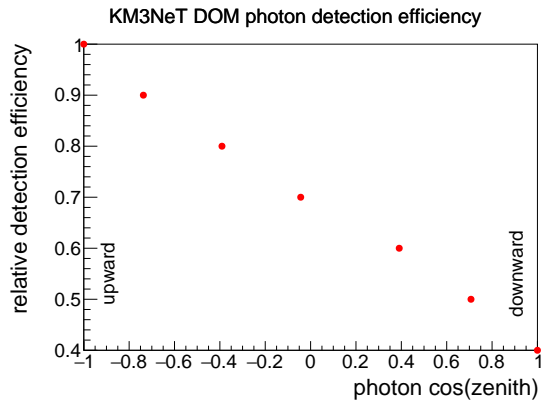


Figure 7.2: Relative detection efficiency as a function of photon arrival zenith direction. Data retrieved from Ref. [4, Fig. 5.3].

- Intrinsic sensitivity on photon arrival direction:** The segmentation of the photocathode area preserves the directional information of the registered photons. This can be exploited in advanced algorithms for event reconstruction, but also to refine the definition of local coincidences.
- Close to uniform angular acceptance:** The segmentation within a multi PMT module provides uniform angular acceptance for photons in azimuth. In zenith, the detection efficiency is $\sim 2.5\times$ higher for upward- compared to downward-travelling photons, as shown in Fig. 7.2. This is a significant improvement with respect to single PMT modules, which reach a 2π space angle coverage at best.
- Risk reduction:** The photocathode area of a module is only reduced marginally if single PMTs fail.

(2) and (3) are particularly useful to define coincident *hits* for event triggering in Sec. 7.4. (4) affects the detection efficiency of events not only after trigger, but also in the final event selection in Sec. 10.2. The consequences from failure of detection channels, (5), are evaluated in Sec. 9.4.2.

A large fraction of the modules for a meanwhile funded upgrade to the IceCube detector at the South Pole will also follow a multi PMT approach in order to exploit these benefits [108].

7.2 | The Detection Unit (DU)

In ORCA, 18 DOMs are attached to two vertical Dyneema® ropes spaced 9.3 m on average. Within KM3NeT, these vertical structures are called *Detection Units (DUs)*. At the bottom, the DU is fixed to the sea bed by an anchor. At the top, an additional subsea buoy increases the self-bouyancy of the DOMs such that the DU is held straight.

For the installation, the DU is furled onto a deployment device depicted in Fig. 7.1 (right), which can be lowered to the sea floor. After lowering the device, the DU can be connected and tested while still furled. A remotely operated deep sea robot can then mechanically release the deployment device from the anchor. The DU will unfurl thanks to buoyancy of both the DU itself and the deployment device. The deployment device is collected after reaching the sea surface and re-used.

The fact, that DUs need to fit on the deployment device sets constraints to the vertical inter-DOM spacings. Along the DU they are symmetric along the z -axis and alternate between 9.4 m and 8.7 m except for DOMs 6↔7 and 12↔13, where the spacing is larger, 10.9 m instead of 8.7 m.

7.3 | The ORCA Detector

The full ORCA detector will comprise 115 DUs anchored to the seabed at 2.5 km depth off-shore Toulon in France. DUs will be arranged in an almost circular footprint as shown in a preliminary map for the deep sea infrastructure in Fig. 7.3. This map foresees a conservative average 23 m horizontal spacing between DUs. Two main electro-optical cables (MEOCs) supply power to the DUs and transmit all data digitised on each individual DOM to shore via five nodes. Each node in turn joins up to six daisy chains of four DUs. The connection of additional devices for calibration and environment monitoring is also foreseen (indicated by CB and IU/MII, respectively, in Fig. 7.3).

In September 2017 the first ORCA DU has been deployed and started data taking. Data taking was interrupted after a fault in the MEOC between December 2017 and February 2019. After succeeding sea operations, data taking continued with 1 (02/2019), 2 (05/2019), and 4 (07/2019) DUs.

Since the sea operation end of January 2020, 6 DUs are currently installed and in operation. Their approximate positions are marked in blue on the map. Additional ORCA DUs are planned to be installed in the second half of the year 2020.

The deployment of the first DUs has shown that metre precision positioning accuracy on the sea bed can be achieved. Consequently, a reduction of the average inter-DU spacing to 20 m is judged feasible from a deployment perspective.

For sensitivity studies Monte Carlo mass productions have been generated for 115 DU detector configurations with both 23 m and 20 m average inter-DU spacing. To study the reconstruction performance and the physics potential of ORCA at an early phase, a Monte Carlo mass production for 7 DUs (marked in blue/green) has been prepared. A more detailed description of the different sets of Monte Carlo mass productions for ORCA is given in Sec. 8.2.

7.4 | Signal digitisation and data transmission

7.4.1 | L0 hits

On the DOM, the signals of the PMTs are digitised. For the conversion to registered signals, called *hits*, the analogue waveform is transformed into a rectangular signal by using a comparator with an adjustable threshold. The threshold value is typically set to 30% of the amplitude expected from a single photo-electron. The time at which this threshold is surpassed defines the start time of a *L0* (level zero) *hit*. In addition to the start time, the time-over-threshold (ToT) and the PMT identifier constitute all information stored in a hit.

KM3NeT follows an ‘all data to shore’ principle. Each DOM sends all L0 hits to shore. The transferred data is chunked in time-slices of 100 ms length. For a full building block this will

7. The KM3NeT detector design

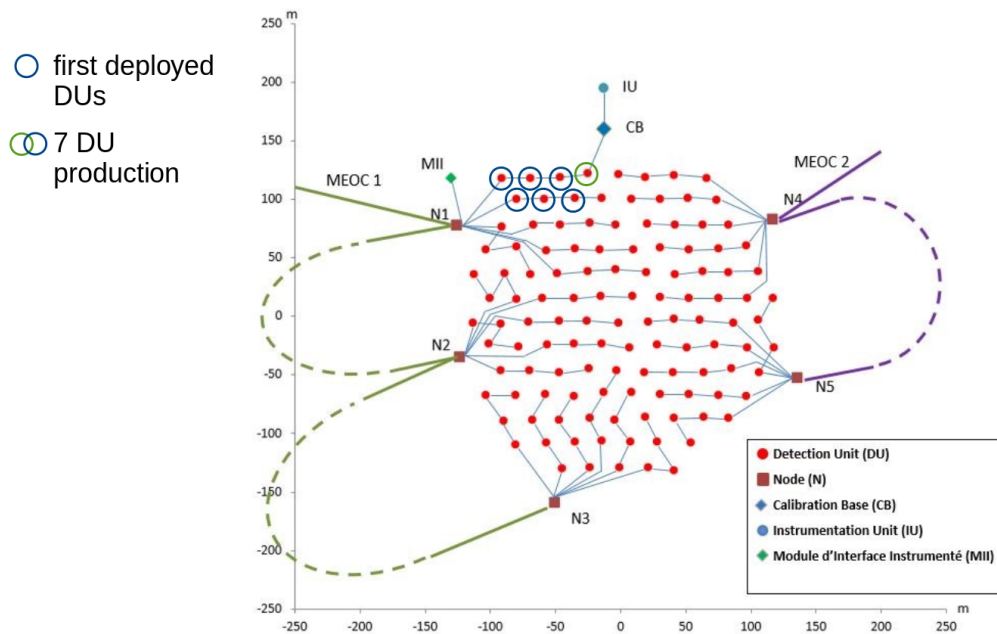


Figure 7.3: Layout of the full ORCA array, depicting the 115 (+5 contingency) Detection Units, cabling, connectors and infrastructure devices. The figure is an updated version of Ref. [1, Fig. 6]. The 6 (7) Detection Units already in operation (used in the simulation of a small sub-array detector) are marked.

lead to a data transfer rate of 25 Gb/s. On-shore the time-slices of all DOMs in the detector are combined and the amount of data is filtered using software triggers.

7.4.2 | L1 and L2 hits for the trigger

Since the L0 hit rate on each PMT is 7 kHz, the computational effort to filter data of a whole building block prevents triggering based on L0 hits alone.

Therefore, additional higher-level hits, L1 and L2 hits are defined. A L1 condition is satisfied, if two L0 hits occur on the same DOM within a short coincidence time window of < 10 ns. Similarly, a L2 hit is a L1, but with the additional constraint that the PMTs forming the coincidence are oriented in similar directions with an opening angle of $< 90^\circ$. This significantly reduces the probability of chance coincidences induced by background light. Currently, L0 and L2 coincidences are used to trigger events. The amount of data is reduced by $\mathcal{O}(10^3)$ when writing only short snapshots of L0 data while a trigger condition is met rather than the full L0 stream to disk. Event triggering for ORCA is described in detail in [Sec. 9](#).

8 Monte Carlo simulations for ORCA

In this chapter the Monte Carlo mass productions for ORCA are described. The simulation chain is summarised in Fig. 8.1 and consists of six major subsequent steps:

1. **Generation:** The set of outgoing particles in neutrino interactions or atmospheric muon bundles are simulated.
2. **Propagation:** Light output for the outgoing particles is generated and propagated onto the photo-cathode surfaces.
3. **Triggering:** Electronics response and addition of optical background light is simulated and software trigger algorithms are applied. From this stage onwards, simulated data events of all types – neutrinos, atmospheric muons and pure noise events – are similar to data taken off-shore.
4. **Reconstruction:** Triggered events are then reconstructed by track and shower reconstruction algorithms. After reconstruction, additional parameters based on the reconstruction outcome are calculated. Summary files are produced with a flat table structure to facilitate usage in the event identification (step 5) and analysis (step 6).
5. **Event Identification (EID):** To classify events, machine-learning based EID is applied to the summary files.
6. **Analysis:** The classified output can be used for high-level physics analyses.

This chapter is consists of two parts. In Sec. 8.1, the Monte Carlo simulation chain and software packages used for the individual event types are described. Section 8.2 gives details on the layouts of ORCA for the different mass productions with a realistic detector. Therein details on the simulated datasets are provided.

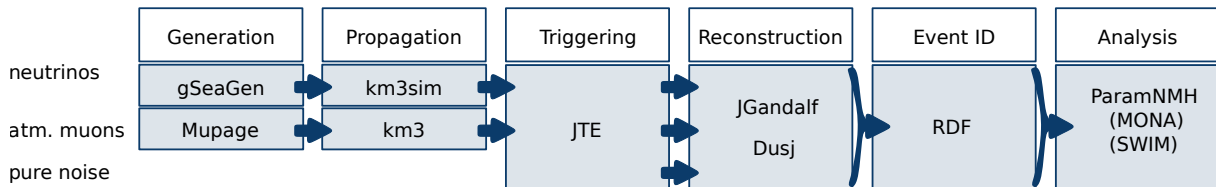


Figure 8.1: The simulation stages of ORCA and corresponding software packages used in this work. The simulation chain differs for atmospheric neutrinos, muons and pure noise up to trigger-level. More detail is given in the text.

8.1 | Simulation chain up to trigger-level

The response of the detector is simulated using detailed Monte Carlo (MC) simulation of the neutrino signal, the atmospheric muon bundles and the optical pure-noise background.

The Monte Carlo chain features three subsequent software stages starting with the generation of initial particles in the events, followed by the production of Cherenkov light and tracking through sea water onto the PMT surfaces, and, finally simulation of the electronics response, readout, and data filtering. In the last step also background noise hits are added to the simulation. The software used is similar to the description in Ref. [1]. In the following, more details on the simulation packages for the three different categories of events are given.

Simulation of neutrino events The neutrino interactions in sea water are simulated using gSeaGen [109], a software package based on the GENIE (version 2.12.10) [110, 91] neutrino event generator, which is widely used in the neutrino community. Neutrino events are simulated in the energy range from 1 GeV to 100 GeV and obtain event weights such that they can be weighted according to an atmospheric flux spectrum in the analysis.

To handle the decay of τ -leptons, gSeaGen interfaces PYTHIA [111]. In the software version used, polarisation of the produced τ -leptons is not taken into account and τ -leptons are forced to decay without energy loss along their trajectory.¹ At the energies relevant for $\vec{\nu}_\tau$ appearance these two simplifications are a good approximation. Especially the short decay length (cf. Sec. 6.2.2) of the τ allows to safely neglect energy loss during τ propagation.

All particles produced at generation stage are propagated with the GEANT4 based KM3Sim [114] package. KM3Sim generates Cherenkov photons from the primary input particles and the secondary particles that emerge in the generated cascades. KM3Sim then tracks the generated Cherenkov photons taking absorption and scattering in the sea water into account and records photons impinging on the PMT surfaces. The sea water is parametrised with an effective absorption length of 67.5 m following measurements at the NEMO site in Italy [115]. This water was chosen for the better agreement with observations at the nearby ANTARES site [74, p. 100ff] compared to a previously measured ANTARES absorption curve [73] (55 m effective absorption length) which had been adopted for MC simulations in the LoI [1] (see also Sec. 5.2).

Simulation of atmospheric muon bundles The MUPAGE [116] package is used to generate atmospheric muon events. This software uses parametrisations derived from data taken with the multi-purpose underground detector MACRO [117, 118] to draw muon bundles matching the expected distributions in the deep sea with regard to rate, zenith angle and energy, as well as multiplicities and lateral spacing between muon tracks within bundles.

For the simulation of Cherenkov photons and propagation onto the PMTs the KM3 package [49] is used, to keep the computational effort manageable. In contrast to KM3Sim, KM3 is based on parametrisations rather than individual photon tracking. The computational effort thus does not scale linearly with deposited energy. As for neutrinos, an effective absorption length of 67.5 m is used for KM3.

¹Note that the most recent version of gSeaGen properly takes into account the polarisation of the τ by interfacing the TAUOLA package [112]. It also allows for energy loss along the τ trajectory via the TAUSIC package [113].

Simulation of the PMT response and readout The `JTriggerEfficiency` (JTE) software – a custom KM3NeT code from the JPP framework [3] – is used to simulate the electronics’ response of the PMTs to the Cherenkov photon hits and to take care of the data filtering. In this step the optical background is added. The optical background added is described in more detail in the next paragraph. For neutrinos and atmospheric muons background is only simulated around the time of the simulated photon hits. In case of pure noise simulation the requested number of full 100 ms time-slices without signal photon hits are filled with optical background only and processed through the trigger.

Addition of background noise In the trigger, an uncorrelated optical rate of single hits of 10 kHz per PMT is added. This rate is conservative with respect to the ≈ 7 kHz evaluated from data taken with the first DU in situ. The uncorrelated singles’ rate is caused by a sum of background light from the radioactive ^{40}K isotope and by bioluminescence in the sea water.

In addition, ^{40}K also produces correlated higher-fold coincidences within a DOM. An exclusive rate of 600 Hz two-fold, 60 Hz three-fold, 7 Hz four-fold, 0.8 Hz five-fold, and 0.08 Hz six-fold coincidences is added to the simulation. The exclusive rate is calculated after subtraction of accidental coincidences formed by uncorrelated background hits. The stated values had been derived in a preliminary analysis using two DOMs of the first KM3NeT/ARCA detection unit [119].²

The choice of N -fold exclusive coincidences turns out to be slightly higher than observed in the data in a more elaborate full analysis published in Ref. [120]. The latter is based on a larger set of DOMs with a better calibration of the PMTs’ time-offsets and detection efficiencies and different subtraction of accidental N -fold coincidences. The values for the N -fold coincidence rates, named hit multiplicity, found in the analysis are shown in Fig. 8.2. The 2–5-fold coincidence rates are completely dominated by ^{40}K and are approximately 500, 50, 5, and 0.5 Hz, respectively. Higher-fold coincidences are dominated by atmospheric muons and are higher for ORCA than ARCA due to the shallower depth of the detector.

8.2 | Monte Carlo mass productions for realistic detector setups

As an essential part of the LoI, the sensitivity of ORCA to determining the NMO has been studied for different instrumentation densities. The optimum DOM density found has an average spacing of ~ 20 m in xy and 9 m in z , but is based on an evenly spaced array of DOMs.

Using this optimisation result, realistic detector setups are now simulated that satisfy all requirements necessary for (safe) deployment. More precisely, the specified vertical spacings on the DUs to fit on the deployment device (Sec. 7.2), and a 20 m minimum (23 m average) horizontal spacing between DUs is respected. The simulated detector now follows the deployment plan in Fig. 7.3. After experience gathered during deployment of the first lines, the latter constraint was refined to 17 m minimum (20 m average) spacing. A second set of Monte Carlo simulations has been generated with this denser detector by scaling the xy positions.

Simulation sets are generated for the four different neutrino types, $\bar{\nu}_e^{\text{CC}}$, $\bar{\nu}_\mu^{\text{CC}}$, $\bar{\nu}_\tau^{\text{CC}}$ and

²The data suggested a $\sim 10\%$ higher PMT effective area. N -fold coincidences consequently have approximately a 1.1^N higher probability to occur.

8. Monte Carlo simulations for ORCA

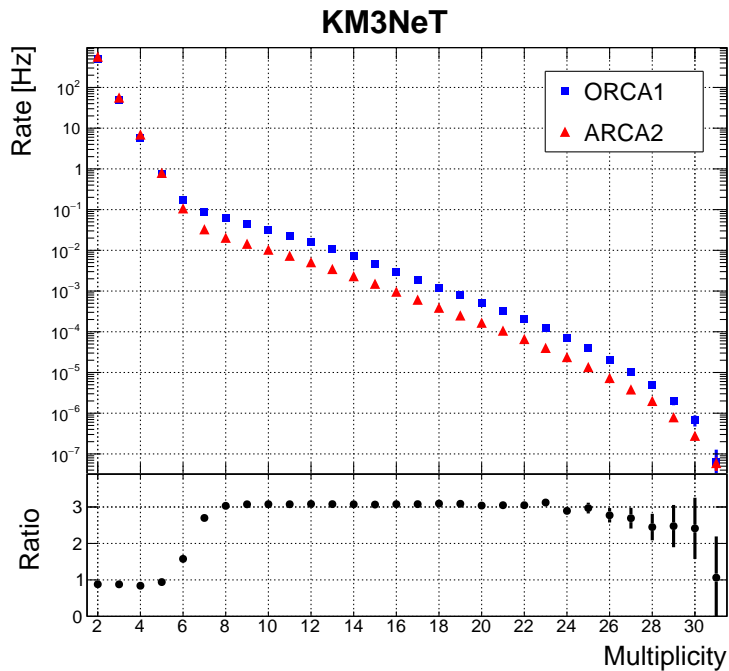


Figure 8.2: Exclusive DOM coincidence rates as function of the multiplicity averaged over DOMs in the first lines of ORCA (ORCA1) and ARCA (ARCA2). Figure taken from Ref. [120].

$\bar{\nu}_e^{\text{NC}}$ ³ Neutrino simulations are split in two parts with a harder simulated spectrum at the threshold than at high energies. This is to avoid the generation of too many sub-threshold neutrinos and optimise computation time in KM3Sim (light generation / propagation) and JTriggerEfficiency (trigger).

For the 23 m simulation, 14 days of atmospheric muons, and 1.7 days of pure noise have been generated. Since the production of sufficient livetime of background, is computationally expensive, no background simulation has been produced for the 20 m production.

For the 23 m production with seven DUs⁴, KM3Sim output for neutrinos and atmospheric muons has been used to re-run the trigger with the reduced detector layout. Pure noise was newly generated and is significantly faster for few DUs. Since the pure noise contribution reduces when keeping the trigger settings unchanged, 10.4 days have been simulated.

The simulated livetimes for background, energy ranges and spectral indices for neutrinos and the number of events remaining after the trigger (which is discussed in the chapter below) are tabulated in Tab. 8.1 for the 23 m production, in Tab. 8.2 for the 7 DU sub-array, and in Tab. 8.3 for the 20 m production.

Note that the simulated livetime of pure noise is such that the number of events surviving the trigger roughly matches the sum of simulated neutrinos. The spectral indices and number of simulated neutrino events for the 20 m production were chosen to roughly follow the atmospheric fluxes for $\bar{\nu}_e$ and $\bar{\nu}_\mu$. In addition the complication of the energy overlap between the two energy ranges present in the 23 m production was removed.

³Note that the NC does not depend on flavour. Hence only one, $\bar{\nu}_e^{\text{NC}}$, has been set in the configuration of the simulation code.

⁴The first ORCA DUs have been deployed following the deployment plan for 23 m.

Table 8.1: Simulated event statistics for 115 DU setup with 23m average DU spacing.

background simulation	equiv. livetime [days]	$N_{\text{trigger}}/10^6$
pure noise	1.74	8.02
atmospheric μ	14.0	65.2
neutrino simulation	spectral index	$N_{\text{trigger}}/10^6$
ν^{NC} : 1 – 5 GeV / 3 – 100 GeV	E^{-1} / E^{-3}	1.03 / 1.83
$\bar{\nu}_e^{\text{CC}}$: 1 – 5 GeV / 3 – 100 GeV	E^{-1} / E^{-3}	1.48 / 1.99
$\bar{\nu}_\mu^{\text{CC}}$: 1 – 5 GeV / 3 – 100 GeV	E^{-1} / E^{-3}	1.69 / 2.05
$\bar{\nu}_\tau^{\text{CC}}$: 3.4 – 100 GeV	E^{-3}	2.08

Table 8.2: Simulated event statistics for 7 DU setup with 23m average DU spacing.

background simulation	equiv. livetime [days]	$N_{\text{trigger}}/10^5$
pure noise	10.4	9.8
atmospheric μ	14.0	100
neutrino simulation	spectral index	$N_{\text{trigger}}/10^5$
ν^{NC} : 1 – 5 GeV / 3 – 100 GeV	E^{-1} / E^{-3}	0.50 / 1.2
$\bar{\nu}_e^{\text{CC}}$: 1 – 5 GeV / 3 – 100 GeV	E^{-1} / E^{-3}	0.75 / 1.4
$\bar{\nu}_\mu^{\text{CC}}$: 1 – 5 GeV / 3 – 100 GeV	E^{-1} / E^{-3}	0.87 / 1.6
$\bar{\nu}_\tau^{\text{CC}}$: 3.4 – 100 GeV	E^{-3}	1.6

Table 8.3: Simulated event statistics for 115 DU setup with 20m average DU spacing.

neutrino simulation	spectral index	$N_{\text{trigger}}/10^6$
ν^{NC} : 1 – 10 GeV / 10 – 100 GeV	$E^{-2.8} / E^{-3.05}$	0.26 / 0.44
$\bar{\nu}_e^{\text{CC}}$: 1 – 10 GeV / 10 – 100 GeV	$E^{-2.9} / E^{-3.4}$	1.56 / 0.56
$\bar{\nu}_\mu^{\text{CC}}$: 1 – 10 GeV / 10 – 100 GeV	$E^{-2.8} / E^{-3.1}$	2.83 / 1.95
$\bar{\nu}_\tau^{\text{CC}}$: 3.4 – 10 GeV / 10 – 100 GeV	$E^{-2.8} / E^{-4.0}$	0.77 / 1.75

9 Triggering in ORCA

Software triggers are in place to scan through the data sent to shore and reduce the amount of data written to disk. This chapter describes the optimisation of the triggers for a realistic detector layout of ORCA. The effects of bioluminescent background and missing detection channels on the trigger effective volumes and the possible consequences for oscillation analyses are quantified.

9.1 | Description of the triggers used in ORCA

Trigger algorithms scan through the time-slice data and look for clusters of hits that are interesting to store for off-line reconstruction and analysis.

When a trigger condition is satisfied, the trigger ‘fires’ and a snapshot of all hits in the detector is saved. These snapshots are commonly referred to as ‘events’. The timespan of an event ranges from first to last triggered hit with added safety margin to make sure no hits from the event are missed. The safety margin is of order $\sim 1 \mu\text{s}$ and corresponds to the time needed for light to traverse the detector. Series of trigger clusters which overlap in time, called overlays, are merged. [Figure 9.1](#) displays a recorded event with the mentioned properties.

Currently, three trigger algorithms exist in ORCA, which are described in the following subsections. Importantly, a new trigger algorithm, MXShower, has been developed by the Collaboration and is used for the first time in Monte Carlo mass productions. Its main purpose is to lower the energy threshold. All triggers have been optimised for the mass productions with a realistic detector layout. The optimisation procedure is presented in detail in [Sec. 9.2](#) and the performance is evaluated in [Sec. 9.3](#). [Section 9.4](#) analyses the robustness with respect to missing channels and bioluminescence activity. The optimal trigger settings derived are already used for the first detection units during ongoing construction. In-situ performance is evaluated in [Sec. 9.5](#). Finally, in [Sec. 9.6](#), MXShower is also applied to simulations for detector configurations with a denser instrumentation than ORCA – named Super-ORCA – which would be necessary when aiming for the determination of the CP-violating phase δ_{CP} .

9.1.1 | Triggers based on L2 hits

Two trigger algorithms, named 3DMuon and 3DShower and referred to as 3D triggers, have been already used in the LoI [1]. Both algorithms search for interesting clusters of at least N_{hits} causally connected L2 hits (as defined in [Sec. 7.4](#)) in the time-slices. The causality criteria are different for both algorithms and, as the names suggest, cover the two expected event topologies of light emission along a muon track for 3DMuon and spherical emission from a single point for 3DShower, respectively. For these triggers, L2 hits need to be on different DOMs to be counted, $N_{\text{hits}} = N_{\text{modules}}$.

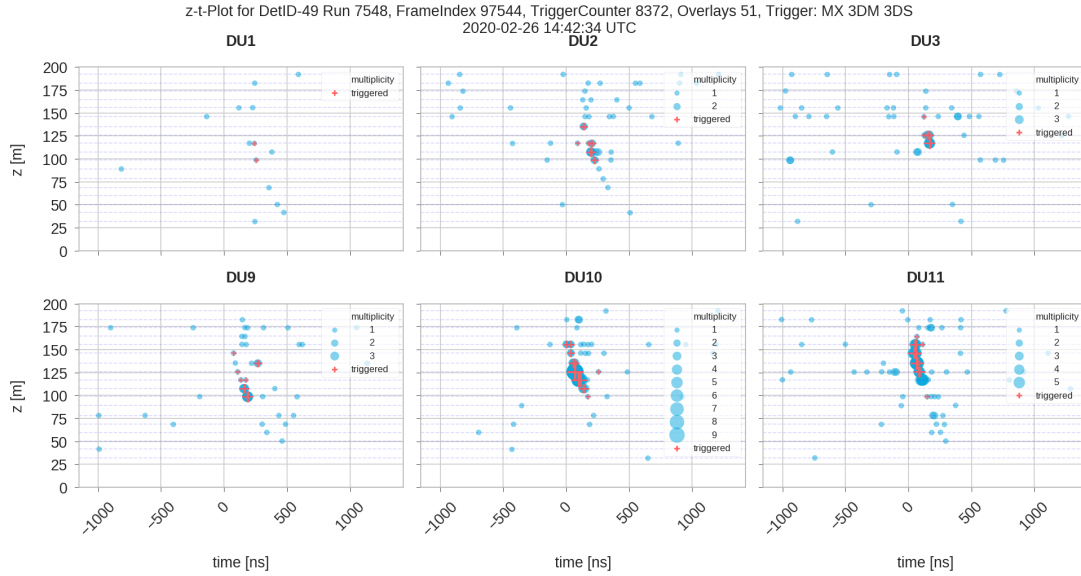


Figure 9.1: Online monitor of a triggered ORCA event recorded with six DUs where all three trigger algorithms have fired. Axes are hit time with respect to the first triggered hit versus height of the DOM above sea floor. The event contains an overlay of 51 trigger clusters. Hits contributing to a trigger cluster are marked as ‘+’, all hits in the snapshot are marked as dots. Sizes correspond hit multiplicities on the respective DOM. Taken from [121].

For the 3DShower trigger, two hits (i and j) are considered to be causally connected if they fulfil the following condition:

$$c \cdot |t_i - t_j| \leq \eta |\vec{r}_i - \vec{r}_j| + c \cdot t_{\text{extra}}, \quad (9.1)$$

where $\vec{r} = (x, y, z)$ and t represent the hit position and time and η is the refractive index of sea water. The parameter t_{extra} is an additional tolerance and set to $t_{\text{extra}} = 10$ ns. It can accommodate uncertainties in the time and position calibration of the detector and larger values lead to a decreased signal to noise ratio. In addition to N_{hits} , the maximum distance D_{max} is a parameter subject to trigger optimisation. It sets a limit on the distance of L2 hits that can contribute to a cluster,

$$D_{\text{max}} \geq |\vec{r}_i - \vec{r}_j|. \quad (9.2)$$

The causality criterion for the 3DMuon is

$$c \cdot |t_i - t_j| \leq (z_i - z_j) + \eta \sin \theta_c \sqrt{(x_i - x_j)^2 + (y_i - y_j)^2} + c \cdot t_{\text{extra}}, \quad (9.3)$$

with the Cherenkov angle θ_c (cf. Eq. 5.1) and the remaining parameters as defined in Eq. 9.1. Hits are clustered with this causality condition for 200 evenly distributed test directions across a 4π sphere. The coordinate system in Eq. 9.3 is chosen such that the z component of the hit position $\vec{r} = (x, y, z)$ aligns with the respective test direction.

In addition to N_{hits} , the second parameter for 3DMuon to be optimised is the maximum radial distance of hits, R_{max} . It limits the size of the square root of the inequality Eq. 9.3,

$$R_{\text{max}} \geq \sqrt{(x_i - x_j)^2 + (y_i - y_j)^2}. \quad (9.4)$$

9. Triggering in ORCA

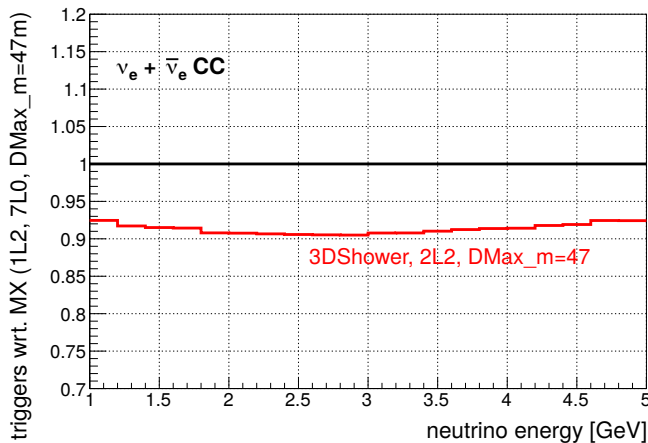


Figure 9.2: Comparison of the MXShower trigger efficiency for a single L2 hit and seven additional L0 hits in the vicinity (i.e. $N_{\text{modules}} = 8$) with a 3DShower trigger requiring two L2 hits and the same D_{max} .

Figuratively speaking, $R_{\text{max}} (D_{\text{max}})$ defines the size of the tube (ball) in which to look for causally connected L2 hits.

9.1.2 | Low-energy trigger MXShower

ORCA's sensitivity to NMO and other physics searches crucially depends on the detection threshold. In order to increase the trigger efficiency for events towards lower energies, the MXShower trigger was developed in addition to the 3D triggers described in Sec. 9.1.1. It uses only one single L2 hit as seed to look for $N_{\text{hits}} - 1$ additional L0 hits in vicinity that satisfy the causality condition for showers in Eq. 9.1. Especially at low neutrino energies the light yield often is not sufficient to produce even two L2 coincidences. A new trigger based on only one L2 coincidence plus surrounding L0 hits therefore outperforms even a too loosely configured L2-based trigger that only requires two causally connected L2s by up to 10% in the few-GeV energy region. This is shown in Fig. 9.2.

For MXShower, the L0 hits that contribute to the trigger condition do not need to be all on separate DOMs to be counted, i.e. $N_{\text{modules}} \leq N_{\text{hits}}$. Requiring $N_{\text{modules}} > 2$ reduces the number of triggers on pure noise events caused by very bright emission near one DOM as can occur during bioluminescent bursts. However, large N_{modules} reduce the efficiency gain over the 3D triggers at low energies. Therefore, performance of MXShower can be optimised on N_{modules} in addition to N_{hits} and D_{max} .

9.2 | Trigger optimisation

In ORCA the trigger parameters are optimised such that the neutrino efficiency is maximised while keeping the used disk space and computing resources required to further process the triggered events manageable. Therefore, a reasonable target is that the rate of stored events caused by pure noise shall not exceed the irreducible trigger rate from atmospheric muons, which for ORCA is ≈ 55 Hz. Individual triggers are optimised such that the pure noise rate amounts to ~ 10 Hz for 3DMuon and ~ 20 Hz for both 3DShower and MXShower. The event sample written to disk is therefore physics dominated and sums to ~ 100 Hz for the full ORCA

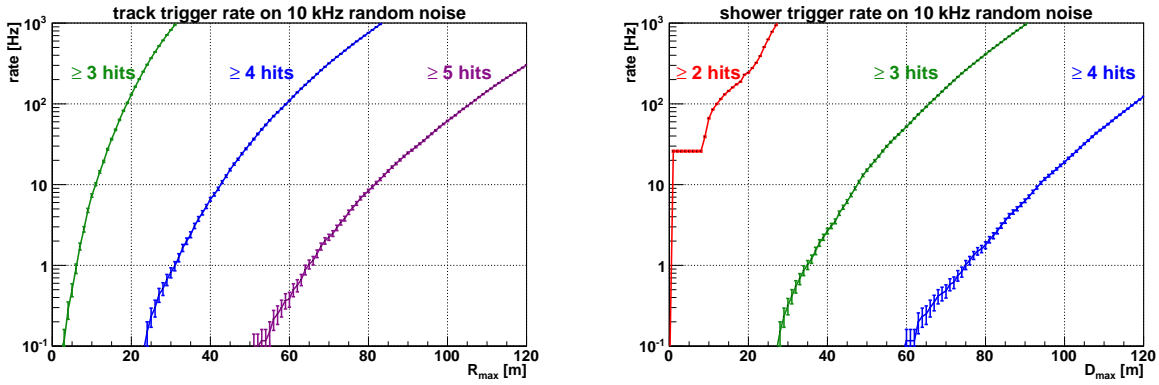


Figure 9.3: Triggered event rate of pure noise for the 3DMuon (left) and 3DShower (right) triggers for scans of the extension parameters R_{\max} and D_{\max} . Colours represent different N_{hits} .

detector.

The trigger studies presented in the following have been done for an ORCA detector with 23 m average horizontal spacing unless stated otherwise.

9.2.1 | Trigger optimisation for the 3DTrack and 3DShower triggers

The optimisation target of the two 3D trigger algorithms was chosen to allow pure noise events to be recorded with a rate below 10 Hz for 3DMuon and below 20 Hz for 3DShower. As explained in [Sec. 9.1.1](#), each of the algorithms has two parameters that can be optimised to maximise neutrino efficiency under this condition. [Figure 9.3](#) shows the rate of pure noise triggers for different N_{hits} and R_{\max} (D_{\max}) for 3DMuon (3DShower). A minimum of $N_{\text{hits}} = 4$ is needed for the 3DMuon. Requiring only three L2 hits can lead to artificial trigger inefficiencies dependent on the direction and position of events. This is because the R_{\max} parameter required to reach a sufficiently low noise contamination is similar in size to the average spacing between adjacent DOMs. On the other hand, moving to five L2s, the R_{\max} parameter could be loosened beyond one absorption length, where the probability to find an additional L2 coincidence is reduced significantly. A similar argument holds for the 3DShower trigger, for which $N_{\text{hits}} = 3$ is optimal.

The pure noise events triggered by the two 3D triggers are almost disjoint and the resulting combined pure noise rate for the optimised parameters adds to ≈ 30 Hz (cf. [Fig. 9.4](#)). [Table 9.1](#) lists the optimised parameter values for the mass productions with a realistic ORCA detector. The obtained values are consistent with the ones found for an idealised detector [1].

9.2.2 | Trigger optimisation for the MXShower trigger

While the best choice for the N_{hits} parameter is obvious for the 3D triggers, the decision is not straightforward for the MXShower trigger, since reasonable D_{\max} values are obtained for several values of N_{hits} . In addition, single L0 hits originating from the neutrino interaction can occur at large distances from the vertex more easily than L2 coincidences. [Figure 9.5](#) shows a parameter scan for N_{hits} in conjunction with D_{\max} . The trigger effective volumes

9. Triggering in ORCA

Figure 9.4: Combined rate of pure noise triggers for different values of R_{\max} for the 3DMuon trigger and D_{\max} for the 3DShower trigger. Black lines indicate the optimisation result for R_{\max} and D_{\max} .

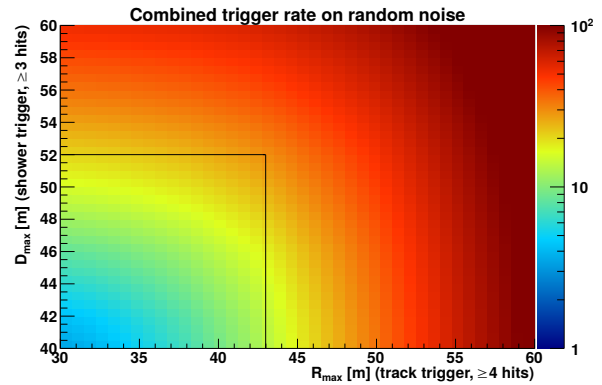


Table 9.1: Optimised trigger parameters for the complete ORCA detectors with 23 m and 20 m horizontal spacing.

trigger	parameter	23m prod.	20m prod
3DMuon	N_{hits}	4	4
	R_{\max} [m]	43	38
3DShower	N_{hits}	3	3
	D_{\max} [m]	52	46.5
MXShower	N_{hits}	8	8
	N_{modules}	3	3
	D_{\max} [m]	47	43.3

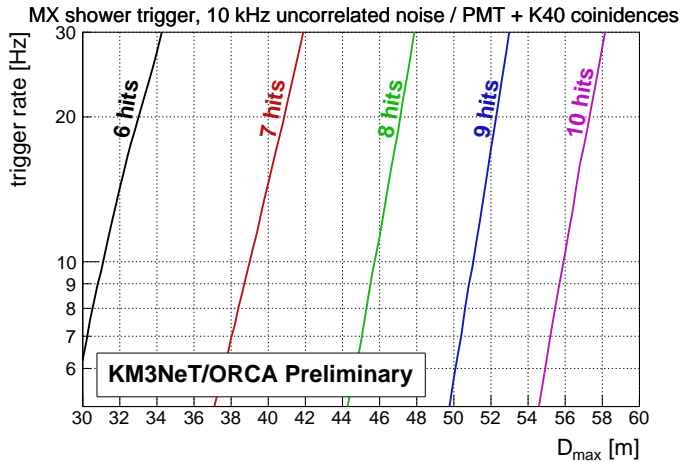


Figure 9.5: Rate of pure noise events triggered with MX-Shower for different values of the N_{hits} and D_{max} parameters.

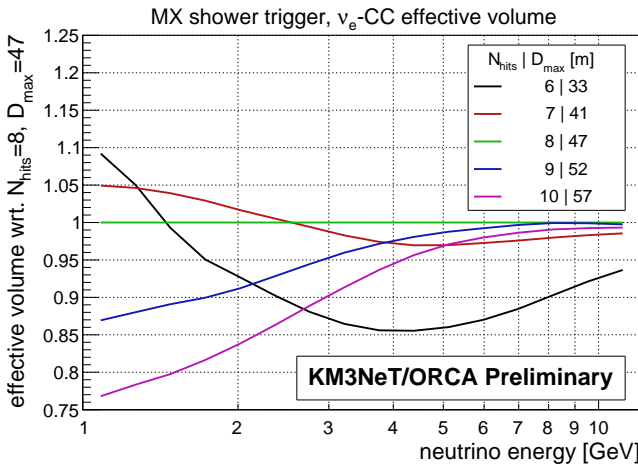


Figure 9.6: MXShower $\bar{\nu}_e$ -CC effective volume ratios for N_{hits} and D_{max} combinations corresponding to 20 Hz pure noise rate with respect to $N_{\text{hits}}=8$.

for $\bar{\nu}_e$ -CC events are compared for the parameter combinations with a 20 Hz contamination of pure noise in Fig. 9.6.

For MXShower $N_{\text{hits}} = 8$ turns out optimal. Higher values decrease the efficiency especially below ~ 5 GeV, because of the small light yield of low-energy events. Less than eight hits only give a modest increase in efficiency right at the detection threshold, but the corresponding smaller D_{max} values decrease the detection efficiency in the energy region between 3 GeV and 6 GeV, which is of prime importance for the measurement of oscillation parameters, in particular the NMO (as was motivated in Sec. 3.2.3).

In the target range of D_{max} , the MXShower trigger is stable and the effective volume shows linear increase with D_{max} . This can be seen in the comparison of the MXShower and the optimised 3DShower triggers for a wide range of D_{max} in Fig. 9.7. Only for D_{max} smaller than the optimised value, exclusive 3DShower events yield an increased rate of neutrino triggers. Triggering is stable up to $D_{\text{max}} \approx 60$ m. Beyond, the effective volume increases steeply. In this region only a small fraction of the hits in a trigger cluster is contributed by the neutrino interaction itself while the majority is caused by background noise.

Figure 9.8 compares the trigger efficiency for different values of the N_{modules} parameter. The efficiency loss by requiring $N_{\text{modules}} = 3$ is negligible compared to $N_{\text{modules}} = 2$. In-

9. Triggering in ORCA

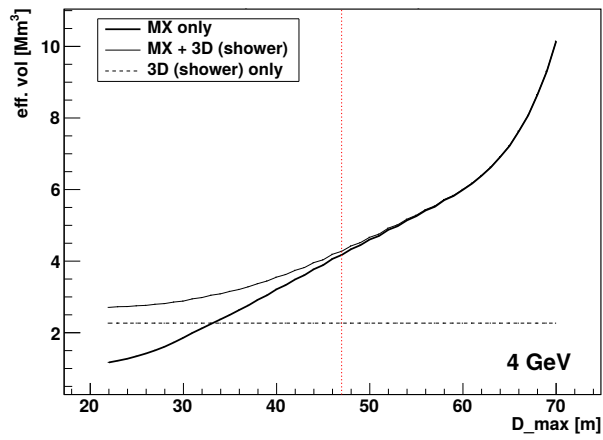


Figure 9.7: Effective volume for the MXShower trigger with $N_{\text{hits}}=8$ and an extremely wide range of D_{max} parameters for $\bar{\nu}_e^{\text{CC}}$ with ≈ 4 GeV energy. The red line indicates the optimised value $D_{\text{max}} = 47$ m

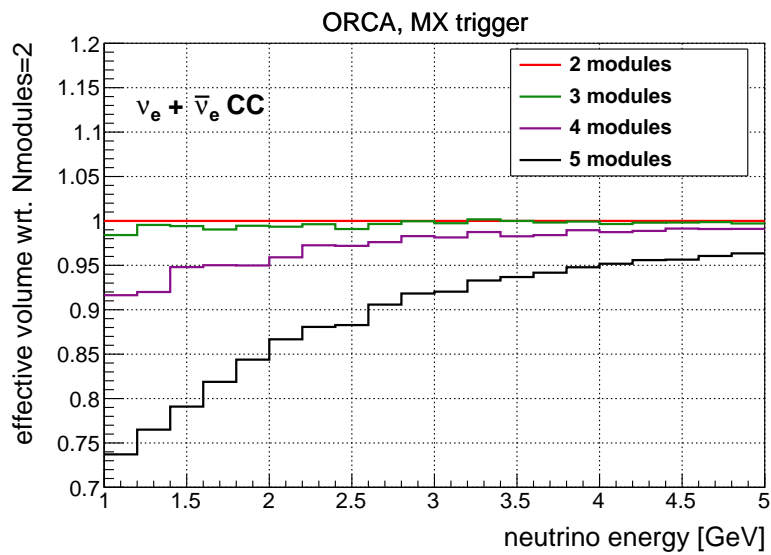


Figure 9.8: Comparison of $\bar{\nu}_e^{\text{CC}}$ MXShower trigger effective volumes for different values of the N_{modules} parameter.

creasing the parameter further turned out not to be necessary from data-taking with the first detection strings, but would result only in a marginal loss of neutrino events for $N_{\text{modules}} = 4$. Only $N_{\text{modules}} \geq 5$ results in a significant deterioration and reduce the gain achieved with the MX with respect to the 3D triggers.

All optimised parameter values obtained for the mass productions with a realistic detector setup are tabulated in [Tab. 9.1](#).

9.3 | Evaluation of trigger performance

In this section, the optimised parameter values determined in [Sec. 9.2](#) are used. The performance gain by the additional MXShower trigger is evaluated with respect to the already previously used 3D triggers in [Sec. 9.3.1](#). In [Sec. 9.3.2](#) effective volumes of the realistic detector setup are compared with the idealised detector configuration used in the LoI [1].

9.3.1 | Performance of MXShower compared to the 3D triggers

Compared to the 3D triggers alone, the inclusion of the MXShower trigger doubles the effective volume right at the threshold. This can be seen from [Fig. 9.9](#). Even at 10 GeV, a gain of 20% in the effective volume is observed, diminishing with higher energies. Most importantly, the fraction of 3D-only triggers is small across the entire energy range. While the effective volume is not much improved, the use of the 3D triggers may continue to be helpful as a flag for events surpassing a certain "brightness" at trigger level. The gain triggered neutrino events as a function of energy is shown for all neutrino flavours in [Fig. 9.10](#). Right at the threshold, the triggered rate is decreased to $\sim 1/4$ when excluding the additional MX trigger, and increases until the detector is $\sim 100\%$ efficient at ~ 15 GeV for $\bar{\nu}_{\mu}^{\text{CC}}$ and $\bar{\nu}_{e}^{\text{CC}}$. For $\bar{\nu}_{\tau}^{\text{CC}}$ and $\bar{\nu}^{\text{NC}}$ the overall behaviour is similar with the detection threshold shifted towards higher energies.

9.3.2 | Trigger comparison with the idealised setup

The two significant improvements in the simulations at trigger level that have been made since the LoI [1] are that the idealised detector is upgraded to the realistic detector setup described in [Sec. 8.2](#) and the introduction of the additional low-energy MXShower trigger.

The individual effects of the larger instrumented volume and the new trigger are presented in [Fig. 9.11](#). While the larger instrumented volume increases trigger efficiency at ≈ 25 GeV by $\sim 20\%$, the threshold is shifted to higher energies as a consequence of the reduced instrumentation density. The additional MXShower trigger increases efficiency especially in the low-energy range, such that the resulting trigger effective volume is larger than before for all energies and $\sim 30\%$ higher at ≈ 25 GeV with the 23 m setup. The qualitative effect is similar for $\bar{\nu}_{e}^{\text{CC}}$ and $\bar{\nu}_{\mu}^{\text{CC}}$ (see [Fig. 9.12](#)).

It deciding to opt for a construction of ORCA with a 20 m horizontal inter-DU spacing instead of the studied 23 m, the overall rate of triggered events reduces by $\sim 10\%$ only. While the reduction at high energies scales with instrumented volume, the trigger threshold is shifted to lower energies.

9. Triggering in ORCA

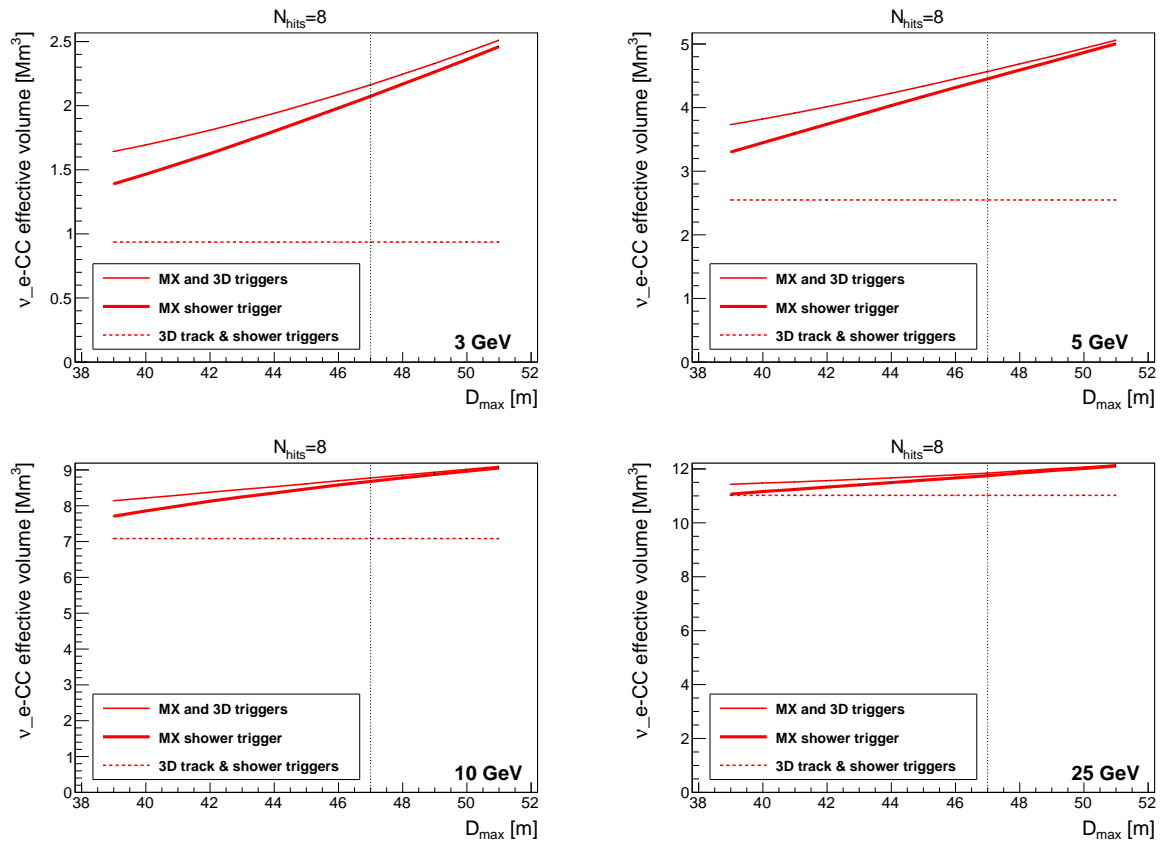


Figure 9.9: Trigger effective volumes for a scan of D_{max} . Different lines indicate the 3D triggers only (dashed), MXShower only (thick solid) and the combination (thin solid). The respective neutrino energies are indicated in the bottom right of the panels.

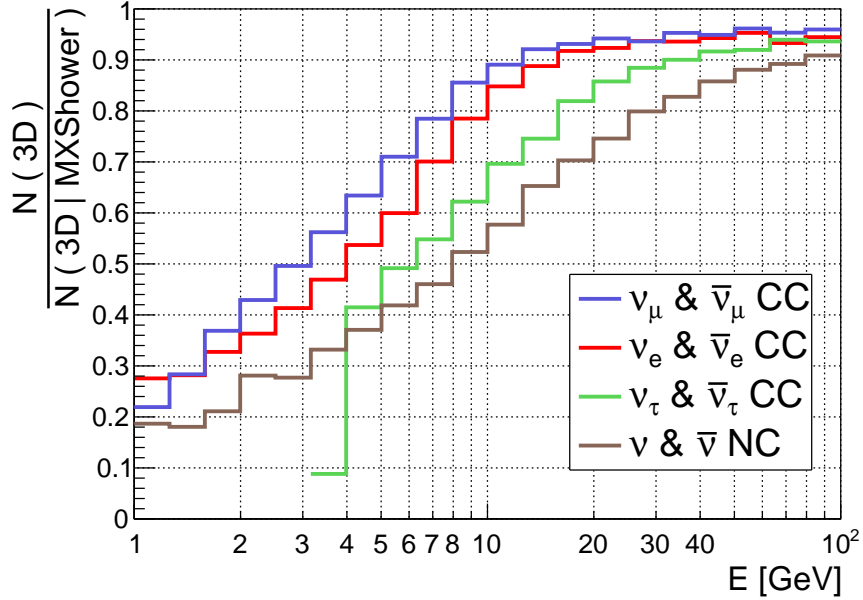


Figure 9.10: Trigger efficiency comparison for 3DMuon and 3DShower with and without the additional MXShower for different neutrino types.

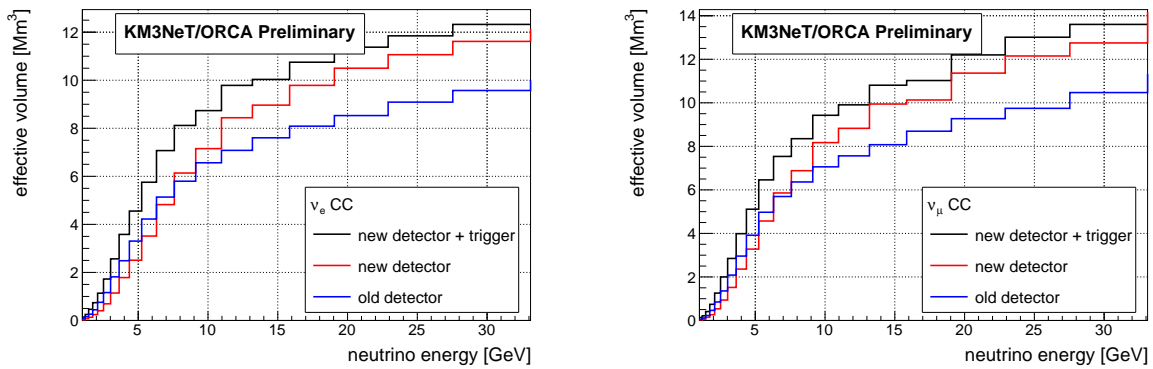


Figure 9.11: Comparison of trigger effective volumes for the idealised detector (blue) and 3D triggers, the realistic 23 m detector with 3D-triggers only (red) and including the new MXShower trigger (black). Effective volumes are shown for $\bar{\nu}_e^{CC}$ (left) and $\bar{\nu}_\mu^{CC}$ (right).

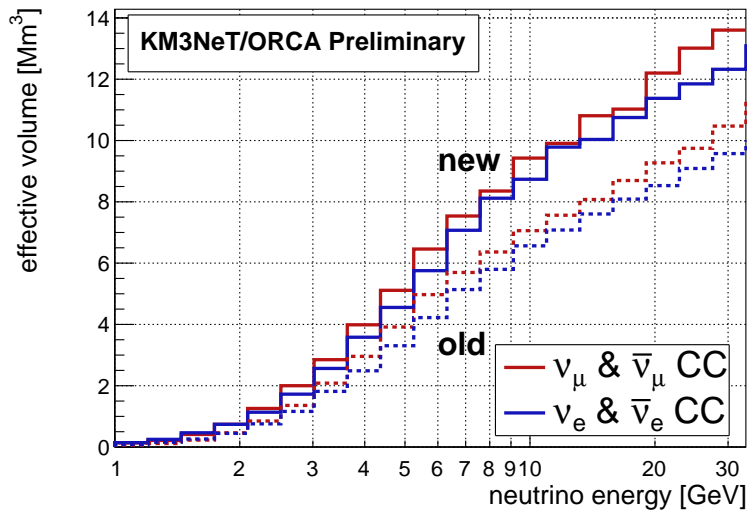


Figure 9.12: Trigger effective volume for $\bar{\nu}_e^{\text{CC}}$ and $\bar{\nu}_\mu^{\text{CC}}$ events for a realistic detector with 23 m horizontal spacing and including MXShower (new) compared to the idealised detector simulation [1] and 3D triggers only (old).

9.4 | Impact of data-taking conditions on the trigger performance

In this section, data-taking conditions that negatively affect trigger performance are studied.

A "high rate veto" (HRV) is in place to flag PMTs during time-slices in which they have an excessive background noise rate. The threshold rate is adjustable and set to 19 kHz in ORCA. The influence of the HRV threshold on the trigger rate for the full ORCA detector is analysed in [Sec. 9.4.1](#) using a model for bioluminescent bursts that has been tuned on ANTARES data.

If a PMT goes into HRV, the corresponding time-slice data of that PMT is ignored by the trigger, effectively reducing the number of active sensors. Equally, it is inevitable that not all of the deployed PMTs will be working during the entire lifespan of the detector. Over time single PMTs, or even entire DOMs and DUs may break permanently or do not transmit data due to technical instabilities for short periods of time. The impact of missing channels on the trigger performance is studied in [Sec. 9.4.2](#).

[Section 9.4.3](#) concludes this section with quantifying the impact of the above effects on oscillation analyses.

9.4.1 | Bioluminescence bursts and high rate veto

Emission of bioluminescence light is induced in the turbulences that occur downstream the water flow around the detector structures. Previous studies based on ANTARES data have already demonstrated a strong correlation of the optical background from bioluminescence with sea current velocity (cf. [4, Fig. 10.15]).

[Figure 9.13](#) shows the mean optical background rate per run measured in ORCA. The displayed data has been taken during eight months with 6 and 8 DUs. The mean optical rates vary in time around a median of 8.5 kHz but can spike up to 14 kHz during short periods of time.

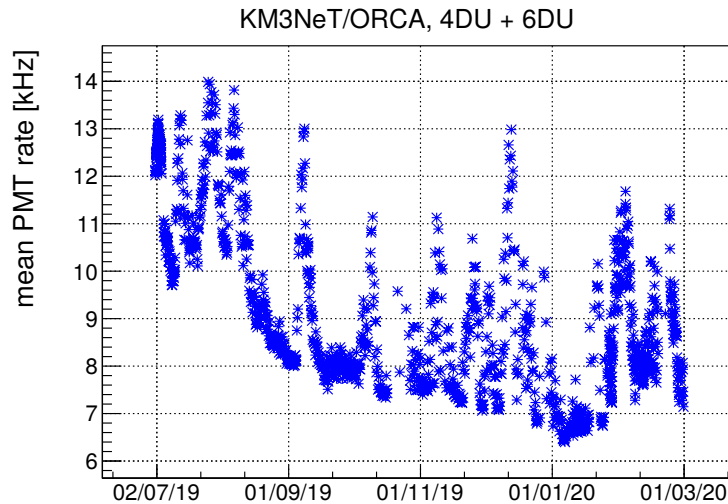


Figure 9.13: Mean optical rates retrieved from the KM3NeT database. ORCA physics runs taken between 01/07/2019 and 01/03/2020 (244 calendar days, 203 days integrated livetime).

For 75% of the livetime, the mean rates are below 10 kHz, which is the constant assumption for the single PMT rate in the Monte Carlo mass productions used in this thesis. Hence, the chosen 10 kHz singles rate is conservative.

The distributions of the optical rates measured by the PMTs in the course of data taking can be retrieved from summary time slices. Summary slice data is written with a frequency of 10 Hz and contain the average optical rates per PMT during the 0.1 s summary slice interval.

The PMT rate distribution for the considered 6 DU data taken during the first weeks of operation is given in Fig. 9.14. For an average run, the PMT rate is roughly Gaussian around a mean value with only a small few-percent tail towards high rates. The constant background assumption in the simulations is therefore justified for the bulk of the data recorded. Runs with bad data-taking conditions however, show a significant tail extending above the HRV threshold of 19 kHz. For the example runs in Fig. 9.14 (red, green) with bad data-taking conditions, an active HRV results in several 10% of PMT timeslices being ignored in JTE.

A model for the calculation of bioluminescence bursts expected for ORCA has been prepared in Ref. [4] and the suggested values derived from ANTARES data on the burst extension and brightness have been used here. The output of the simulation code is a distribution of predicted rates for the PMTs. To use these values, the trigger processor software has been used in a modified version to accept the predicted rate distributions. For this, the PMT singles' rates are set individually to match the predicted distributions. The prediction is shown in Fig. 9.15. The peak value has been set to 10 kHz per PMT. If the HRV is set to 20 kHz (i.e. close to the 19 kHz used in situ), the rate of triggered pure noise events in 100 sample simulations in Fig. 9.16 (left) for the rates drawn from the distribution is in between the resulting rates when uniformly setting all non-HRV PMTs to the same value, either to the peak value of 10 kHz, or to the average over all PMTs below the HRV threshold. In case of doubling the HRV value from 20 kHz to 40 kHz in the bioluminescence simulation tool, a tail towards a higher rate of pure noise triggers emerges, as can be seen in Fig. 9.16 (right). A HRV set to 19 kHz is therefore a justified choice and should ensure stable data-taking even with a full ORCA detector. For the data-taking now and in the future, run-by-run simulations are fore-

9. Triggering in ORCA

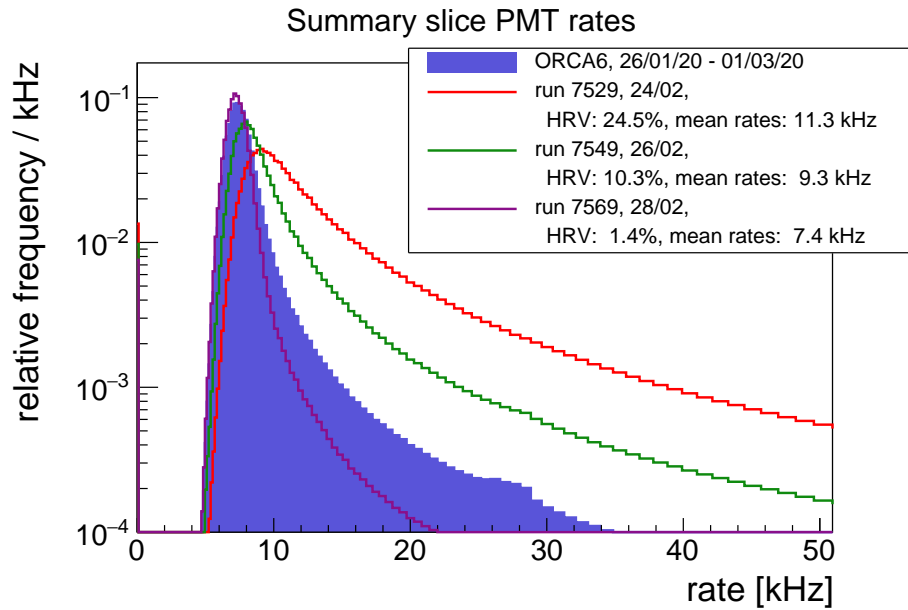


Figure 9.14: PMT rates for ORCA physics runs taken with 6 DUs. Three example runs are overlaid.

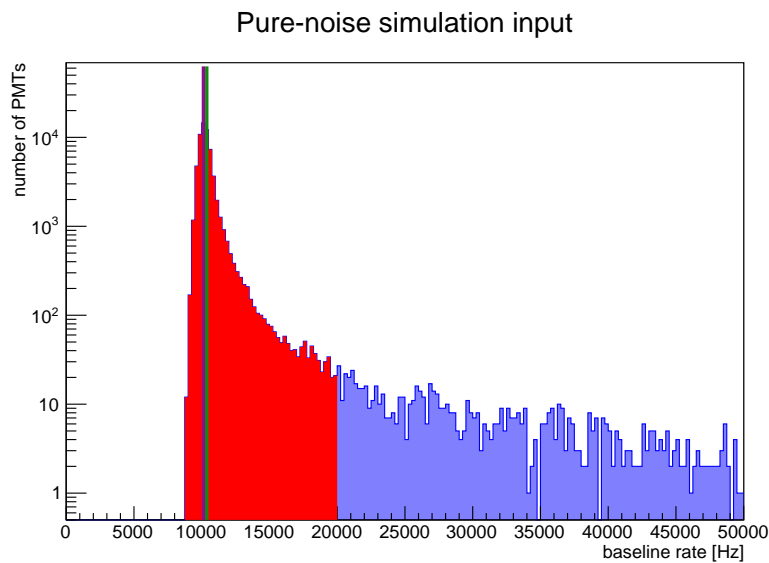


Figure 9.15: Baseline scenarios obtained with the bioluminescence simulator provided in Ref. [4]. All PMTs (below a set HRV threshold) are indicated in blue (red). The violet and green lines represent the peak value set to 10 kHz, and the average over the PMTs below the HRV, respectively.

seen, which take the singles rates directly from the summary time slices. This will ensure better agreement between measured and simulated data. According to the pure-noise trigger rates distributions resulting from the burst simulator, the set HRV is expected to be sufficient to avoid bursts of triggered pure-noise events. The 10 kHz constant background rate remains an acceptable conservative choice for the simulations.

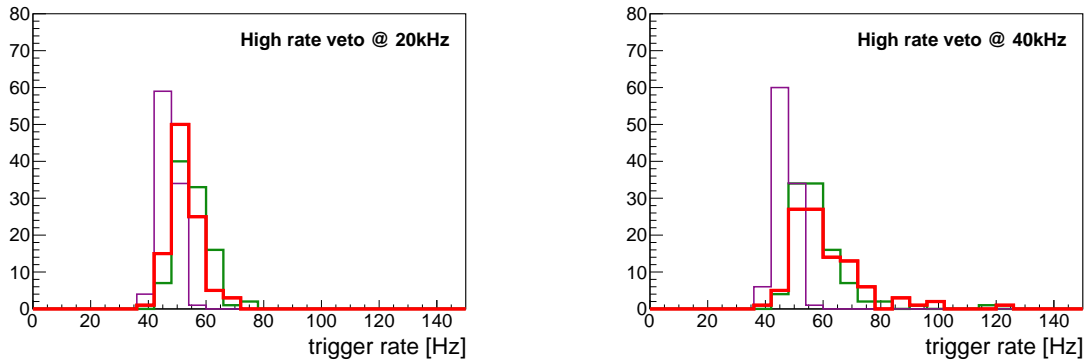


Figure 9.16: Trigger rates for a number of random noise simulations with the background simulation tool. Colours correspond to the ones used in Fig. 9.15.

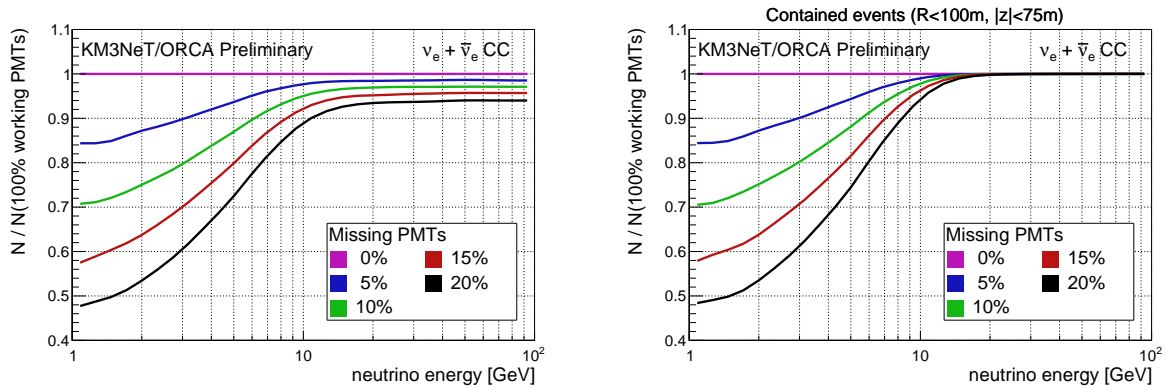


Figure 9.17: Loss in triggered $\bar{\nu}_e \rightarrow \bar{\nu}_e$ CC events as a function of neutrino energy for different fractions of randomly disabled PMTs in the detector. The loss is shown for all events (left panel) and events with interaction vertex well contained inside the instrumented volume (right panel).

9.4.2 | Missing channels

The loss in neutrino efficiency is studied for when a part of the PMTs is switched off in the simulations. To this end, a certain fraction is randomly assigned a quantum efficiency $QE=0$ during triggering with the JTE software. The result is shown in Fig. 9.17 with and without requiring an interaction vertex inside the detector ($R < 100$ m, $|z| < 75$ m). For contained events, the loss at trigger level is negligible in the scanned range above ~ 12 GeV neutrino energy. At lower energies, the loss is energy dependent and reaches up to 50% at threshold if 20% of PMTs are missing.

Instead of randomly choosing single PMTs whose QE is set to zero, it is possible to switch off all PMTs belonging to a randomly chosen DOM or even entire DU. As can be seen from Fig. 9.18, the loss is reduced right at the threshold but has a turnover to more severe decrease in effective area in the latter cases.

The high rate veto fraction is defined as the fraction of channels in HRV averaged over a run. Figure 9.19 shows the HRV fraction over time. In the analysed runs, 60%/70%/90% of the integrated livetime has a HRV fraction below 5%/10%/20%.

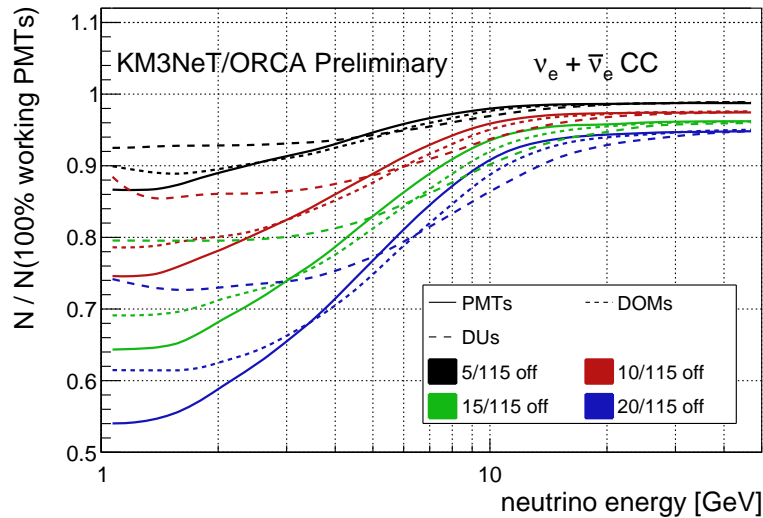


Figure 9.18: Loss in triggered $\bar{\nu}_e^{CC}$ events as a function of neutrino energy. The colours represent different fractions of randomly disabled channels. The effect of disabling of individual PMTs, entire DOMs or whole DUs is shown by different line styles.

9.4.3 | Consequences for neutrino analyses

The above observations PMTs being broken or in HRV are now used to estimate the fraction of neutrino events which fall below the trigger threshold. To this end, the energy dependent loss in Fig. 9.17 is convolved with the livetime-weighted in-situ HRV fraction taken from Fig. 9.19. The result is shown in Fig. 9.20. Accounting for the loss induced by the HRV fraction only, leads to sizeable a $\sim 10\%$ reduction at the energies relevant for NMO (~ 5 GeV). With ongoing construction it can be expected that the detector integration procedures becomes more reliable. Consequently, the fraction of deployed channels being broken is likely to reduce. A pessimistic extrapolation of the 5% non-operative channels present in the first six ORCA DUs to the full detector results in a $\sim 1.5\times$ larger expected loss than for HRV alone. Since this estimated reduction of detected neutrino events is non-negligible it should be included in future neutrino studies where large part of the sensitivity is contributed by the few-GeV energy range. In particular, this is true for the study of NMO. For the sensitivity if $\bar{\nu}_\tau$ appearance, where the main sensitivity stems from the ~ 25 GeV oscillation maximum, the loss is small and will be neglected in the later chapters of this work.

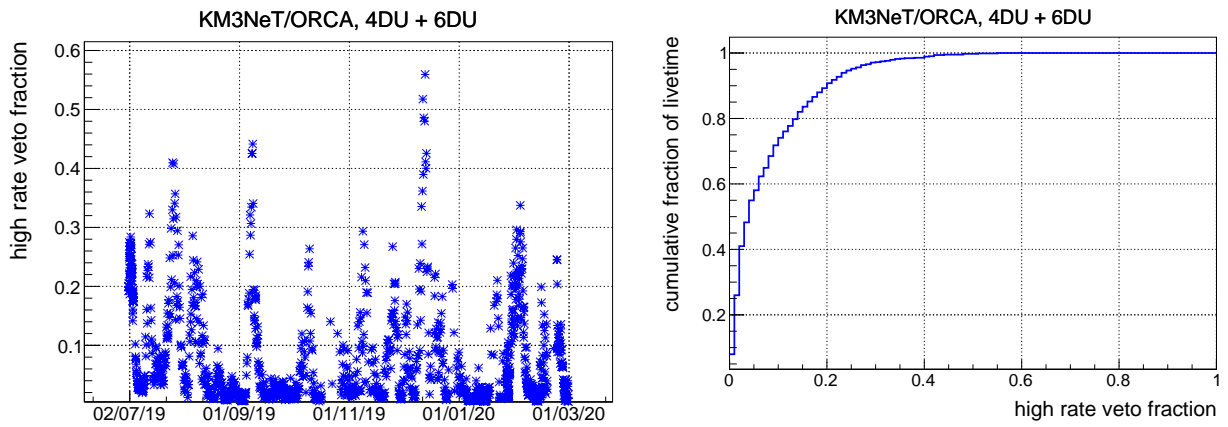


Figure 9.19: High rate veto fractions retrieved from the KM3NeT database. ORCA physics runs taken between 01/07/2019 and 01/03/2020 (244 calendar days, 203 days integrated livetime).

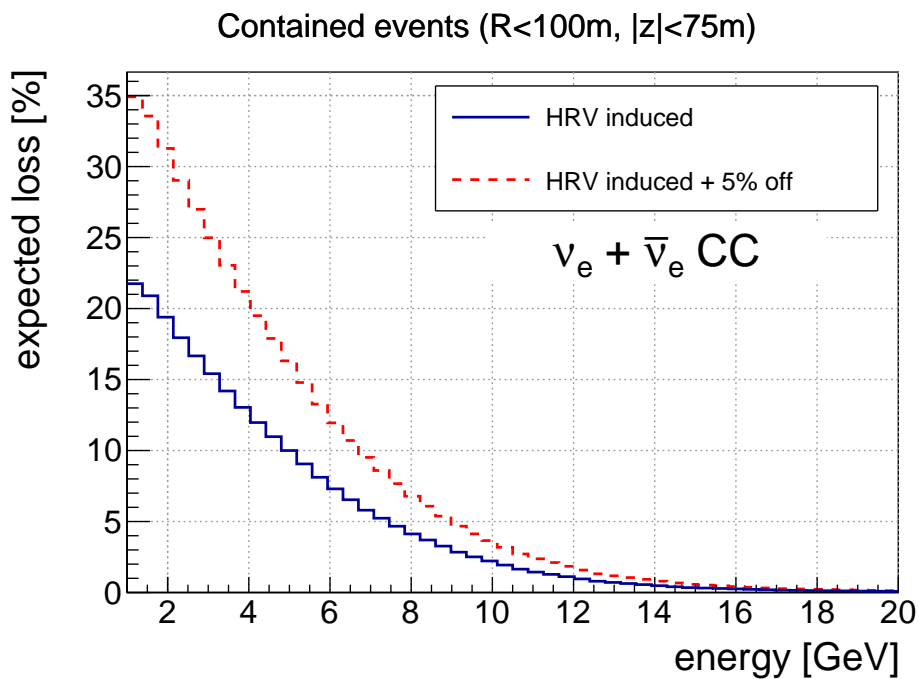


Figure 9.20: HRV and broken channel induced loss in triggered neutrinos.

9.5 | In situ verification of trigger rates for a small sub-detector

Already during the construction phase, in-situ data is taken with the trigger settings optimised for the full ORCA detector (23 m horizontal spacing, Tab. 9.1). An online monitoring snapshot of the trigger rate with six DUs shortly after the deployment of two additional DUs in the last week of January 2020 is depicted in Fig. 9.21.¹ The median trigger rate of ~ 8.2 Hz is dominated by the MXShower, with an additional contribution of only ~ 0.1 Hz exclusively triggered by the 3D triggers. The rate of pure noise events for the small detector with only six DUs is small ($\mathcal{O}(0.1$ Hz)), such that the rate of recorded events is dominated by atmospheric muons.

The rate of recorded atmospheric muons will increase more rapidly during the first 10–20 deployed DUs until ORCA effectively transitions from a surface detector to a volume detector. The expected rates of triggered muons have been determined for a growing detector and are shown in Fig. 9.22. Despite the different arrangement of DUs on the sea floor, the expected rate from the atmospheric muon simulation agrees well with the in-situ measurement (≈ 8.1 Hz for a six-DU setup).

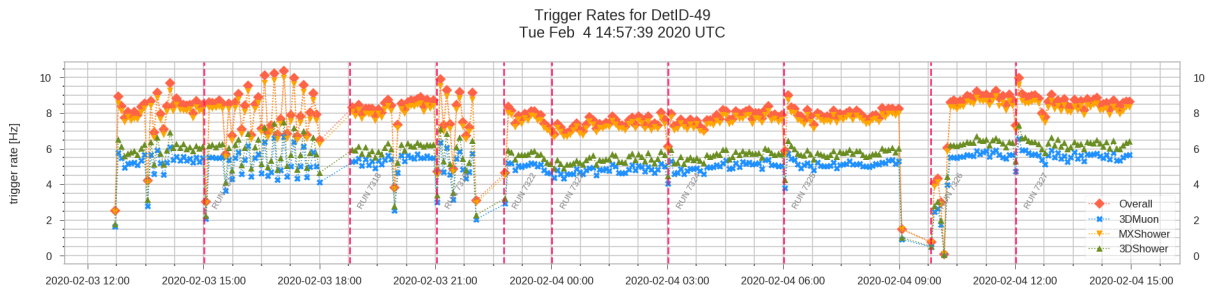


Figure 9.21: Online monitoring of the trigger rates during the first week of operation with six ORCA DUs. The data-taking hickups and interruptions most prominent at 15:00 h, 21:00h, and 8:30h have meanwhile been solved and are not related to the trigger.

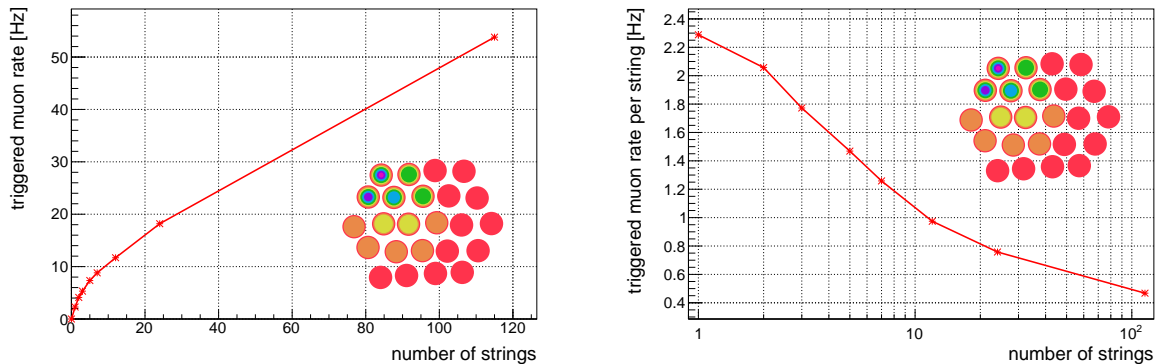


Figure 9.22: Triggered rate of simulated atmospheric muons for different numbers of installed DUs.

¹The given snapshot has been deliberately taken only shortly after DU deployment and shows that not everything is worth printing on glossy paper right from the start.

Table 9.2: Optimised MXShower trigger parameters for a SuperORCA detector.

D_{\max} [m]		MXShower N_{hits}					
		7	8	9	10	11	12
horizontal spacing	10 m	13.7	17.3	20.2	22.5	24.7	26.9
	12 m	15.9	19.6	23.0	25.5	28.0	30.3
	14 m	18.0	21.9	25.5	28.6	31.1	33.6
	17 m	21.1	24.8	29.0	32.6	35.6	38.4

9.6 | Triggering for higher instrumentation density

To determine the CP-violating phase δ_{CP} , detectors with even higher instrumentation density than ORCA are needed. Even when including a possible neutrino beam from Protvino in Russia to the ORCA site [5], a denser detector boosts sensitivity. For the study of the physics potential of higher instrumentation densities in the sub-GeV to few-GeV energy region in Refs. [5, 6, 122], a detector named Super-ORCA has been considered. In the simulation, Super-ORCA has an instrumented height and radius similar to ORCA, but ~ 10 times higher instrumentation density. Consequently, 54 DOMs are aligned on each DU with a vertical spacing of 3 m. Different horizontal spacings between DUs have been tested, namely 10 m, 12 m, 14 m, and 17 m, resulting in corresponding total numbers of 477, 330, 240, and 171 DUs.

At these very low energies, the MXShower trigger dominates the efficiency for triggering neutrino events and the L2-based triggers can be neglected. As for ORCA, the MXShower parameters are optimised to 20 Hz expected trigger rate on pure noise background. The obtained values for D_{\max} and N_{hits} for the four different horizontal spacings are tabulated in Tab. 9.2. The best common value for all horizontal spacings is $N_{\text{hits}} = 10$ and has been evaluated to maximise the detection efficiency of $\bar{\nu}_e^{\text{CC}}$ events. For 17 m (10 m) horizontal spacing, a reduced N_{hits} leads to an increase in efficiency only below 0.5 GeV (0.2 GeV). However, at energies above these values and up to 2 GeV the resulting efficiencies are reduced by 5 – 10% (10 – 20%). The efficiency of the MXShower trigger with a higher N_{hits} is reduced with respect to $N_{\text{hits}} = 10$ below 0.7 GeV (0.4 GeV) and identical above.

The trigger effective volumes of $\bar{\nu}_e^{\text{CC}}$ and $\bar{\nu}_\mu^{\text{CC}}$ events for different spacings are shown in Fig. 9.23. The detection threshold can be lowered with a Super-ORCA configuration by one order of magnitude, and the effective volume reaches the instrumented volume at 2 GeV. Other than for ORCA, where $\bar{\nu}_e^{\text{CC}}$ and $\bar{\nu}_\mu^{\text{CC}}$ effective volumes are similar even at the threshold, the latter is suppressed significantly for Super-ORCA due to the μ^\pm rest-mass.

Effective volumes for all neutrino channels are shown in Fig. 9.24 and 10 m Super-ORCA configuration. Although the final-state neutrinos' invisible energy lowers the effective volume for both neutral current events and $\bar{\nu}_\tau^{\text{CC}}$, the $\bar{\nu}_\tau^{\text{CC}}$ effective volume jumps right at the τ^\pm generation threshold. This is because the light yield of the τ^\pm tends to be sufficient for detection even when decaying almost at rest.

9. Triggering in ORCA

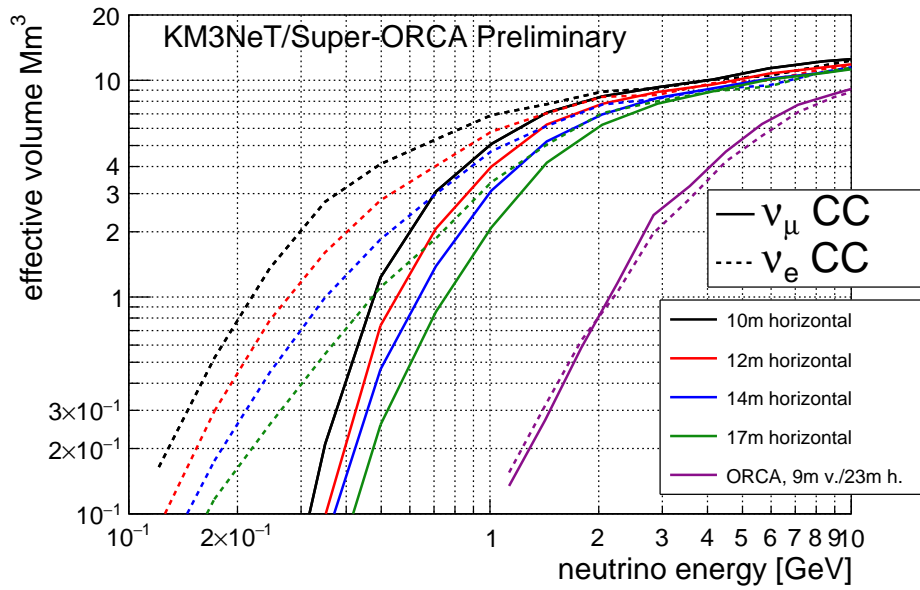


Figure 9.23: Trigger effective volumes for $\bar{\nu}_e^{CC}$ and $\bar{\nu}_\mu^{CC}$ and different possible horizontal inter-DU spacings for Super-ORCA. The effective volumes for ORCA are added for comparison.

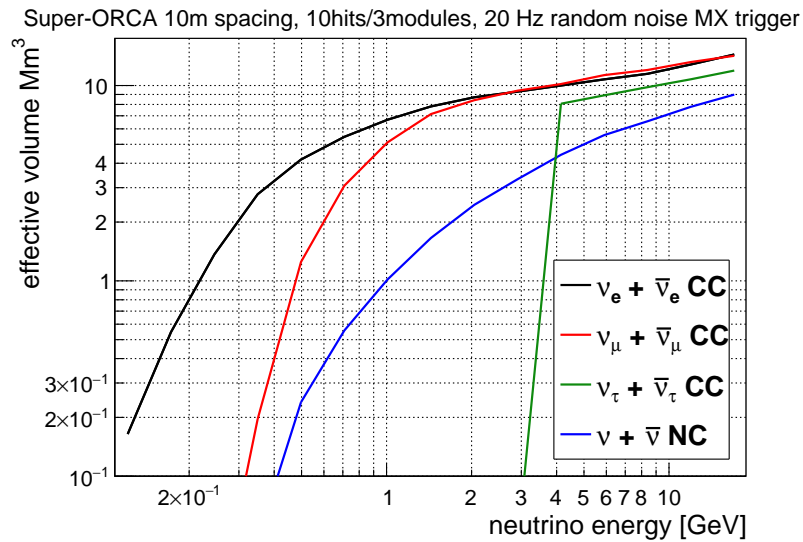


Figure 9.24: Trigger effective volume for the Super-ORCA configuration with 10 m horizontal spacing between DUs.

10 Event reconstruction and pre-selection of analysis event sample

This chapter introduces the event reconstruction algorithms applied to the triggered data and the pre-selection of an event sample for analysis based on the reconstruction output. In [Sec. 10.1](#) the maximum-likelihood based default reconstructions for track- [\[123\]](#) and shower-like signatures [\[4\]](#) within ORCA are described. The reconstruction algorithms are executed in sequence and are independent of each other.

An event pre-selection is defined based on the output of these reconstruction algorithms in [Sec. 10.2](#). This pre-selection is similar to what has been shown in Ref. [\[1\]](#), with a modified definition for event containment to account for the realistic detector configuration.

The event pre-selection is applied in order to ensure good reconstruction quality and for a first de-selection of background events. However, as will be shown, a simple event pre-selection cannot achieve sufficient background elimination. The pre-selected reconstructed output serves therefore as an input to the subsequent classifier for the event type identification in [Sec. 11](#). The resolutions for the track and shower reconstruction algorithms will be shown based on the classified event type thereafter, in [Sec. 11.6](#).

Note, that in addition to the default reconstruction chain using maximum likelihood fits used in this thesis, an alternative reconstruction chain based entirely on convolutional neural networks (CNNs) exists [\[124\]](#). It has been developed in the scope of a parallel PhD thesis [\[125\]](#). Provided CNN performance postulated there is achievable on real data, it is at least competitive and in parts also superior to the default reconstruction chain. The largest boost in performance using this alternative approach is expected by an improved energy resolution of the CNN for track-like event signatures [\[125\]](#).

10.1 | Reconstruction of track- and shower-like event signatures

10.1.1 | Shower reconstruction algorithm Dusj

The steps of the shower reconstruction algorithm Dusj are summarised in [Fig. 10.1](#). A detailed explanation of the shower reconstruction can be found in Ref. [\[4\]](#).

- The basic assumption behind a shower vertex fit is that all photons are emitted at the same time from a common point. The first vertex fit is designed to be robust against noise hits, and an imprecise starting point for the fit.
- If the hit distribution with respect to the found vertex does not match a point-like emission and the event has many hits (i.e. is bright), it is likely to be an atmospheric muon. Due to the dominant rate it can be decided that these events are not processed further, to spare computing resources.

10. Event reconstruction and pre-selection of analysis event sample

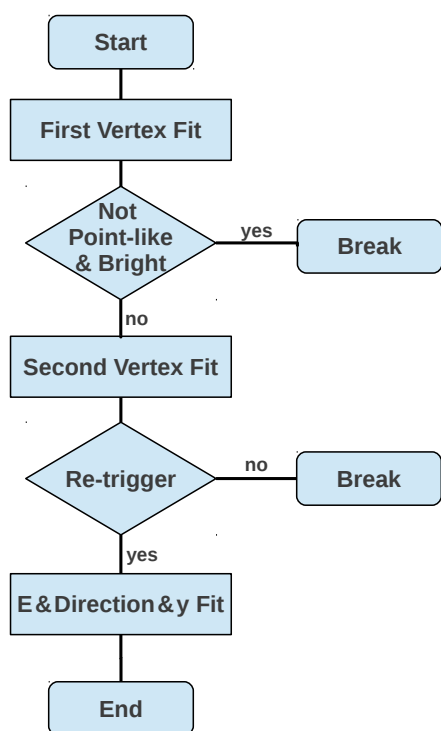


Figure 10.1: Subsequent steps for the shower reconstruction algorithm Dusj. Taken from Ref. [4].

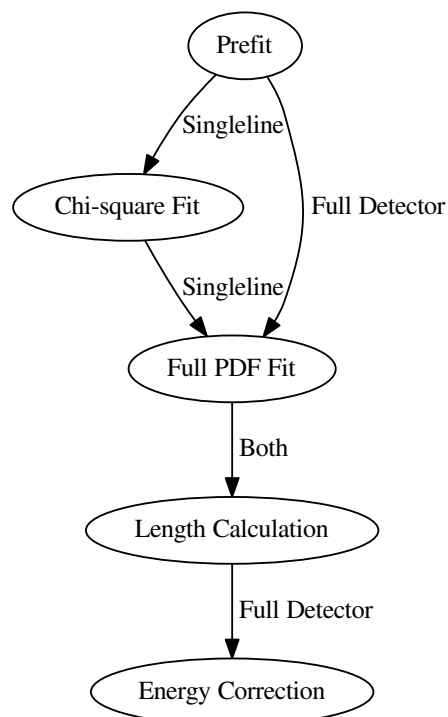


Figure 10.2: Subsequent steps for the track reconstruction algorithm JGandalf. Singleline is not used here. Taken from Ref. [123].

- A second vertex fit then uses a more precise signal-like hit selection to arrive at a refined solution for the vertex.
- Events, which would not have fired the trigger condition if light were emitted from the fitted vertex can then be skipped. Such events tend to have bad reconstruction accuracy.
- In a full maximum-likelihood fit based on probability density functions of the hits under a shower-hypothesis, the remaining event parameters (energy, direction and an estimate for the Bjorken y of the interaction) are fit in one step.

In addition to the event variables, many quality parameters are calculated and written to the output. These can help to select a well-reconstructed event sample later.

10.1.2 | Track reconstruction algorithm JGandalf

The flowchart in Fig. 10.2 summarises the steps of the track reconstruction algorithm JGandalf. A detailed explanation is given in Ref. [123].

The essence of the steps in the fit is

1. First a prefit is run start directions that are spread evenly (with 5° spacing) across the sky. Light emission from an infinite track under the Cherenkov angle θ_c is assumed, such that hits can be projected back onto the track hypothesis. The tracks are then

ranked based on a χ^2 value derived from the time-residuals to the track hypothesis and the number of compatible DOM hits. The highest-ranked tracks are passed to the next stage.

2. The position and direction is then obtained by maximising a likelihood function over the registered hits, which is based on probability density functions (PDFs) for the signal in the PMTs .
3. The length of the reconstructed muon track is calculated by projecting the hits back on the reconstructed track, if they surpass a certain likelihood to be signal-like. The length is then the distance from first to last back-projected signal hit. For minimum ionising μ^\pm this can be readily converted to an energy equivalent.
4. An energy correction is finally applied to correct for systematic offsets between the energy distributions of the simulation and the reconstruction.

10.2 | Event pre-selection

The triggered ORCA dataset contains a rate between 0.5 Hz and 2 Hz of reconstructable atmospheric muons per detection unit (cf. Fig. 9.22) and, on average, a comparable level of pure noise events is expected. As the rate of neutrino events is in the mHz range, the triggered dataset is hence highly imbalanced. To ensure good reconstruction resolution and already reject part of the predominant background, an event pre-selection is applied prior to classification. It is designed to select events based on quality and position of the reconstruction results. While the quality selection criteria are identical for the different simulations¹, the volume of accepted reconstruction positions is adapted to the respective instrumented volume of the detector. Below, the event pre-selection applied to the Monte Carlo mass productions is described in Sec. 10.2.1 for the track- and in Sec. 10.2.2 for the shower-reconstruction output.

Hereafter, only events reconstructed below the horizon are considered for classification and analysis. It must be noted however, that downward travelling neutrinos could turn out useful in reducing flux systematics thanks to the up–down symmetry of the atmospheric neutrino flux mentioned in Sec. 2.2. A first feasibility study for downward going neutrinos has been performed within the scope of a Master’s thesis [126]. However, suppression of atmospheric muons and thus selection of a pure neutrino sample is challenging above the horizon and not considered for this thesis.

10.2.1 | Event pre-selection for the track reconstruction

Reconstructed tracks are pre-selected, if the following four selection criteria are fulfilled:

1. **Valid reconstruction result:** The reconstruction is only valid if the final fit has converged and the reconstructed track has a non-zero track-length. Otherwise no direction and energy output is available.

¹i.e. the simulations in Sec. 8.2

10. Event reconstruction and pre-selection of analysis event sample

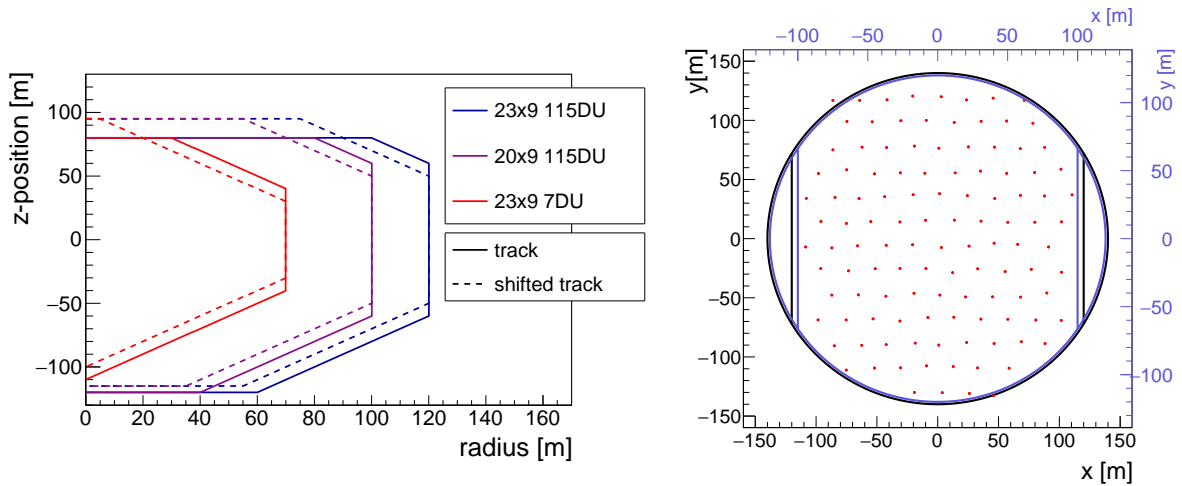


Figure 10.3: *Left:* Containment volumes for the starting points of the track reconstruction algorithm and track starting points shifted into the reconstructed direction. *Right:* In addition to the maximal radius and z position dependent selection, x position is restricted for the 23m (black) / 20m (blue) full detector setups to account for the non-circular footprint of ORCA.

2. **Reconstructed as upward-going:** To reduce the amount of atmospheric muons only events reconstructed below the horizon are considered, $\cos(\text{zenith}) < 0$.
3. **Sufficient reconstruction quality:** Only a cut defined in Ref. [123] on the negative reduced χ^2 of the track reconstruction algorithm is applied: $\chi^2/\text{number_of_hits} < -0.5$.
4. **Position pre-selection:** Good reconstruction performance is only guaranteed if a significant amount of the produced Cherenkov light reaches the detector and has the chance to hit the photo-sensors. The position containment requires the vertex to be inside a defined containment volume around the detector centre of gravity. Good direction resolution is also expected for events that interact in the vicinity and for which the produced μ^\pm track traverses the instrumented volume. Therefore event hypotheses are also accepted, if the vertex shifted by 30 m in the reconstructed direction is contained.

The containment volumes for tracks and shifted tracks have been adapted to the different mass productions and are depicted in Fig. 10.3. The maximum allowed radial distances from the detector centre for the complete ORCA detector have the same margin around the instrumented footprint, 120 m and 100 m, respectively. For the small 7 DU setup, the chosen maximum radial distance is 70 m and allows for a larger margin to increase event statistics.

10.2.2 | Event pre-selection for the shower reconstruction

Similar to the track reconstruction output, requirements for showers are defined to pre-select an event sample for further analysis. A more elaborate quality selection is applied for showers. Reconstructed showers pass the pre-selection, if the following selection criteria are met:

1. **Valid reconstruction result:** The reconstruction is considered successful if the final fit has converged and the reconstructed shower has a non-zero reconstructed energy.
2. **Reconstructed as upward-going:** To reduce the amount of atmospheric muons only events with a reconstructed origin below the horizon are considered, $\cos(\text{zenith}) < 0$.
3. **Quality selection and rejection of pure noise events:** A set of cuts on different quality parameters is then applied to reject poorly reconstructed events. Cuts are applied that efficiently reject the pure noise backgrounds [4]. They show no strong dependence with the detector setup (density, size) [10], such that the optimised selection can be applied to the different detector configurations without modification.
4. **Position pre-selection:** Other than for tracks, where containment is only dependent on the (shifted) vertex, the event selection for showers is based on a ‘coverage’ variable. This variable serves as a proxy for the fraction of the light cone that is contained within the instrumented volume and can be observed. Events are accepted if $> 40\%$ of the cones not only right at the Cherenkov angle, but also at smaller/larger angles around are covered.² The fraction of events passing this selection criteria as a function of position in the detector is given in Fig. 10.4 for isotropically distributed event directions. For upward travelling events, it can be seen from the right side of Fig. 10.4 that events at the bottom are accepted from outside the instrumented volume. On the contrary, they are rejected if they interact in the top region of the detector, but the light signal points away from the detector.

10.2.3 | Pre-selected event sample

The event rates passing the pre-selection after each of the listed steps above are shown in Fig. 10.5. The reconstruction efficiency is still close to 100%. Hence, even with the new low-energy MXShower trigger, events triggered in ORCA are bright enough such that they are still reconstructable. The requirement of an upward reconstruction reduces the event sample by almost 50% for the individual reconstructions. Yet, considering events must either pass the event selection for tracks or showers the reduction is less. The event rate is further reduced in the subsequent steps. Overall, the behaviour is similar for the 20 m and 23 m detectors, with 20% more events accepted for the larger 23 m detector. Almost 40% of triggered neutrino events pass the final stage of the neutrino event pre-selection for either showers or tracks.

At the same time, the background is reduced more significantly by more than two orders of magnitude, even when requiring either the pre-selection for tracks or for showers is passed. This is summarised in Tab. 10.1. Comparing the individual background contributions for the two reconstruction algorithms separately, it can be seen that the efficiency to reject atmospheric muons and pure noise is opposite for the track and shower pre-selection. The shower pre-selection almost entirely rejects the pure noise contribution. The atmospheric muon level in events passing the track pre-selection is also reduced efficiently, but remains still as high as the expected neutrino rate.

²more precisely, cones at 20° , 45° , 60° and 75° need $>40\%$ coverage.

10. Event reconstruction and pre-selection of analysis event sample

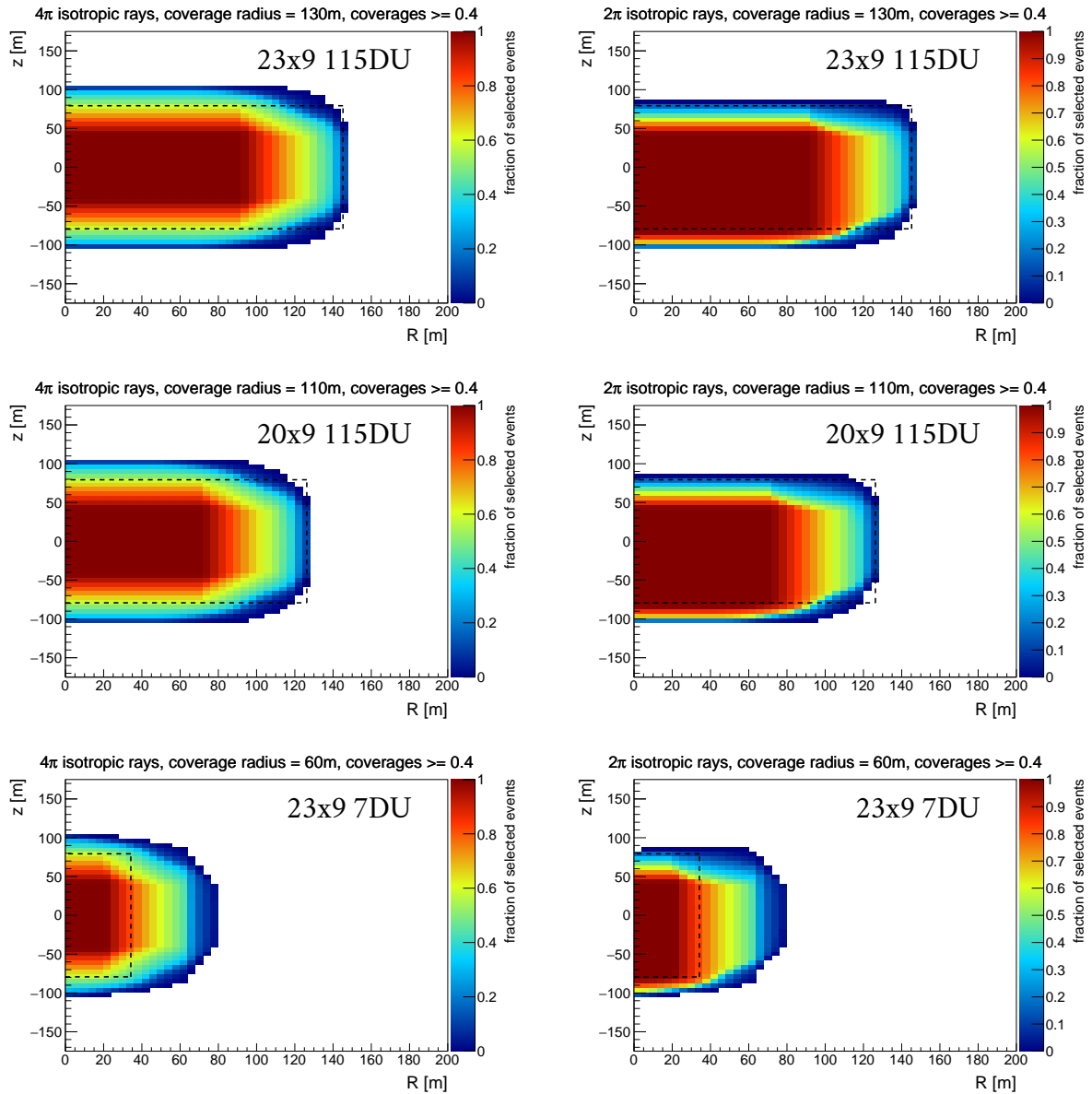


Figure 10.4: Fraction of reconstruction directions to fulfill the containment criteria for showers. Distribution is isotropic in 4π (left) and for upward travelling directions (right), respectively. The instrumented volume is indicated by the dashed line.

10. Event reconstruction and pre-selection of analysis event sample

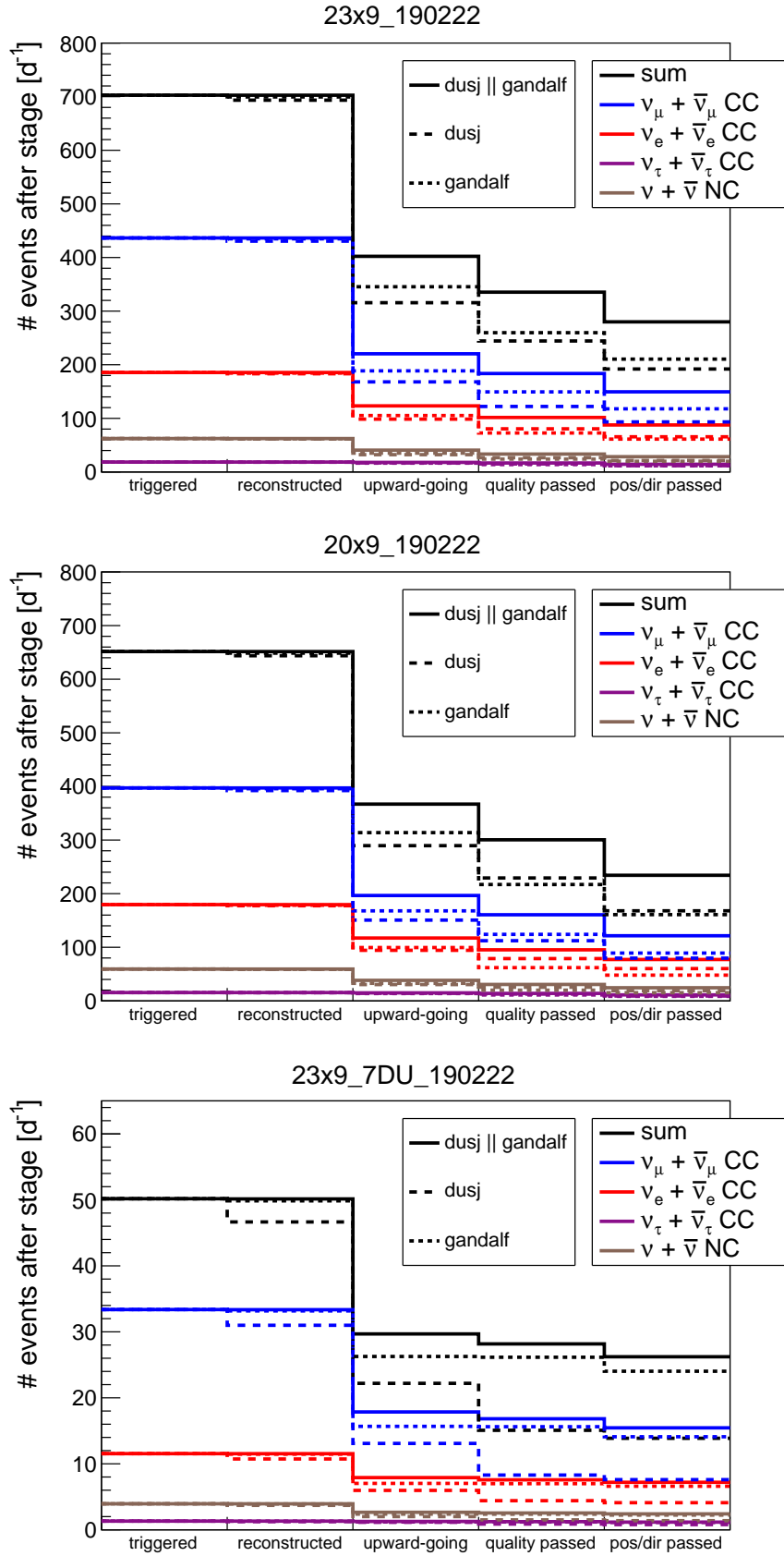


Figure 10.5: Number of events remaining after the subsequent event selection stages. Neutrinos are weighted with an oscillated [62] atmospheric HKKM flux [41].

10. Event reconstruction and pre-selection of analysis event sample

A more efficient method of background classification is therefore needed in order to suppress the remaining background to an acceptable small level. An appropriate means for this is the use of machine-based classifiers. This is done in the next chapter.

Table 10.1: Background rate after trigger and pre-selection for the 23 m ORCA detector

23x9/115	triggered	pre-selection passed		
		gandalf OR dusj	gandalf (track)	dusj (shower)
atm μ	$4.4 \times 10^6 \text{ d}^{-1}$	$5.5 \times 10^3 \text{ d}^{-1}$	290 d^{-1}	$5.2 \times 10^3 \text{ d}^{-1}$
pure noise	$4.6 \times 10^6 \text{ d}^{-1}$	$2.4 \times 10^4 \text{ d}^{-1}$	$2.4 \times 10^4 \text{ d}^{-1}$	5 d^{-1}

11 Event type identification in ORCA

As seen in the previous chapter, the backgrounds from pure noise events and atmospheric muons outnumber the neutrino signal still by 1–2 orders of magnitude after event pre-selection. Also, oscillation analyses depend on the possibility to distinguish between track- and shower-like signatures as a proxy for the interacting neutrino flavour.

The required categorisation – or classification – of the recorded events is achieved using *machine learning* techniques. Hereafter, the classification of events is collectively referred to as *Event type IDentification (EID)*.¹

This chapter describes the EID models trained using the Random Decision Forest (RDF) [127] technique. At the time of writing this thesis, the EID output presented here is used by default in most sensitivity studies for ORCA. Several of the presented plots are part of the paper draft ‘Determining the Neutrino Mass Ordering and Oscillation Parameters with KM3NeT/ORCA’ [2].

[Section 11.1](#) gives a general overview of machine learning techniques currently employed within ORCA and ANTARES. The RDF technique is explained in more detail in [Sec. 11.2](#). A significant improvement with respect to previous EID results in ORCA [1] has been achieved by adding input variables calculated from probability density functions (PDF) for the light emission under the hypothesis of a track or shower inside the detector (provided in [Sec. 11.2.4](#)).

The suppression of background events and the classification of neutrino event signatures is presented in [Sec. 11.3](#) and [Sec. 11.4](#), respectively.

At the end of this chapter, the trained RDF model is used to define neutrino event classes for analysis ([Sec. 11.5](#)), and evaluate the detector performance within these classes ([Sec. 11.6](#)).

11.1 | Machine learning in ORCA and ANTARES

In recent years, machine learning has become a popular tool ubiquitously applied throughout the field of (astro-)particle physics.

Supervised machine learning techniques can be used to reconstruct continuous output variables via regression or to categorise events into different classes according to the signatures they leave in the detector. In supervised learning, detailed Monte Carlo (MC) simulations are used in the training. For these the true target values, named *labels*, are known. The classifier can use these true values to optimise on during the training.

In contrast, in *unsupervised* learning the target classes are not known. Instead, events can be clustered into different previously unknown groups. One possible application of unsupervised learning would be for example to find clusters in background events and with this

¹Within the community, the term Particle Identification (PID) is also common. However, since noise events are no ‘particle’, the more appropriate term ‘Event type IDentification’ is used here.

11. Event type identification in ORCA

identify distinct contributors to the overall background. However, only supervised machine learning has been used up to now in ANTARES and KM3NeT:

Classical machine learning tools used in ANTARES Models for regression and classification have already been trained and shown to be successful on ANTARES data. More specifically, the ANN energy regressor [128] is based on a neural net and provides an estimate for the track energy. Since several years it has been serving as the standard energy estimate of ANTARES and is used in the majority of analyses. Random Decision Forest (RDF) [127] based classifiers have found applications in the separation of upward- from downward-travelling tracks ('SGClassify' [7]). In addition, a classification model trained on selecting the most precise out of several reconstruction algorithms for a specific event ('SelectFit') yields on average better resolution for the event sample [129].

Classical machine learning for ORCA For continuity with previous work for the LoI, the above mentioned SGClassify RDF originally developed for ANTARES [7] is also used in this work.

The RDF is a classical machine learning technique. It uses a number of floating-point or categorical high-level variables derived from the data as input. These are also referred to as *features*. Based on these high-level input features, a classifier model is trained to predict the output label. A significant part of the work to develop feature-based classification models lies in the design of useful input features.

Deep Learning for ORCA In contrast to classical machine learning techniques, 'deep learning' (DL) has gained popularity only recently thanks to the availability of GPU clusters and the resulting possibility to train computationally expensive classification models.² Using DL techniques it is possible to pass the information of the recorded signals – in case of ORCA the PMT hits with their associated position, time, and orientation – directly to the network. In doing so, the burdensome and difficult task of designing suitable features as input to the classifier can be skipped. Instead, it is left to the network to learn the features, provided pictures of the event hits binned in (x, y, z) -position, time, and PMT channel.³

A deep neural network project named 'OrcaNet' [130] has explored this approach in the context of ORCA for the first time [124, 125]. On simulated data OrcaNet achieves similar or better performance for both EID and event reconstruction compared to the RDF approach and maximum-likelihood based fits of direction and energy. It remains to be seen whether the DL performance shown on simulated data is robust against the varying data-taking conditions of ORCA. The DL results, however, are highly encouraging and represent an independent (and potentially superior) analysis chain to the established approach followed in this thesis. At the very least they provide a guideline to the parts of the classical chain where the signal information is not yet fully exploited. As will be demonstrated in [Sec. 11.2.4](#), shallow EID

²The less complex classical machine learning techniques are therefore sometimes informally referred to as 'shallow learning'. However, there is no fixed number of network layers marking the transition between 'shallow' and 'deep'.

³Depending on the architecture, the input dimensions are limited and this may require reduction of the used input dimension.

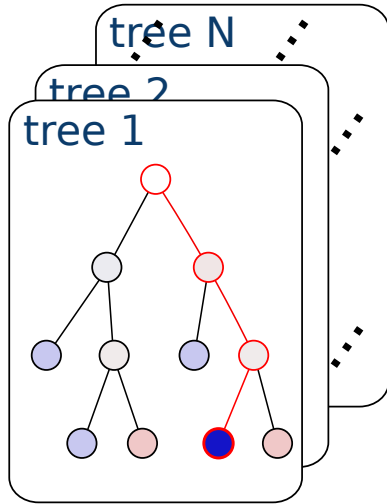


Figure 11.1: Schematic representation of a Random Decision Forest with N trees. The red lines indicate the path of an example event with output class 'blue'.

has been able to catch up through the implementation of the hit-based features, such that the largest potential for improvement is at the moment the track energy estimate [125].

11.2 | Random Decision Forest technique

A Random Decision Forest (RDF) [127] is an ensemble of individual decision trees. Each of the trees is trained on a random subset of both the available training events and the available features. A schematic drawing of a RDF is shown in Fig. 11.1. Each node of a tree represents a split based on one of the training features.

The assignment of features to the nodes and the value at which to split the data are determined during the training process to yield best separation between the event classes.

Events propagate along the trees in Fig. 11.1 from top to bottom until the last node assigns the result class predicted by the respective tree.

The RDF is a parallel ensemble method and as such the base learners, i.e. the individual decision trees, are trained independently of each other. In the machine learning community this procedure is called 'bagging'. In contrast, ensembles of sequentially generated base learners can put more weight on previously misidentified events to boost the overall performance. However, parallel ensembles prove more robust in the application to real data thanks to the reduced variance of the ensemble [131, 132].

The training is based on *supervised learning* using the detailed MC simulations for neutrinos as well as the two background sources – atmospheric muons and pure noise described in Sec. 8.2.

Individual RDF models have been trained to make binary decisions between two classes only. With this choice, an output score variable \mathcal{S} can be defined as the fraction of trees voting for the respective target class:

$$\mathcal{S} = \frac{N(\text{trees voting for target class})}{N(\text{total trees})}. \quad (11.1)$$

Several individual RDFs for each of the simulated detector configurations in Sec. 8.2 have been trained and are used for oscillation analyses. They can be grouped according to their two

11. Event type identification in ORCA

Table 11.1: Settings for the trained Random Decision Forests. More details are provided in the text.

RDF parameter	value
Number of trees	101
Number of training events per class	50000
↔ of which used per cross-validation	40000
Number of features	155/165/255
Fraction of events per tree	0.6
Fraction of features per tree	0.4
Cross-validation folds	5

main goals:

- (1) Obtain an analysis sample with high neutrino purity:
 - the atmospheric muon classifier presented in [Sec. 11.3.2](#)
 - the pure noise classifier presented in [Sec. 11.3.3](#)
- (2) Classify neutrino events according to their topology; which is crucial to study neutrino oscillations:
 - the track ↔ shower classifier presented in [Sec. 11.4.1](#)

A single training with four output classes – track, shower, atmospheric muon, and pure noise – would have been technically possible. However, the training on binary output decisions brings with it two decisive advantages. Firstly, the dominant backgrounds can be suppressed efficiently by choosing tight cuts on the atmospheric muon and pure noise score variables to arrive at a clean event sample. Secondly, the obtained neutrino sample can be split into two or more analysis classes based on the track ↔ shower classification output. This cut can be tuned to optimise the sensitivity of the analyses.

11.2.1 | RDF architecture and training settings

A C⁺⁺-based implementation of the RDF technique is provided within the SGClassify package which has been developed previously for ANTARES. This implementation is also used here to preserve continuity with the LoI. A python wrapper has been written to facilitate I/O conversion from the summary files extracted from the reconstruction output (hdf5 format) to the custom csv format required by SGClassify. The use of another RDF implementation has been cross checked to provide comparable results [133].

The RDFs have been trained on the pre-selected neutrino and background data described in [Sec. 10.2](#). To train the classifiers, $\bar{\nu}_{\mu}^{\text{CC}}$ events have been used to represent track-like event topologies. For showers $\bar{\nu}_{e}^{\text{CC}}$ and $\bar{\nu}^{\text{NC}}$ events have been used. The neutrino event distributions were flattened in decadic logarithm of neutrino energy and balanced between tracks and showers. In contrast, background was fed to the classifier with the expected true spectra.

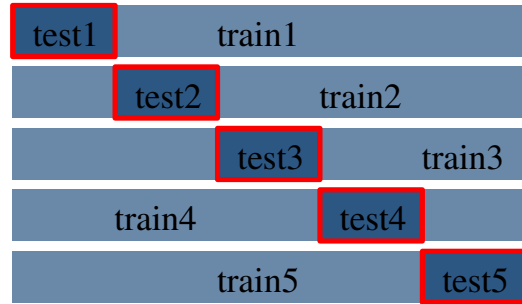


Figure 11.2: Five-fold cross validation scheme.

The RDF setup that has been used in this work is summarised in [Tab. 11.1](#). An ensemble of 101 individual decision trees⁴ were trained on the input features. Randomisation of the forest is achieved by showing 60% of the training events and 40% of the available features to each tree.

11.2.2 | Cross validation

N -fold cross validation is a commonly used tool to prevent problems like overfitting and bias in the training process. For the mass productions $N = 5$ folds were used. Before training, the training set is split evenly into five parts. Then, five classification models are trained. In each of them 4/5 of the data are used for training the classifier in turns while leaving out the remaining 1/5 as test data set. The principle of cross validation is illustrated in [Fig. 11.2](#).

Due to the large computational effort to produce high statistics of Monte Carlo data, especially for the background, cross validation has been used also in a different manner in the mass productions in order to not lose events during the training process: Training events keep the classifier scores from the cross validation fold in which they were in the test set. After cross validation, another RDF classifier is trained with a random 80% subset of available training events. The output model obtained is then stored and used to classify the remaining events never used during training.

11.2.3 | Training features

The features used in the classifier can be divided in three groups:

- (1) fit results and quality parameters of the maximum-likelihood based track and shower reconstruction algorithms
- (2) relative differences between the track and shower reconstruction results, e.g. the distance between fitted vertices.
- (3) additional features derived from hit distributions expected for tracks and showers

While features from (1) and (2) have been used for all classification models, (3) have not been used in background suppression, since they were specifically designed to be sensitive to the differences in the hit distributions of track- and shower-like neutrino signatures. In total,

⁴The uneven number of trees prevents inconsistent analysis results between different implementations of score cuts ('<' vs. '≤').

11. Event type identification in ORCA

155 features have been used for the background suppression, and 255 (165) for track–shower classification with(out) hit distribution based features.

The set of used input features is rather large. However, insensitive variables are ignored in the RDF algorithm. This is because only the features which yield best separation between the classes are used at each split. For a simulation-based sensitivity study it is therefore not necessary to perform a detailed feature optimisation and reduction in this case. Once real data is available, agreement of the distributions in data and Monte Carlo needs to be verified. Features passing this criterium can then be used by the classifier.

11.2.4 | Additional hit distribution based features

For improved separation between track- and shower-like event signatures, features based on the differences in the expected hit distributions are added to the classifier.

In order to design these features, sets of probability density functions (PDFs) have been generated from $\overleftarrow{\nu}_\mu^{\text{CC}}$ and $\overleftarrow{\nu}_e^{\text{CC}}$ events with Monte Carlo energies below 30 GeV. Energies above are neglected, since classification is already efficient without hit-based features in the plateau. The PDFs are generated by populating, five-dimensional sparse histograms with respect to a reconstructed reference vertex x_r and direction v_r by using the

- distance from the DOM to x_r ,
- cosine of the angle between v_r and the vector from the x_r to the DOM position,
- time residual with respect to the light travel time from x_r to DOM,
- number of hits on the DOM
- energy

To evaluate the log-likelihood ratio the reconstructed vertex direction and energy are taken from the shower reconstruction output. Hence, no MC truth information is used.

For $\overleftarrow{\nu}_e^{\text{CC}}$, the shower reconstruction algorithm reliably finds the vertex in close vicinity to the point of interaction. For $\overleftarrow{\nu}_\mu^{\text{CC}}$, typically the brightest point close to the interaction or the middle of the track are reconstructed, depending on the inelasticity of the event [4].

The reference particle positions to generate the PDFs take into account the offset between the Monte Carlo vertex and the position of brightest light emission.

Hit-based PDFs are therefore filled for a position 1 m from the interaction vertex for $\overleftarrow{\nu}_e^{\text{CC}}$ to take into account that the brightest point is shifted upfront the interaction vertex [4]. For $\overleftarrow{\nu}_\mu^{\text{CC}}$, the offsets are 1 m and, in addition, 40% of the expected muon track length.⁵

Based on the filled PDFs, log-likelihood-ratio variables can then be defined and fed to the classifier.

11.3 | Background reduction

After event pre-selection the atmospheric muon and pure noise backgrounds still dominate the event sample. Both of these background components need to be suppressed efficiently in order to extract a clean neutrino sample. This is necessary to perform the intended oscillation analyses, which are to test few-percent level differences in the distributions of neutrino events.

⁵at these energies, the muon range $r_\mu(E_\mu) \sim 4.25 \text{ m} \times E_\mu[\text{GeV}]$ [56]

Each of the two background sources is suppressed separately with an independent RDF model. The training setup and procedure for performance evaluation is common in both trainings and therefore detailed in [Sec. 11.3.1](#). Results for atmospheric muon suppression ([Sec. 11.3.2](#)) and pure noise suppression ([Sec. 11.3.3](#)) are then presented.

11.3.1 | Training and analysis of the background classifier

Training setup In the background trainings, the neutrino sample consists of 50% $\bar{\nu}_\mu^{\text{CC}}$ representing tracks and 50% $\bar{\nu}_e^{\text{CC}}$ and $\bar{\nu}^{\text{NC}}$ to represent showers. The neutrino sample is flattened in decadic logarithm of neutrino energy. This choice prevents bias from different spectral indices simulated for individual flavours and/or energy regions. High energy events are over-represented with respect to the atmospheric flux spectrum to ensure sufficient statistics over the whole energy band seen by the classifier. No $\bar{\nu}_\tau$ events have been included in the training since their signatures are either track- or shower-like and are already covered by the other flavours. The background events are randomly drawn and follow the expected true spectra generated in the simulation step. The training set is balanced between neutrinos and the respective background class using a 50/50 split; in total 5×10^4 background events, and 5×10^4 neutrino events (2.5×10^4 track-like and 2.5×10^4 shower-like) are used for training the RDF models. No hit-pdf based features are used for the background classification.

Performance evaluation After training and classification, background can be suppressed by applying an upper cut s_{max} on the resulting background score variable defined in [Eq. 11.1](#),

$$\mathcal{S}_{\text{bg}} < s_{\text{max}}, \quad \mathcal{S}_{\text{bg}} \in \{\text{atmospheric muon score, pure noise score}\}. \quad (11.2)$$

A useful quantity to evaluate the classifier performance, is the fraction of background events after the cut. This is referred to as the *background contamination*,

$$\mathcal{C}_{\text{bg}}(s_{\text{max}}) = \frac{N_{\text{bg}}(s_{\text{max}})}{N_\nu(s_{\text{max}}) + N_{\text{bg}}(s_{\text{max}})}. \quad (11.3)$$

Here, s_{max} represents the cut value on the respective background score variable, with ‘bg’ being either atmospheric muons or pure noise.

In addition, the fraction of neutrino events surviving the cut is referred to as the *neutrino efficiency*,

$$\varepsilon_\nu(s_{\text{max}}) = \frac{N_\nu(s_{\text{max}})}{N_{\nu, \text{pre-selected}}}, \quad (11.4)$$

For the calculation of ε_ν and \mathcal{C}_{bg} , the neutrino events are re-weighted to an oscillated atmospheric flux. Consequently, they do not reflect the number of simulated events, but the true event rate expected in ORCA data. The variables are calculated based on the event sample with pre-selection cuts applied. A 100% neutrino efficiency therefore implies, that all pre-selected neutrino events are accepted in the final sample and pass the background rejection classifier. With this definition, $\varepsilon_\nu(1) = 1$.

Currently, for the oscillation analysis sample a background contamination of below $\sim 3\%$ for each of atmospheric muons and pure noise is aimed for. With this, the two sources of background can – as for now – be neglected in the subsequent oscillation analyses. This simplification is made because the generation of background events with (several) years of equivalent

11. Event type identification in ORCA

lifetime is computationally too expensive. Due to the low neutrino-to-background ratio in the data sample and given the simulated statistics, no smooth distribution in reconstructed direction and energy can be obtained. For an analysis of in-situ ORCA data, the planned run-by-run simulations will provide sufficient statistics in order to generate such a smooth expectation for the background distributions. For later data analyses, backgrounds can be included as an additional component in the fit to measured data.

11.3.2 | Atmospheric muon classifier

The distribution of the atmospheric muon score, $\mathcal{S}_{\text{atm.}\mu}$, for neutrinos, atmospheric muons and pure noise events is shown in Fig. 11.3a. The integral of each contribution is normalised to one. There is a clear separation between atmospheric muons and neutrinos. The increase of neutrino events with an $\mathcal{S}_{\text{atm.}\mu} \approx 1$ comes from $\bar{\nu}_{\mu}^{\text{CC}}$ and $\bar{\nu}_{\tau}^{\text{CC}}$ events with τ^{\pm} decay to μ^{\pm} and is absent for other neutrino channels. Pure noise events have not been shown to the classifier during the training. Since these events are faint, the resulting $\mathcal{S}_{\text{atm.}\mu}$ values are spread over the central region, i.e. these events are neither identified as clear neutrino nor clear atmospheric muon. In particular, most atmospheric muons are bright, and therefore pure noise event distribution cuts off at $\mathcal{S}_{\text{atm.}\mu} \sim 0.8$ such that events are practically never unambiguously identified as atmospheric muons.

The performance of the atmospheric muon classifier is shown in Fig. 11.3b. Each cut value on the atmospheric muon score $\mathcal{S}_{\text{atm.}\mu}$ corresponds to an atmospheric muon contamination $\mathcal{C}_{\text{atm.}\mu}$. The neutrino efficiency ε_{ν} is stable down to a contamination of $\sim 2 - 4\%$ and drops rapidly below (cf. black line in Fig. 11.3b). For shower-like event signatures, ε_{ν} is not strongly dependent on the neutrino energy. Only for track-like signatures of high energies, the fraction of events surviving the cut is lower owed to their resemblance of atmospheric muon events.

At $\mathcal{S}_{\text{atm.}\mu} < 0.05$, or, equivalently, $\mathcal{C}_{\text{atm.}\mu} \sim 3\%$ the loss in neutrino events is $\approx 5\%$ for all neutrino flavours. Only for track-like signatures of high energies, the loss is slightly larger, $\approx 7\%$ at $E_{\nu} = 15$ GeV.

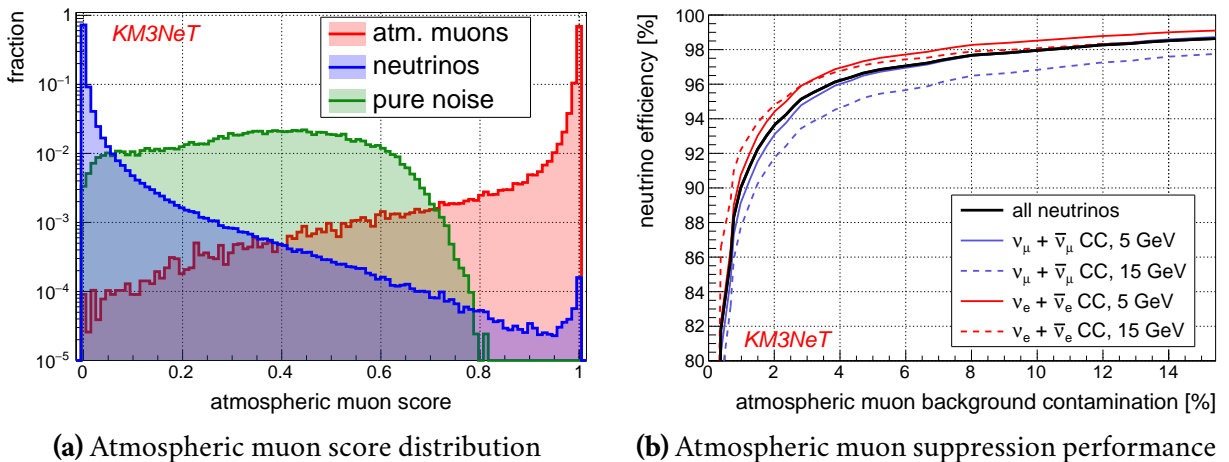


Figure 11.3: Atmospheric muon classification result. Figure prepared for Ref. [2].

11.3.3 | Pure noise classifier

The results for pure noise rejection are given in Fig. 11.4. Similar as for the atmospheric muon classifier, the different normalised event contributions are shown as a function of the resulting pure noise score, $\mathcal{S}_{\text{noise}}$ in Fig. 11.4a. The classification score $\mathcal{S}_{\text{noise}}$ shows clearer separation between trained background and neutrinos than the $\mathcal{S}_{\text{atm.}\mu}$.

Due to the intrinsically low light yield of pure noise events, atmospheric muons which have not been shown to the RDF classifier during the training tend to obtain low $\mathcal{S}_{\text{noise}}$. The small exaltation for atmospheric muons around $\mathcal{S}_{\text{noise}} \approx 0.5$ are expected for a random decision of each tree in the RDF, and are likely induced by faint events that do not match either of the hypotheses the RDF was trained on.

The performance of the pure noise classifier is shown in Fig. 11.4b. Analogous to above, each cut value on the pure noise score $\mathcal{S}_{\text{noise}}$ can be related to a pure noise contamination $\mathcal{C}_{\text{noise}}$. The neutrino efficiency remains $\varepsilon_\nu \gtrsim 99\%$ down to extreme cuts on $\mathcal{S}_{\text{noise}}$ (cf. black line in Fig. 11.4b). High energy events practically never get rejected. Even at low energies the loss is negligible compared to the loss introduced due to the high rate veto in the trigger (see Sec. 9.4.3).

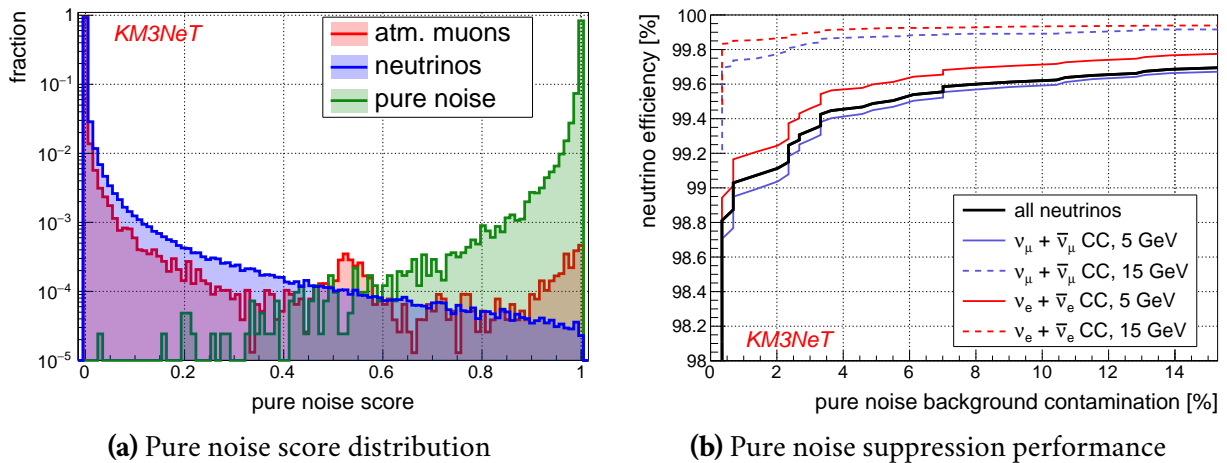


Figure 11.4: Pure noise classification result. Figure prepared for Ref. [2].

11.3.4 | Conclusions from the background rejection outputs

The rejection performance of both types of dominant background events over the neutrino sample show that rejection using RDFs is possible to the few-percent level in the final event sample. The separation between neutrinos and pure noise is better than for atmospheric muons. The latter remains consequently the dominant background distribution after background rejection using the classification output.

At this stage, and with the simulated statistics, the remaining event rates become too small to use them as a separate components in the oscillation analyses. Ways around this lack of statistics have been developed using the classed output provided within other projects in the Collaboration [134, 10]. They adopt the following procedure[134]:

11. Event type identification in ORCA

1. a loose cut on the score value, s_{\max} , is applied to generate a smooth background distribution
2. the background normalisation is determined from the final s_{\max} .
3. The normalisation from (2) is used to scale (1) and use it as a smoothed approximation for analysis

The obtained distribution can then be included in the fit. A caveat is however, that using this approach it is not guaranteed that the obtained smoothed distribution agrees with the statistically limited one at small background scores, \mathcal{S}_{bg} . In reality a shift is evident, and setting the s_{\max} value to different values for the distributions of the 'data' and the 'fit' shifts the value of best fit for the determined $\overleftrightarrow{\nu}_\tau$ normalisation for 7 DUs by up to 15% [10].

Inclusion of the background muons with an identical distribution in the data and the fit only leads to a marginal decrease in sensitivity for both the NMO study with the full detector and the $\overleftrightarrow{\nu}_\tau$ study using the 7 DU sub-array.

For the denser 20 m production used in the $\overleftrightarrow{\nu}_\tau$ appearance study in [Sec. 12.3](#) no atmospheric muons have been simulated. However, it would have been possible to estimate the neutrino efficiency ε_ν from the \mathcal{S}_{bg} distributions for 23 m and assume comparable ε_ν can be reached and apply energy dependent scaling functions to the events. Since ε_ν are however close to one, and the scaling cannot differentiate between well/poorly reconstructed events, for which smaller/larger \mathcal{S}_{bg} are expected, this option is currently not followed for physics analyses with the 20 m production.

The conclusion to be drawn is, that both background contributions can be rejected down to a contamination of 3 – 5% individually. The loss in neutrino efficiency ε_ν is negligible for the pure noise background, and below $\approx 3\%$ for all flavours not involving a high energy μ^\pm track. For the latter, the expected loss is larger, $\approx 7\%$.

11.4 | Event type identification

11.4.1 | Separation between tracks and showers

Neutrino events induce only two clearly distinct signatures. Events with a μ^\pm in the final state may appear track-like because they propagate as minimum-ionising particle and leave tracks with $\sim 4.25 \text{ m/GeV}$ length. Such μ^\pm are produced only in $\overleftrightarrow{\nu}_\mu^{\text{CC}}$ interactions or the $\sim 17\%$ $\overleftrightarrow{\nu}_\tau^{\text{CC}}$ interactions with a leptonic $\tau \rightarrow \mu \overleftrightarrow{\nu}_\mu \nu_\tau$ decay. All other events appear shower-like in the detector. Their shower is either an electromagnetic cascade emerging from an e^\pm or a hadron-induced shower. Direct distinction between electromagnetic and hadronic showers however is challenging and an attempt to use exploit these differences at analysis level has shown only limited success so far [4]. An attempt to distinguish between $\overleftrightarrow{\nu}_e^{\text{CC}}$ and $\overleftrightarrow{\nu}^{\text{NC}}$ yielded only inferior distinction⁶ to Ref. [4] and has not been pursued further. As will be shown later, using more than two EID classes is more promising.

Minimum track length An ad-hoc requirement for a μ^\pm to be reconstructable by the track reconstruction algorithm is a minimum energy $E_\mu^{\text{min}} \sim 2 \text{ GeV}$. At this energy the track-length

⁶ 10% in the separation power metric defined in [Eq. 11.7](#)

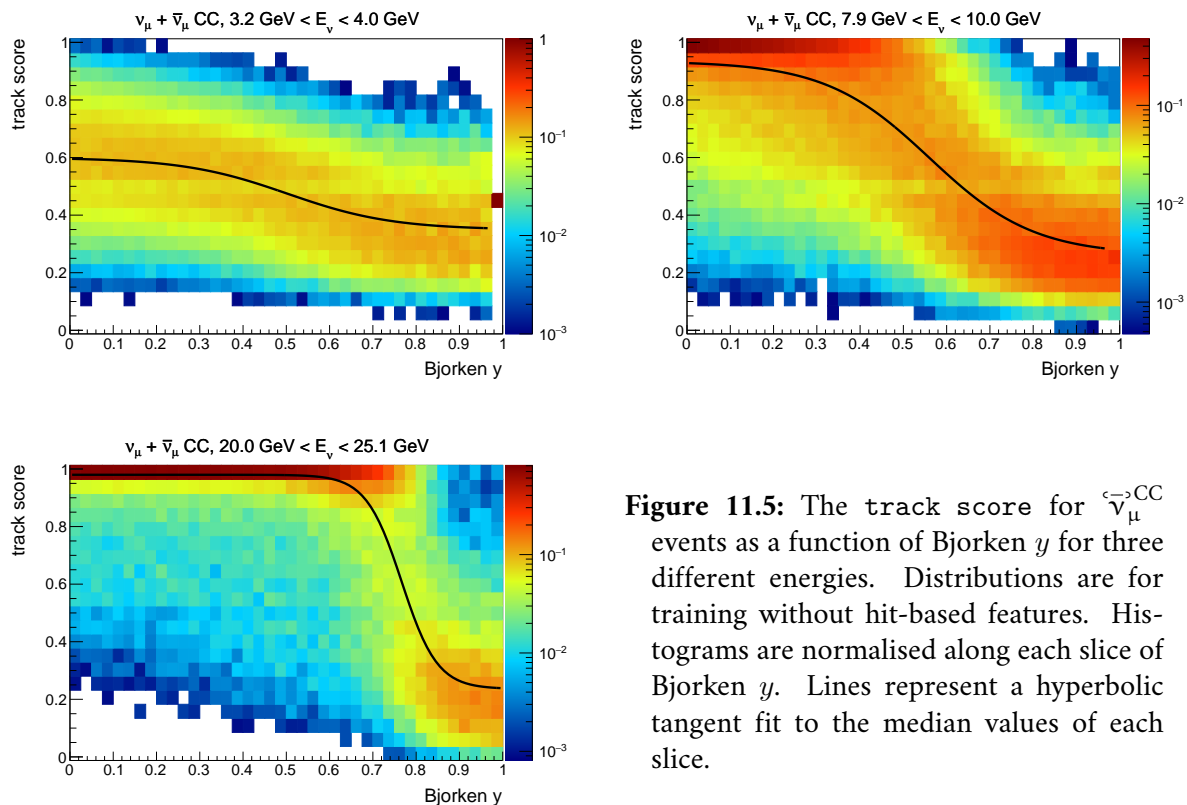


Figure 11.5: The track score for $\bar{\nu}_\mu^{\text{CC}}$ events as a function of Bjorken y for three different energies. Distributions are for training without hit-based features. Histograms are normalised along each slice of Bjorken y . Lines represent a hyperbolic tangent fit to the median values of each slice.

is roughly the spacing between DOMs on adjacent floors. However, if the μ^\pm is outshined by the light yield from the hadronic vertex shower, identification as track will not be possible – at least it is higher than the absolute minimum required for the track reconstruction to converge. In this paragraph, the track score is therefore analysed as a function of the Bjorken y (or, inelasticity y of the interaction) to find the minimum μ^\pm energy needed for events to appear track-like.

For $\bar{\nu}_\mu^{\text{CC}}$ interactions the track score is shown for different neutrino energies as a function of the Bjorken y in Fig. 11.5. Already at the detection threshold a small pull towards higher score values is observed if more than $\sim 50\%$ of the energy is transferred to the μ^\pm (i.e. $y < 0.5$). Only at higher energies a maximum at track score ≈ 1 appears, corresponding to a clear track-like signature. The threshold value y_t up to which unambiguous identification is possible increases with neutrino energy.

To analyse this in a more quantitative way, the distributions shown in Fig. 11.5 are substituted by the median score \tilde{s} in each slice of y and fit using a hyperbolic tangent function

$$\tilde{s}(y) = \frac{(s_0 + s_1) - (s_0 - s_1) \tanh\left(\frac{y-y_t}{w}\right)}{2}, \quad (11.5)$$

with two asymptotic values at low (s_0) and high (s_1) inelasticity, a transition point y_t , the width of the transition w . The lines added in Fig. 11.5 correspond to these fitted hyperbolic tangent functions. Figure 11.6 shows the E_ν dependence of the best fit values for the asymptotic $s_{0,1}$ and the y_t . The separation between the low and high y asymptotic values, $s_0 - s_1$, reaches the plateaus at ~ 9 GeV. The threshold y_t for identification increases steadily from 0.5 up to 0.9.

11. Event type identification in ORCA

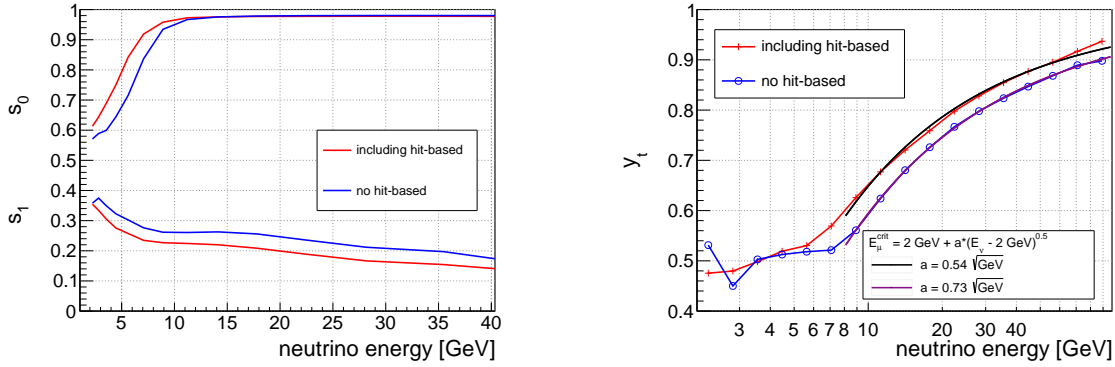


Figure 11.6: Results from hyperbolic tangent fits to the median track score distributions as shown in Fig. 11.5.

Hence, at high energies the μ^\pm in ORCA is already clearly identified as track when receiving at least 10% of the neutrino energy. Above $E_\nu = 10$ GeV – i.e. in the plateau region – the increase in y_t is well described by an empiric square root dependence for the threshold muon energy,

$$E_\mu^{\text{crit}} = E_0 + a \cdot \sqrt{E_\nu - E_0} \cdot \sqrt{\text{GeV}}, \quad (11.6)$$

with the already stated reconstruction threshold $E_0 = 2$ GeV and one free parameter.

Since $E_\mu^{\text{crit}} = (1 - y_t) \times E_\nu$, the above results can be also converted to the minimum μ^\pm energy needed for clear track identification and the result is shown in Fig. 11.7. The bands indicate the width of the fitted transition region, w .⁷ When including the hit-based variables, the E_μ^{crit} can be lowered by 20% compared to not including these variables.

11.4.2 | Dependence on instrumentation density and input features

To quantify the difference in classification performance between different detector configurations and classifier setups, the separation power, $S(\Delta E)$, is used.

$$S(\Delta E) = 1 - C(\Delta E) = 1 - \frac{\sum_i P_{i,\text{score}}^{\vec{\nu}_\mu}(\Delta E) \cdot P_{i,\text{score}}^{\vec{\nu}_e}(\Delta E)}{\sqrt{\sum_i \left(P_{i,\text{score}}^{\vec{\nu}_\mu}(\Delta E) \right)^2 \cdot \sum_i \left(P_{i,\text{score}}^{\vec{\nu}_e}(\Delta E) \right)^2}}. \quad (11.7)$$

It is defined as the opposite part of the correlation coefficient, $C(\Delta E)$, and quantifies the overlap in the track score distributions between $\vec{\nu}_\mu^{\text{CC}}$ and $\vec{\nu}_e^{\text{CC}}$ events as a function of neutrino energy ΔE .⁸ For calculating the separation power, the $\vec{\nu}_\mu^{\text{CC}}$ and $\vec{\nu}_e^{\text{CC}}$ events are binned in the track score, and the separation power is calculated by summing over bins i of the filled histograms.

In the limit $S \rightarrow 0$, the distribution of $\vec{\nu}_\mu^{\text{CC}}$ and $\vec{\nu}_e^{\text{CC}}$ are the same. For $S \rightarrow 1$ the overlap between the two histograms is zero, i.e. they are completely separated.

⁷More precisely, w is the region at which the median is in the central 50% between max and min value.

⁸For practical reasons intervals in E are used for the calculation.

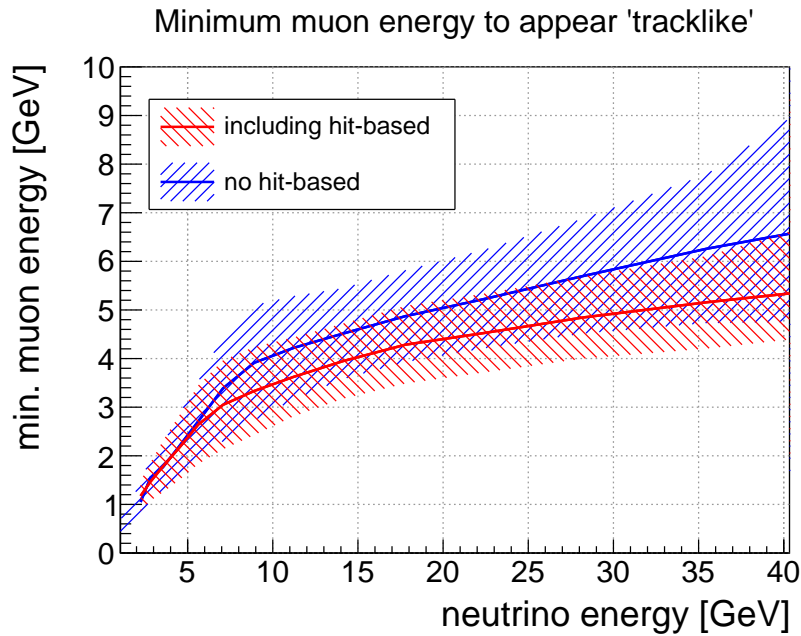


Figure 11.7: Minimum muon energy needed for clear identification as track as a function of neutrino energy. The transition region between the track- and shower-like regime is indicated by the shaded bands.

The separation power for training with and without inclusion of the hit-PDF based features (cf. [Sec. 11.2.4](#)) and different horizontal ORCA spacings is compared in [Fig. 11.8](#).

For all configurations, close to optimal separation power is achieved above 20 GeV. The distributions however differ in the turn-on. To compare the different setups using this turn-on behaviour the value at $S = 50\%$ can be determined. It is 9.1 GeV / 7.2 GeV for the 23 m configuration without / with the hit-based features. Equivalently, $S = 50\%$ is reached for the 20 m configuration at 7.3 GeV / 5.5 GeV. A 25% lowering in turn-on is therefore achieved by using the improved training for both detector configurations. A gain of same size results from the denser instrumentation (23 m vs. 20 m horizontal inter-DU spacing). This highlights the importance of the feature design for the RDF. Combining both changes, the improved RDF model and denser instrumentation leads to a $\sim 40\%$ lower RDF turn-on.

11.5 | Classification of the event sample

The fact that the RDFs are trained on a binary decision problem facilitates the distribution of the event sample into different analysis classes. For the division in the analysis, cuts on the track score variable $\mathcal{S}_{\text{track}}$ can be used. While earlier studies have used only two classes to image the two different event signatures – tracks and showers –, a third analysis class is now used to absorb events that are more ambiguous to classify, which is referred to as middle class below. The three analysis classes are defined as follows:

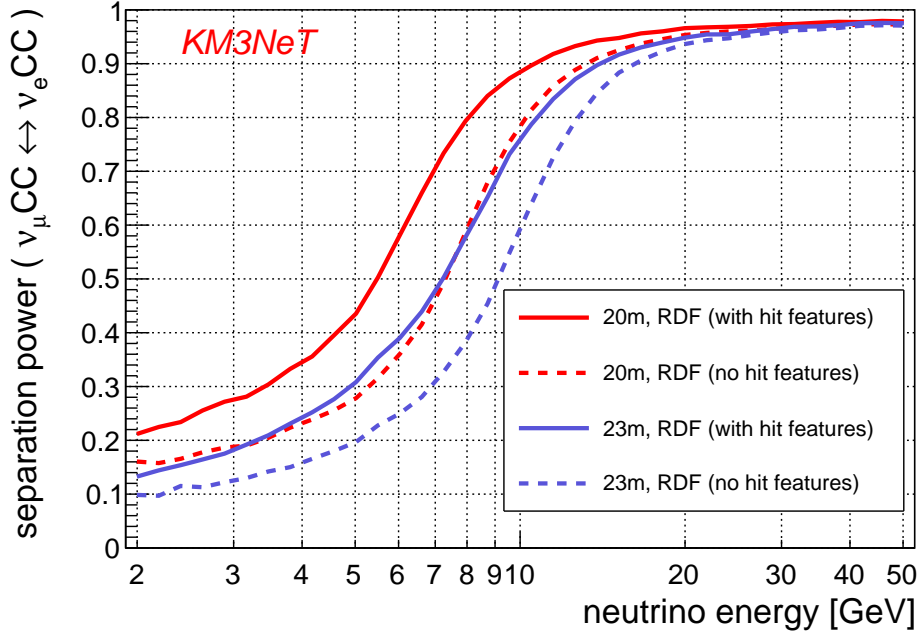


Figure 11.8: Comparison of the classifier performance in terms of the separation power metric as defined in Eq. 11.7. Detector configurations with 20 m (*red*) and 23 m (*blue*) average horizontal inter-DU spacing, and training with (*solid*) and without (*dashed*) hit-PDF based features are shown. Figure prepared for Ref. [2].

$$\begin{aligned}
 \text{track class:} & \quad 0.7 < \mathcal{S}_{\text{track}} \\
 \text{middle class:} & \quad 0.3 < \mathcal{S}_{\text{track}} \leq 0.7 \\
 \text{shower class:} & \quad \mathcal{S}_{\text{track}} \leq 0.3
 \end{aligned} \tag{11.8}$$

The choice of critical values 0.3 and 0.7 is a result of a parameter scan and maximises the sensitivity to the NMO [9, 135]. The use of three EID classes is also pursued in other experiments (e.g. in the IceCube analysis in Ref. [136]).

With this definition of the classes, the resulting fractions of events for the neutrino flavours are given in Fig. 11.9. For all flavours, the fraction of events in the middle class is dominant at the threshold, $\gtrsim 60\%$ below 3 GeV, and decreases steadily with increasing energy. For the shower-only event channels, $\bar{\nu}_e^{\text{CC}}$ and $\bar{\nu}^{\text{NC}}$, the fraction of events wrongly classified as track is only few percent over the entire energy range. The overall behaviour is similar for $\bar{\nu}_\tau^{\text{CC}}$, with the difference that the fraction of events in the track class is larger and increases slightly with energy. With $\sim 13\%$ classified as track, the fraction almost reaches the 17% branching ratio to μ^\pm in the τ^\pm decay.⁹ In Fig. 11.10, the $\bar{\nu}_\tau^{\text{CC}}$ sample is split into the different τ decay channels. This shows clearly, that the track-like fraction is entirely contributed by $\bar{\nu}_\tau^{\text{CC}}$ events with a $\tau \rightarrow \mu$ decay.

For $\bar{\nu}_\mu^{\text{CC}}$, the behaviour is opposite to the other flavours, and with increasing energy more events are correctly classified as track, 80% at ~ 50 GeV. The difference in Bjorken y between

⁹Especially when taking into account that part of the energy goes into neutrinos in the τ^\pm decay, and 80% of events are identified as track-like for $\bar{\nu}_\mu^{\text{CC}}$, a $\sim 13\%$ track class fraction is expected.

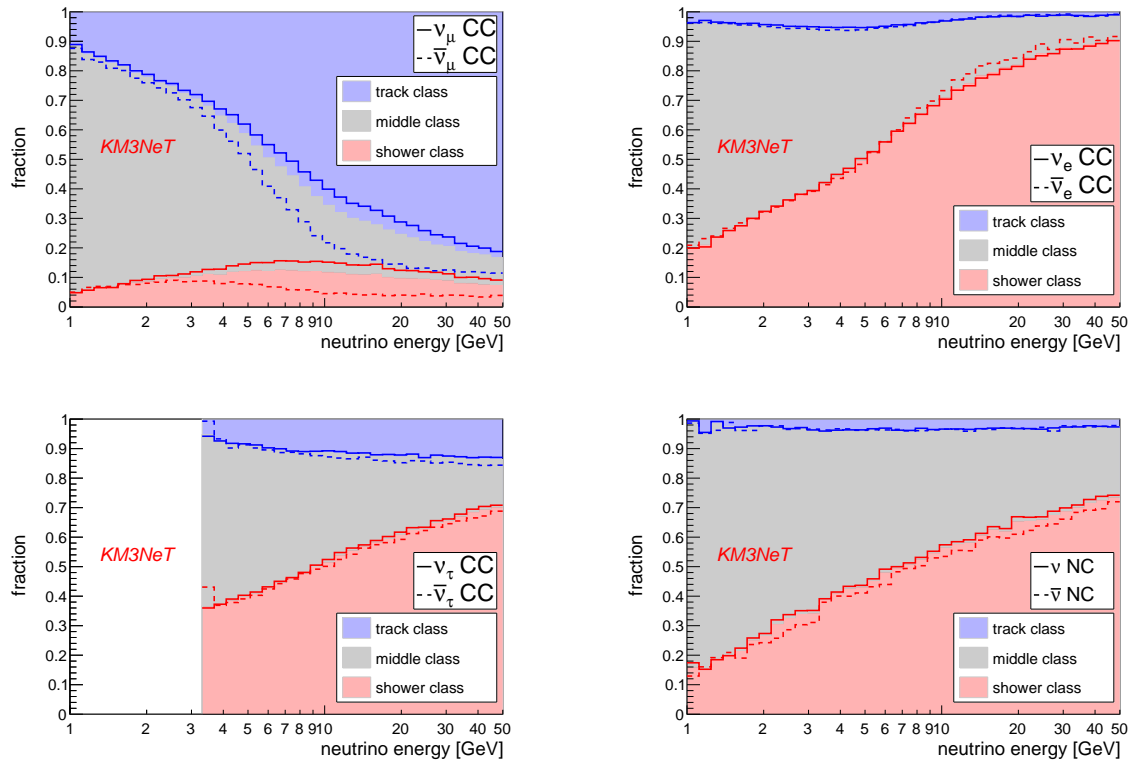


Figure 11.9: Fractions of events per class following the definition in Eq. 11.8. Coloured areas correspond to a $\nu/\bar{\nu}$ average expected in the atmospheric flux. Dashed/solid lines show the fractions for ν and $\bar{\nu}$ individually. Figures prepared for Ref. [2].

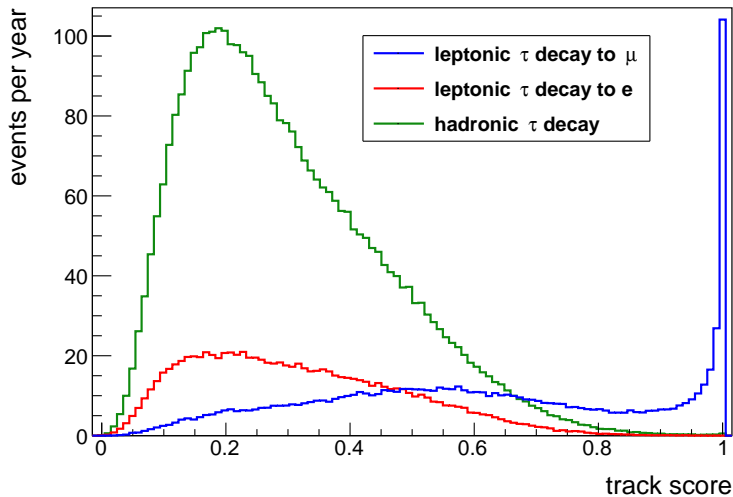


Figure 11.10: Distribution of the track score $\mathcal{S}_{\text{track}}$ for $\bar{\nu}_\tau$ events for the different τ decay channels.

ν_μ^{CC} and $\bar{\nu}_\mu^{\text{CC}}$ becomes apparent when looking at (anti-)neutrinos separately (solid (dashed) lines in Fig. 11.9). Due to the lower average y of $\bar{\nu}_\mu^{\text{CC}}$ (see Sec. 4.3), they are up to 20% more likely to be correctly identified as track than ν_μ^{CC} of the same energy.

11.6 | Detector resolutions for the pre-selected and classified event sample

With the separation of the event sample into the different classes as defined above, the resolutions of the realistic 20 m ORCA setup are evaluated for $\bar{\nu}_\mu^{\text{CC}}$ and $\bar{\nu}_e^{\text{CC}}$ events. These are the neutrino flavours for which the track and shower reconstruction algorithms had been optimised. As the Dusj shower energy estimate yields better accuracy than the track-length estimate from JGandalf, the shower energy estimate is used for all events. In principle, it would be possible to develop a more accurate combined energy estimate accounting for both track and emission from the vertex cascade. Improvement of the energy reconstruction for track-like events remains a future development task for ORCA.

The effective volume for upward-going events in the final analysis sample is calculated using Eq. 5.6. The result is shown in Fig. 11.11. The effective volume comprises selected events in the track class passing the event selection for JGandalf (tracks) and selected events in the other two classes passing the event selection for Dusj (showers). The effective volume for the shower-dominated flavours levels off 20% below the instrumented volume of 6.7 Mm^3 . This is mainly because a more stringent coverage criterium is applied for showers (cf. Fig. 10.4). For $\bar{\nu}_\mu^{\text{CC}}$, the μ^\pm tracks entering the detector from outside and the looser criteria of JGandalf allow for a steady increase of the effective volume also beyond 10 GeV. The turn-on is faster for anti-neutrinos than for neutrinos in the $\bar{\nu}_e^{\text{CC}}$ and $\bar{\nu}_\mu^{\text{CC}}$ channels as a direct result of the different inelasticity. For the same reason, the behaviour for NC events is reversed, because only the hadronic vertex component is visible and the produced neutrino leaves the detector unseen. For $\bar{\nu}_\tau^{\text{CC}}$, the effective volume is similar for neutrinos and anti-neutrinos. This is because high y are suppressed as a consequence of the τ^\pm lepton mass (cf. Sec. 6.2.1).

The energy resolution is evaluated for selected and correctly classified events ($\bar{\nu}_\mu^{\text{CC}}$ in the track class, $\bar{\nu}_e^{\text{CC}}$ in the shower class) in Fig. 11.12. In both cases a pull towards higher reconstructed energies is observed right at the threshold. This behaviour is expected, since only relatively bright events tend to be reconstructed and would fall below the threshold otherwise. For ν_e^{CC} classified as tracks, the median reconstructed energy is identical to the true neutrino energy with decreasing width. For $\bar{\nu}_\mu^{\text{CC}}$ events classified as track, the 1σ band of reconstructed energy is broader above 10 GeV. Above 20 GeV the probability that all the light from both the $\bar{\nu}_\mu^{\text{CC}}$ vertex and the track are fully contained decreases. An even larger impact is the fact that the Dusj energy estimate is used. The hits from long tracks then have a time residual with respect to the shower hypothesis which is too large to be accepted. The energy reconstruction therefore saturates and grows less than linear with neutrino energy with a larger spread.

For the middle class, the energy resolutions for both flavours are shown. While the most probable reconstructed energy remains on the diagonal, a significant tail towards low reconstructed energies is observed for both $\bar{\nu}_\mu^{\text{CC}}$ and $\bar{\nu}_e^{\text{CC}}$. The middle class therefore serves its purpose and collects events which are less accurately reconstructed and therefore neither classified clearly as track or shower.

The angular resolution for ν_μ^{CC} and ν_e^{CC} events correctly identified as track or shower, respectively, are given in Fig. 11.14. The median resolution is close to the intrinsic limit expected from the scattering angle between neutrino and lepton (cf. Fig. 4.1, or Ref. [65] directly). The influence of the inelasticity y is seen in the better resolution for $\bar{\nu}$ than ν . The resolution on $\bar{\nu}_\mu^{\text{CC}}$ is slightly better than for $\bar{\nu}_e^{\text{CC}}$ in the range $4 \text{ GeV} \lesssim E_\nu \lesssim 20 \text{ GeV}$. Below 4 GeV

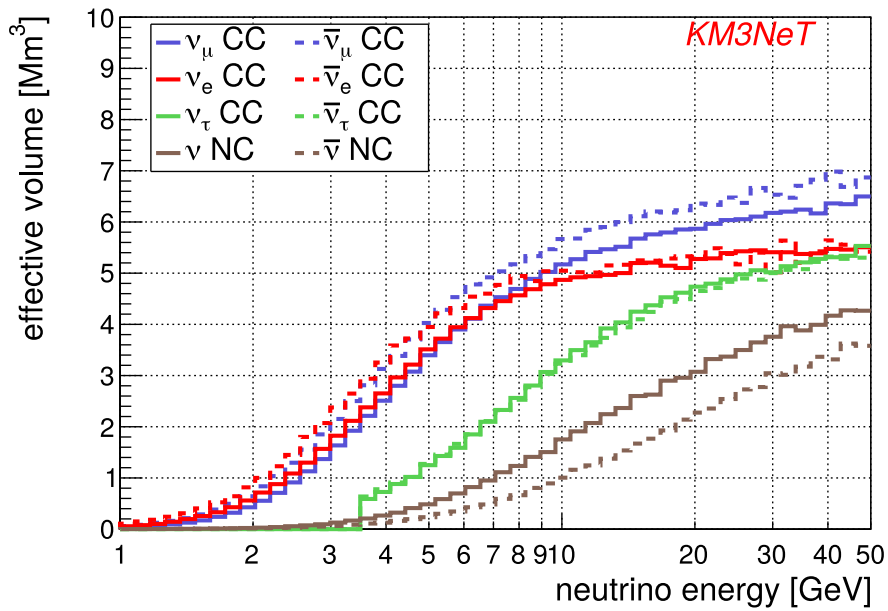


Figure 11.11: Effective volume of the 20 m ORCA detector at analysis stage, after EID and event selection. Figure prepared for [2].

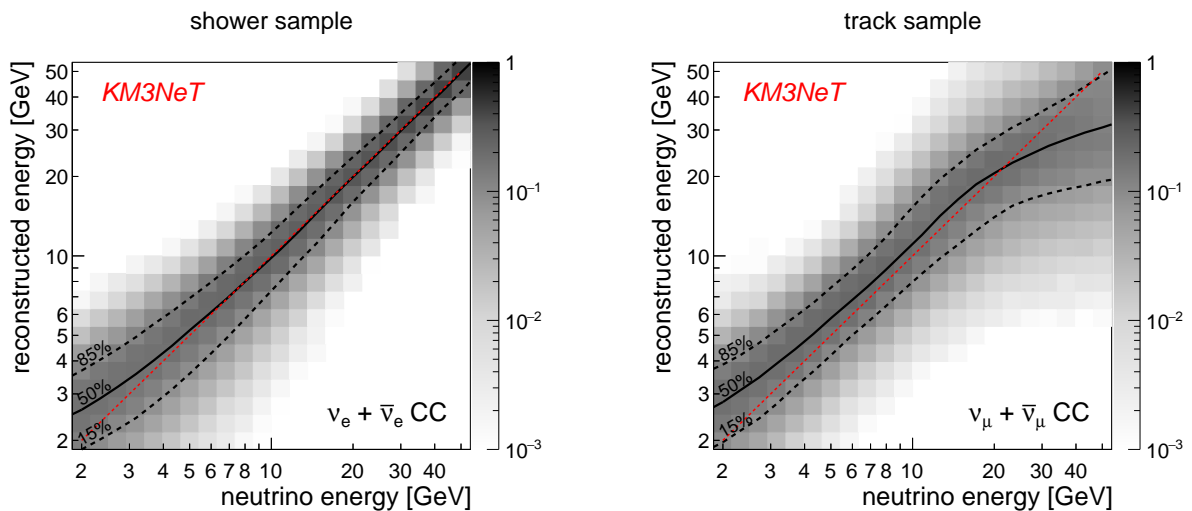


Figure 11.12: Energy resolution for $\bar{\nu}_e^{\text{CC}}$ events classified as shower and $\bar{\nu}_\mu^{\text{CC}}$ events classified as track of the 20 m / 115 DU detector configuration. Each slice of neutrino energy is normalised to one. Figures prepared for Ref. [2].

11. Event type identification in ORCA

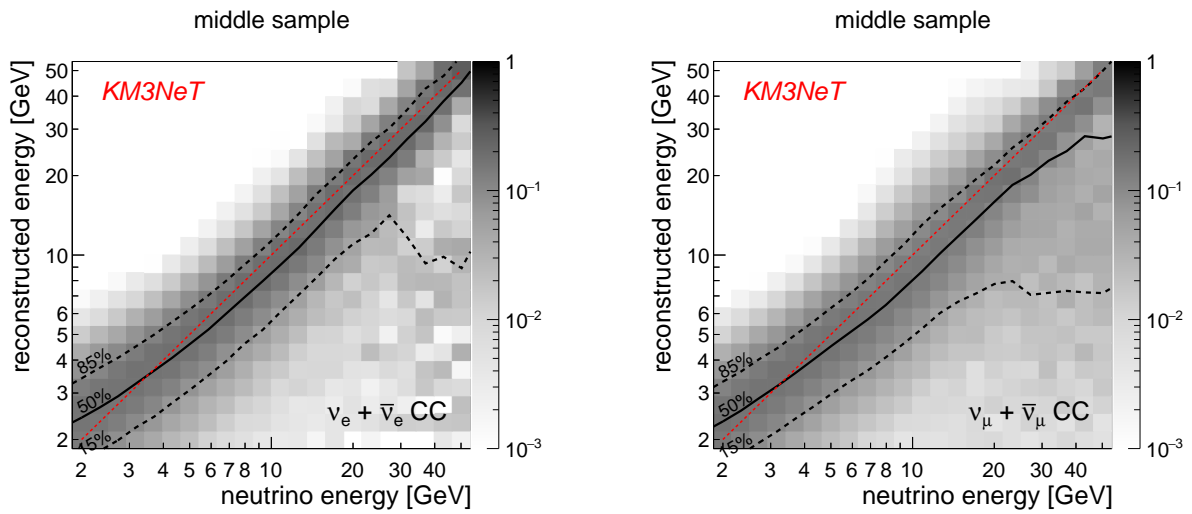


Figure 11.13: Energy resolutions for $\bar{\nu}_e^{CC}$ and $\bar{\nu}_\mu^{CC}$ events in the middle class corresponding to the 20 m / 115 DU detector configuration. Each slice of neutrino energy is normalised to one.

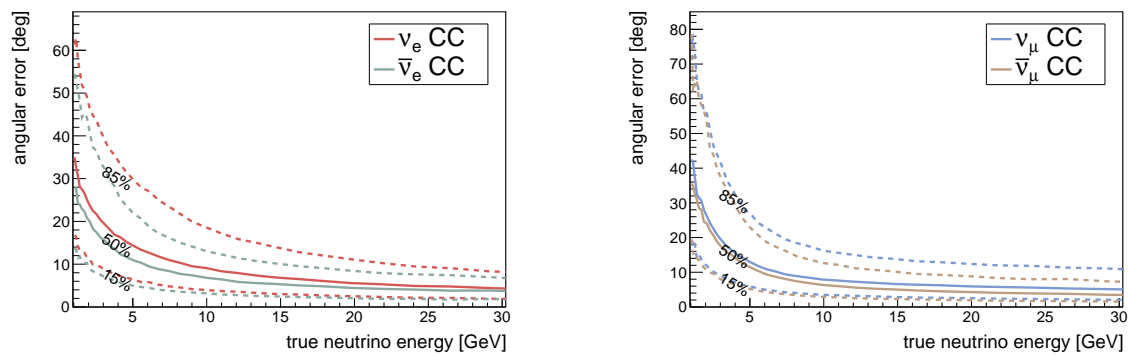


Figure 11.14: Median angular resolutions (space angle between neutrino direction and reconstructed direction) for $\bar{\nu}_e^{CC}$ classified as shower (left) and $\bar{\nu}_\mu^{CC}$ events classified as track (right) with the 20 m / 115 DU detector configuration. Dashed lines represent 15% and 85% quantiles.

the performance is worse due to the short μ^\pm track. This is shown in the direct comparison of the median resolutions for $\bar{\nu}_\mu^{CC}$ events in the track sample and $\bar{\nu}_e^{CC}$ events in the shower sample in [Fig. 11.15](#).

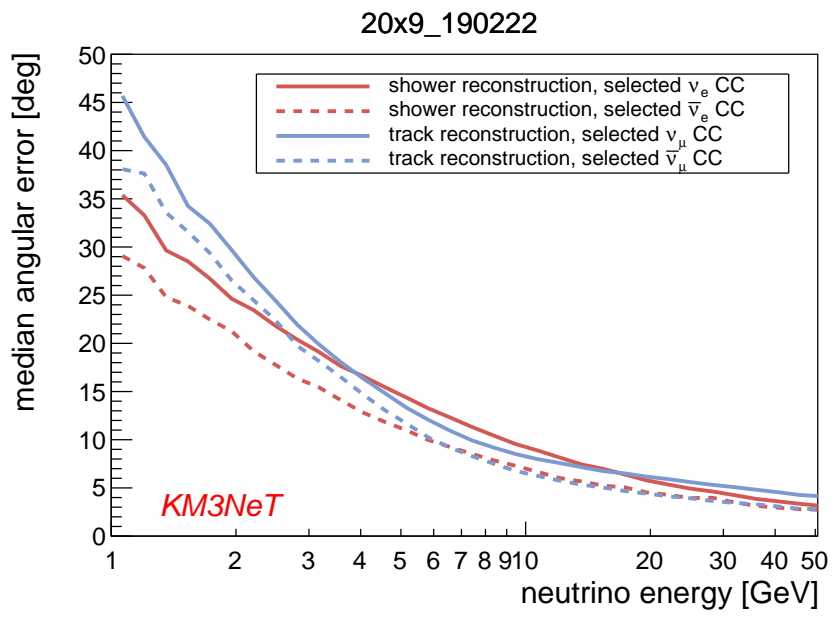


Figure 11.15: Direct comparison of the median angular resolutions of Fig. 11.14 for the 20 m / 115 DU detector configuration. Figure prepared for Ref. [2].

12 Sensitivity of ORCA to $\bar{\nu}_\tau$ appearance

In this chapter, the sensitivity to the measurement of $\bar{\nu}_\tau$ appearance with ORCA is studied. The study evaluates the sensitivity of ORCA to determine the normalisation, n_τ , of the $\bar{\nu}_\tau$ component in the atmospheric neutrino flux through oscillation. The measured normalisation is larger (smaller) than one if more (less) $\bar{\nu}_\tau$ neutrinos are observed than are expected from unitary mixing and the assumed $\bar{\nu}_\tau$ cross section. Since the atmospheric flux is essentially free of $\bar{\nu}_\tau$ neutrinos when produced, the $\bar{\nu}_\tau$ component is measured in appearance mode, which justifies the designation as $\bar{\nu}_\tau$ appearance study.

The analysis presented in the following assumes a realistic 115 DU ORCA detector layout with an average 20 m horizontal spacing. The detector design under study complies with what is currently planned for deployment.

In the previous chapters, the effective volume after event selection, the performance of the event identification (EID) and the resolution of the reconstruction have been shown for this configuration. Using the reconstructed quantities of the Monte Carlo simulation allows to identify where the $\bar{\nu}_\tau^{\text{CC}}$ appearance measurement is sensitive in [Sec. 12.1](#).

For a full analysis systematic uncertainties need to be accounted for. In this analysis, the software package ParamNMH [8] developed by the KM3NeT Collaboration is used. ParamNMH uses a parametrised detector response derived from fits to the detailed Monte Carlo simulations for the ORCA detector (i.e. a parametrisation of the results in [Sec. 8.2](#)).

To study the $\bar{\nu}_\tau$ appearance sensitivity, the ParamNMH software has been enhanced as part of this thesis to allow for an independent scaling of the neutral- and charged-current $\bar{\nu}_\tau$ event contributions in the *null* and *alternative* hypotheses. The null and alternative hypotheses correspond to the event distributions of the presumed measured data and the event rate given a certain model assumption during the fit, respectively.

ParamNMH and the extension for $\bar{\nu}_\tau$ appearance is described in [Sec. 12.2](#). The sensitivity study for the 115 DU detector is presented in [Sec. 12.3](#).

As will be demonstrated, ORCA is capable of providing relevant $\bar{\nu}_\tau$ appearance results already in an early construction phase of the experiment without prior knowledge of the true NMO. A summary of the analysis in Ref. [10] for the sensitivity to $\bar{\nu}_\tau$ appearance with the simulated 7 DU sub-detector is given in [Sec. 12.4](#). The results indicate that with a future analysis of data currently taken in-situ, a first $\bar{\nu}_\tau^{\text{CC}}$ appearance measurement is already feasible. With this, [Part II](#) can be concluded in [Sec. 13](#).

12.1 | Measurement principle and sensitive region

The $\bar{\nu}_\tau$ appearance study in this analysis uses the normalisation n_τ as a single parameter as an overall scale to the signal strength of the $\bar{\nu}_\tau$ contribution. This approach has been followed previously by other experiments [107, 104, 106]. It allows for a model-independent test whether the assumption of unitary 3×3 neutrino mixing in combination with the cross

section predicted by the Standard Model of particle physics (SM) are realised in nature. In this case, a normalisation $n_\tau \equiv 1$ is expected. Significant deviation of the n_τ parameter from unity can indicate that the picture of 3×3 neutrino mixing is incomplete, or that the modelled SM cross sections for $\bar{\nu}_\tau^{\text{CC}}$ are wrong. At least the former would be an intriguing indication for new physics. But, as outlined in [Sec. 6.3](#), to date the error bars on the measured normalisations are still very large, allowing only to convincingly rule out non-appearance, i.e. a vanishing contribution, $n_\tau \equiv 0$.

12.1.1 | Region of interest for the $\bar{\nu}_\tau$ appearance measurement

The analysis is carried out in the two-dimensional parameter space of energy and cosine zenith angle, in the track, shower and middle class of the EID.¹ The reconstructed event numbers after EID expected in the analysis sample after one year of operation are shown in [Fig. 12.1](#). The events are split between $\bar{\nu}_\tau^{\text{CC}}$ (left) and the sum of the other flavours ($\bar{\nu}_e^{\text{CC}}$, $\bar{\nu}_\mu^{\text{CC}}$, $\bar{\nu}^{\text{NC}}$) (right). In total, 3.3×10^3 (2.0×10^3 shower, 0.85×10^3 middle, 0.43×10^3 track) $\bar{\nu}_\tau^{\text{CC}}$ events remain in the analysis sample, of which $\sim 61\%$ are classified as showers. The other 5.8×10^4 neutrino events in the analysis sample are distributed almost evenly between the three classes (2.0×10^4 shower, 1.8×10^4 middle, 2.0×10^4 track).

The $\bar{\nu}_\tau^{\text{CC}}$ event distribution traces the oscillation maximum of $\bar{\nu}_\mu \rightarrow \bar{\nu}_\tau$. In the reconstructed energy the distribution is however shifted to lower energies with respect to the oscillation maximum. This is in part a result of the unseen energy carried away by the additional neutrinos in τ^\pm -decay. The lower light output of the predominantly hadronic showers with respect to electromagnetic cascades, for which the shower reconstruction has been optimised [4], induces an additional shift.

It is also apparent from [Fig. 12.1](#) that faint events accumulate in the middle class. In addition to the peak at low reconstructed energies, a feature of the shower reconstruction algorithm is visible in $2 \text{ GeV} \lesssim E_{\text{rec}} \lesssim 6 \text{ GeV}$ and $\cos(\theta_{z,\text{rec}}) \approx -1$. The feature has been analysed carefully and is understood. It is induced mainly due to the higher photocathode density of the DOMs in the downward pointing hemisphere (as was shown in [Fig. 7.2](#)), lowering trigger and reconstruction thresholds for events with upward pointing showers.² This feature is absent in the track channel because of the higher turn-on energy.

While $\bar{\nu}_\tau^{\text{CC}}$ only amount to $\sim 5\%$ of the total event count, they are centered at higher reconstructed energies and towards upward-going directions. In order to identify the sensitive regions prior to the full analysis, the statistical significance per bin i can be used [86],

$$S_i = \frac{N_i(n_\tau = 1) - N_i(n_\tau = 0)}{\sqrt{N_i(n_\tau = 1)}} = \frac{N_i(\bar{\nu}_\tau)}{\sqrt{N_i(\text{all } \bar{\nu})}}. \quad (12.1)$$

Here, N_i is the sum of oscillated neutrino events ending up in the respective bin i of reconstructed quantities.³ S_i represents a per-bin significance in units of standard deviations σ .

¹See [Eq. 11.8](#) for the precise definition of the classes.

²Horizontal events where the light emitting shower is scattered into the upward direction has a higher probability to be detected, and will be reconstructed as upward going.

³While for now for simplicity the scaling is considered to affect the CC contribution only, later in the full analysis also the case of combined CC+NC scaling will be studied. The more precise notations n_τ^{CC} and $n_\tau^{\text{CC+NC}}$ will then be used to make clear a distinction.

12. Sensitivity of ORCA to $\bar{\nu}_\tau$ appearance

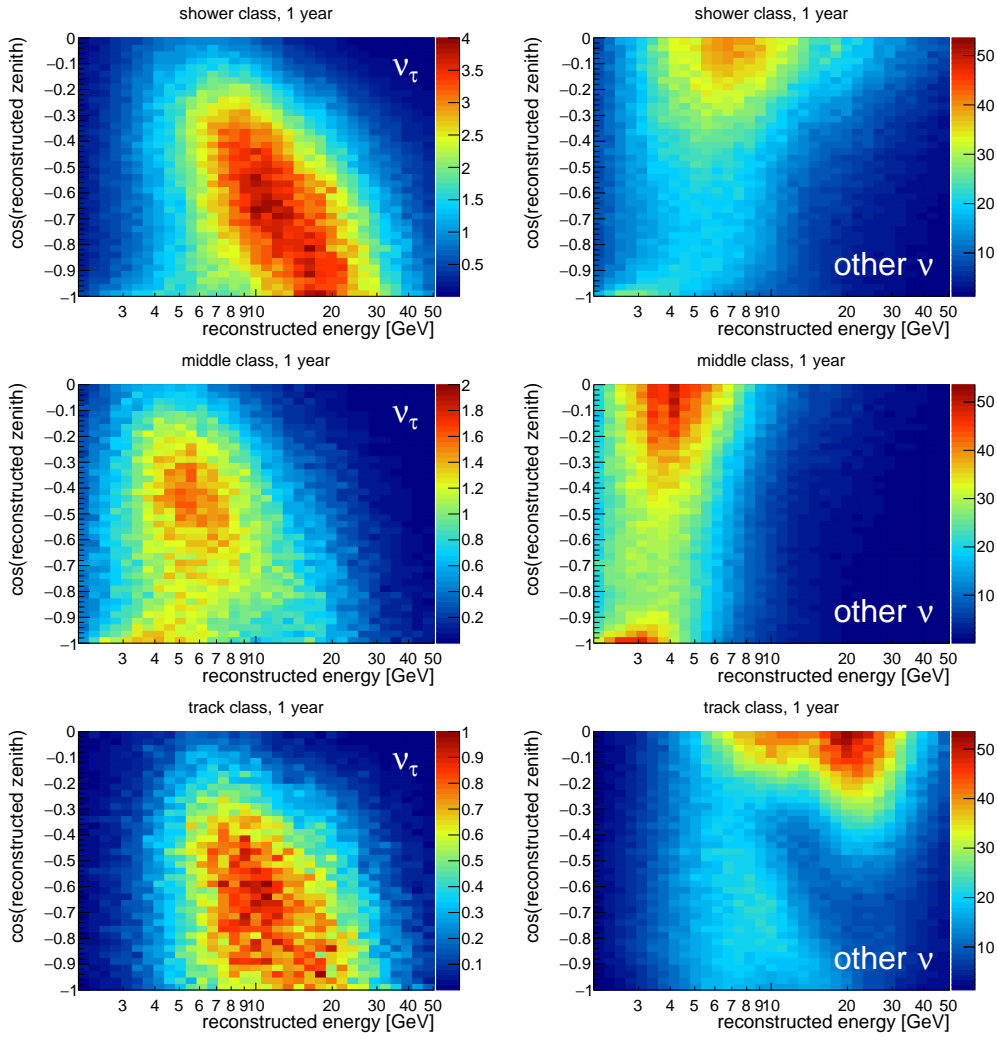


Figure 12.1: Reconstructed event distribution in the analysis sample of the 20 m detector configuration and for one year of data-taking. Distributions are shown per EID class for $\bar{\nu}_\tau^{\text{CC}}$ (left) and the sum of $\bar{\nu}_e^{\text{CC}}$, $\bar{\nu}_\mu^{\text{CC}}$, and all $\bar{\nu}^{\text{NC}}$ (right). Note, that a different z -scale between left panels to emphasise features in the distributions.

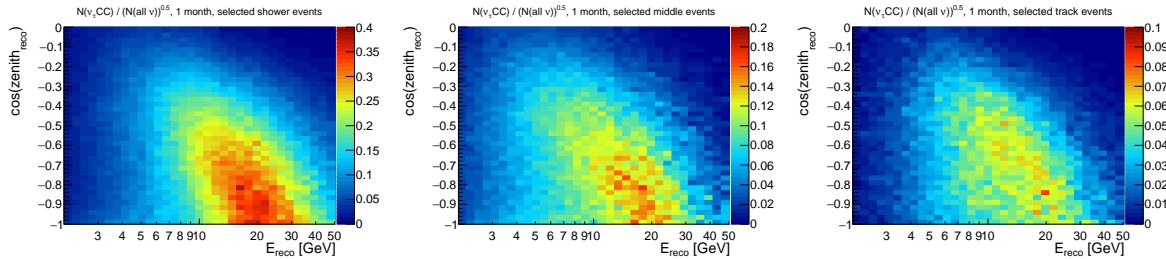


Figure 12.2: Statistical per-bin significance for the detected ν_τ -signal in the shower, middle, and track class for one month of data taking. Calculated from the scaled distributions in Fig. 12.1. Note, that a different z -scale is chosen.

Squared summation yields the overall significances for each class: $S_{\text{track}} = 5.2\sigma$, $S_{\text{middle}} = 2.6\sigma$, and $S_{\text{shower}} = 1.1\sigma$ for an event normalisation corresponding to one month of data-taking. Most of the sensitivity stems from the shower class with the region around 15–25 GeV for straight upward-going neutrinos being most important for the $\bar{\nu}_\tau$ appearance measurement.

This simple method is good for a first estimate of the sensitivity. However it only takes the distribution of reconstructed quantities without account for systematic uncertainties. Another caveat is that statistical fluctuations due to finite Monte Carlo statistics in the event distributions are already evident from Fig. 12.1. The analysis framework chosen for this analysis, ParamNMH, avoids statistical bin-to-bin fluctuations by parametrising the detector response for each flavour and EID class.

12.2 | Oscillation fit using ParamNMH

When testing two particular values for the normalisation against each other, the fundamental problem is reduced to a binary test between two hypotheses. These are commonly referred to as the *null* and the *alternative* hypothesis. In the $\bar{\nu}_\tau$ appearance case they correspond to the normalisation assumed to be realised in nature (or at least in the simulated pseudo data), n_τ^{data} , and the particular normalisation during the fit, n_τ^{fit} , respectively. This problem is similar in the study of the NMO, where the two hypotheses are normal and inverted ordering. For the $\bar{\nu}_\tau$ appearance analysis the analysis frameworks developed by the Collaboration primarily in order to study NMO can therefore be used. A parameter scan by iteratively fitting with different fixed normalisations n_τ^{fit} yields the best-fit value and the sensitivity contour for the normalisation n_τ^{data} .

12.2.1 | Oscillation analysis frameworks for ORCA

As outlined in Sec. 6.4, the analysis frameworks need to incorporate a series of steps in order to arrive at the distributions of neutrino events for analysis.

The first part comprises all steps necessary to calculate the interaction rates in the detector per unit volume for each flavour as a function of the true energy and direction. These steps are a common task for all frameworks⁴ and use the atmospheric neutrino flux prediction by the HKKM group [41], the OscProb [62] package with a 43 step approximation of the PREM [48] matter density profile of the Earth to calculate oscillation probabilities for the produced $\bar{\nu}_\mu/\bar{\nu}_e$ flavours to the flavour composition in the detector, and the neutrino cross sections from the GENIE [110] event generator.

The second part covers the response of the detector and provides the selected neutrino event rates in the final analysis sample as a function of reconstructed energy, direction and EID class. The implementation of these steps differs between the analysis frameworks, but in some way they all need to incorporate the following four components:

1. an *effective volume* for each flavour at the final analysis stage to calculate event rates from the interaction rates per unit volume,

⁴however with individual implementation

12. Sensitivity of ORCA to $\bar{\nu}_\tau$ appearance

2. *classification fractions* per EID class to split the sample into the shower, track and (meanwhile in most analyses also) middle events,
3. *angular resolutions*, i.e. the event smearing from simulated to reconstructed direction, and
4. *energy resolutions*, i.e. the smearing from simulated to reconstructed neutrino energy.

Note, that for the 20 m configuration of ORCA, these steps should reproduce the detector responses evaluated as part of this thesis in [Sec. 11.5](#) and [Sec. 11.6](#).

For the $\bar{\nu}_\tau$ appearance results presented here, the ParamNMH [8] oscillation analysis software is used. It is written in C++ and based on the ROOT [137] data analysis framework. The Minuit2 minimisation package available within ROOT is used for the fit to the binned expected event distributions. ParamNMH uses parametrised functions for the detector response which are tuned to match the Monte Carlo simulated data.

In addition to ParamNMH, two other analysis tools, MONA and SWIM, have been developed and are maintained within the KM3NeT Collaboration. In contrast to the parametrisations in ParamNMH, they both populate migration matrices from simulated to reconstructed event parameters directly with the distributions from the Monte Carlo simulation output. For these latter frameworks it has been ensured that the NMO sensitivity result is not artificially increased by event fluctuations from finite Monte Carlo statistics [134]. For ParamNMH, the event distributions are smooth by construction thanks to the use of the parametrisation functions.

12.2.2 | Implementation of detector response in ParamNMH

ParamNMH uses a parametrisation for each of the four points listed in the previous section.

- the effective volume is parametrised as function of the true energy and true zenith angle of the neutrino individually for each of the eight different flavour types (three CC flavours and NC, for ν and $\bar{\nu}$).
- the classification fractions are parametrised as a function of energy. From here on 24 (8×3 individual sets are used below)
- the migration $\cos(\theta_{z,\nu}) \rightarrow \cos(\theta_{z,\text{rec}})$ is parametrised as a function of the true quantities $\theta_{z,\nu}$ and E_ν
- the migration $E_\nu \rightarrow E_{\text{rec}}$ is parametrised as a function of E_ν .

[Figure 12.3](#) shows a histogram generated from the ParamNMH effective volume matching the effective volume from the Monte Carlo simulation in [Fig. 11.11](#) to visualise the agreement of the parametrised response. Parametrisations provided for 20 m [138] have been used as input for the sensitivity presented here.

The 24 sets of detector responses can be used to calculate the expected event numbers.

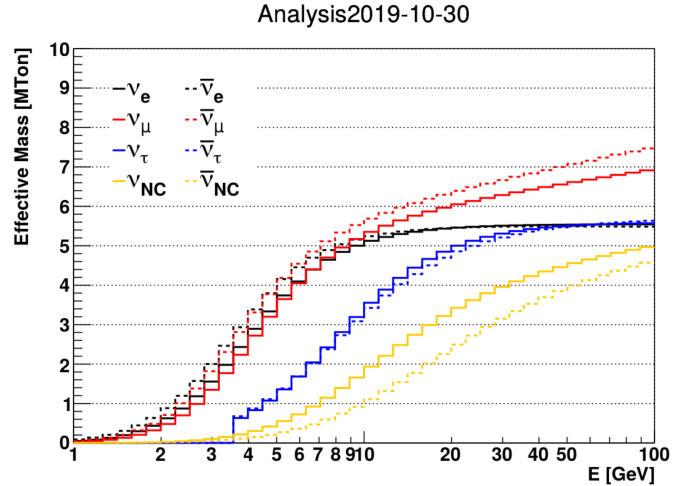


Figure 12.3: Detector effective mass derived from the Param-NMH parametrisation for the 20m ORCA detector. Figure obtained from [138].

12.2.3 | Event distribution histograms

The analysis uses a three dimensional binning of the events in the reconstructed quantities energy, cosine of the zenith angle, and EID class. In each bin i of the three dimensional distribution, $i \mapsto [E_j^{\text{rec}}; \cos \theta_k^{\text{rec}}; \text{class } c]$, the number of events N_i , is then

$$N_i = \left[\sum_{t \notin t_\tau} N_i^t(\theta_{23}, \Delta M^2, \dots) \right] + n_\tau \cdot \left[\sum_{t \in t_\tau} N_i^t(\theta_{23}, \Delta M^2, \dots) \right]. \quad (12.2)$$

It is obtained by summing over the contributions from twelve individual (anti-)neutrino types t ,

$$t = \{ \bar{\nu}_e^{\text{CC}}, \bar{\nu}_\mu^{\text{CC}}, \bar{\nu}_\tau^{\text{CC}}, \bar{\nu}_e^{\text{NC}}, \bar{\nu}_\mu^{\text{NC}}, \bar{\nu}_\tau^{\text{NC}} \}, \quad (12.3)$$

which depend on the oscillation and other systematic parameters.

The pure noise background and the atmospheric muon contribution are neglected in the sum,⁵ but could be included in general if available. They can be suppressed efficiently without significantly reducing the neutrino effective volume further, as has been shown in [Sec. 11.3.1](#). The n_τ parameter in [Eq. 12.2](#) represents the normalisation of the $\bar{\nu}_\tau$ appearance signal. A vanishing contribution of the second sum in case of $n_\tau \equiv 0$ corresponds to non-appearance of $\bar{\nu}_\tau$. In case $n_\tau \equiv 1$, the event number calculation reduces to the procedure for the NMO and other oscillation analyses.

CC-only vs. CC+NC $\bar{\nu}_\tau$ scaling There are two possible approaches to scale the n_τ parameter in the analysis.

Previous $\bar{\nu}_\tau$ appearance measurements have measured the normalisation of charged current interactions only (n_τ^{CC}) [100, 107, 104], or in addition included a normalisation measurement for charged and neutral current events ($n_\tau^{\text{CC+NC}}$) [106] of the $\bar{\nu}_\tau$ flux. In the case of a CC-only normalisation fit, only the CC contribution from ν_τ and $\bar{\nu}_\tau$ is scaled,

$$t_\tau^{\text{CC}} = \{ \bar{\nu}_\tau^{\text{CC}} \}, \quad (12.4)$$

⁵In ParamNMH they are currently not implemented, but there is no general obstacle in doing so. The event-based frameworks support inclusion of the background components.

12. Sensitivity of ORCA to $\bar{\nu}_\tau$ appearance

otherwise also the NC contribution is scaled,

$$t_\tau^{CC+NC} = \{\bar{\nu}_\tau^{CC}, \bar{\nu}_\tau^{NC}\}. \quad (12.5)$$

Due to the flavour-independent interaction for NC events, the detector response is identical for each flavour. As a consequence, oscillation does not affect the NC contribution and – as for other oscillation analyses – does not need to be accounted for in the case of CC-only scaling. The number of (anti-)neutrino types in Eq. 12.3 then reduces to eight in the default implementation of ParamNMH, six for the CC (anti-)neutrino flavours and two for the NC part.

If both CC and NC are scaled, the NC histograms are filled separately while calculating the oscillated fractions of each neutrino flavour. The $\bar{\nu}_\tau$ part is filled with the appropriate scaling of its normalisation.

To allow for such scaling, the functions for filling the NC histogram needed to be extended to include oscillation probabilities. In total, four scaling parameters now enter the code for the CC and NC contributions in the null and alternative hypotheses. In this work, the parameters are fixed in the code to test a specific normalisation, it is possible to free them during the fit. This feature is now included as a systematic without prior to account for a potential mis-modelling of the $\bar{\nu}_\tau^{CC}$ cross sections in the NMO study [2]. The impact on the NMO sensitivity turns out to be small.

12.2.4 | Fit statistic

One possibility to estimate the sensitivity to $\bar{\nu}_\tau$ appearance would be to evaluate the log-likelihood ratio distributions of the null and alternative hypothesis with respect to randomly generated pseudo experiments. This approach has been studied in detail for NMO in ORCA in Ref. [134]. For high CL, many⁶ datasets need to be generated. The datasets are drawn using the Poisson probabilities around the expected event counts for n_τ^{data} in each analysis bin. Since this approach is however computationally expensive⁷, the so-called Asimov dataset approach is used by ParamNMH instead. In the Asimov dataset approach the outcomes of the pseudo experiments are represented by only one average dataset, where every histogram bin content, is set to its expectation value.⁸ In this case the dataset is equivalent to the null hypothesis⁹, such that a fit is only necessary for the alternative hypothesis.

The test statistic minimised in the fit consists of a statistical and a systematic part, which are explained in the following.

⁶Depending on the desired CL up to $10^5 - 10^8$ might be necessary to accurately describe the tails of the distributions [134].

⁷For each of the pseudo experiments the null and the alternative hypothesis must be fit. In addition, many free parameters in the fit can lead to secondary minima. Hence, iteration of the minimisation from different initial values might be necessary.

⁸Note, that unlike for the pseudo experiments, where integer Poisson numbers are drawn, the expectation values are floating point numbers. Hence, this average dataset is not equivalent to a real measurement.

⁹Hence, the name n_τ^{data} which was already introduced earlier is appropriate to refer to the normalisation of the null.

Table 12.1: Values for the oscillation parameters used in the $\bar{\nu}_\tau$ appearance fit. The small and large mass-squared splittings correspond to $\Delta m^2 = \Delta m_{12}^2$ and $\Delta M^2 = |\Delta m_{23}^2|$, respectively.

parameter	null hypothesis value		prior
	NO	IO	
θ_{12}	33.82°		fixed
Δm^2 [eV ²]	7.39×10^{-5}		fixed
θ_{13}	8.60°	8.64°	$\pm 0.13^\circ$
θ_{23}	48.6°	48.8°	free
ΔM^2 [eV ²]	2.528×10^{-3}	2.436×10^{-3}	free
δ_{CP}	221°	282°	free

Table 12.2: Values for the fitted systematics used in the $\bar{\nu}_\tau$ appearance fit.

parameter	initial value	prior
$\nu_e/\bar{\nu}_e$ flux ratio	0	$\mu = 0, \sigma = 7\%$
$\nu_\mu/\bar{\nu}_\mu$ flux ratio	0	$\mu = 0, \sigma = 5\%$
$\bar{\nu}_e/\bar{\nu}_\mu$ flux ratio	0	$\mu = 0, \sigma = 2\%$
spectral tilt	0	$\mu = 0, \sigma = 5\%$
$\cos(\theta)$ tilt	0	$\mu = 0, \sigma = 2\%$
$\nu/\bar{\nu}$ ratio	0	$\mu = 0, \sigma = 3\%$
NC scale	1	$\mu = 1, \sigma = 10\%$
E -scale shift EM shower	0	$\mu = 0, \sigma = 5\%$
E -scale shift hadronic shower	0	$\mu = 0, \sigma = 6\%$
track channel norm	1	free
shower channel norm	1	free
middle channel norm	1	free

12. Sensitivity of ORCA to $\overleftrightarrow{\nu}_\tau$ appearance

12.2.5 | Statistical likelihood

In the fit, test statistic \mathcal{L}_0^2 is calculated in bins of reconstructed energy, cosine zenith angle and EID class, $i \mapsto [\cos \theta_j^{\text{rec}}; E_k^{\text{rec}}; \text{class}]$:

$$\mathcal{L}_0^2 = \sum_{\text{bins } i} \mathcal{L}_{0,i}^2 = -2 \sum_{\text{bins } i} \left(N_i^{\text{fit}} - N_i^{\text{data}} - N_i^{\text{fit}} \cdot \ln \frac{N_i^{\text{fit}}}{N_i^{\text{data}}} \right). \quad (12.6)$$

This test statistic corresponds to the logarithm of a Poisson likelihood with the usual factor two to equal a $\Delta\chi^2$ value.

In Eq. 12.6, the N_i^{data} and N_i^{fit} are the expected numbers of events in the i^{th} bin. They are calculated by summing over the different flavour types using Eq. 12.2 under the *null* and *alternative* hypothesis. Typically, the alternative hypothesis is fixed iteratively to different values of the $\overleftrightarrow{\nu}_\tau$ normalisation, n_τ^{fit} and fitted to the assumed data by minimising \mathcal{L}_0^2 over all relevant nuisance parameters in the calculation of the event numbers N_i^{fit} . For the assumed data all parameters and hence the event distribution is equivalent to the null hypothesis and the $\overleftrightarrow{\nu}_\tau$ normalisation is n_τ^{data} .

12.2.6 | Nuisance parameters with Gaussian priors

External constraints on the nuisance parameters can be taken into account by adding Gaussian priors of width σ_α to the test statistic:

$$\mathcal{L}_{\text{eff}}^2 = \mathcal{L}_0^2 + \sum_{\alpha \in \text{sys.params}} \left(\frac{p_\alpha^{\text{exp}} - p_\alpha^{\text{obs}}}{\sigma_\alpha} \right)^2. \quad (12.7)$$

Note that this sum corresponds to the logarithm of multiplicative Gaussian functions, where constant sum terms in the sum can be omitted.

As has been derived mathematically in Ref.[139], the median sensitivity in the Asimov dataset approach is

$$\tilde{S} = \sqrt{\mathcal{L}_{\text{eff}, \text{min}}^2}. \quad (12.8)$$

Nuisance parameters without prior are allowed to float freely without adding a penalty to the test statistic.

12.2.7 | Nuisance parameters accounted for in the $\overleftrightarrow{\nu}_\tau$ appearance fit

Oscillation parameters fitted with and without prior are tabulated in Tab. 12.1. The current global uncertainties on the oscillation parameters [59] allow to fix the oscillation angle θ_{12} and the small mass splitting $\Delta m^2 = \Delta m_{12}^2$ in the oscillation fit. The atmospheric oscillation parameters ($\theta_{23}, \Delta M^2 = |\Delta m_{23}^2|$) and the undetermined δ_{CP} are fitted unconstrained, such that only θ_{13} is fitted with prior. The $\overleftrightarrow{\nu}_\tau$ appearance results are produced assuming NO, since the dependence of the sensitivity on the true ordering is found small. This is verified by fitting with IO in Sec. 12.3.4.

In [Tab. 12.2](#) the used priors for the other fitted nuisance parameters are tabulated. These additional parameters account for modelling uncertainties in the fitted dataset and can be grouped as follows.

The first group of parameters accounts for the uncertainties on the detected neutrino flux [\[140\]](#). Three parameters reflect the uncertainties on the flux ratios between neutrino and anti-neutrino for $\bar{\nu}_e$ and $\bar{\nu}_\mu$ individually and the relative scaling between $\bar{\nu}_e$ and $\bar{\nu}_\mu$. Two additional skew parameters account for a possible tilt in the index of the energy spectrum and the ratio between upward-travelling and horizontal events.

The uncertainty in the cross section is accounted for by the second group. This group consists of an overall scale for the NC events and the total ratio between neutrinos and anti-neutrinos. As opposed to the priors in this study (see [Tab. 12.2](#)) they are fitted unconstrained in the results in the draft in Ref. [\[2\]](#). For $\bar{\nu}_\tau$ appearance, the difference in sensitivity is however only few-percent for the NC scale. The $\nu/\bar{\nu}$ ratio systematic has no impact on the fit result.

The third group accounts for uncertainties in the detector response.

The E -scale shift parameter accounts for the uncertainty in the absolute energy scale of the detector. It is influenced by the knowledge of the PMT efficiencies and the optical properties of sea water discussed in [Sec. 5.2](#). The PMT efficiencies are monitored continuously within the DOM by using the coincidence rate of ^{40}K . Several different methods to monitor the optical properties in-situ are under study. These comprise calibration measurements from ^{40}K coincidence rates on neighbouring DOMs, flashes of signal from optical beacons, or Cherenkov light from atmospheric muons and are projected to constrain the energy scale to a few percent [\[2\]](#). A 5% prior is therefore assumed here for this systematic.

A second energy scale parameter accounts for uncertainties in the light yield of hadronic showers and the 6% prior value is derived from the comparison of the simulation outputs of the Geisha and Fluka softwares [\[65\]](#).

Last, the overall normalisation of each class is allowed to vary freely. This accounts not only for a redistribution between the different event classes, but also leaves the overall normalisation free. The uncertainties from the background rejection and EID classifiers are not accounted for in more detail. To quantify the agreement of the classified true and simulated classifier fractions in more detail (e.g. as a function of reconstructed energy) than just by overall scaling factors remains a future task.

12.3 | Sensitivity study to $\bar{\nu}_\tau$ appearance with ORCA

In this section, the sensitivity of the ORCA detector to $\bar{\nu}_\tau$ appearance is evaluated. The assumed setup has an average 20 m horizontal spacing between DUs.

The analysis is performed in the two-dimensional plane of reconstructed energy and cosine of the zenith angle in three different event classes. A binning of 40 bins in logarithm of reconstructed energy, $1 \text{ GeV} < E_{\text{rec}} < 100 \text{ GeV}$, and 40 bins in cosine zenith angle, $-1 < \cos \theta_{z,\text{rec}} < 0$, is used. The event classes are defined using the track score, $\mathcal{S}_{\text{track}}$, of the EID in [Eq. 11.1](#) with the cut values taken from [Eq. 11.8](#) (showers: $\mathcal{S}_{\text{track}} \leq 0.3$, middle: $0.3 < \mathcal{S}_{\text{track}} \leq 0.7$, tracks: $\mathcal{S}_{\text{track}} > 0.7$). In the fit, nuisance parameters are accounted for as described in [Sec. 12.2.7](#).

12.3.1 | Resulting sensitivities for the full ORCA detector

Without any systematics, the sensitivity of the ORCA detector to measure the $\overleftrightarrow{\nu}_\tau$ flux normalisation can be calculated using Eq. 12.6 for a scan in n_τ^{fit} while leaving all nuisance parameters fixed to the values assumed in the *null* hypothesis. The result is shown in Fig. 12.4. The assumed data taking period is one year. In this case, the overall test statistic \mathcal{L}_0^2 (which can be seen as a χ^2 value, as axis labels in Fig. 12.4 suggest) is a sum of test statistics $\mathcal{L}_{0,c}^2$ over the EID classes c . The relative contribution from a class c ,

$$\text{rel. contribution of class } c : \frac{\mathcal{L}_{0,c}^2}{\sum_{j \in \{\text{classes}\}} \mathcal{L}_{0,j}^2} = \frac{\mathcal{L}_{0,c}^2}{\mathcal{L}_0^2}, \quad (12.9)$$

is presented in Fig. 12.4b. The overall significance is dominated by the shower class, contributing a relative 80% to the summed χ^2 for $n_\tau^{\text{fit}} = 0$, decreasing only marginally towards higher n_τ^{fit} . The remaining sensitivity comes from the middle class with only little contribution from the track class.

Including all uncertainties on the oscillation parameters in Tab. 12.1 and the other nuisance parameters in Tab. 12.2 in the fit reduces the overall significance by a factor ~ 2 . The influence of individual nuisance parameters considered in the fit is studied in more detail below, in Sec. 12.3.4. The resulting sensitivity for a scan in, n_τ^{fit} , is given in Fig. 12.5.

After one year of data taking, the normalisation n_τ can be constrained to $1_{-0.21}^{+0.23}$ ($1_{-0.29}^{+0.32}$) at a median 3σ confidence level (CL) in case of a combined CC+NC scaling (CC-only scaling). At 1σ CL, ORCA will be able to constrain n_τ to $\sim \pm 10\%$. This result can be set in relation with the relative half-width of the 1σ ranges, for current measurements,

$$w_{n_\tau}^{1/2} = \frac{1}{2} \frac{\Delta_{1\sigma}(n_\tau)}{n_\tau}, \quad (12.10)$$

where $\Delta_{1\sigma}(n_\tau)$ denotes the complete width of the measured 1σ range.

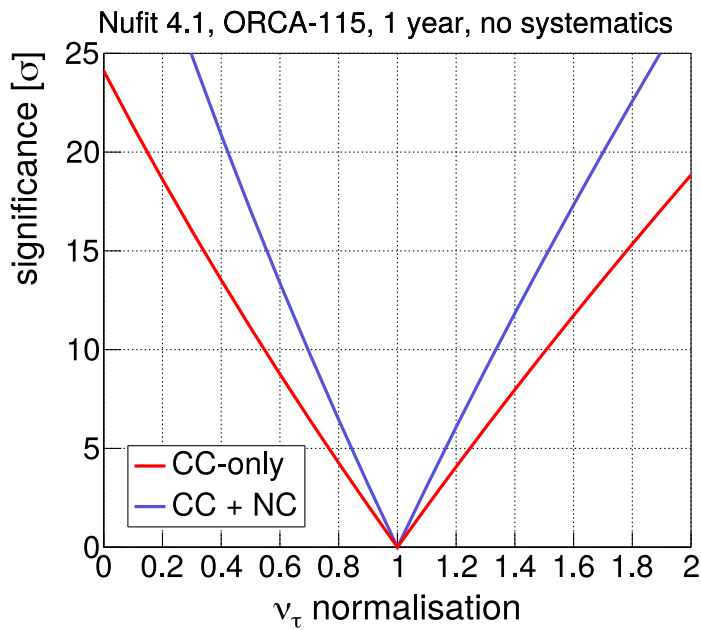
Compared to the limits from OPERA ($w_{n_\tau}^{1/2} = 40\%$) [107], Super Kamiokande ($w_{n_\tau}^{1/2} = 22\%$) [104] and the DeepCore extension of IceCube ($w_{n_\tau}^{1/2} = 57\%$ for CC-only) [106], the expected 1σ uncertainty is at least a factor two better than the current best measurement precision on n_τ .

The lines for 1, 3 and 5σ CL exclusion are shown as a function of data taking time in Fig. 12.6, assuming $n_\tau^{\text{data}} \equiv 1$ realised in nature. Already with two months of data taking with the full ORCA detector, an exclusion of the non-appearance of $\overleftrightarrow{\nu}_\tau$ (i.e. $n_\tau \neq 0$) is possible with a median significance of more than 5σ CL.

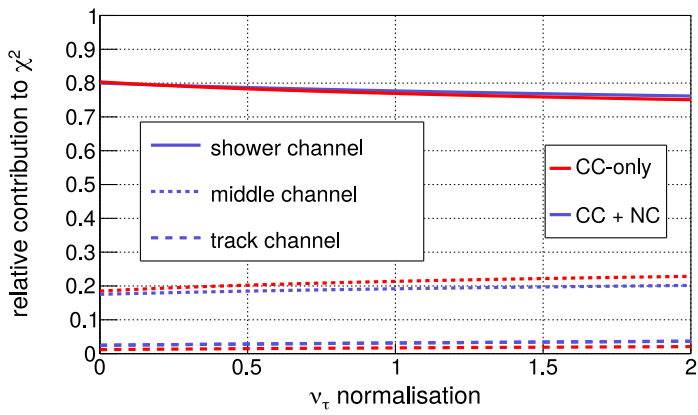
In contrast to the existing $\overleftrightarrow{\nu}_\tau$ appearance measurements, and in particular to OPERA, event statistics are high in ORCA. Systematic errors will therefore rapidly dominate the uncertainty of the measurement. This is visible in the asymptotic behaviour of the significance lines.

12.3.2 | Non-unitary mixing: the $n_\tau < 1$ scenario

A flux normalisation of $n_\tau = 1$ is expected for unitary mixing, and a correct modelling of the $\overleftrightarrow{\nu}_\tau^{\text{CC}}$ cross section. It is possible to evaluate the sensitivity if in reality the normalisation is assumed to deviate from $n_\tau^{\text{data}} = 1$.



(a)



(b)

Figure 12.4: ORCA sensitivity without any systematics to $\bar{\nu}_\tau$ appearance for a data taking period of one year.

Panel (a): Significance for a scan of the $\bar{\nu}_\tau$ normalisation, n_τ .

Panel (b): Individual contributions from the three channels to the combined \mathcal{L}_0^2 (named χ^2 here).

12. Sensitivity of ORCA to $\bar{\nu}_\tau$ appearance

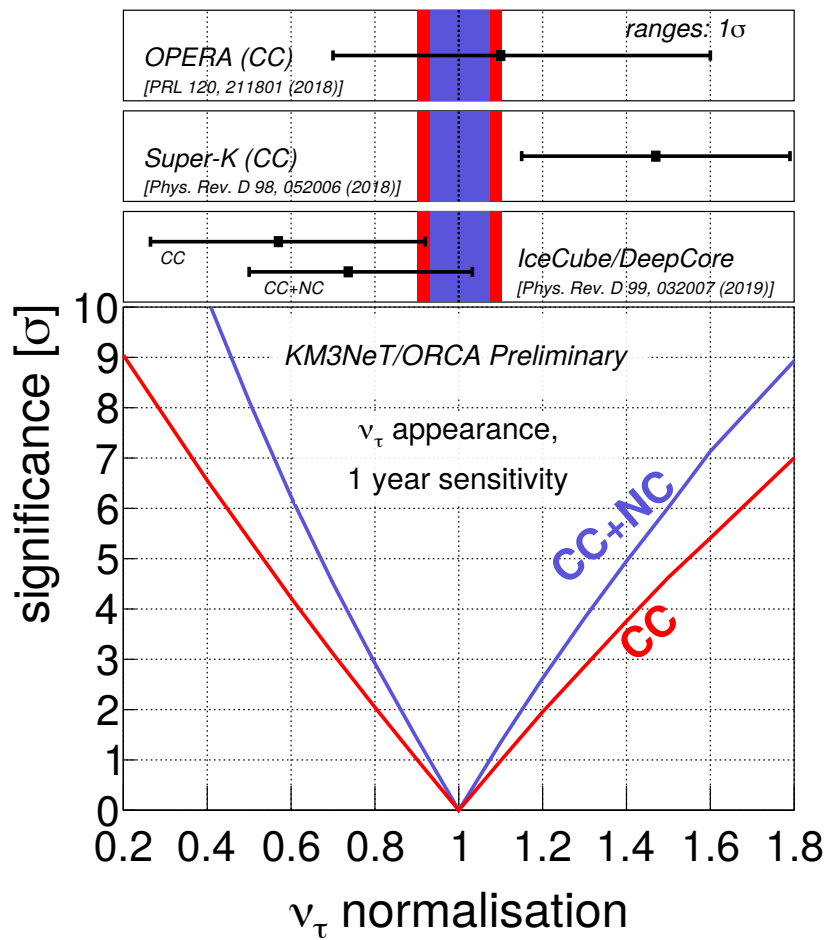


Figure 12.5: Sensitivity for ORCA after one year of operation to measure the $\bar{\nu}_\tau$ normalisation if the true value realised in nature is unity. The derived 1σ ranges for CC-only and combined CC+NC scaling are drawn in the top panels to compare with results from OPERA [107], Super-Kamiokande [104], and IceCube [106].

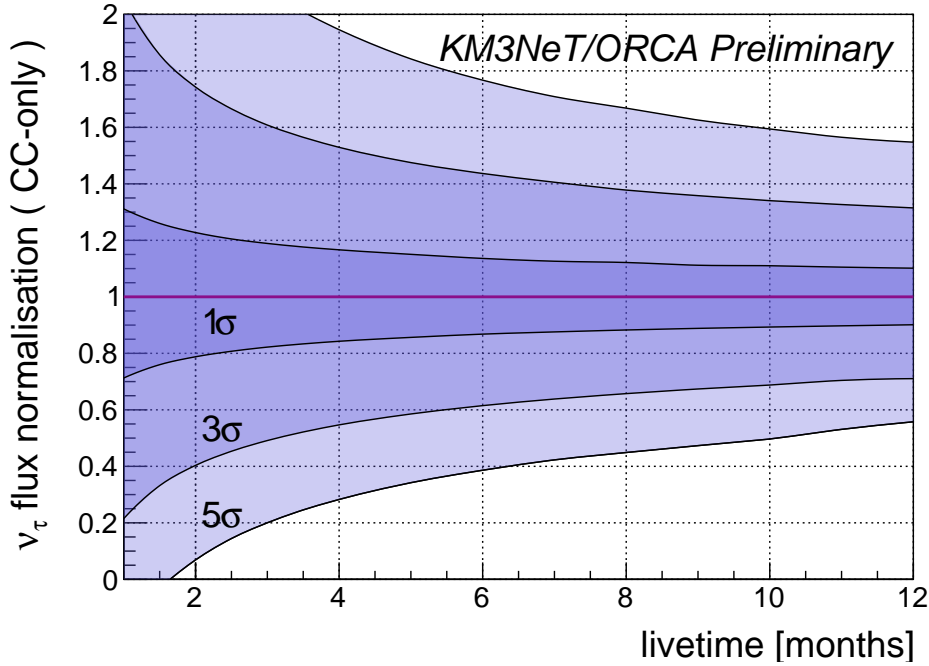


Figure 12.6: Sensitivity of the ORCA detector to $\bar{\nu}_\tau$ appearance as a function of operation time. A $\bar{\nu}_\tau^{\text{CC}}$ normalisation of one is expected in the case of unitary mixing and correct modelling of the cross section.

In case additional today unidentified flavours of neutrinos are present, part of the flux might oscillate into these channels. Consequently, the measured normalisation of the $\bar{\nu}_\tau$ flux will be smaller than the expectation, i.e. $n_\tau^{\text{data}} < 1$. Also, the current theoretical uncertainties on the $\bar{\nu}_\tau^{\text{CC}}$ cross-section are still sizeable and not strongly constrained experimentally. Likewise, normalisations $n_\tau^{\text{data}} > 1$ could be considered. However, values larger than one imply, that additional events appear on top of the initial atmospheric flux, which is not easy to motivate. If such a value is measured, it is likely that the currently assumed $\bar{\nu}_\tau^{\text{CC}}$ cross section is underestimated.

The sensitivity to measure $n_\tau < 1$ has been analysed for the CC-only case using Param-NMH for $n_\tau^{\text{data}} \in \{0.7, 0.8, 0.9\}$. The resulting exclusion curves are presented in Fig. 12.7. Given that the KM3NeT components are designed to be operated for at least a decade, a 3σ CL evidence for incompatibility of the measured data with $n_\tau = 1$ is possible within manageable (2.5 years operation with 100% of the livetime available for analysis) data taking periods if $n_\tau^{\text{data}} \leq 0.8$.

12.3.3 | CC-only vs. combined CC+NC scaling

Up to this point, all results have been presented separately for either CC-only or combined CC+NC scaling of the $\bar{\nu}_\tau$ normalisation. This is in line with the results published by the other experiments. Given the tighter constraint on the normalisation expected from ORCA, the question arises, whether ORCA can distinguish between the two scenarios. The motivation behind this study is that the error on the assumed $\bar{\nu}_\tau^{\text{CC}}$ cross section might be large; up to $\sim 20\%$ (see Sec. 6.2.1) and does affect the CC contribution only. In this section we may assume

12. Sensitivity of ORCA to $\vec{\nu}_\tau$ appearance

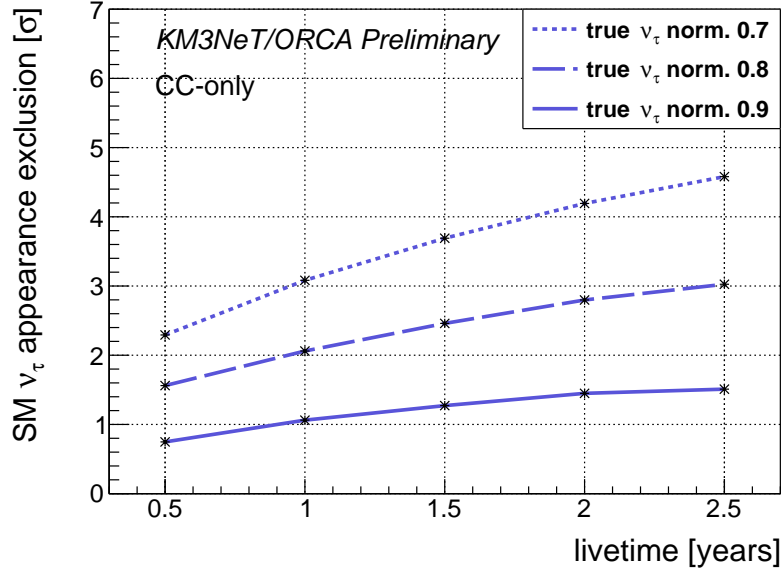


Figure 12.7: Sensitivity to exclude non-unitarity as a function of operation time for a 115 DU ORCA detector. Oscillation parameter uncertainties and other systematics as listed in [Tab. 12.1](#) and [Tab. 12.2](#) are included while assuming NO.

non-unitarity leads to an overall combined CC+NC scaling. Under these circumstances it could happen that:

1. A deviation from unity in the normalisation is measured, but the cause (mis-modelled cross section or non-unitary mixing) cannot be identified.
2. The measured normalisation is compatible with unity, but a mis-modelled cross section hides an actual non-unitary mixing.

To investigate the distinction power for ORCA, two scaling parameters are used,

- n_τ^{overall} : this overall scaling factor affects both the $\vec{\nu}_\tau^{\text{CC}}$ and the $\vec{\nu}_\tau^{\text{NC}}$ component
- n_τ^{xCC} : an additional scaling factor affecting exclusively the $\vec{\nu}_\tau^{\text{CC}}$ component

While the scaling of the NC component is then just $n_\tau^{\text{NC}} = n_\tau^{\text{overall}}$, the CC component is affected by both factors, such that in total $n_\tau^{\text{CC}} = n_\tau^{\text{overall}} \times n_\tau^{\text{xCC}}$.

The result of a two dimensional scan in n_τ^{overall} and n_τ^{xCC} is given in [Fig. 12.8](#). A data taking period of five years has been assumed to reduce the contribution from the statistical component to the median sensitivity \tilde{S} for exclusion. The Asimov data sample is set to $(n_\tau^{\text{overall}}, n_\tau^{\text{xCC}}) = (1, 1)$.

An elongated minimum is found. Due to the NC component in the fitted event distributions, the minimum shows a pull towards $n_\tau^{\text{overall}} \rightarrow 1$ with respect to the $n_\tau^{\text{xCC}} \times n_\tau^{\text{overall}} = n_\tau^{\text{CC}} \equiv 1$ line.

Given the wide extension of the exclusion bands in [Fig. 12.8](#) even for $\tilde{S} = 1\sigma$, it must be concluded that while the sensitivity of ORCA to n_τ is high, a distinction between a mis-

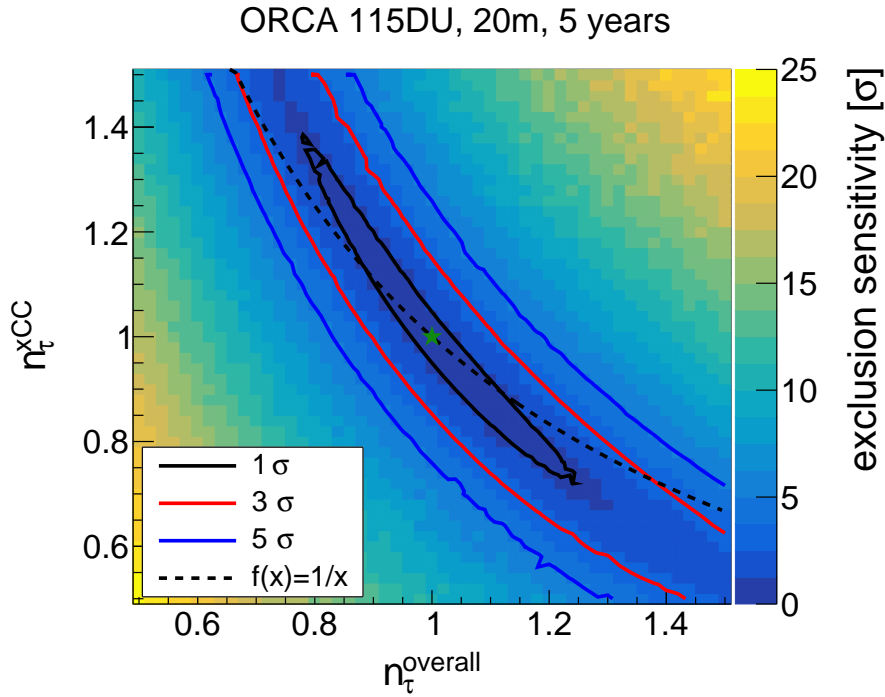


Figure 12.8: Sensitivity to distinguish deviations from unity in the overall $\bar{\nu}_\tau$ normalisation n_τ^{overall} and a scaling affecting exclusively the $\bar{\nu}_\tau^{\text{CC}}$ component, n_τ^{xCC} . Sensitivity corresponds to five years of operation with a full ORCA detector, and a true value of (1, 1).

modelling of the $\bar{\nu}_\tau^{\text{CC}}$ cross section and an overall scale of the oscillated $\bar{\nu}_\tau$ flux in this model-independent approach remains a challenge. To overcome this,

- uncertainties on the cross section side need to be reduced by additional theoretical calculations for $\bar{\nu}_\tau^{\text{CC}}$ and/or supplemental measurements of the structure functions in $\bar{\nu}_\tau^{\text{CC}}$ interactions (as proposed e.g. by SHiP [95, c.7.1]).
- the model-independent $\bar{\nu}_\tau$ appearance measurement can serve as a hint to find discrepancies between data and the assumed model. For $n_\tau \neq 1$, model-dependent searches for new physics (e.g. oscillation in the 3 (active) + 1 (sterile) neutrino model) need to follow.

12.3.4 | Influence of nuisance parameters

Relative importance of nuisance parameters

The importance of individual nuisance parameters considered in ParamNMH is studied in this section. To compare the relative impact of individual nuisance parameters on the fit result, scans in n_τ are performed while fixing each of the parameters, denoted ϑ , to its true value used to generate the Asimov dataset. The same procedure is repeated while fixing groups of nuisance parameters. The relative change in width of the 3σ interval in the n_τ profile with respect to when all parameters are fitted with their respective priors is given as

$$I(\vartheta) = \frac{n_\tau(3\sigma|n_\tau > 0, \vartheta \text{ fitted}) - n_\tau(3\sigma|n_\tau < 0, \vartheta \text{ fitted})}{n_\tau(3\sigma|n_\tau > 0, \vartheta \text{ fixed}) - n_\tau(3\sigma|n_\tau < 0, \vartheta \text{ fixed})} - 1. \quad (12.11)$$

12. Sensitivity of ORCA to $\vec{\nu}_\tau$ appearance

This quantity is a measure for the impact of the parameter (or set of parameters) ϑ under study on the fit result. The results for the $I(\vartheta)$ determined for all different nuisance parameters are summarised in Fig. 12.9. These can be grouped into oscillation parameters (red), atmospheric flux (atmospheric flux ratios and flux skews; blue), the overall neutrino/antineutrino ratio (green), and scale systematics (yellow). The $I(\vartheta)$ for these groups are also shown in Fig. 12.9.

The largest impact of the oscillation parameters is contributed by the large mass-squared splitting, $I(\Delta m^2) = 5\%$. This dominates the impact from fixing all oscillation parameters ($I(\text{oscillation}) = 7\%$). The three flux ratio parameters in the atmospheric flux uncertainties have only a small impact ($I(\text{flux ratios}) = 3\%$) compared to the tilts ($I(\text{flux tilts}) = 11\%$) consisting of the tilt in energy spectrum and up-to-horizontal ratio. The latter systematic ($I(\cos(\theta) \text{ skew}) = 11\%$) is the dominant systematic according to the used I -metric by itself and dominates the overall flux systematics ($I(\text{flux}) = 16\%$), making it the group of systematics with the highest impact on the fit sensitivity.

The overall $\nu/\bar{\nu}$ ratio has negligible impact on its own, although it must be noted that fixing single parameters can lead to an absorption in others, in this particular case the $\vec{\nu}_e$ and $\vec{\nu}_\mu$ ratios, if priors allow.

The scalings of the NC component and the energy scales to accommodate uncertainties in the detector response after the flux systematics all have a noticeable impact. In sum, they are the second most important group of systematics ($I(\text{detector response}) = 7\%$). After the up-to-horizontal tilt and Δm^2 the two detector systematics show the largest impact on the fit result, $\sim 3\text{--}4\%$ individually.

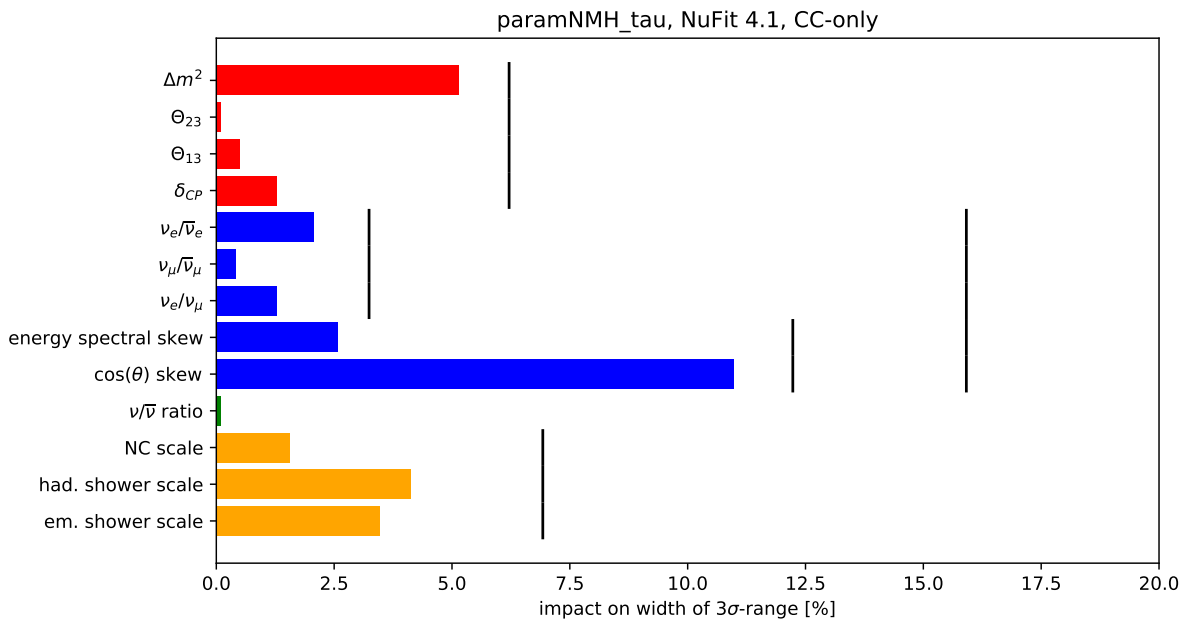


Figure 12.9: Influence of fixing individual considered nuisance parameters in the $\vec{\nu}_\tau$ appearance sensitivity for one year and CC-only. Values represent the relative change to the width of the 3σ interval. Colours indicate groups of systematics. Vertical lines correspond to the relative change when fixing all associated nuisance parameters.

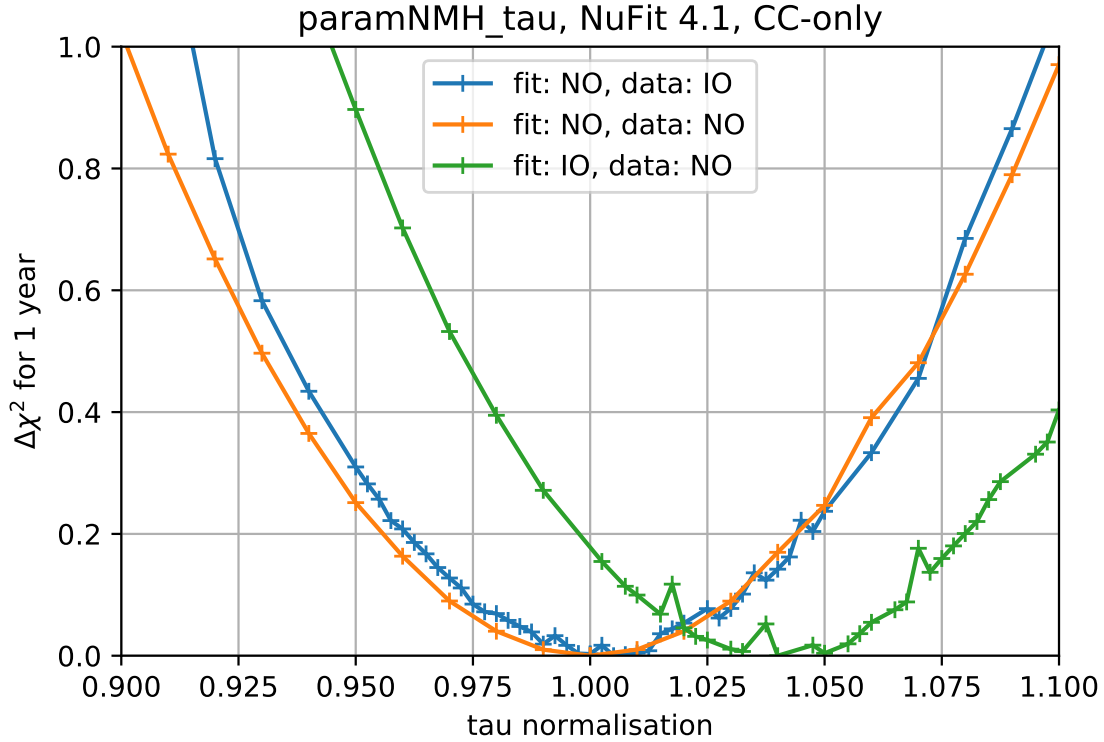


Figure 12.10: Robustness against an unknown neutrino mass ordering. $\Delta\chi^2$ is shown as a function of n_τ^{CC} for the default scenario of normal ordering (NO) in both Asimov dataset and fit, and with one of either being inverted ordering (IO).

Robustness against a wrong assumption of the NMO

The above results have been produced assuming NO both for the Asimov dataset and in the fit. However, given the high sensitivity of ORCA to $\bar{\nu}_\tau$ appearance, the NMO is likely still unknown at the time when $\bar{\nu}_\tau$ appearance can be measured. To verify that the stated results do not depend on a prior knowledge of the true NMO, the scan in n_τ is repeated while switching to the wrong assumption in both the Asimov dataset and the fit. The result is shown in Fig. 12.10. The small jumps to higher $\Delta\chi^2$ values indicate that a secondary minimum is found in the fit. In general this unsteady behaviour can be avoided by rerunning the fit starting from the result of the adjacent n_τ^{fit} . This has not been done here as these points do not impact the conclusions drawn from this plot.

In both cases the shape of the $\Delta\chi^2$ (corresponding to \tilde{S}^2 in Eq. 12.8) curve is similar to the default (fit=NO, data=NO). Only for IO assumed during the fit, the minimum is shifted by 4% to higher normalisation. When fitting with NO, both position of the minimum and shape are very similar for an Asimov dataset of either ordering. The robustness against an unknown ordering measurement is therefore confirmed and no obstacle for $\bar{\nu}_\tau$ appearance as an early physics result of ORCA.

12. Sensitivity of ORCA to $\bar{\nu}_\tau$ appearance

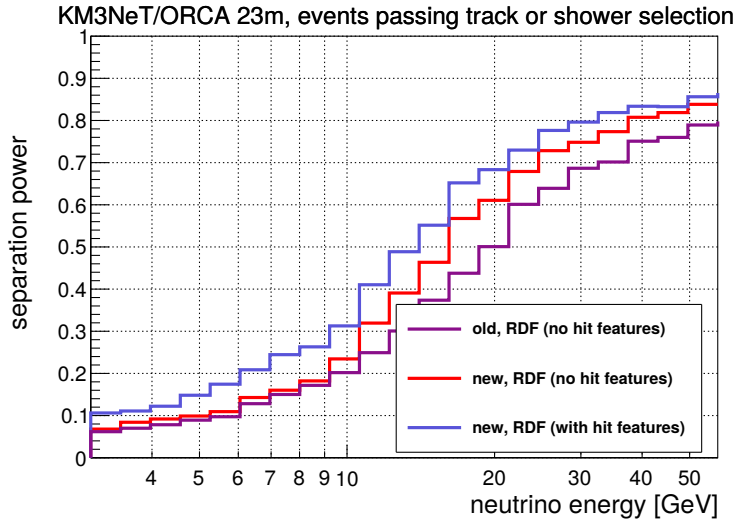


Figure 12.11: Comparison of the classifier performance in terms of the separation power metric as defined in Eq. 11.7 for the 7 DU sub-array. 'old' refers to the EID output used in the oscillation results described here, 'new' to the final RDF setup equivalent to the one described in Sec. 11.4.

12.4 | Tau-neutrino appearance with an early stage sub-array

In the previous section, it was shown that $\bar{\nu}_\tau$ appearance can be measured without knowing true NMO, and that ORCA is sensitive to achieving competitive sensitivity compared to current measurements within the first months of operation. This makes $\bar{\nu}_\tau$ appearance a promising measurement already at an early stage of construction. In a similar way as the Monte Carlo simulations for 20 m, the complete set of simulated data (neutrinos, atmospheric muons and pure noise) for seven DUs has been classified. The classed sample of selected neutrino events was prepared to be used in oscillation analyses. The main results for the early phase sensitivity studies based on the 7 DU simulations were presented in Ref. [9] and included the sensitivity to $\bar{\nu}_\tau$ appearance analysed within the scope of a Master's thesis [10]. The main results of this work are summarised here.

The analysis framework SWIM was used with two event classes, where a track score cut at 0.6 divided the sample into shower- and track-like events. The $\bar{\nu}_\tau$ appearance was studied by scaling the CC component, n_τ^{CC} . A cross check using MONA with three analysis classes and $n_\tau^{\text{CC+NC}}$ scaling yielded consistent results [141]. The MONA analysis used the same setup as for the other oscillation results shown in Ref. [9]. As opposed to the $\bar{\nu}_\tau$ appearance analysis presented in this thesis, both 7 DU analyses did not include the $\cos(\theta_z)$ tilt and the two energy scale parameters to account for the detector systematics, which were found to impact the sensitivity significantly in Sec. 12.3.4.

Even with seven DUs, the pure-noise background component can be rejected efficiently with the RDF classifier. After a cut on the noise score parameter, 0.6 pure-noise events per day are expected to remain in a sample of 33 neutrino candidates [10]. The impact for $\bar{\nu}_\tau$ appearance from this component is small, in particular because the remaining pure noise events are reconstructed below ~ 5 GeV. The background from atmospheric muons on the other hand is more serious and can only be suppressed to a 7% contamination in the final neutrino sample. Once in-situ data will be analysed, this background will need to be modelled carefully with extensive MC simulations. The neutrino EID for 7 DUs shows a less pronounced improvement if trained including the additional hit-based training features described in Sec. 11.2.4 compared to the full 115 DU ORCA detector (see Fig. 12.11). This is shown in Fig. 12.11, where the

Figure 12.12: Fractions of events in the 7 DU analysis sample classified as track (track score > 0.6). Different interaction channels are shown as a function of energy. Figure taken from [10].

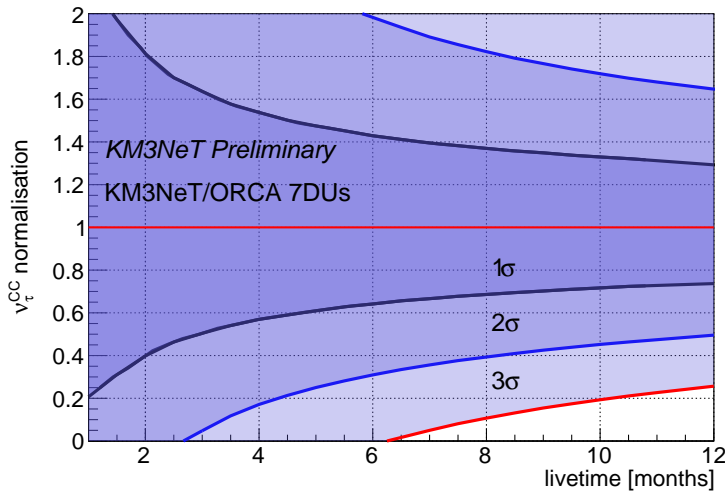
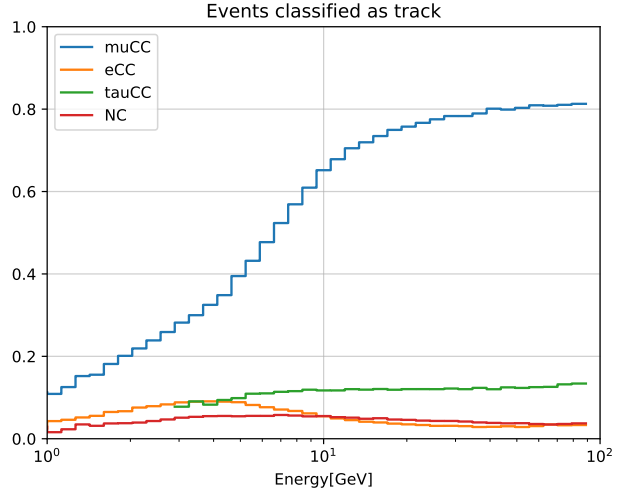


Figure 12.13: Sensitivity to $\bar{\nu}_\tau$ appearance with a 7 DU sub-array of ORCA. Figure prepared for Ref. [9] using data from [10].

intermediate classification output used for the 7 DU studies [9, 10] is compared in terms of the separation power metric (Eq. 11.7) with the final RDF setup equivalent to the one described in Sec. 11.4. In particular, the separation power increases more slowly and only levels off at 80% at 50 GeV (the full ORCA detector reached a plateau value of 97% already for ~ 20 GeV). This is expected because the small sub-array does not allow for events fully contained within the instrumented volume. The fractions of events classified as track for the event sample used in the 7 DU analysis are given in Fig. 12.12. With 80% of the $\bar{\nu}_\mu^{CC}$ classified as track in the plateau, the fraction of $\bar{\nu}_\tau^{CC}$ classified as tracks corresponds to $\sim 0.8 \times 0.18$ and matches the expected fraction of τ^\pm decaying to μ^\pm .

The resulting sensitivity to measure $\bar{\nu}_\tau^{CC}$ appearance with 7 DUs as a function of data-taking time is shown in Fig. 12.13. With a data sample comprising six months of livetime, $\bar{\nu}_\tau$ non-appearance, i.e. n_τ^{CC+NC} is expected to be excluded at the 3σ CL. After one year the normalisation can be constrained to within $n_\tau^{CC} = 1_{-0.26}^{+0.28}$ at 1σ CL. This sensitivity is of similar size as the current measurement by IceCube/DeepCore [106] (c.f. Sec. 12.3).

Given this result, a $\bar{\nu}_\tau$ appearance measurement is judged feasible with a small 7 DU setup based on simulated data.

13 Conclusion on Part II and outlook for measuring $\bar{\nu}_\tau$ appearance in-situ

The presented $\bar{\nu}_\tau$ appearance analysis is based on Monte Carlo simulations that were generated for a realistic detector configuration, as it is currently planned for deployment. This configuration aims for reaching the previously determined optimal spacing for ORCA [1] whilst meeting all constraints from deployment side. Extensive simulation sets have been produced with an average spacing of 23 m and 20 m between the ORCA Detection Units (DUs).

Apart from the $\bar{\nu}_\tau$ appearance study, which extends the physics scope of ORCA, the most important contributions within this part are the optimisation of the trigger, [Sec. 9](#), and the further development of the event identification, [Sec. 11](#).

The optimisation of the additional low-energy trigger MXShower lowers the threshold of the instrument such that about a factor 2 (1.4) more neutrino events are triggered at 3 GeV (6 GeV) for $\bar{\nu}_\mu^{\text{CC}}$ and $\bar{\nu}_e^{\text{CC}}$. The increase is even higher for $\bar{\nu}_\tau^{\text{CC}}$ and $\bar{\nu}^{\text{NC}}$. The loss in neutrino efficiency over the livetime of ORCA due to missing or vetoed channels has been evaluated based on the data from the first installed DUs. It is found sizeable, $\sim 10\%$ for the energies relevant to determine the neutrino mass ordering (~ 5 GeV). The sensitive region for $\bar{\nu}_\tau^{\text{CC}}$ appearance is at higher energies, such that this loss at the threshold can be neglected.

The event identification has been improved thanks to the inclusion of an additional set of hit-based features in the training. The gain can be quantified in two ways: In terms of the μ^\pm energy needed for clear identification as track-like, 20% less energy (= track-length) is required when including the hit-based features. In terms of neutrino energy, the turn-on of the event identification is 25% faster (5.5 GeV instead of 7.3 GeV for the 20 m horizontal spacing configuration) when including hit-based features. A similar size of improvement is achieved, when DUs can be deployed with an average 20 m spacing instead of 23 m between DUs. The former is deemed feasible with the experience from the first deployed DUs. Since the classification tasks are now separated into binary decisions (neutrino vs. pure noise, neutrino vs. atmospheric muon, track vs. shower), the backgrounds can be suppressed individually to a few percent of the neutrino rate. Simulated pure noise events have been included in the full analysis chain for the first time. The binary decision between tracks and showers allows to define multiple event classes, such that meanwhile an additional middle class to absorb ambiguous events is used in most of the recent analyses.

Since the output of the classed event samples are used also for other oscillation analyses, the detector performance is described as part of the paper draft ‘Determining the Neutrino Mass Ordering and Oscillation Parameters with KM3NeT/ORCA’ [2]. The sensitivity study for the determination of $\bar{\nu}_\tau$ appearance is also part of this draft.

Using the classed output, the sensitivity to $\bar{\nu}_\tau$ appearance has been studied for ORCA in [Sec. 12](#). With respect to current measurements, the large effective mass and low energy turn-on of ORCA provides unprecedented statistics of ~ 3300 $\bar{\nu}_\tau^{\text{CC}}$ events remaining in the analysis

event sample per year. The sensitivity of ORCA is high enough to probe deviations from the standard model expectation for the $\bar{\nu}_\tau^{\text{CC}}$ cross section in combination with the $\bar{\nu}_\tau$ normalisation expected in the case of unitary 3×3 neutrino oscillations with $\pm 30\%$ accuracy at the 3σ CL. Within one year of data-taking with the full detector, the current $\sim 10\%$ theoretical uncertainties on the $\bar{\nu}_\tau^{\text{CC}}$ cross sections are in reach. The $\bar{\nu}_\tau$ appearance study extends the physics scope of the experiment with respect to what has been shown before for an idealised detector.

Motivated by the high sensitivity to $\bar{\nu}_\tau$ appearance of the full detector, $\bar{\nu}_\tau$ appearance was also studied for a small sub-array [10]. Exclusion of non-appearance is possible with high confidence after half a year of data-taking with few DUs. The study was based on the provided classed simulation set comprising only seven DUs.

The prepared classed analysis samples for 115 DUs and 7 DUs can be and are used for further sensitivity analyses. While there are a few remaining improvements that can be made also for the full detector, such as a revision of the currently used energy estimate for tracks¹, most of the analysis efforts will need to shift to the analysis of the data taken in-situ with the first deployed DUs.

ORCA has been taking data with six DUs for half a year. Using the track reconstruction output, it has been shown that a clean neutrino sample can be selected even when using only a single DU [142], and that $\bar{\nu}_\mu$ disappearance is already evident in 4 DU data [143]. Before a measurement of the $\bar{\nu}_\tau^{\text{CC}}$ appearance will be possible, the agreement of data with simulations and the ability to select a clean analysis sample needs to be studied in depth, especially for the shower reconstruction algorithm. At the moment, run-by-run simulations have not yet been prepared for the shower reconstruction and compared with real data. The level of agreement between measured and simulated data needs to be evaluated thoroughly before the features can be used for classification. The performance of the event identification must then be verified on real data. Likely, the systematic of the event identification, which is only accounted for by a relative scaling of event numbers between the classes for the complete detector, will need to be quantified in more detail. Once these tasks have been accomplished ORCA is expected to provide a first $\bar{\nu}_\tau$ appearance measurement based on the currently installed six DUs taking data.

¹as mentioned in [Sec. 11.6](#), and underlined through the findings with the alternative Deep Learning based reconstruction framework in Ref. [125].

13. *Conclusion on Part II and outlook for measuring $\overleftrightarrow{\nu}_\tau$ appearance in-situ*

Part III

All-flavour search for a Galactic neutrino-flux from the Fermi Bubbles with ANTARES



In this part, data recorded with the ANTARES neutrino telescope between 2008 and 2015 are analysed to search for neutrino emission from the ‘Fermi Bubbles’ (FB), two giant lobe-shaped structures above and below the centre of the Milky Way, the Galactic Centre. The FB are a bright emission regions of high energy γ -rays, but their origin remains unknown. Both hadronic and leptonic generation scenarios have been proposed, while an associated neutrino emission is present in the former but absent in the latter case.

The presented work is an all-flavour search combining individual analyses for track- and shower-like event signatures.

The current knowledge about the FB and the observed γ -ray flux are summarised in [Sec. 14](#). In [Sec. 15](#), the analysis method and a derivation for the expected neutrino flux are provided. Then, [Sec. 16](#) gives an overview of ANTARES data-taking and the used reconstruction and simulation chains. At the end of the section, the data-set used in the analysis is selected.

[Section 17](#) presents the search for neutrino emission from the FB at high latitudes. In [Sec. 18](#), the dataset and event-selection used for the analysis at high latitudes is used to provide a first estimate of the ANTARES sensitivity for neutrino emission from a central box region of enhanced γ -ray emission. This latter study is motivated by a more recent γ -ray analysis of the FB near the Galactic Centre. [Section 19](#) concludes on the results of this part..



*And there were so many fewer questions when stars were still
just the holes to heaven... – Jack Johnson*

14 The Fermi Bubbles – giant lobes of γ -rays and neutrinos?

The Fermi Bubbles (FB) are two giant lobe-shaped areas of bright high-energy γ -ray emission extending 50° above and below the Galactic Centre (GC). The structure is depicted in Fig. 14.1 and was first observed in 2010 [144, 145] in data recorded by the Fermi-LAT instrument on the Fermi Gamma-Ray Space Telescope. Spatially correlated structures have also been observed at other wavelengths, namely in the radio [146], the microwave [147] and – towards the bases of the FB – in the X-ray [148] bands.

14.1 | Possible origins of the Fermi Bubbles

Today, their origin is still not unambiguously identified. Most of the proposed emission scenarios suggest γ -ray generation by either leptons [150, 151, 152] or hadrons [153, 154, 155]. In hadronic scenarios, high energy protons, diffused from the environment of the GC, produce charged mesons and subsequently γ -rays upon interaction with the ambient gas. In this case the decays of (mainly) charged pions give rise to an accompanying neutrino flux that can be searched for with large-volume neutrino detectors like the ANTARES telescope.

In case the origin is leptonic, the γ -ray flux originates from synchrotron emission off high energy e^\pm and lacks a neutrino counterpart. Ultimately, (non-)observation of a neutrino flux from the FB can therefore constrain the hadronic component of the γ -ray flux.

The symmetric shape of the two lobes with respect to the central region of the Galactic disk suggests that they might originate either from the central supermassive black hole Sgr A* itself or from nearby. A comprehensive list of proposed models would be too long. However, in order to gain an impression it is helpful to outline some intuitive explanations for the FB. While Sgr A* has not been active in recent times, former periods of matter accretion could have led to jet-like emission. The latter has been observed in galaxies with an AGN (active

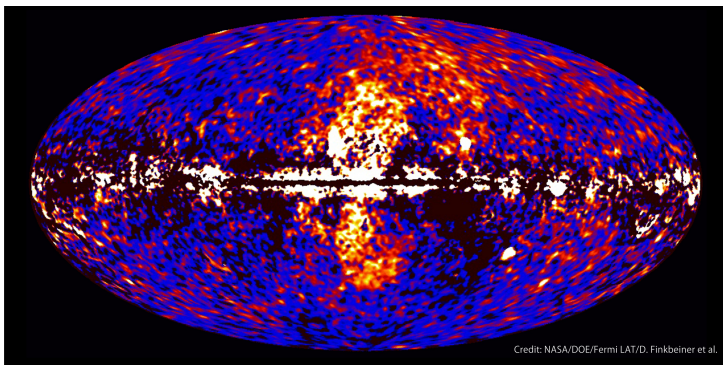


Figure 14.1: The Fermi Bubbles as seen in γ -rays by Fermi-LAT. Figure taken from [149].

14. The Fermi Bubbles – giant lobes of γ -rays and neutrinos?

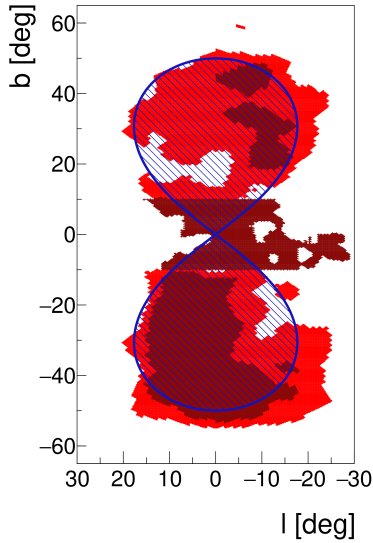


Figure 14.2: Shapes of the Fermi Bubbles' templates observed at high and low latitudes by Fermi-LAT [158, 159]. The hour-glass shape used in the neutrino analysis is indicated in blue. Own figure taken from [12].

galactic nucleus) together with similar structures as the FB [156, 145]. Other scenarios for an origin from Sgr A* itself have also been proposed, such as e.g. outflows of hot plasma, potentially driven by periodic disruptions of stars that were accreted onto the black hole [157]. Alternatively, regions near the GC may have undergone periods of intense star formation followed by a later increased rate of supernova explosions. These may cause a hot wind driving relativistic particles away from the GC [153]. The extension of the lobes in perpendicular direction with respect to the disk in that case is justified by the magnetic field distribution in the Galactic disk [155].

14.2 | Gamma-ray emission measured by Fermi-LAT

The γ -ray flux measured outside the disk region at latitudes $|l| > 10^\circ$ is to first order uniformly bright throughout the extension of the bubbles. When discovered, a hard spectrum close to $\approx E^{-2}$ with no clear cut-off up to several hundred GeV was seen by Fermi-LAT [145]. With higher statistics and after more detailed analysis, either a sub-TeV cut-off or a significant softening at high energies is meanwhile preferred [158]. The measured spectrum is shown in Fig. 15.2 later, when the γ -ray flux assumption is quantified, from which the expected neutrino flux is derived and extrapolated.

The updated γ -ray analysis at high latitude identified also a tentative flux-intense ‘cocoon’ shape region [158]. Further analysis of the ‘cocoon’ does however not favour a jet-like emission scenario.

More recently, the FB have also been analysed at latitudes below 10° [159], which requires more careful modelling of the different components of γ -ray emission in the disk. The regions of the γ -ray emission at high and low latitudes and the suggested ‘cocoon’ region are shown in Fig. 14.2. For the plotted low-latitude FB template, a relatively hard $\sim E^{-2.1}$ spectrum with no cut-off up to several 100 GeV was observed. Also, the γ -ray flux in the low-latitude region is three times higher compared to the rest of the bubbles. This might be a hint for a change in composition of the FB towards low latitudes.

This observation is confirmed in a dedicated analysis of the FB template component around

14. The Fermi Bubbles – giant lobes of γ -rays and neutrinos?

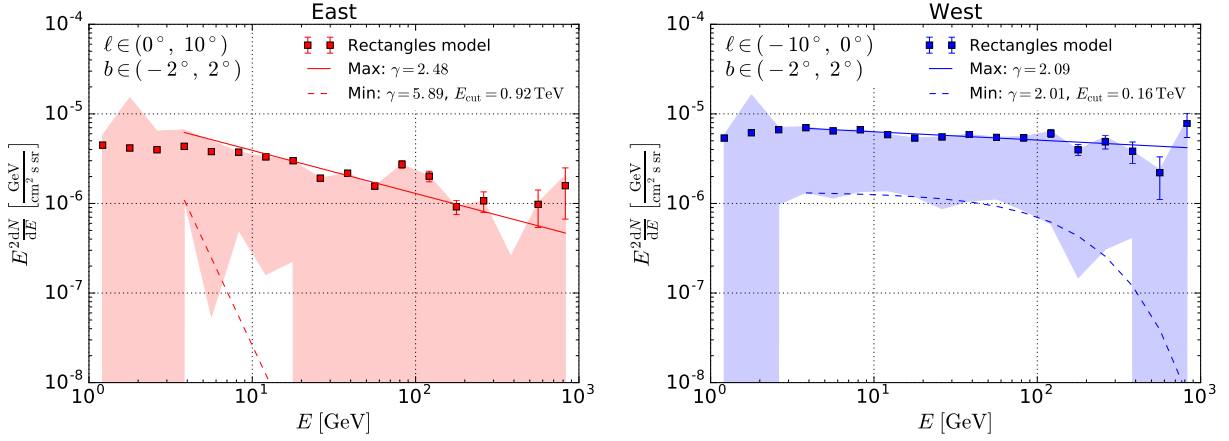


Figure 14.3: Comparison of the FB low-latitude spectral energy densities in boxes of $|b| < 2^\circ$ and $0^\circ < |l| < 10^\circ$ left and right of the GC. The shaded areas show the envelope of the FB’s spectra for a range of foreground models. Figure taken from [160].

the GC [160]. The dedicated analysis finds indication for an offset of the emission region with respect to the GC. This is visualised in Fig. 14.3, where enhanced emission is observed for $l < 0^\circ$ compared to $l > 0^\circ$.

The enhanced flux and hard spectrum of up to $E^{-2.09}$ (assuming no cut-off) observed at low latitudes in Fig. 14.3 raises interest to study this small central region in a future ANTARES analysis. While the complete analysis is beyond the scope of this thesis, a first sensitivity estimate is provided after the main analysis at high latitudes in Sec. 18.

15 Analysis method and expected neutrino flux

15.1 | Analysis method

For the analysis, the signal region is approximated by the hatched shape in Fig. 14.2. The same hourglass region¹ has been used in the previous 2008–2013 FB track analyses [11, 13]. As a function of Galactic longitude l and latitude b , it is defined as

$$(l^2 + b^2)^2 \leq 50^\circ \times 50^\circ \times (b^2 - l^2). \quad (15.1)$$

Although originally defined to approximate the first published FB shape [144], the hourglass still covers 74% of the more detailed FB shape [158] at high latitudes and 91% of the nested ‘cocoon’ area [161].

The background in this signal region, or on-zone, is estimated from three control regions, or off-zones, shifted in time by 1/4, 1/2, and 3/4 sidereal days. This procedure ensures similar visibility for each zone (see Fig. 15.1). The visibility for tracks is similar but slightly lower than for showers. This is because events are accepted up to zenith angles $\cos(\theta_{z,\text{shower}}) < 0.1$ in the shower analysis, while in the track analysis a more stringent selection cut right at the horizon, $\cos(\theta_{z,\text{track}}) < 0$, is required to sufficiently reject atmospheric muon events.

Already within one sidereal day, each of the zones see the same regions on the sky with identical exposure provided data is taken continuously throughout the day. Short regular breaks and data-taking conditions varying over time average out over the course of a year.² Systematic differences in the expected number of events between zones have been evaluated and are found to be $\lesssim 3\%$ based on simulated Monte Carlo data. This number was derived from the simulations for the 2008–2015 dataset used in the analysis. Differences were evaluated as deviation from the mean plotted as a function of daytime and fractional year. For analysis this effect can hence be neglected.

15.2 | Assumed neutrino flux and energy spectrum

For the neutrino emission, one can optimistically assume a purely hadronic emission scenario, in which all γ -ray flux is generated by the interaction of ultra-high energy protons. In that case the accompanying neutrino flux follows the γ -ray flux, $\Phi_{\bar{\nu}}(E) \sim \Phi_{\gamma}(E)$ [162]. Fermi-LAT can measure the γ -ray flux only up to $\mathcal{O}(100 \text{ GeV})$. Due to the dominant atmospheric

¹The shape resembles that of an hourglass.

²The number sidereal days in one year is one higher than the number of calendar days since the Earth orbits the Sun.

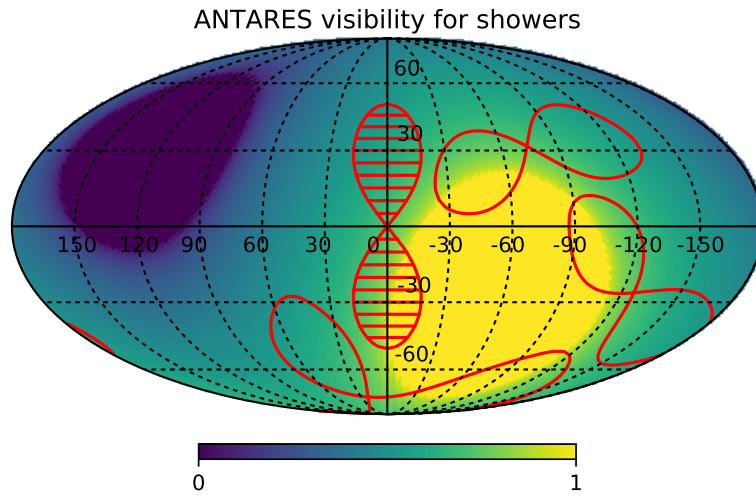


Figure 15.1: On- and off-zones in Galactic coordinates. The colour code shows the fraction of the day during which events are visible (=visibility) for ANTARES in the shower analysis. Own figure taken from [12].

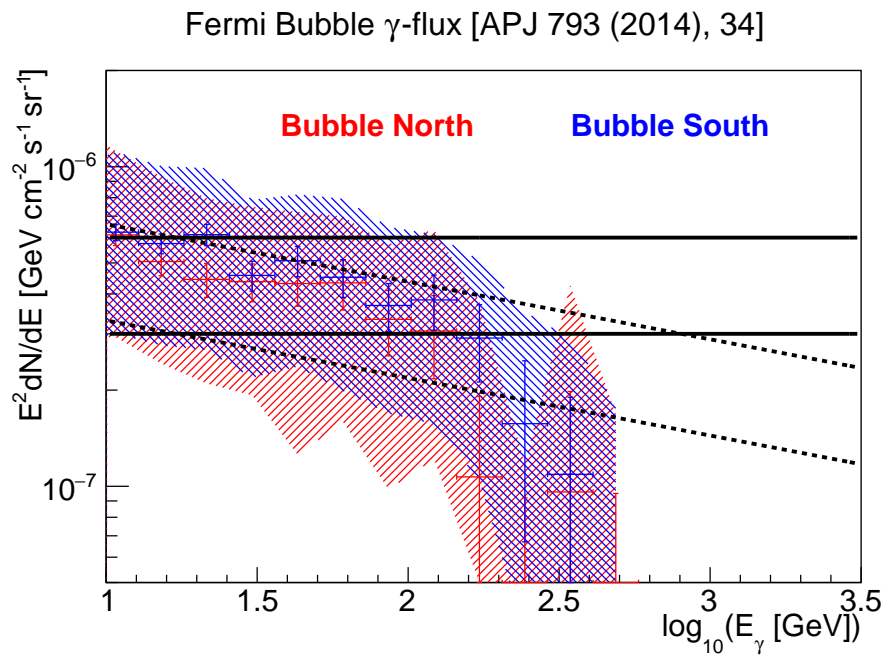


Figure 15.2: The Fermi Bubble γ -ray flux (northern and southern bubble) from Ref. [158] as a function of energy. Error bars (shaded bands) correspond to statistical (systematic) uncertainties of the measured flux. Superimposed black lines indicate $E^{-2.18}$ (dashed) and E^{-2} (solid) spectra. Figure taken from Ref. [161].

15. Analysis method and expected neutrino flux

neutrino background at low energies, ANTARES is only sensitive to a FB flux at TeV energies. The GeV-spectrum measured by Fermi-LAT is hence extrapolated to higher energies.

For the emission, a uniform γ -ray flux of

$$E^{2.18} \frac{d\Phi_\gamma}{dE} = (0.5 - 1.0) \times 10^{-6} \text{ GeV}^{1.18} \text{ cm}^{-2} \text{ s}^{-1} \text{ sr}^{-1}, \quad (15.2)$$

is assumed throughout the signal shape. The spectrum corresponds to that produced by an $\sim E^{-2.25}$ proton flux [163]. In the previous track analyses, ANTARES assumed a harder E^{-2} γ -ray spectrum as the reference,

$$E^2 \frac{d\Phi_\gamma}{dE} = (3 - 6) \times 10^{-7} \text{ GeV cm}^{-2} \text{ s}^{-1} \text{ sr}^{-1}, \quad (15.3)$$

These flux assumptions are overlaid to the γ -ray flux measured by Fermi-LAT in Fig. 15.2.

However, the water Cherenkov γ -ray telescope HAWC in Mexico, has meanwhile been able to constrain the γ -ray flux in the 1–100 TeV energy region in the northern bubble (the southern bubble is not visible to HAWC) [164]. Unless for very low cut-off energies in the GeV domain, assuming an E^{-2} γ -ray spectrum can no longer be justified. As shown in Fig. 15.3, high cut-off energies are meanwhile disfavoured even for the softer spectrum.

For a pion decay dominated flavour ratio at generation $(\nu_e:\nu_\mu:\nu_\tau)=(1:2:0)$, at Earth an equalised ratio $(\nu_e:\nu_\mu:\nu_\tau)=(1:1:1)$ is expected after oscillation (cf. Sec. 3). The proportionality factors to scale between the γ -ray flux and the associated neutrino flux per flavour decrease with softer spectral index [162]. For the assumed $E^{-2.18}$ γ -ray spectrum, 0.188 (0.175) associated (anti-)neutrinos per flavour are expected per γ -ray. For an E^{-2} spectrum, the proportionality factors are 0.211 (0.196) for (anti-)neutrinos [161].

Within our Galaxy, sources are not expected to efficiently accelerate protons beyond 1–10 PeV in energy [153]. As a consequence, this induces a cut-off in the observed γ -ray and neutrino spectra. It can be assumed, that π^\pm generated in the interactions of ultra-high energy protons on average obtain 20% of the proton's energy. Equipartition of these 20% over the four daughters in pion decay, introduced in Eq. 2.3, yields $E_{\text{cut-off},\nu} = 0.05 \times E_{\text{cut-off},p}$ for neutrinos, corresponding to optimistic cut-off energies ranging from 50 to 500 TeV.

Hence, the model neutrino fluxes per flavour to be probed in the analysis are:

$$E^{2.18} \frac{d\Phi_{\text{model}}}{dE} = (1.8 - 3.6) \times 10^{-7} \text{ GeV}^{1.18} \text{ cm}^{-2} \text{ s}^{-1} \text{ sr}^{-1} \times \exp\left(-\frac{E}{E_{\text{cut-off},\nu}}\right), \quad (15.4)$$

with $E_{\text{cut-off},\nu} = [\infty, 500 \text{ TeV}, 100 \text{ TeV}, 50 \text{ TeV}]$.

For completeness, the corresponding neutrino flux expected previously for an E^{-2} spectrum is

$$E^2 \frac{d\Phi_{\text{model}}}{dE} = (1.2 - 2.4) \times 10^{-7} \text{ GeV cm}^{-2} \text{ s}^{-1} \text{ sr}^{-1} \times \exp\left(-\frac{E}{E_{\text{cut-off},\nu}}\right). \quad (15.5)$$

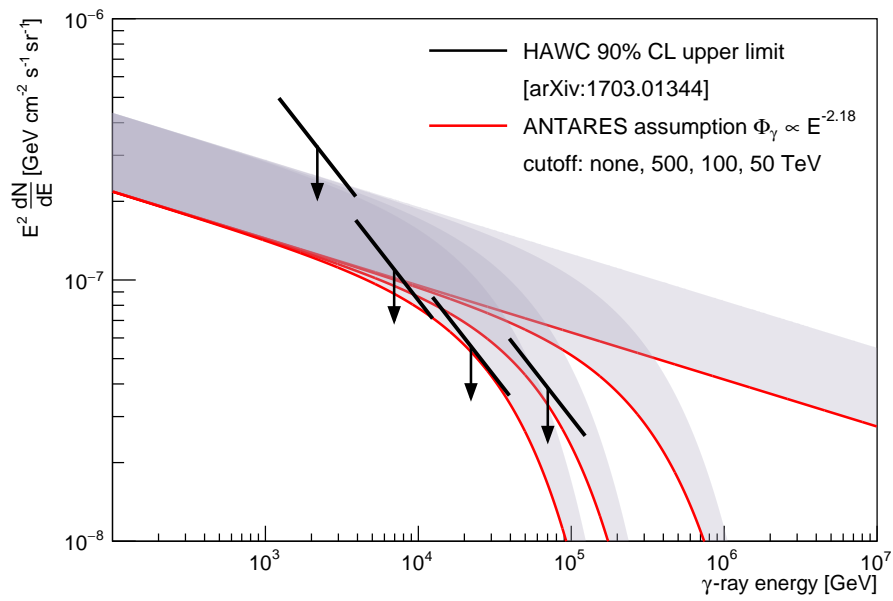


Figure 15.3: Assumed γ -ray flux bands (cf. Eq. 15.2) and HAWC upper limits [164] on the northern bubble. Conservative lower bounds (red lines) were used for the optimisation of the shower event selection. The same cut-off values as assumed for neutrinos are shown for illustration. Own figure taken from [12].

16 Recorded ANTARES data

16.1 | The ANTARES detector

ANTARES [21] is located at the bottom of the Mediterranean Sea off-shore Toulon (France) in a depth of 2.5 km and has an instrumented volume of $\sim 0.01 \text{ km}^3$. It consists of 885 optical modules (OMs) distributed over twelve detection lines. The ANTARES OMs house one single large 10-inch PMT. PMTs are oriented 45° downwards with respect to the horizon to maximise the neutrino effective area for events reaching the modules from below. A graphical visualisation of the instrument was already shown in Fig. 1.2.

The OMs are mounted onto storeys in groups of three. Data from the OMs are collected and digitised in a central module on each storey¹ and sent to shore, where filtering is done using software triggers. Since the OMs each house only one PMT, coincident hits are formed by requiring two hits on a storey within a time window of 20 ns, or one single pulse larger than three single photo-electron equivalent. Single L0 and coincident L1 hits are depicted in Fig. 16.1. Several L1 coincidences on nearby storeys are useful to define trigger conditions, named T2 and T3. They consist of two L1 hits on neighbouring storeys within 100 ns (T2, T3) or on next-to-neighbouring storeys within 200 ns (T3).

Since its completion in 2008, ANTARES has been taking data continuously, with only short periods of maintenance or extraordinarily high bioluminescence rates, during which the instrument needed to be switched off. Over time, parts of the detector from OMs up to entire detection lines have failed. As of September 2020, still more than 50% of the OMs are operational. The photon detection efficiency averaged over all operational OMs has decreased by

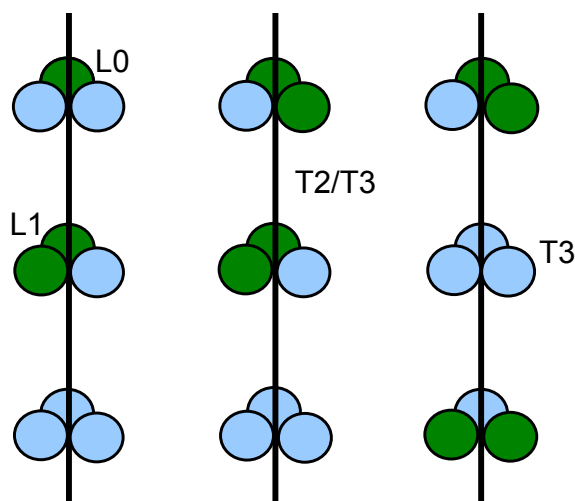


Figure 16.1: OMs with single (L0) and coincident (L1) hits (green) on a storey, and clusters of hits on adjacent storeys (T2, T3) used in the trigger. Modified (vectorised) from Ref. [165].

¹Hence, they are named only Optical Modules as opposed to the Digital Optical Modules in KM3NeT.

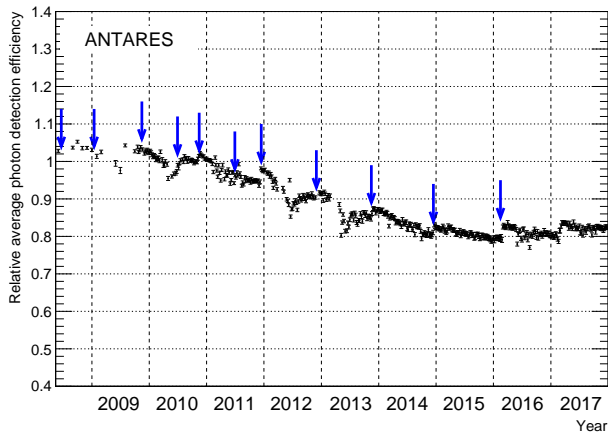


Figure 16.2: Relative OM efficiency averaged over all operational OMs in the detector as a function of time. The blue arrows indicate the times when high voltage tuning of the PMTs has been performed. Taken from Ref. [166].

$\sim 20\%$ over time, with no further deterioration observed in 2015–2017 data. This can be seen in Fig. 16.2. While periodic high voltage tunings can increase the overall detection efficiency, the long-term trend might be attributed to ageing of the PMTs or to growth of structures, on the glass spheres [166]. The latter is known as bio-fouling and reduces light transmittance onto the PMT.

16.2 | Event reconstruction

Several algorithms exist for event reconstruction in ANTARES. As neutrino events have either track- or shower-like appearance in the detector (as motivated in Sec. 5.5.1), these aim for reconstructing continuous Cherenkov light emission along an infinite line or emission from a single point in space and time, respectively. In the following, the AAFit and TANTRA reconstruction algorithms are used for they show the best direction resolution at energies relevant for the FB analysis. To select an event sample for the analysis, some additional parameters from other reconstruction algorithms are employed. However, this section shall focus on introducing the main algorithms used, AAFit for the track analysis and TANTRA for the shower analysis, and their main quality parameters used in the analysis.

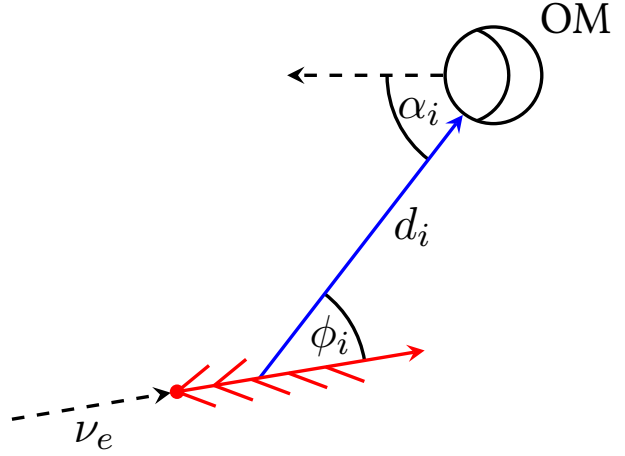
16.2.1 | AAFit for the track analysis

For track-like events in ANTARES, the AAFit [167] reconstruction is used. AAFit reconstructs an infinite track, which is completely defined by five degrees of freedom (three for position, two for direction).

For the fit, the time-residual between registered and expected arrival times of hits in the OMs with respect to the track hypothesis are calculated. The track hypothesis assumes a particle propagating along a straight line with the speed of light whilst emitting light under the Cherenkov angle. Based on the time-residuals and on local coincidences of hits, signal-like hits can be selected for the fit.

Three subsequent pre-fits are run to find an optimum starting point for the final fit, which is maximum-likelihood based. The probability density functions used therein also take into account the charges of hits and the distribution of background hits.

Figure 16.3: Schematic overview of quantities used in the TANTRA likelihood function in Eq. 16.4: photon emission angle ϕ_i , distance from shower to OM d_i , and incident angle α_i . Taken from [168].



The goodness of the fit result is given by the Λ parameter, which is

$$\Lambda = \frac{\log L_{\max}}{N_{\text{used hits}} - 5} + 0.1 \cdot (N_{\text{comp}} - 1) . \quad (16.1)$$

The first term of the right hand side is the maximum-likelihood fit result normalised by the degrees of freedom (the five parameters defining the track are subtracted from the number of used hits). The second is a correction term accounting for the number of other compatible pre-fits (N_{comp}) within 1° of the final fit result.

In addition, an angular error estimate can be calculated from the error matrix of the final fit,

$$\beta = \sqrt{\beta_\theta^2 + \sin^2 \theta \cdot \beta_\phi^2}, \quad (16.2)$$

and combines the errors on the two directions, θ and ϕ , with a $\sin \theta$ term accounting for phase space. AAFit achieves a direction resolution of $\lesssim 0.4^\circ$ at energies relevant for the FB analysis. As energy estimate, the ANN energy, E_{ANN} , [128] is used. ANN is based on a neural net for regression of the neutrino energy using several variables derived from AAFit.

16.2.2 | TANTRA for the shower analysis

Shower-like events in ANTARES are reconstructed with the TANTRA [169, 170] shower reconstruction algorithm in two subsequent steps. First, the shower vertex is determined by minimising a robust M-estimator, M_{est} , using the charge and time of signal-like photon hits on the OMs. The M-estimator is defined as

$$M_{\text{est}} = \sum_{\text{hits } i} \left(q_i \times \sqrt{1 + \frac{t_{\text{res},i}^2}{2}} \right), \quad (16.3)$$

where q_i is the charge of hit i , and $t_{\text{res},i}$ the time residual with respect to the shower hypothesis of hit i . The time residual is the difference between the observed and expected times of a hit.

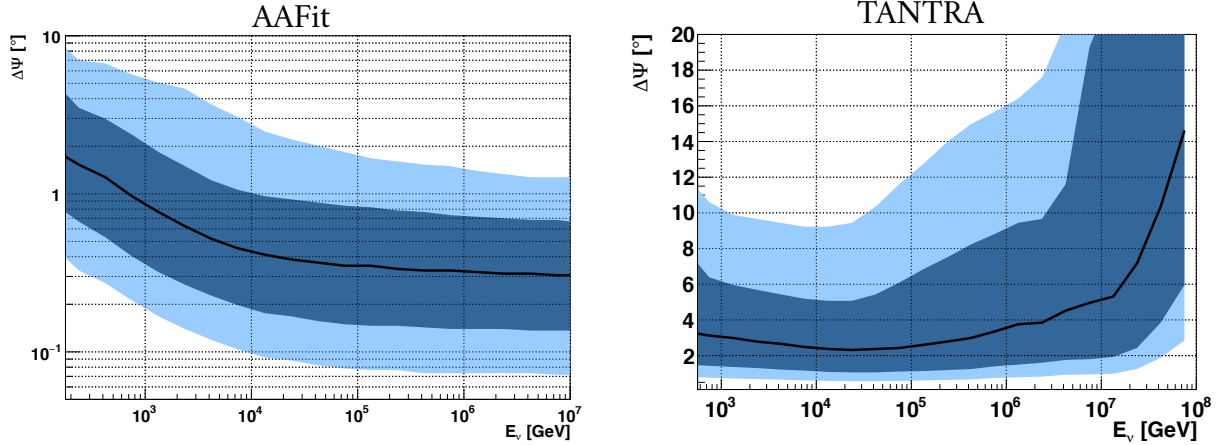


Figure 16.4: ANTARES resolutions on track- and shower-like signatures for an event selection typical for point-source searches. The panels present the reconstruction algorithms for tracks, AAFit (left), and for showers, TANTRA (right). Figures taken from Ref. [171].

In a second step, the obtained vertex and the amplitudes registered by the OMs are used to perform a maximum likelihood fit of the shower direction and to estimate the neutrino energy, E_{shower} . The likelihood is defined as

$$\begin{aligned} \mathcal{L}_{\text{shower}} = & \sum_{\text{PMTs w/ selected hits } i} \log (P_{q>0}(q_i | E_{\text{shower}}, d_i, \phi_i, \alpha_i) + P_{\text{bg}}(q_i)) \\ & + \sum_{\text{PMTs w/o hit } i} \log (P_{q=0}(E_{\text{shower}}, d_i, \phi_i, \alpha_i)), \end{aligned} \quad (16.4)$$

where $P_{q>0}(q_i | E_{\text{shower}}, d_i, \phi_i, \alpha_i)$ is the probability of measuring charge q_i in a PMT when the light is emitted from the shower of energy E_{shower} , at distance d_i , under emission angle ϕ_i with respect to the shower direction, and impinges on the PMT under incident angle α_i . The quantities are illustrated in Fig. 16.3. The other terms in the likelihood function account for the probabilities for hits being caused by background noise $P_{\text{bg}}(q_i)$ and for detecting no charge in a PMT, $P_{q=0}$. With the TANTRA fit, a direction resolution of $\lesssim 3^\circ$ is achieved for shower events.

The resolution of AAFit and TANTRA as a function of neutrino energy is given in Fig. 16.4 for an event-selection that is typical in point-source searches. In both cases, the angular error is small compared to the extension of the FB in the relevant energy range above ~ 10 TeV.

16.3 | ANTARES dataset recorded between 2008 and 2015

Data in ANTARES are recorded continuously in periods of livetime lasting several hours, named runs. During a run, the conditions in the deep sea are monitored continuously. Among other environmental parameters, the optical baseline rates, the frequency of bioluminescent bursts and the operation status are monitored for each OM. Over the long period ANTARES has been taking data, the efficiency to register signal photon hits has reduced. This reduction

and the consequences on neutrino detection are addressed in [Sec. 16.3.1](#). The varying data-taking conditions on shorter timescales are taken into account by the production of dedicated Monte Carlo simulations for each individual run. These so-called run-by-run simulations are used also in the FB analysis and are summarised in [Sec. 16.3.2](#). Runs that are used in the analysis are finally selected in [Sec. 16.3.3](#).

Since the event statistics in the analysis are small, the selection of events needs to be optimised and validated without looking at the event distribution at the final event selection stage during the optimisation process. This would generate an artificial statistical bias, since selection cuts can be tuned to the already known distribution of data events.

ANTARES therefore follows a blinding policy according to which the distribution of data in the signal region is not to be looked at before the final analysis; the data used for the analysis is blinded. To test the agreement between simulations and measured data, runs with a zero in the last digit of the run number (i.e. $\sim 10\%$ of data) can be analysed without restriction. This set of zero-ending runs is usually referred to as the ‘burn sample’.

For the Fermi Bubble analysis the blinding policy is adopted as follows. First, the agreement of data and Monte Carlo are compared at a loose pre-selection level without restriction to the zones using the burn sample. In the next step the off-zones are allowed to be looked at to validate the analysis. For the optimisation of analysis cuts, simulated Monte Carlo data is used. At no point is the event distribution in the on-zone analysed prior to the final analysis. In doing so, the complete dataset can be used in the FB analysis without biasing the analysis result.

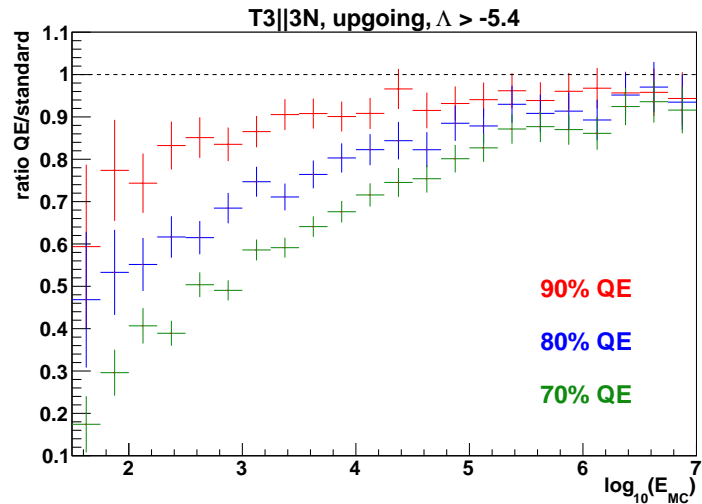
16.3.1 | Evolution of neutrino detection efficiency

Over the years of operating the ANTARES detector not only has the number of active OMs recording data decreased owed to hardware failures, but in addition a continuous quantum efficiency (QE) reduction in data is observed. This was shown in [Fig. 16.2](#). In the analysis of data in 2013 and later, neglecting this deterioration in the Monte Carlo simulations leads to increasing and obvious discrepancies when compared to the event rates observed in data. In the course of developing QE corrected run-by-run Monte Carlo simulations, ~ 100 runs were simulated for a period in fall 2013 with the overall QE of all PMTs reduced to 70%, 80%, and 90% of the nominal. In addition, several attempts have been made in order to best model the QE reduction observed in-situ over time. The meanwhile preferred scaling method² models the behaviour reliably using the rate of ^{40}K coincidences seen in neighbouring pairs of OMs. This and, in addition, an updated modelling of the optical properties of sea water (‘Nemo’ water instead of ‘ANTARES’ water, c.f. [Sec. 5.2](#)) is used in the latest version of run-by-run Monte Carlo simulations, v4. At an intermediate stage, other estimates of the QE reduction (performing less accurately over time) had been produced. One of them is based on the long-term evolution of baseline rates of hits in single OMs. The scaling derived with the latter method is included in the last period of the run-by-run Monte Carlo version used in this work, v3. The period taking QE reduction into account (v3-QE) covers the years 2013–2015.

The effect of an overall quantum efficiency scaling applied to all OMs for the simulated period in fall 2013 is shown in [Fig. 16.5](#). There, the reduction in the rate of recorded neutrinos as a function of neutrino energy is shown. While the loss is small at ultra-high energies, the

²based on the QE evaluation in Ref. [74]

Figure 16.5: Reduction of neutrino event rates as a function of neutrino energy for different overall down-scaling of the quantum efficiency. A loose pre-selection on the reconstruction quality and for events reaching the detector from below the horizon is applied. Error bars represent statistical errors of the simulated dataset.



rate of events is reduced noticeably at 10 TeV^3 for an overall QE scale matching the average observed from ^{40}K coincidences in the given period (by $\sim 15\%$ with only a loose pre-selection based on Λ applied in Fig. 16.5).

Since the reduction is energy dependent, it is useful to express it in terms of loss in signal for an unbroken $E^{-\alpha}$ energy spectrum, with spectral index α . The reduction in the rate of recorded events with uniform QE scaling applied is shown in Fig. 16.6. In the figure, also the reduction resulting from the intermediate QE scaling derived from the baseline rates in the given period in 2013 is added.

From this, several conclusions can be drawn:

- The loss in recorded signal with an expected spectral index $\alpha \approx 2$ is less pronounced than for the softer atmospheric neutrino flux.
- The reduction is enhanced, when events need to surpass certain quality criteria, such as in Fig. 16.6 (right), where the selection applied resembles that of a typical neutrino search. For signal fluxes $\sim E^{-2} \dots E^{-2.2}$, the resulting reduction is $\sim 15\%$ instead of 5% for the intermediate QE scaling.
- In the simulated period, the intermediate QE scaling behaves similar to an overall QE down-scaling to 80% after quality selection. On the other hand, the loss without any selection is smaller and similar to a 90% QE down-scaling. This shows, that a full account of the QE scaling of each individual OM cannot be mimicked by a simple overall factor in the QE. Therefore, in the v3-QE period and in v4, a time-dependent QE reduction is determined for each individual OM.
- The behaviour is dependent on energy and reconstruction quality. Any attempt to re-scale a wrongly modelled QE reduction should therefore at least depend on these two parameters, rather than applying a simple scale to the number of neutrino events.

The above points underline the need to take the evolution of QE into account on an OM basis.

³The region above the stated 10 TeV is the region of interest for the FB neutrino analysis.

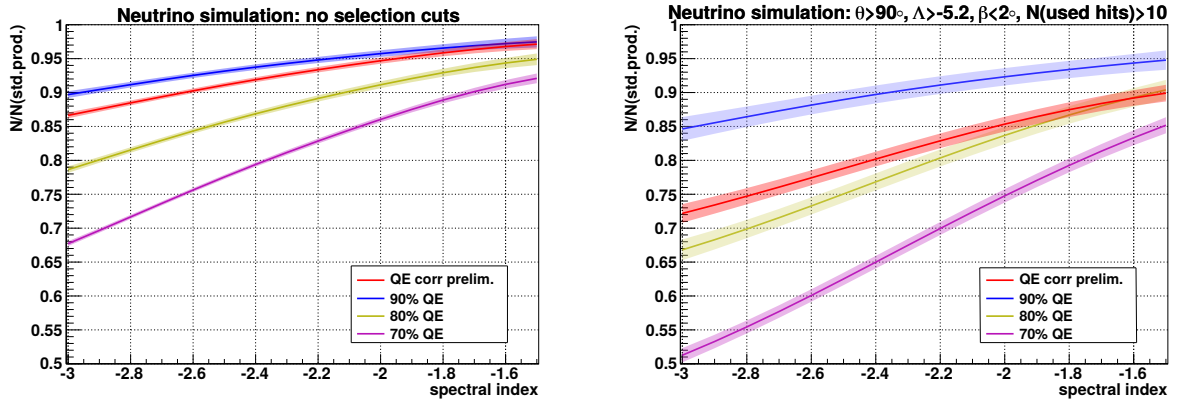


Figure 16.6: Reduction of neutrino events as function of spectral index for an un-broken power-law spectrum. Lines represent different overall downscaled quantum efficiencies, and a scaling derived from the baseline rate evolution in the ANTARES OMs. Simulated data correspond to a period in fall 2013. Error bands indicate statistical uncertainties on the simulated Monte Carlo. *Left:* Loss without any event selection. *Right:* Dummy selection for a neutrino sample based on quality and origin from below the horizon applied.

16.3.2 | Run-by-run Monte Carlo simulations

For each data-taking run, a corresponding Monte Carlo (MC) simulation is produced taking into account the environmental conditions during the run. This simulation is hence often referred to as run-by-run Monte Carlo. In the Fermi Bubble analyses in this work the version v3 is used. For the 2013–2015 neutrino simulations a preliminary quantum efficiency correction is taken into account (v3-QE), as motivated in [Sec. 16.3.1](#) above.

Neutrino events are simulated for $\bar{\nu}_e^{CC}$, $\bar{\nu}_e^{NC}$, $\bar{\nu}_\mu^{CC}$, and $\bar{\nu}_\mu^{NC}$ using the GENHEN [172] neutrino event generator. The simulated events obtain event weights for an atmospheric flux and for a flat energy spectrum. The latter can be used for reweighting the simulation to an arbitrary flux spectrum. Like this, the same simulations can be used to generate an expectation for the atmospheric neutrino flux and also the signal spectrum. In the v3 run-by-run simulations, the $\bar{\nu}_\tau$ channel has not been simulated. The contribution of $\bar{\nu}_\tau$ is included by scaling the $\bar{\nu}_\mu^{CC}$, $\bar{\nu}_e^{CC}$, and $\bar{\nu}_e^{NC}$ contributions adequately. Appropriate scaling factors have been derived in a different analysis [173] and are

- 1.09 for $\bar{\nu}_\mu^{CC}$ (+0.09 for the leptonic $\tau \rightarrow \mu$ decay),
- 1.12 for $\bar{\nu}_e^{CC}$ (+0.12 for the leptonic $\tau \rightarrow e$ decay), and
- 4.74 for $\bar{\nu}_e^{NC}$ (+1 from $\bar{\nu}_\tau^{NC}$, +2.74 from hadronic τ decays).

Atmospheric muon background events are simulated using MUPAGE [116]. For the MUPAGE simulations the actual livetime of the runs are subsampled by a factor 1/3 or 1/10.

Background noise hits are added to the simulated events when processed in the trigger simulation. The event reconstruction for simulated data is identical to that for real data after the trigger.

16.3.3 | Run selection for analysis

For analysis, runs are selected, during which the data-taking proceeded without problems. This section describes the run selection employed for the FB analysis. First, the general selection criteria that apply for both track and shower analysis are given. Then, the particular selection procedures for the track and shower analysis are explained.

General run selection criteria

In ANTARES, the quality of recorded data is evaluated with a quality basic parameter, QB. This parameter labels each data run with an integer number ranging from 0 to 4, which is stored in a central database. For the FB analysis, only runs with $QB \geq 1$ are used, as recommended by the data quality working group. This requirement ensures that data was recorded continuously without interruptions of the data-taking. Higher QB would impose additional requirements – a minimum fraction of sensors actively taking data, and low optical background rates from bioluminescence activity.

In addition, runs with certain other data quality flags in the database are excluded. These are (a) runs taken for monitoring purposes during or shortly after optimising parameter settings in the data acquisition, (b) runs with reduced PMT gain, and (c) runs registered as ‘sparking’ in the database.⁴ The runs with reduced PMT gain (b) had been taken in an attempt to continue data taking even with high optical background rates. Since these data are however hard to calibrate and analyse, the approach was not followed further.

Sparking runs (c) have to be identified carefully and excluded from the analysis. In ANTARES it was observed, that single malfunctioning PMTs can occasionally produce sparks of light. These are supposed to be generated in the dynode structure of the PMT and illuminate the detector repeatedly during short periods up to (typically) several minutes. Since they are extremely bright, they can be erroneously reconstructed as neutrino event signature of high energy and – unfortunately – with good reconstruction quality. The standard test exploits the brightness of sparks and identifies problematic runs by a high rate of reconstructed events with many hits. It was observed that their vertex is typically reconstructed close to the problematic OM by the shower reconstruction algorithm DUSJ [174]. Hence, an additional test was developed and was able to identify additional sparking runs based on their vertex clustering in the detector [161]. The vertex clustering method has been used to identify sparking runs also in 2014/15. In total, 10 runs are identified and are removed from the analysis.⁵

Run selection for the 2014/15 track sample

For the track analysis of 2014/15 data, the same event selection criteria as for the analysis of previous years are employed. In addition to the general run-selection criteria defined above, two additional criteria need to be fulfilled:

1. The run-by-run Monte Carlo set needs to be complete. For this, all Monte Carlo simulation files corresponding to a data run must be available. This additional requirement

⁴In the ANTARES database, the corresponding flags are (a) SCAN and PRELIM, (b) HALF and OVER and (c) SPARKING.

⁵In the 2014 dataset, ten runs were found to be sparking. The run numbers are 75148, 75634, 75667, 76219, 76244, 76247, 76256, 76359, 77459, 78305. The test for sparking runs in 2015 revealed none.

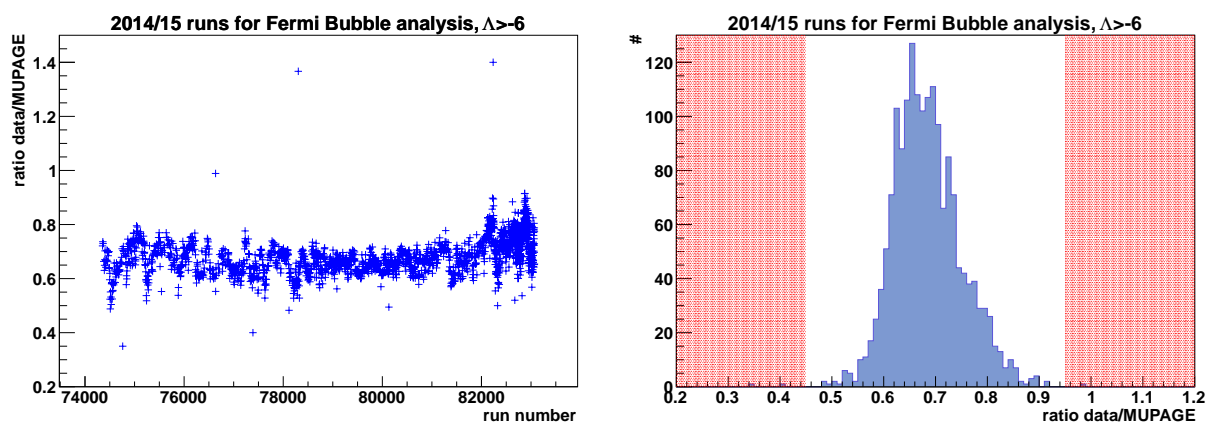


Figure 16.7: Ratio of recorded and MUPAGE simulated events passing a loose Λ selection cut. The ratio is completely dominated by atmospheric muons.

reduces the analysed livetime by 15% in 2014/15.

2. The measured event rates need to agree with the expectation from simulated atmospheric muons. For the comparison, only a loose pre-selection on the track-fit quality Λ is applied, $\Lambda > -6$. The pre-selection cut on Λ is necessary to reject events induced by noise when optical background rates are high. A more detailed description on the procedure is given in Ref. [161]. The agreement of simulated MUPAGE events and data is constant over time in the 2014/15 dataset, as shown in Fig. 16.7. Only a few runs (in the shaded region) are excluded from the analysis.

With all run-selection criteria applied, a livetime of 593 days remains for the track analysis of 2014/15 data. The analysed livetime in the track analysis per year in 2008–2015 is given in Tab. 16.1.

Run selection for the 2008–2015 shower sample

The additional criterium in the track analysis to use only runs with a complete Monte Carlo dataset results in a significant reduction of analysed livetime. For the shower analysis, the run selection was consolidated with the ANTARES searches for diffuse and point-like sources (see e.g. [171]), and the additional requirements of the track analysis above were abandoned. With this, a 16% increase in analysed livetime is achieved. The increase in livetime is especially large in 2012, where at the time of un-blinding the 2014/15 track analysis, many simulated runs had still been incomplete.

However, in case part of the Monte Carlo is missing, this needs to be taken into account for the analysis. In other searches, a simple scaling of the available Monte Carlo to match the total livetime in data is applied. The FB shower analysis employs a more complex method to avoid biases in the visibility of the analysis regions induced by a simple re-scaling. In the used method, simulated events enter the analysis a second time with a smaller weight accounting for the missing livetime and with new Galactic coordinates. These new coordinates are calculated from the local coordinates (zenith, azimuth) by randomly drawing an artificial simulated time in one of the missing periods. The method is applied for each year separately.

Table 16.1: Livetime per year used for the analysis of the FB with tracks and showers.

year	track analysis livetime [d]	shower analysis livetime [d]	difference
2008	134.5	140.2	+4%
2009	197.2	208.5	+5%
2010	225.1	244.2	+8%
2011	272.4	289.8	+6%
2012	145.0	248.1	+42%
2013	197.6	273.6	+28%
2014	291.9	338.6	+14%
2015	301.2	354.1	+15%
2008-2015	1764.9	2097.1	+16%

Also for the shower analysis, the analysed livetime is given on a yearly basis in [Tab. 16.1](#). In addition, the table states the gain achieved by re-weighting the simulated data with the method outlined above. In the 2008–2015 shower analysis, 2097 days are analysed.

17 All-flavour search for neutrinos from the Fermi Bubbles at high Galactic latitudes

This chapter describes the all-flavour search for neutrinos from the Fermi Bubbles at high Galactic latitudes. The analysis consists of two individual searches for track- and shower-like event signatures. The results of both are combined afterwards to set an all-flavour upper limit on the FB signal flux.

The key points of the analysis procedure are similar for tracks and showers and are outlined in [Sec. 17.1](#). In [Sec. 17.2](#), the previous track search for a FB signal in 2008–2013 data is extended by two more years using data recorded in 2014 and 2015. In [Sec. 17.3](#), the shower search using data recorded between 2008 and 2015 is presented. Results from the track and shower search are combined in [Sec. 17.4](#).

17.1 | General analysis procedure

For the Fermi Bubbles analysis, one signal region (on-zone) and three control regions (off-zones) as defined in [Sec. 15.1](#) are used. The off-zones have same shape and visibility as the on-zone. They are used to estimate the expected background in the signal region in a data-driven approach.

Monte Carlo simulated data are still required to optimise the selection cuts in the analysis, and when setting an upper limit on the signal flux. However, for the upper limit only simulated signal neutrinos enter the calculation and not the atmospheric muon background, for which the simulated statistics at the final selection stage are typically small.¹ Furthermore, any excess in the on-zone is observed purely based on measured data.

The track and shower analysis have the following key points in common, which have been established in Refs. [[175](#), [161](#)]:

- 1) First, a set of suitable variables to select a FB event sample while suppressing the backgrounds from atmospheric neutrinos and muons needs to be identified. For this set of variables, the agreement between data and Monte Carlo simulations is verified.
- 2) The final event selection is optimised such that the analysis is expected to yield the most stringent upper limit on the FB signal flux. To this end, the event selection cuts are optimised using the Model Rejection Factor (MRF) technique. This technique minimises the average

¹Depending on the Monte Carlo production, 1/3 or 1/10 of the real livetime is simulated with MUPAGE for atmospheric muons. Few remaining events in the final analysis sample with weight 3 or 10 therefore introduce a large statistical error on the expected atmospheric muon background.

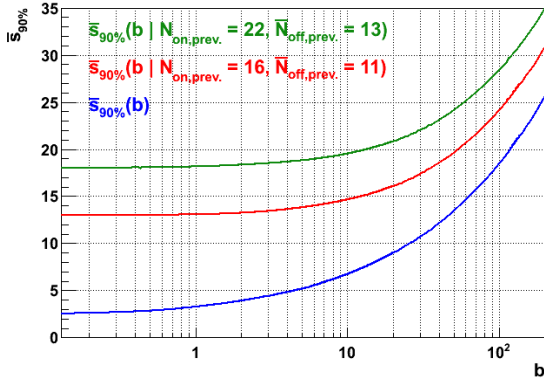


Figure 17.1: Average (90% CL) signal upper limits as a function of the background count, b . Lines represent the original calculation (blue) and the calculation taking into account the previous 4-/6-year track results (red/green).

90% CL flux upper limit,

$$\bar{\Phi}_{90\%} = \Phi_{\text{model}} \times \text{MRF} = \Phi_{\text{model}} \times \frac{\bar{s}_{90\%}(b)}{s}. \quad (17.1)$$

The result of the minimisation corresponds to the flux sensitivity of ANTARES. In Eq. 17.1, s is the number of selected signal neutrinos assuming a model flux Φ_{model} . These need to be generated and reconstructed within the on-zone, from where a signal flux is expected. Similarly, b is the averaged number of simulated background events which are generated over the entire sky and reconstructed within the off-zone regions. The average signal upper limit,

$$\bar{s}_{90\%}(b) = \sum_{k=0}^{\infty} \mu_{90\%}(k, b) \times \text{Poisson}(k|b), \quad (17.2)$$

is obtained by summing over the $\mu_{90\%}$ for all possible measured event counts in the on-zone, k , weighted with their respective Poisson probability. The individual $\mu_{90\%}$ represent Feldman and Cousins signal upper limits [176] at 90% CL, given k events are observed and background b is expected in this observation.

Already in the analysis in Ref. [161], a modified average signal upper limit has been used. It calculates the upper limit under the condition that a previous analysis has already found $N_{\text{on,prev.}}$ on-zone events and an average of $\bar{N}_{\text{off,prev.}}$ off-zone events. In this case, Eq. 17.2 is superseded by

$$\begin{aligned} \bar{s}_{90\%}(b_{\text{add.}} | N_{\text{on,prev.}}, \bar{N}_{\text{off,prev.}}) &= \\ &= \sum_{k=0}^{\infty} \mu_{90\%}(k + N_{\text{on,prev.}}, b_{\text{add.}} + \bar{N}_{\text{off,prev.}}) \times \text{Poisson}(k|b_{\text{add.}}), \end{aligned} \quad (17.3)$$

where $b_{\text{add.}}$ represents the expected background in the additional dataset to be analysed, while s in Eq. 17.1 is the total expected signal from the previous and additional dataset. The $\bar{s}_{90\%}$ values are shown as a function of the expected background events in Fig. 17.1 for the standard calculation and after the previous 4-/6-year track analyses of the FB.

The MRF minimisation step results in the final set of selection cuts for the analysis.

3) The analysis method using on- and off-zones is to be validated. To this end, the agreement between data and Monte Carlo in the off-zones is verified for a pre-selected event sample. Then, two additional tests are used to ensure agreement of the event counts amongst zones.

The first test compares the numbers of events observed in data within the off-zones amongst each other. For the variables used for the MRF optimisation above, various combinations of possible selection cuts up to the final cut level are applied. The resulting event number differences amongst combinations of zones $(i,j) = \{(1,2), (2,3), (3,1)\}$ are calculated as

$$\text{diff}_{ij} = \frac{N_i - N_j}{\overline{N}_{\text{off}}} \times 100\% . \quad (17.4)$$

These differences can be checked to be consistent with fluctuating randomly around equipartition.

The second test compares the on-zone with the off-zones based on Monte Carlo data only, in order not to un-blind data in the signal region. Again, while scanning possible cut values for the event selection, the numbers of events from the signal region are compared to the average from the off-zones,

$$\text{diff}_{\text{on/off}} = \frac{N_{\text{on}}^{\text{sim}} - \overline{N}_{\text{off}}^{\text{sim}}}{\overline{N}_{\text{off}}^{\text{sim}}} \times 100\% . \quad (17.5)$$

If the zones are found to agree based on these validation tests, the dataset is ready for unblinding.

4) Using the final selection cuts obtained in 2), the analysis is then un-blinded. The event counts in the signal region and in the off-zones are obtained.

If an excess in the signal region is found, its statistical significance S can be estimated using the method described by Li and Ma [177], which is valid for an on-/off-zone measurement with low event statistics:

$$S = \sqrt{2} \left\{ N_{\text{on}} \ln \left[\frac{1 + \alpha}{\alpha} \left(\frac{N_{\text{on}}}{N_{\text{on}} + N_{\text{off}}} \right) \right] + N_{\text{off}} \ln \left[(1 + \alpha) \left(\frac{N_{\text{off}}}{N_{\text{on}} + N_{\text{off}}} \right) \right] \right\}^{1/2} , \quad (17.6)$$

where $1/\alpha = 3$ is the number of off-zones. N_{on} is the total number of events observed in the on-zone, N_{off} the total number observed in all three off-zones together. It was shown [177], that S corresponds to a one-sided tail of a Gaussian distribution, and hence represents a significance in units of standard deviations σ confidence level (CL). For three off-zones used in the FB analysis, the significance in terms of average number of events observed in the off-regions and the excess over the off-zone expectation is shown in Fig. 17.2. If the found excess is significant, i.e. by convention exceeds 3σ (or 5σ) CL, evidence for (or detection of) a FB signal can be claimed.

Unless significant excess in the on-zone is observed, an upper limit can be set on the signal flux from the FB. The 90% CL upper limit is set using again the calculation by Feldman and Cousins [176],

$$\Phi_{90\%} = \Phi_{\text{model}} \times \frac{\mu_{90\%}(N_{\text{on}}, \overline{N}_{\text{off}})}{s} , \quad (17.7)$$

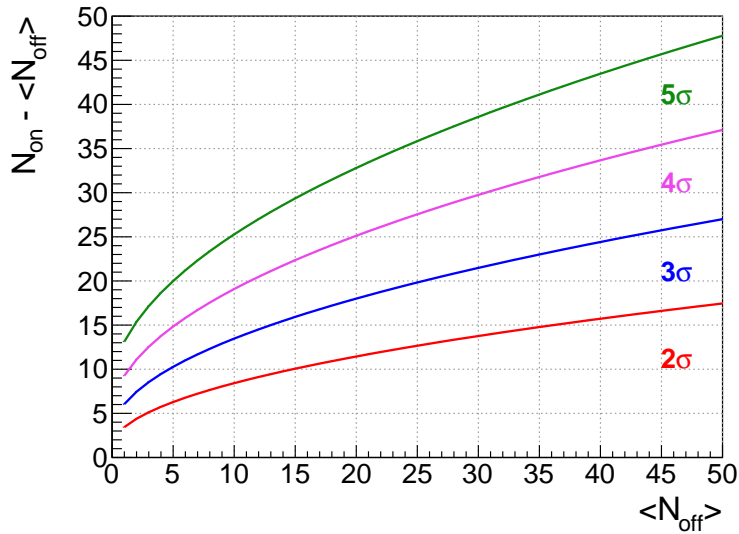


Figure 17.2: Li and Ma significances in Eq. 17.6 evaluated for three off-zones, $1/\alpha = 3$. Lines represent 2–5 σ confidence level. Axes are the average number of events per off-zone, $\langle N_{\text{off}} \rangle = \alpha \cdot N_{\text{off}}$, and the on-zone excess over background expectation.

based on the observed N_{on} on- and \bar{N}_{off} average off-zone events and the total number of expected signal events s derived from Monte Carlo.

These four points of the analysis procedure are reflected in the structure of the individual searches for track- and for shower-like event signatures. An upper limit on the FB neutrino flux is set when combining both individual analyses thereafter.

17.2 | Track analysis of the 2014/15 dataset

For the search for track-like neutrino signatures from the FB in 2014/15 data, recorded runs with stable data-taking conditions and an available corresponding run-by-run Monte Carlo simulation were selected with the criteria defined in Sec. 16.3.3. With this selection, a total livetime of 593 days in 2014/15 is added to the previous 2008–2013 dataset which has found 22 events in the on-zone with an expected background of 13 events. Whilst not statistically significant (1.9σ according to Eq. 17.6), the found 6-year excess in tracks is intriguing and motivates the presented analysis of additional ANTARES data.

17.2.1 | Data pre-selection of the track analysis

For the track analysis, several selection cuts are applied to the data in order to retain well-reconstructed signal events and suppress the atmospheric muon and neutrino backgrounds. As the result of AAFit is used in the analysis, most of the event selection cuts are based on parameters from this reconstruction algorithm. The set of analysis cuts is listed in Tab. 17.1 and explained in the following.

The event rate in the detector is totally dominated by atmospheric muons penetrating to a depth of $\gtrsim 2$ km. In the analysis, only events reconstructed as upward-travelling, $\theta_{z,\text{track}} > 90^\circ$, or equivalently $\cos(\theta_{z,\text{track}}) < 0$, are selected. This selection is more stringent than the one for showers shown in the visibility map in Fig. 15.1. It is required since atmospheric muons

Table 17.1: Variables used for the event pre-selection and for the final event selection in the FB track analysis.

parameter	pre-selection	final analysis cut
$\theta_{z,\text{track}}$	$> 90^\circ$	idem
$N_{\text{used hits}}$	> 10	idem
β	$< 1^\circ$	idem
BBFit quality	$\chi_{\text{track}}^2 < \chi_{\text{shower}}^2$	idem
Λ	> -6.5	> -5.14
E_{ANN}	none	$> 10.8 \text{ TeV}^*)$

*) For reproducibility, the precise cut value applied is $E_{\text{ANN}} > 10^{1.0\bar{3}} \text{ TeV}$.

passing the detector sometimes mimic upward-going tracks and are mis-reconstructed. As a consequence, the overall visibility for the zones in the track analysis is slightly lower than in the shower analysis.

Three additional pre-selection cuts are applied to select well reconstructed events in the analysis. Events with only very few hits used in the final fit, more precisely $N_{\text{used hits}} \leq 10$, are rejected. This is because events with almost no hits but energies in the TeV range are prone to inaccurate reconstruction. A cut on the angular error estimate $\beta < 1^\circ$ ensures good pointing resolution. In addition to the used AAFit variables, the χ^2 values of a second fit algorithm, BBFit, are used. BBFit minimises two hypotheses, assuming light emission from a track and from a bright point (shower). For a track analysis, requiring $\chi_{\text{track}}^2 < \chi_{\text{shower}}^2$ selects event signatures for which the hit distribution matches a track hypothesis better than that of a bright point.

The neural-net based ANN energy, E_{ANN} is used as an estimate for the neutrino energy. The energy is the key discriminating variable to distinguish a possible FB signal with hard energy spectrum from the softer $\sim E^{-3.7}$ atmospheric neutrino flux. The lower cut value on E_{ANN} can be optimised for the suppression of atmospheric neutrinos.

The selection on $\theta_{z,\text{track}}$ and β alone is insufficient to suppress the atmospheric muon background. However, the goodness of the likelihood fit tends to be worse for mis-reconstructed events. The quality parameter Λ can hence be used as a parameter to reject the remaining atmospheric muon background. The cut on this parameter can be optimised. Requiring a minimum $\Lambda > -6.5$ in the pre-selection ensures events reconstructed due to pure noise are rejected.

Data and the QE corrected run-by-run Monte Carlo simulations for 2014/15 used (v3-QE) are compared for this loose pre-selection cut on Λ . The distributions of data and the corresponding simulations in the off-zones with pre-selection cuts in [Tab. 17.1](#) applied are shown in [Fig. 17.3](#). The QE corrected Monte Carlo matches well with data in Λ both in overall normalisation and in shape. The MUPAGE simulations for atmospheric muons are down-scaled by a factor of 0.5 to match in normalisation. Note, that the applied scaling is more than the deficit observed in the down-going ratio in [Fig. 16.7](#), because of the quality- and zone pre-selection applied. This behaviour is similar to what has been shown for neutrinos in [Fig. 16.6](#).

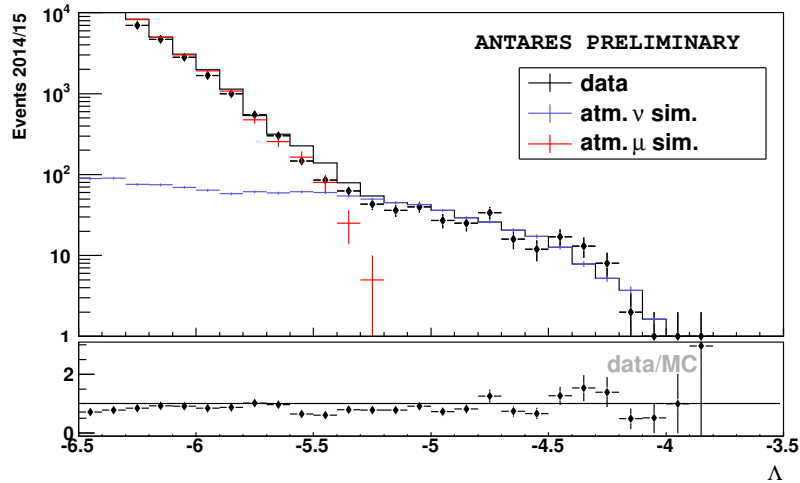


Figure 17.3: Events as a function of the quality parameter Λ in the off-zones for the 2014/15 dataset. Atmospheric muon simulation was scaled down by a factor 0.5 to match the observed event counts. Figure presented in Ref. [13].

In Fig. 17.4 (left), the cumulative distribution of the burn sample observed in the entire sky is shown for a pure neutrino sample (with a stringent selection on the track fit quality, $\Lambda > -5.1$). A small discrepancy, or ‘bump’, is seen around 10 TeV and from the yearly comparison can be attributed to the 2014 data sample. The same observation was made for events reconstructed inside the off-zones. While the cumulative distribution is prone to enhance small over-fluctuations and makes them seem more significant, this discrepancy has never the less been analysed further. A comparison of the used HKKM flux with an added prompt component (see Fig. 2.2) with the alternative flux model by the Bartol group [140] only leads to a slightly worse match in overall normalisation. Checks against using the number of hits or an alternative energy estimate based on the loss along the trajectory, dE/dx , showed the same behaviour. This strongly discouraged changing the energy estimate in the analysis of the additional years with respect to the previous FB analyses. Loosening the selection to $\Lambda > -5.2$ reduces the ‘bump’ structure and shows good agreement. The level of agreement between data and Monte Carlo is hence judged sufficient to proceed with the analysis by defining the final event selection. The event distribution in the off-zones is shown in Fig. 17.5 with the final selection cut on Λ applied and shows excellent agreement with the Monte Carlo expectation. There also the levels of different assumed signal fluxes scaled to the number of off-zone events are overlaid.

17.2.2 | Test for possible re-optimisation of analysis cuts

Suppression of atmospheric muons and neutrinos is possible based on only two parameters, Λ and E_{ANN} , respectively. This is obvious from the event distributions shown above, in Fig. 17.3 and Fig. 17.5. The final selection cuts on these parameters had been optimised for the previous FB track searches. In the 4- and 6-year analyses, the cuts

$$\Lambda > -5.14 \quad \text{and} \quad E_{\text{ANN}} > 10.8 \text{ TeV}, \quad (17.8)$$

were used. These had been optimised for a signal flux following an E^{-2} spectrum.

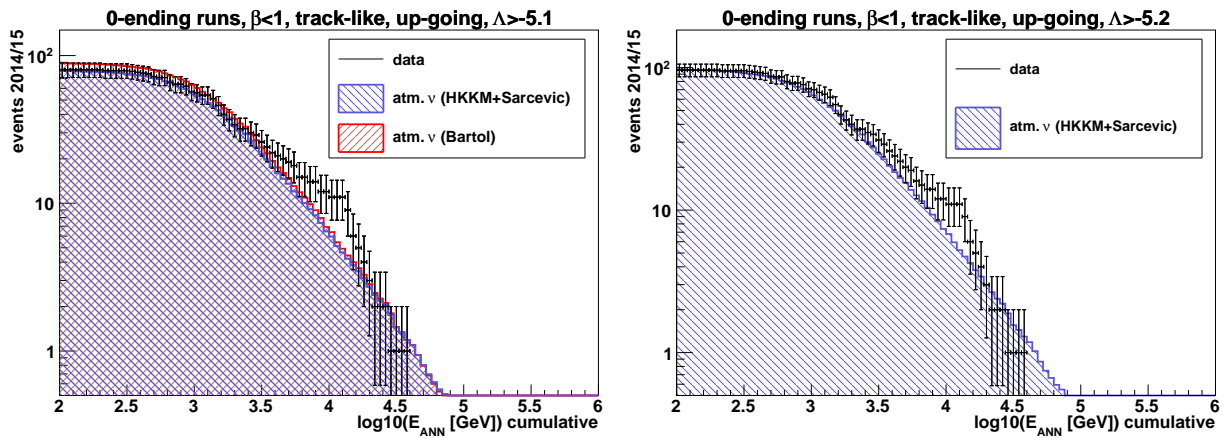


Figure 17.4: Cumulative distributions in reconstructed track energy E_{ANN} for the burn sample (run numbers ending with 0) for pre-selected events (no zone selection). The additional selection cuts on the track fit quality are $\Lambda > -5.1$ (left) and $\Lambda > -5.2$ (right).

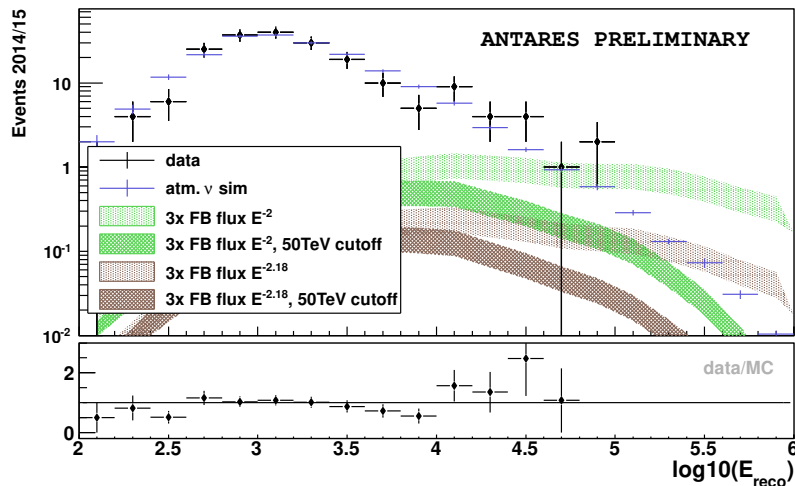


Figure 17.5: Comparison of 2014/15 data and corresponding Monte Carlo in the off-zones for the reconstructed energy E_{ANN} with $\Lambda > -5.14$ applied. Figure presented in Ref. [13].

Table 17.2: MRF optimisation result for the 2014/15 analysis assuming an E^{-2} signal flux spectrum with exponential energy cut-off values above 50 TeV. 4-/6-year cut values are $\Lambda > -5.14$ and $E_{\text{ANN}} > 10.8$ TeV.

cut-off energy [TeV]	∞	500	100	50
optimal cut on Λ	-5.33	-5.32	-5.32	-5.32
optimal cut on $\log_{10} E_{\text{ANN}}$	3.85	3.67	3.58	3.48
events background MC	8.85	14.1	17.5	22.8
events signal MC	2.20	1.60	1.01	0.78
MRF	2.97	4.53	7.79	11.6
events background MC (4/6-year cut values)	4.13	4.13	4.13	4.13
events signal MC (4/6-year cut values)	1.79	1.10	0.58	0.37
MRF (4/6-year cut values)	3.06	4.74	8.47	13.2

To test for a possible improvement of the analysis with a re-optimisation of the Λ and E_{ANN} analysis cuts, the MRF procedure described in Sec. 17.1 is used, including the previously found 22 on-zone and average 13 off-zone events in the 6-year analysis. The MRF is minimised in the bi-dimensional plane of reconstructed energy E_{ANN} and reconstruction quality Λ . The result of this re-optimisation is shown in Tab. 17.2. While the MRF optimisation in 2014/15 results in softer cut values in both Λ and E_{ANN} , this would increase the background by a factor ~ 2 – 5 compared to the previous selection. The overall MRF gain ranges between only 3% (no cut-off) and 14% (50 TeV cut-off) depending on the cut-off energy in the neutrino flux. The only small gain in MRF, or likewise sensitivity, is due to the already seen excess in the 6-year analysis. This excess is also the reason, why the sensitivity is above the model flux, even for the optimisation based on the optimistic E^{-2} spectrum shown in Tab. 17.2. As a result, the original values for Λ and E_{ANN} are applied without modification also to the new dataset, even if fewer signal events are expected. This last statement holds in particular also for the meanwhile more probable $E^{-2.18}$ flux scenario, for which a higher selection cut on energy reduces the signal yield even more.

17.2.3 | Data – Monte Carlo agreement

To ensure comparable visibility for all zones, and that the reconstruction behaves similarly in the zones, the tests on the event number differences defined in Eq. 17.4 and Eq. 17.5 are performed for the 2014/15 analysis sample. In these tests, the number of events seen in the different zones are compared for combinations of cuts on E_{ANN} and Λ .

For data, only the off-zone event counts can be compared in order to not analyse the on-zone prior to the final un-blinding. However, the off-zones can be examined to exclude biases in the event numbers expected between zones. The relative difference of events observed in data for pairs of off-zones $(i,j) = \{(1,2), (2,3), (3,1)\}$ is calculated as defined in Eq. 17.4. The result is shown in Fig. 17.6.

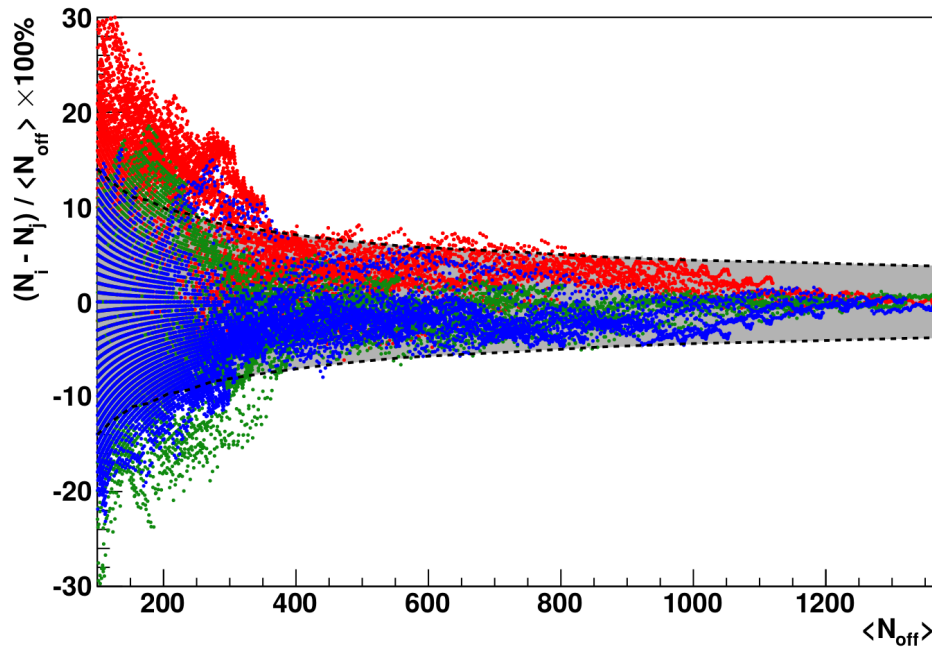


Figure 17.6: Event number differences seen in 2014/15 track data between pairs of off-zones $(i,j) = \{(1,2), (2,3), (3,1)\}$ as a function of the mean off-zone count. Points correspond to different cut combinations on Λ and E_{ANN} . The grey area represents the 68% statistical error band.

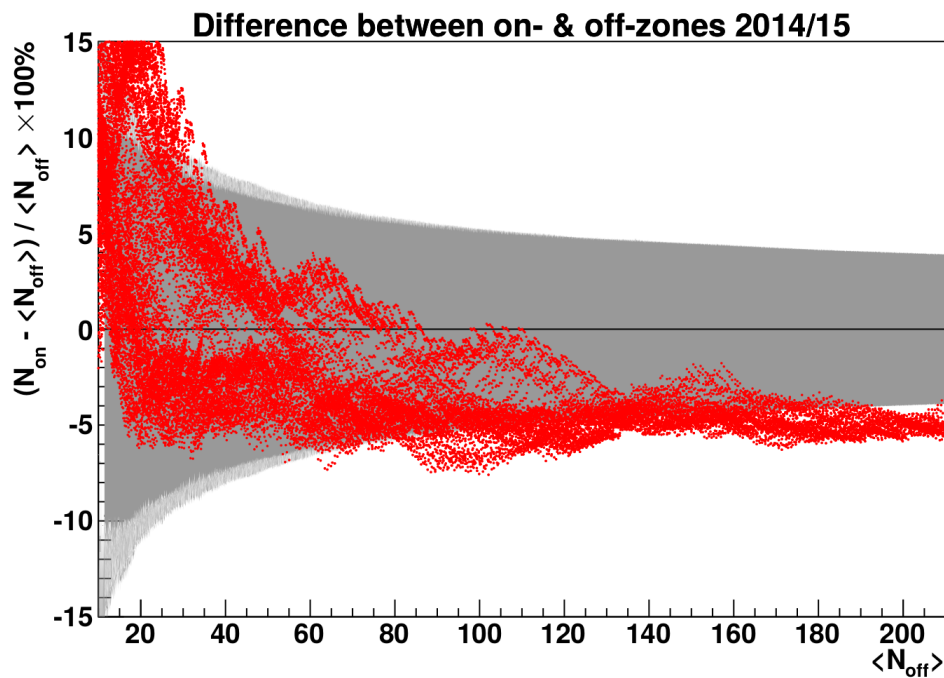


Figure 17.7: Difference between on- and average from the off-zones for a simulated atmospheric neutrino flux. The difference is shown as a function of the average off-zone count for various different cut combinations on Λ and E_{ANN} . The statistical error band is indicated in grey.

For loose cuts, all points lie within the band of 1σ CL statistical fluctuation (grey band in Fig. 17.6). For tighter cuts, zone 2 sees a slight deficit. However, since $\sim 32\%$ of the points are expected to lie outside the band, it appears that the event numbers in the zones agree reasonably well. This consideration even ignores that similar cuts result also in a similar selection of events and are thus correlated. Correlation leads to the band-like structures of neighbouring points observed. The distribution is cut at an average off-zone count of $\langle N_{\text{off}} \rangle = 100$ in order to blind the region of the final selection.

To test the agreement for the signal region, the difference between on- and average of the off-zones is compared using Eq. 17.5. Using this formula for atmospheric neutrino Monte Carlo, the number of events seen in the on-zone is compared to the average of the off-zones in Fig. 17.7.

A small ($\sim 5\%$) deficit in the on-zone Monte Carlo is seen for very loose cuts. The distribution however turns back towards the grey band of the statistical error of each point, when tightening the event selection. Therefore, no clear bias is seen in the event expectation from on- and off-zones in 2014/15.

17.2.4 | Observed track events and track-only flux upper limits

With the analysis of 2014/15 data, an additional livetime of 593 days is added to the FB track search. After applying all event selection cuts, the un-blinded dataset yields 6 events in the signal region and a background of $20/3 = 6.7$ events averaged over the three off-zones. Together with the previous years, the total analysed livetime comprises 1765 days recorded between 2008 and 2015. In total, 28 track events are observed in the signal region. The corresponding background expectation from the three off-zones is on average $59/3 = 19.7$ track events.

Comparing the observed event counts in the signal region with the expectation from the off-zones gives a non-significant excess of 1.5σ CL significance according to the Li and Ma formula in Eq. 17.6. Figure 17.8 compares the event distribution as a function of the reconstructed ANN energy estimate, E_{ANN} observed in the on-zone with the average of the offzones. Within statistical errors, the distributions show good agreement below the cut value with the small excess found being visible above. In empty bins, arrows indicate the 90% cumulative Poisson probability value for observing zero events.

Since there is no excess observed in the on-zone in 2014/15 data, the 8-year track-only limits [13] are more stringent by about a factor two compared to the 6-year analysis covering the period from 2008 to 2013. The final flux upper limits are derived in combination with the result of the subsequent shower analysis in Sec. 17.4.

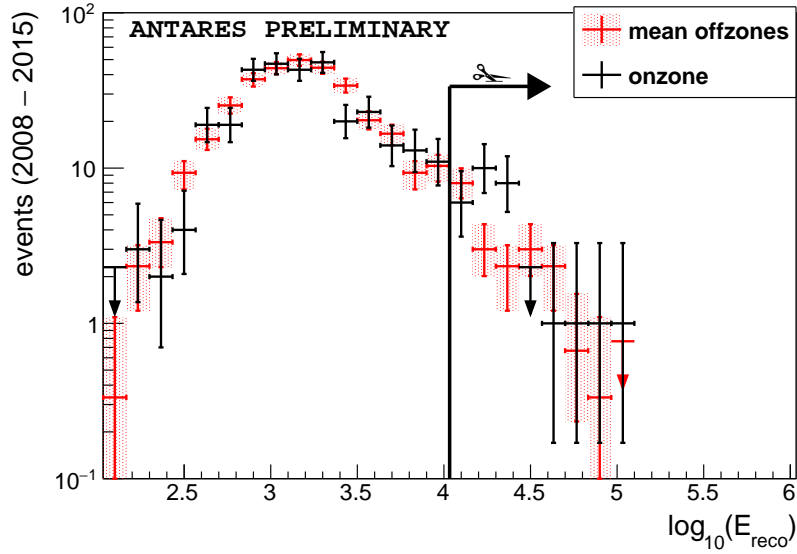


Figure 17.8: Energy distribution for data from the on- and off-zones in the track analysis (including 1σ Poisson intervals) after event selection. The lower cut on the energy estimate $E_{\text{ANN}} > 10^{4.03}$ GeV (=10.8 TeV) is indicated. Figure presented in Ref. [13].

17.3 | Search for shower-like signatures

In this section, a search for a neutrino flux from the FB is performed using shower-like event signatures reconstructed with the TANTRA [170] algorithm. While ANTARES has a higher effective detector volume and better direction resolution on track-like events, the shower channel has a lower atmospheric neutrino background, which has a lower contribution from $\vec{\nu}_e$ compared to $\vec{\nu}_\mu$. The former naturally produce shower-like event signatures, while the latter appear mostly track-like in the detector. Also, the extension of the FB is large compared to the $\sim 3^\circ$ median angular resolution of the shower reconstruction algorithm. The presented search is the first analysis of the FB using shower-like events and follows the key points outlined in Sec. 17.1.

17.3.1 | Data pre-selection of the shower analysis

For the shower analysis, all recorded runs with stable data-taking conditions are selected using the criteria in Sec. 16.3.3. In the ANTARES dataset from 2008 to 2015, a total livetime of 2097 days is used.

Atmospheric neutrinos may only be discriminated from a FB signal thanks to their softer energy spectrum. As a consequence, a lower cut on the energy estimate E_{shower} is imposed. The possibility of using the number of hits used by TANTRA as an alternative estimate for the neutrino energy was considered, but showed worse separation between the two neutrino flux components. As for the track sample, the event rate of reconstructed showers is dominated by atmospheric muons which reach the detector from above. Other analyses have shown, that in the shower channel, the atmospheric muon background can still be suppressed sufficiently when accepting reconstructed directions slightly above the horizon, up to $\cos(\theta_{z,\text{shower}}) < 0.1$.

Since many mis-reconstructed atmospheric muons have their fitted shower vertex far out-

Table 17.3: List of selection cuts for shower events. Further details on the parameters are given in the text. Cuts labeled with (*) have been optimised to yield the optimal sensitivity for a neutrino cut-off at 50 TeV. The others have been applied for pre-selection.

parameter	cut value			
R_{shower}	< 300 m	...		
$ z_{\text{shower}} $	< 250 m	$\cos(\text{zenith}_{\text{shower}})$	< 0.1	(*)
M_{est}	< 1000	β_{shower}	$< 30^\circ$	(*)
GridFit_R	> 0.7	RDF	> 0.4	(*)
does not pass track selection		L_{shower}	> 20	(*)
...		E_{shower}	> 2290 GeV	(*)

side the detector, only events reconstructed close to the instrumented volume are selected. Consequently, the radial and vertical distance from the detector centre are restricted to

$$R_{\text{shower}} < 300 \text{ m} \quad \text{and} \quad |z_{\text{shower}}| < 250 \text{ m}, \quad (17.9)$$

respectively. In addition, only events that did not pass the final event selection of the track analysis are accepted. This ensures that the analysed event samples are disjoint, which simplifies the combination of track and shower results afterwards (in [Sec. 17.4](#)).

To further reduce the contribution from atmospheric muons and reject badly reconstructed events in the analysis, a series of additional selection cuts is applied. Events are selected based on output parameters provided by the TANTRA shower reconstruction algorithm:

- the M_{est} parameter defined in [Eq. 16.3](#),
- a cut on the shower likelihood ratio, L_{shower} , which uses information of the shower hits used in the fit, and
- a cut on the angular error estimate β_{shower} .

Then, two additional cuts on quality parameters from other reconstruction algorithms are used, namely

- the quality parameter of a grid-scan based track reconstruction algorithm, R_{GridFit} , and
- the RDF output variable of a Random Decision Forest classifier trained on the fit result of a second shower reconstruction algorithm, named *Dusj* [[174](#)].

The mentioned selection variables are summarised in [Tab. 17.3](#), their optimal values listed are optimised in [Sec. 17.3.2](#) below.

Data and Monte Carlo have been compared for these analysis variables with only the position/direction pre-selection and the anti-track-analysis cut applied, and in addition:

$$M_{\text{est}} < 1000, \quad \beta_{\text{shower}} < 30^\circ, \quad R_{\text{GridFit}} > 0.7. \quad (17.10)$$

That is, only a basic and loose quality pre-selection is imposed for a first comparison between data and Monte Carlo.

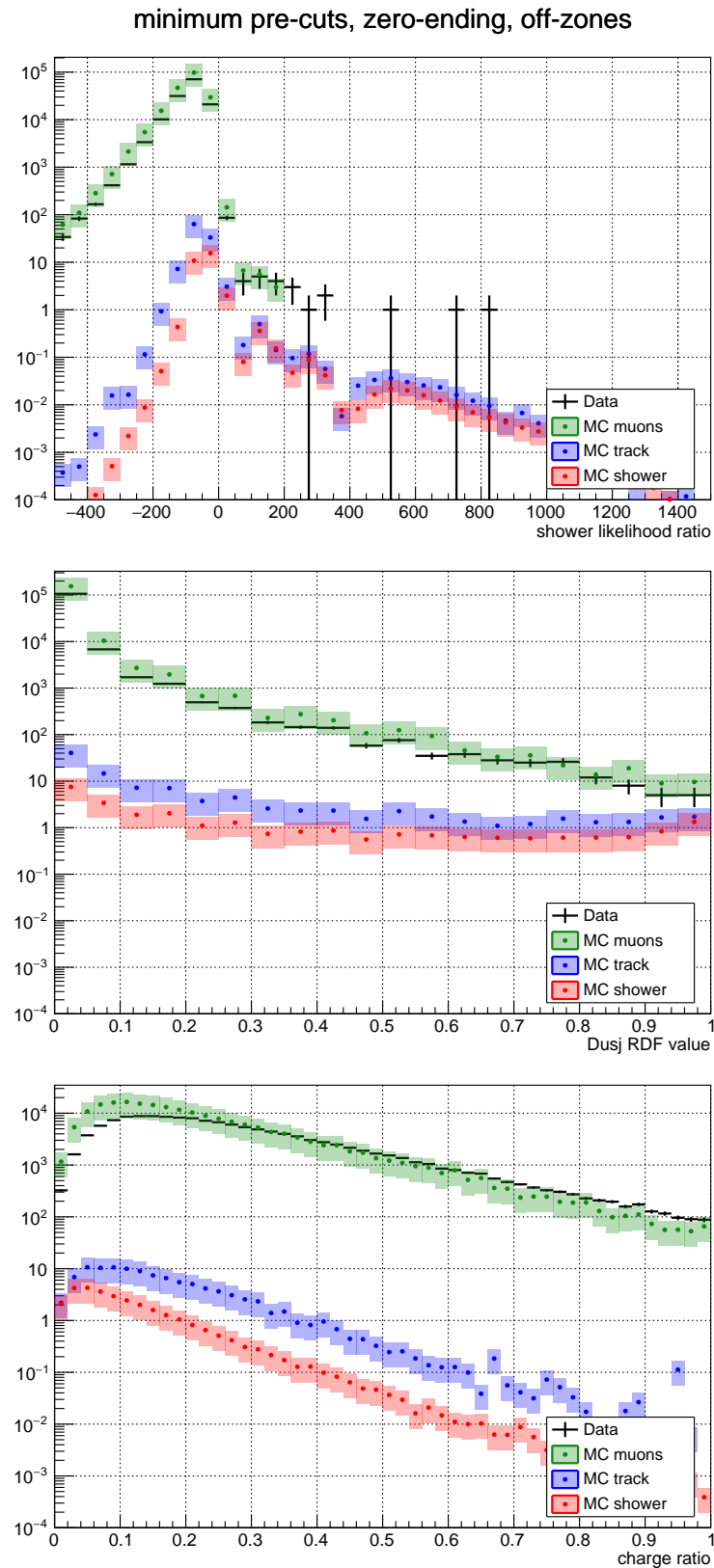


Figure 17.9: Agreement between data and Monte Carlo simulation for the quality parameters L_{shower} (top), RDF (middle), and the charge ratio parameter (bottom). The last was removed from the analysis due to the poor agreement. The comparison shows pre-selected events in the burn sample which are reconstructed in the off-zones.

17. All-flavour search for neutrinos from the Fermi Bubbles at high Galactic latitudes

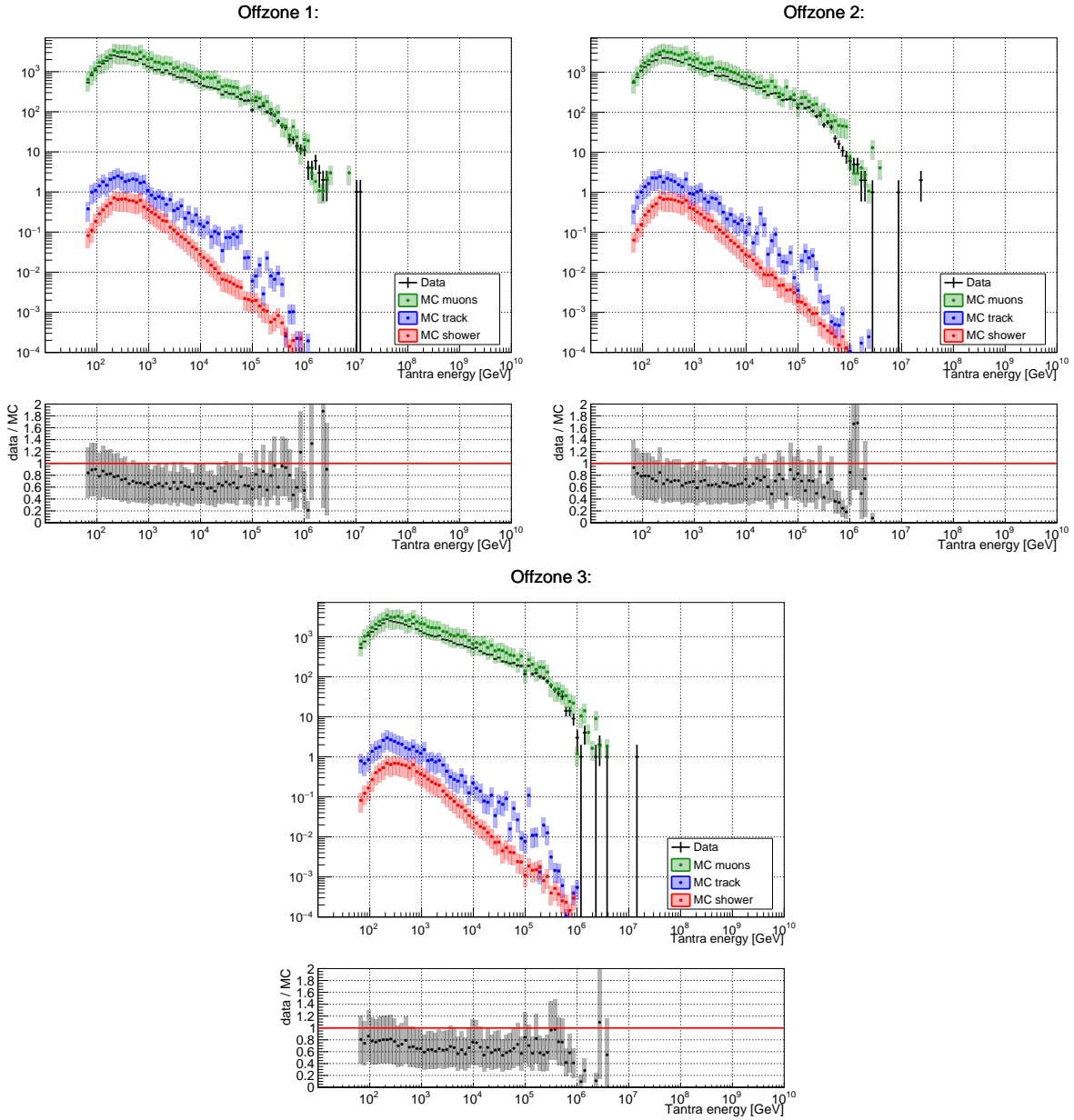


Figure 17.10: Agreement between data and Monte Carlo simulation for the shower energy estimate E_{shower} in the three off-zones after minimum pre-selection cuts.

In this comparison, an additional charge ratio variable showed poor agreement and was not considered further, although it had been proposed in the first shower analysis using TANTRA [168]. In accordance with other shower analyses (e.g. [171]), the RDF variable is used instead. All other listed parameters above showed good agreement when comparing first the all-sky distributions in the burn sample, and thereafter selecting only events reconstructed within the off-zones. The level of agreement is shown exemplarily in Fig. 17.9 for the quality parameters L_{shower} and the RDF value. Also, the excluded charge ratio parameter is provided, for which the shape is tilted in data with respect to Monte Carlo.

The agreement in the off-regions as a function of E_{shower} is presented in Fig. 17.10 for the three off-zones. They show excellent agreement in shape when comparing the distributions amongst off-zones. Also, data and Monte Carlo agree in shape, however with a 30% excess in simulated muons.

17.3.2 | Analysis cut optimisation

To obtain the most stringent upper limit on the signal flux, the MRF technique in Eq. 17.1 is used to optimise the selection cuts in the analysis. The minimum MRF is obtained by using a fine binning in E_{shower} and a coarse scan in the parameters $\cos(\theta_{z,\text{shower}})$, β_{shower} , L_{shower} and RDF . The optimisation is performed for the different assumed values for the flux cut-off down to 50 TeV. The resulting cuts on the quality parameters remain unchanged with respect to the cut-off value. In the optimisation, only the cut on the shower energy variable depends strongly on the assumed signal cut-off, and is presented as a one-dimensional scan in Fig. 17.11. Individual optimisation results for each of the different flux assumptions are given in Tab. 17.4.

The best found MRF – or flux sensitivity – is a factor ~ 2.4 better for the no cut-off scenario compared to 50 TeV, with expected signal/background ratios of 0.33 and 0.05, respectively. Nevertheless, the optimisation for the 50 TeV cut-off results in an energy cut at $E_{\text{shower}} > 2.29$ TeV, which is used in the un-blinding for the analysis. The full set of final selection cuts is listed in Tab. 17.3. The number of background expected from Monte Carlo simulation with this set of cuts is 8.9 events per off-zone.

The decision to use the 50 TeV cut-off optimisation result, instead of the one for no cut-

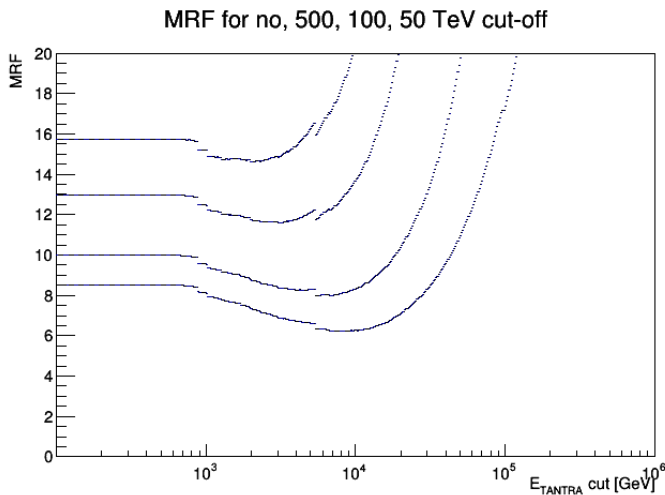


Figure 17.11: MRF optimisation curves as a function of the cut in reconstructed shower energy. For no (lowest curve) to 50 TeV (highest curve) cut-off in the flux spectrum.

Table 17.4: Shower MRF optimisation result for different values for the flux cut-off in neutrino energy.

cut-off	best MRF	$E_{\text{shower,min}}$	N_{signal}	$N_{\text{background}}$
none	6.21	7.59 TeV	0.62	1.89
500 TeV	7.96	5.45 TeV	0.56	3.05
100 TeV	11.6	3.02 TeV	0.50	6.75
50 TeV	14.6	2.29 TeV	0.44	8.91

Table 17.5: MRF values for the resulting optimal shower cut with no / 50 TeV flux cut-offs.

cut-off	$E_{\text{shower}} > 7.59 \text{ TeV}$		$E_{\text{shower}} > 2.29 \text{ TeV}$	
	MRF	N_{signal}	MRF	N_{signal}
none	6.21	0.62	7.24	0.90
500 TeV	8.03	0.48	8.67	0.75
100 TeV	12.5	0.31	11.7	0.55
50 TeV	17.7	0.22	14.6	0.44

off, was made based on the still better compatibility with the HAWK γ -ray flux upper limit shown in Fig. 15.3. The MRF results for the different signal fluxes with the two corresponding optimised cuts are given in Tab. 17.5. With the chosen value $E_{\text{shower}} > 2.29 \text{ TeV}$, the deterioration is only 17% even for the no cut-off scenario and less otherwise. The sensitivity in the shower channel alone is approximately an order of magnitude above the assumed flux. It worsens significantly for even lower cut-off energies due to the dominant atmospheric neutrino flux at low energies.

17.3.3 | Data – Monte Carlo agreement

Good agreement in the off-zones between data and Monte Carlo has been verified also with the final selection excluding the selection cut on E_{shower} for the variables used in the event selection. Only for E_{shower} , data has not been looked at. Instead, only the Monte Carlo distributions are verified to agree between zones. This is shown in Fig. 17.12. In comparison to the distributions after only a loose pre-selection applied (see Fig. 17.10), the atmospheric muon background is clearly suppressed. In addition, the event sample is now dominated by shower-like events at high reconstructed energies E_{shower} .

Before un-blinding the analysis in the signal region, the quality checks done for the track analysis and defined in Sec. 17.1 are repeated for the shower channel. These validate the use of the data-driven estimate for the background using three off-zones, and exclude systematic biases in the on-zone event count.

The events reconstructed in each of the off-zones are compared by calculating the relative difference of events between zones, diff_{ij} , as given in Eq. 17.4. The difference is calculated for the different possible cut values on the parameters used during the optimisation².

²I.e. for cut values of the parameters indicated with (*) in Tab. 17.3

17. All-flavour search for neutrinos from the Fermi Bubbles at high Galactic latitudes

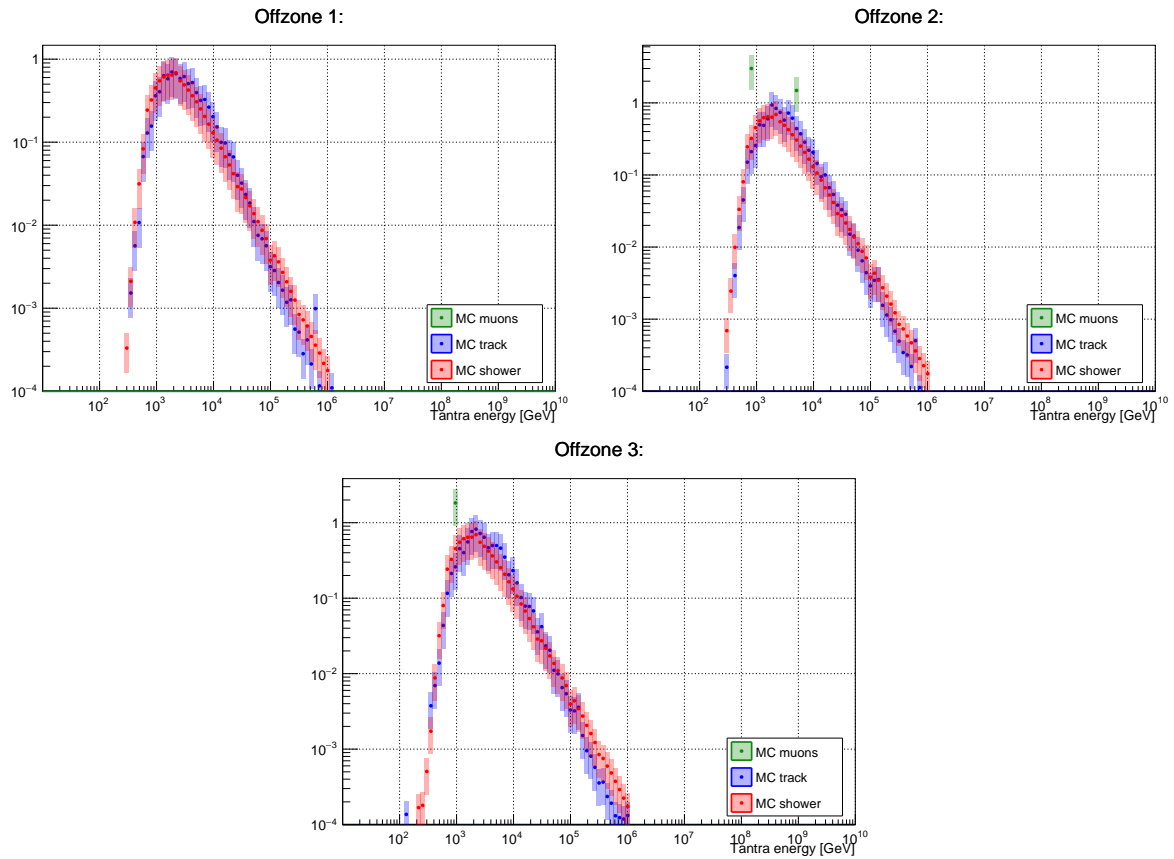


Figure 17.12: Monte Carlo agreement between the three off-zones for the shower energy estimate E_{shower} with the final event selection cuts except the cut on E_{shower} applied. Note, that the y -scale differs between panels.

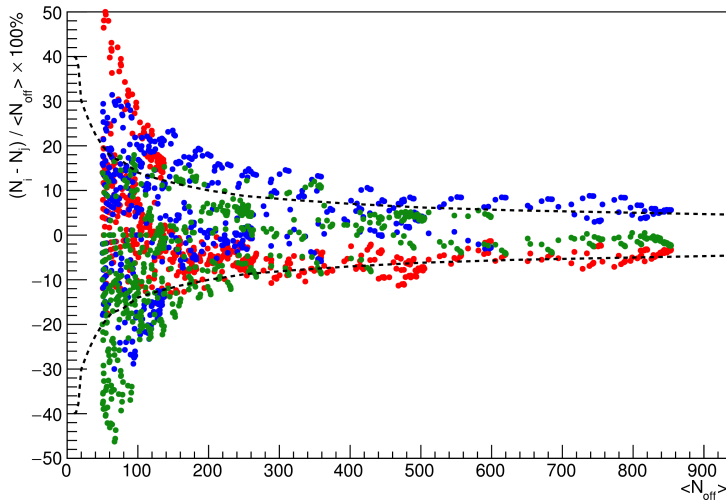


Figure 17.13: Event number differences seen in 2008–2015 shower data between pairs of off-zones $(i,j) = \{(1,2), (2,3), (3,1)\}$ as a function of the mean off-zone count. Points correspond to different cut combinations for variables used in the optimisation. The dashed lines represent the 68% statistical error band.

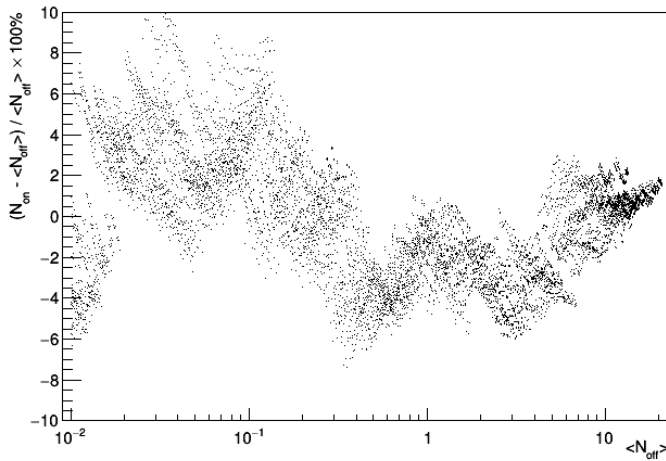


Figure 17.14: Difference between on- and average from the off-zones for a simulated neutrino flux. The difference is shown as a function of the average off-zone count for various different cut combinations on parameters used in the cut optimisation.

The result of this quality test is presented in [Fig. 17.13](#). The majority of points agree with the 68% (1σ CL) statistical error band, which in analogy to the track analysis is calculated for random Poisson fluctuation of the off-zone event count. From [Fig. 17.13](#), no significant bias in the numbers of events arriving from the individual off-zones is expected. The cut values are again not scanned down to only few remaining events to leave the final event count blinded.

The data in the on-zone is not looked at before the final selection cuts are defined. Therefore, the agreement between on- and off-zones is verified based on simulated neutrino Monte Carlo only. [Figure 17.14](#) shows the comparison between the number of simulated events arriving from the signal region with the average over the three off-zones using the calculation defined in [Eq. 17.5](#). From this, agreement between on- and off-zones on the few-percent level is expected. The difference was formed using simulations of neutrino events only in order to not be affected by statistical fluctuations of the MUPAGE simulations of atmospheric muons.

With the shown agreement of the off-zone simulations among each other at the final cut level, the agreement amongst off-zones based on data and the agreement between off-zones and the on-zone using Monte Carlo simulated neutrinos, the shower analysis is un-blinded with the selection stated in [Tab. 17.3](#).

17.3.4 | Observed shower events

Applying the event selection described above to the 2008-2015 dataset comprising 2097 days livetime, a total of 40 events are observed in the three off-zones, resulting in an expected background of 13.3 events for the signal region. Here, 16 events are detected. This corresponds to a small and non-significant excess of 0.6σ in the shower channel alone using the method by Li and Ma (see Eq. 17.6). The E_{shower} distribution of the events in the on- and off-zones is presented in Fig. 17.15. Observed event counts in the zones slightly exceed the atmospheric Monte Carlo expectation indicated in green. The range of assumed model fluxes is indicated by the blue histograms. Especially for the 50 TeV cut-off (lower curve), the modelled signal is small compared to the atmospheric backgrounds. To account for flux uncertainties, an additional 30% error on the neutrino flux is included in the error bands. In the selected event sample, the statistics of simulated atmospheric muons is extremely low, which might explain the small excess of events seen in data with respect to the simulations. Single events could also be contributed from an isotropic astrophysical neutrino flux. For the evaluation of the analysis results however, the background is determined from off-zones without use of Monte Carlo simulations. Here, the event distribution in the on-zone is in excellent agreement with the off-zones.

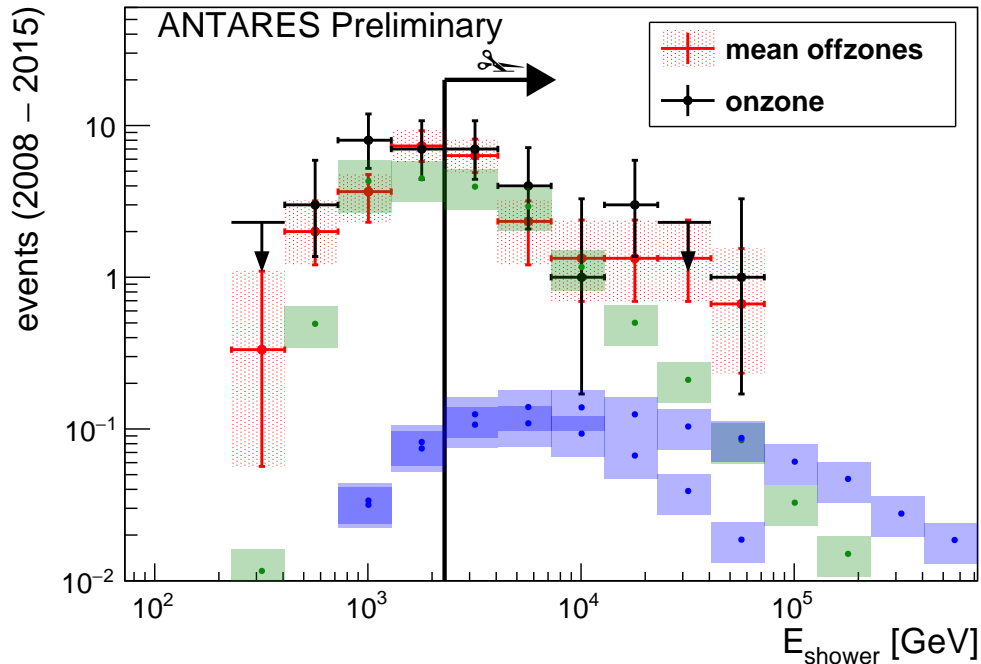


Figure 17.15: Energy distribution of data (including 1σ Poisson intervals) in the shower analysis with the event selection applied. The sum of the simulated Monte Carlo expectation from atmospheric and the possible Fermi Bubble flux with 50 TeV cut-off and no cut-off are shown as green and blue bands, respectively. The cut on the energy estimate $E_{\text{shower}} > 2.29$ TeV is indicated. Figure presented in Ref. [12].

17.4 | All-flavour result and combined flux upper limits

Since events in the shower analysis were preselected to exclude all events that entered the track analysis, the two analyses have no overlap. This choice of disjoint event samples allows for straightforward combination of the two analyses.

The track analysis has observed 28 on-zone events with a background expectation of 19.7 in 1765 days of livetime. The shower analysis has found 16 events with an expected background of 13.3 in 2097 days. The event numbers of both analyses thus are of similar magnitude.

While small over-fluctuations in the signal region with respect to the expected background are found both in the track (1.5σ) and in the shower analysis (0.6σ) for data recorded between 2008 and 2015, they are too small to claim evidence for an observed neutrino flux from the Fermi Bubbles at high latitudes. Therefore, the on-zone counts and the off-zone counts per zone observed in the track (t) and shower (s) analyses ($N_{\text{on},t/s}, \bar{N}_{\text{off},t/s}$) are used to derive combined 90% CL upper limits on the Fermi Bubble neutrino flux (cf. Eq. 17.7),

$$\Phi_{90\%} = \Phi_{\text{model}} \times \frac{\mu_{90\%} (N_{\text{on},t} + N_{\text{on},s}, \bar{N}_{\text{off},t} + \bar{N}_{\text{off},s})}{s_t + s_s}. \quad (17.11)$$

The modelled signal in the track and shower analysis, $s_{t/s}$, is tabulated in Tab. 17.6. As before, the $\mu_{90\%}$ represent 90% CL Feldman and Cousins upper bounds assuming the on-zone count is a mere background fluctuation. The way of combining the track and shower analysis is valid since the overall background counts and the expected number of signal events are of similar size.

Resulting upper limits are put in the neutrino energy region where the central 90% of the possible signal from the track and shower channel ($s_{t/s}$) overlap. The result is shown in Fig. 17.16. The stated bounds account for statistical uncertainties and do not include additional systematics. The latter can be expected from inaccurate modelling of the PMTs' quantum efficiencies and the assumed absorption length of the sea water. They would however only enter the calculation in the denominator in Eq. 17.11. An accurate systematic error may be taken into account beyond the scope of this thesis using the later run-by-run v4 simulations with appropriate systematics runs simulated.

The reported upper limits are higher than the sensitivity of ANTARES due to the observed excess in both channels. Thanks to the inclusion of showers, the resulting combined upper limits are a factor 0.72 (no cut-off) to 0.61 (50 TeV cut-off) more stringent compared to the upper limits obtained from the track analysis alone [13].

Table 17.6: Number of signal events expected in the 2008–2015 analyses from Monte Carlo for the track analysis, s_t , and the shower analysis, s_s .

cut-off energy [TeV]	∞	500	100	50
$s_t, E^{-2.18}$ spectrum	1.23	0.94	0.59	0.42
$s_s, E^{-2.18}$ spectrum	0.90	0.75	0.55	0.44

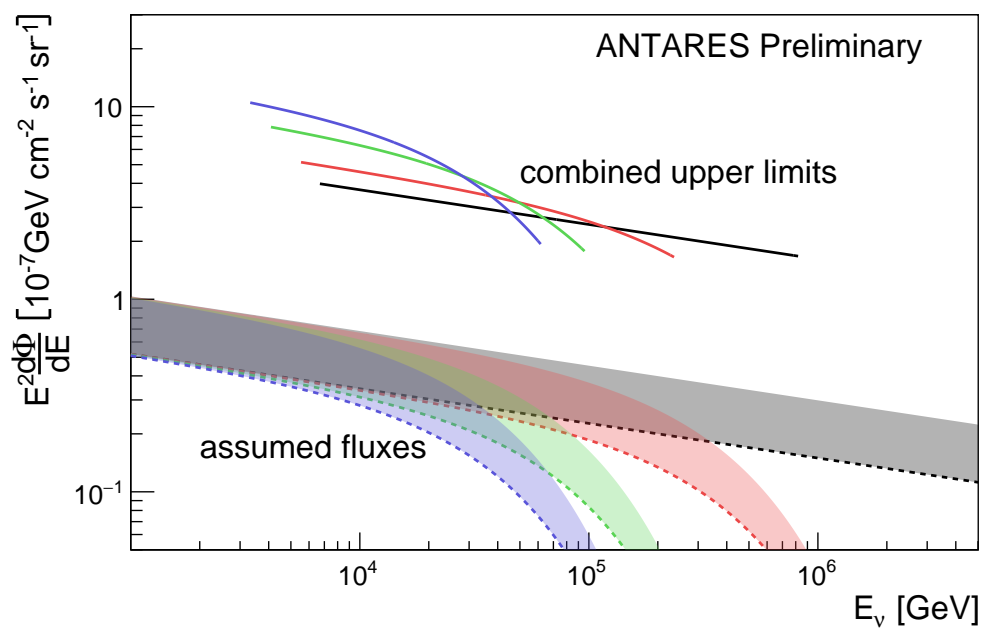


Figure 17.16: Combined 90% CL upper limits on the neutrino flux from the Fermi Bubbles for 50 TeV, 100 TeV, 500 TeV and no cut-off. Upper limits are restricted to the regions where the central 90% of signal from the track and shower channel overlap. Figure presented in Ref. [12].

18 Prospects for detecting low-latitude emission with ANTARES

The first FB analyses by Fermi-LAT at high latitudes have masked the region below $|b| < 10^\circ$ to avoid contributions from the Galactic disk in the analysis. More recently, the γ -ray emission in the vicinity of the GC has been studied and revealed a bright emission zone with a slight offset from the GC, which matches a FB template spectrum. This emission is particularly interesting for neutrino telescopes not only because of its high flux and hard spectrum, but also could an offset from the GC be an indication for a likely hadronic origin, e.g. a contribution from starburst activity or supernova remnants.

The ANTARES sensitivity in this central region is estimated assuming a box-shaped emission region in the Galactic longitude range $-10^\circ < l < 0^\circ$ and the Galactic latitude range $-3^\circ < b < +3^\circ$. This area corresponds to 0.018 sr in solid angle. In comparison, the hour-glass shape used for the high latitude analysis was ~ 0.76 sr and therefore a factor 42 larger in size. The smaller size allows to define a large set of off-zones even when allowing for a safety margin around the high latitude bubbles, as demonstrated with the use of 18 off-zones in Fig. 18.1.

Preliminary results suggested [178] that in this search box a hard $\sim E_\gamma^{-2}$ spectrum and a flux $E^2 \frac{d\phi_\gamma}{dE} = 7 \times 10^{-6} \text{ GeV cm}^{-2} \text{ s}^{-1} \text{ sr}^{-1}$ is an optimistic but still realistic assumption. This flux is about a factor 10 higher than in the high latitude bubbles. In addition Fermi-LAT data showed no clear indication of a cut-off at low energy. Comparison with the final published

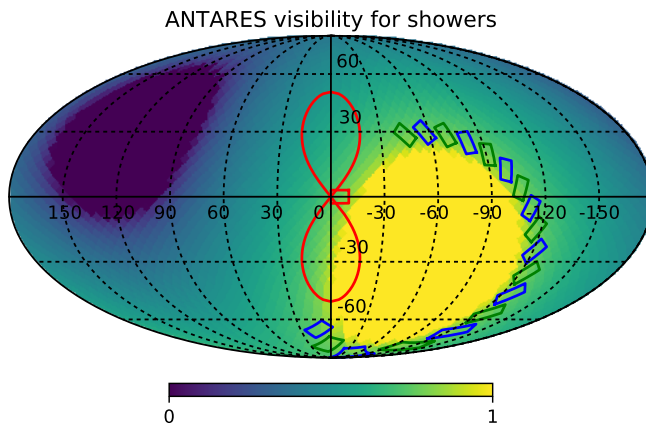


Figure 18.1: Possible definition of 18 off-regions for a small $10^\circ \times 6^\circ$ central search region.

Table 18.1: Estimated number of low-latitude signal events in the on-zone and background in 18 off-zones from Monte Carlo in the 2096 days livetime used for the shower analysis.

	background		signal / cut-off [TeV]				
	atm μ	atm. ν	no cut-off	500	100	50	10
track analysis	0	8.42	4.41	2.77	1.46	0.94	0.19
shower analysis	4.8	4.40	1.69	1.32	0.89	0.68	0.23
sum	4.8	12.82	6.10	4.09	2.35	1.62	0.42

analysis result [160] in Fig. 14.3 shows, that this assumed flux is far off the fitted maximum model ($E^{-2.09}$ spectrum) for the low latitude emission, although the authors suggest a cut-off in the 10 – 50 TeV range.

Neglecting differences in the visibility, the background can first be roughly estimated by a mere scaling of the background events observed in the high-latitude track (19.7 events / 1765 days) and shower analyses (13.3 events / 2096 days). This scaling yields an expected background derived from the high-latitude data of 0.9 events (0.3 shower, 0.6 track) for 2096 days of livetime. Note that a future analysis will include the additional years from 2016 onwards and thus analyse a longer livetime.

For a sensitivity estimate, the simulated Monte Carlo data from the track and shower analyses can be used in the new on- and off-regions in Fig. 18.1, while leaving the analysis selection cuts unchanged. Since the analysis cuts could be re-optimised for the higher signal flux and the modified size, the derived sensitivity estimate will be conservative. The remaining background events in the 18 off-zones and signal events for different cut-off energies in the on-zone are tabulated in Tab. 18.1. Scaling the background contribution to one zone results in a background expectation of $8.4/18=0.47$ events in the track channel and $(4.4+4.8)/18=0.24+0.27$ events in the shower channel. The expectation of ~ 1 background event per zone is therefore consistent with the expectation derived from the high-latitude data, although the single atmospheric muon event surviving the zone selection with a high weight leads to some uncertainty. In the most optimistic scenario from Tab. 18.1, an E^{-2} flux with no cut-off, 4.4 track and 1.7 shower signal events are expected, significantly exceeding this assumed background.

The flux sensitivity (Eq. 17.1) is given by the assumed model flux multiplied by the model rejection factor MRF. Given the expectation of ~ 1 background event with some uncertainty, the MRF is presented as a function of the expected signal events for 1–3 background events in Fig. 18.2. From the expected signal events in Tab. 18.1, it can be concluded that ANTARES is sensitive to constrain cut-off energies above $\sim 200 - 500$ TeV for the assumed model flux. The constraint will however be loosened in case of a softer signal spectrum or in scenarios with less than 100% hadronic emission. A measurement of the low-latitude γ ray flux with Imaging Air Cherenkov Telescopes (the current HESS Telescope, or the future CTA) could provide valuable input to refine the assumed model flux.

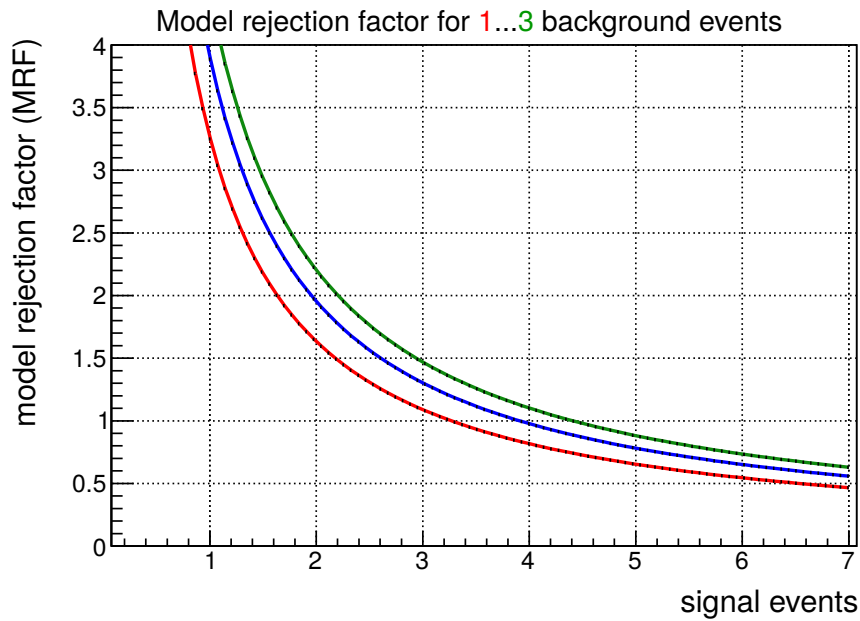


Figure 18.2: Model rejection factor for 1, 2 and 3 measured background events as a function of the expected number of signal events. For $MRF < 1$, the analysis is sensitive to set an upper limit below the assumed model flux.

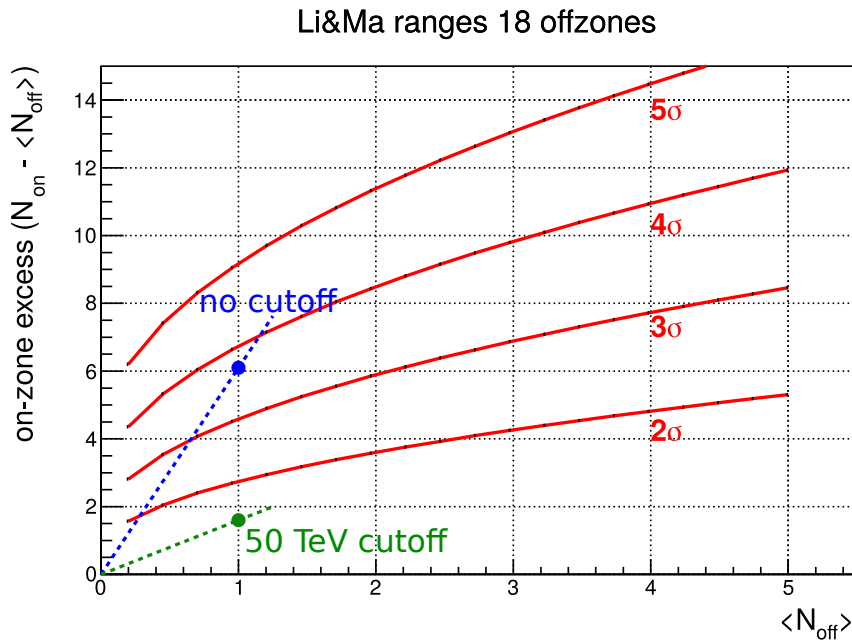


Figure 18.3: Li and Ma significance (Eq. 17.6) for on-zone excess as a function of the expected background for 18 off-zones. Added points correspond to the presented 2096 day livetime expectations for no/50 TeV energy cut-off.

19 Conclusion on Part III and prospects for observing a Fermi Bubble neutrino flux

In this part, data collected with the ANTARES telescope between 2008 and 2015 are analysed to search for neutrino emission from the Fermi Bubbles at high Galactic latitudes, two giant lobes of γ -ray emission observed by Fermi-LAT. The analysis uses data observed in three off-zones to derive the background expectation in the signal region. Data are analysed with two individual searches for track- and shower-like event signatures, respectively. The results are then combined to put an all-flavour upper limit on the neutrino flux.

The track analysis in this work extends a previous 6-year analysis of the Fermi Bubbles by two additional years, 2014/15. In 2014/15, 6 events are observed in the on-zone with a background expectation of 6.7. Together with the excess seen in the first six years, 28 track events are observed in the signal region with an expected background of 19.7. The total analysed livetime amounts to 1765 days. Since the event count in the signal region does not exceed the background expectation in 2014/15, the total non-significant excess in the track analysis alone is reduced to 1.5σ CL.

The Fermi Bubble region is analysed for the first time also using shower-like event signatures in the same period from 2008 to 2015. A different procedure of selecting data-taking runs while taking into account the expected signal in case no corresponding Monte Carlo simulations are available, allows for an increased livetime of 2097 days in the shower analysis. In the on-zone, 16 events are observed with an expected 13.3 background events. Again, the small excess found is non-significant, 0.6σ CL.

The results of the shower and track analyses are then combined and an overall 90% CL flux upper limit is put in the ~ 10 – 100 TeV neutrino energy region. The assumed signal flux is modelled to follow an $E^{-2.18}$ spectrum with several assumed exponential cut-off energies above 50 TeV.

With the recent upper limits on the high energy photon flux from the Fermi Bubbles, more optimistic assumptions for the neutrino flux to which ANTARES is most sensitive are disfavoured. The derived combined upper limits are consequently an order of magnitude above the tested flux with an $E^{-2.18}$ spectral index. Owing to the seen excess, they are above the flux sensitivities of ANTARES.

Since ANTARES is continuing to take data still in 2020, and possibly beyond, the analysed dataset can be extended by the additional years from 2015 onwards. Since meanwhile a consistent Monte Carlo dataset taking into account the efficiency loss of the ANTARES OMs is available, the addition of the new years should face no major obstacles. However, at large latitudes, the more recent analyses of the Fermi-LAT γ -ray data tend to disfavour even the $E^{-2.18}$ model fluxes with high cut-off energies assumed in the analysis, reducing the sensitivity of ANTARES to the allowed neutrino flux. In eight years of ANTARES data, a small excess of neutrino candidate events from the regions of the high-latitude Fermi Bubbles has been observed. It is nevertheless interesting if the found excess is also observed in additional data or

whether more stringent upper limits on the neutrino flux can be set.

More recently, a bright emission region near and slightly offset with respect to the Galactic Centre has been identified in γ -rays. While this region is about 40 times smaller compared to the high latitude bubbles, the observed γ -ray spectrum is hard, compatible with $\sim E^{-2}$ and may extend beyond TeV energies.

Using the analysis selection of the track and shower analysed at high latitudes without further optimisation, the sensitivity of ANTARES to measure a low-latitude Fermi Bubble flux in this region is estimated.

If the γ -ray excess found has a corresponding neutrino flux extending to high energies, ANTARES is sensitive to constrain cut-off energies above ~ 200 – 500 TeV on the assumed model flux, provided the emission has a purely hadronic origin. Further optimisation and additional data will also increase the sensitivity for low latitudes making it an interesting target for future searches.

All neutrino searches for a Fermi Bubble emission would benefit from a more accurate flux prediction if the γ -ray flux was known accurately beyond TeV energies. Future measurements with Imaging Air Cherenkov Telescopes could provide this input removing the need to extrapolate the γ -ray fluxes measured by Fermi-LAT by about three orders of magnitude [179].

Currently, no evidence for a neutrino excess from the Fermi Bubbles region is observed in IceCube data [180, 181]. Icecube, due to its location at the South Pole, can observe the region mostly using shower events reaching the detector from above. The detectors in the northern hemisphere, currently ANTARES and also the GVD detector in lake Baikal have a good view towards the Fermi Bubbles region. In future, the KM3NeT/ARCA detector under construction in the Mediterranean Sea will improve the event statistics and the sensitivity in the region of the bubbles [182]. In particular, the direction resolution of the instrument and its view towards the central region of our Galaxy is suitable to search also for a corresponding neutrino flux in the bright low-latitude γ -ray emission region. The sensitivity to the low-latitude emission with KM3NeT/ARCA has been evaluated and a neutrino signal is expected to be observable within five years of operation with one building block (50% of what is foreseen in the Letter of Intent for KM3NeT 2.0 [1]) even for pessimistic cut-off energies at ~ 100 TeV. However, as the construction of ARCA is still in the beginning, the more than ten years of data recorded with ANTARES are a valuable dataset to look for a neutrino emission from the Fermi Bubbles in the near future.

List of Abbreviations

AAFit	ANTARES track fit
ANN	A Neural Net, used to estimate track energy in ANTARES
CC	charged current
CL	confidence level
CNN	Convolutional Neural Net
CP	charge parity
CR	cosmic ray
DOM	KM4NeT Digital Optical Module
DU	KM3NeT Detection Unit
Dusj	Shower reconstruction algorithm
EID	Event IDentification
FB	Fermi Bubbles
GC	Galactic Centre
HRV	High Rate Veto
IO	Inverted Mass Ordering
JGandalf	KM3NeT track reconstruction algorithm
JPP	the KM3NeT C ⁺⁺ -based analysis software framework
JTE	JTriggerEfficiency, the trigger software of KM3NeT
LoI	Letter of Intent for KM3NeT 2.0
MC	Monte Carlo
MONA	oscillation analysis framework for ORCA
MRF	Model Rejection Factor
NC	neutral current
NMO	Neutrino Mass Ordering
NO	Normal Mass Ordering
OM	ANTARES Optical Module
ParamNMH	parametrisation-based oscillation analysis framework for ORCA
PDF	Probability density functions
PMT	photomultiplier tube
POT	protons on target
PREM	Preliminary Reference Earth Model, the matter density of the Earth
QE	quantum efficiency
RDF	Random Decision Forest
SM	Standard Model of particle physics
SN	supernova
SWIM	oscillation analysis framework for ORCA
TANTRA	ANTARES shower reconstruction algorithm

List of Figures

1.1	Mass spectra of the fermions of the Standard Model	3
1.2	Artists' impressions of ANTARES and KM3NeT	4
1.3	Feynman diagrams for the fundamental CC and NC interaction vertices	6
2.1	Neutrino flux across energy scales	7
2.2	Contributions from air shower components to the atm. ν flux	10
2.3	Flavour ratios of atm. ν / atm. μ at ground level	11
2.4	Energy dependency of the atmospheric neutrino flux (HKKM)	11
2.5	Zenith angle dependency of the atmospheric neutrino flux (HKKM)	12
3.1	Earth matter density profile (PREM)	14
3.2	Two-flavour oscillation formula in atmospheric/galactic units.	18
3.3	Feynman graphs for the coherent forward scattering of neutrinos.	18
3.4	Matter density profile vs. ν_τ appearance probability	20
3.5	OscProb oscillation probabilities vs. E_ν and $\cos(\theta_z)$	21
4.1	Intrinsic scattering angle in neutrino interactions	22
4.2	Feynman-like diagram for deep inelastic neutrino–nucleon scattering	23
4.3	Total CC cross section per nucleon for ν_μ and $\bar{\nu}_\mu$	24
5.1	Cherenkov effect: Dielectric medium and Cherenkov angle	26
5.2	Absorption lengths in sea water	28
5.3	Light transmittance of components in the KM3NeT DOM	29
5.4	Optical background rates of adjacent DOMs	30
5.5	Schematic illustrations of different event topologies	32
5.6	Trigger effective volumes of ANTARES, ORCA, and ARCA	34
6.1	First observation of atmospheric $\bar{\nu}_\mu$ dis-appearance	38
6.2	Graphical representations of the CKM and PMNS matrices	39
6.3	Unitarity constraints in rows/columns of the mixing matrix	41
6.4	Graphical representation of the PMNS matrix with(out) unitarity	41
6.5	Cross section predicted by GENIE for ν_τ and $\bar{\nu}_\tau$	42
6.6	$\sigma_{\bar{\nu}_\tau}^{\text{CC}}/\sigma_{\bar{\nu}_\mu}^{\text{CC}}$ total cross section ratio	43
6.7	Differential DIS cross section for $\bar{\nu}_\tau^{\text{CC}}$	44
6.8	Feynman diagram for leading order τ decays	44
6.9	DONUT ν_τ CC candidate event	46
6.10	ν_τ CC interactions in OPERA for the integrated CNGS POT	47
6.11	ν_τ CC interactions in DUNE for the annual LBNE POT	48

List of Figures

6.12	ν_τ CC interactions per megaton for the annual atmospheric flux	49
6.13	Current constraints of $\bar{\nu}_\tau$ appearance	50
6.14	Computation scheme for event distributions in oscillation analyses	51
7.1	KM3NeT Digital Optical Module and furled Detection Unit	52
7.2	DOM detection efficiency vs. photon arrival direction	53
7.3	ORCA detector layout	55
8.1	Software chain of ORCA	56
8.2	Exclusive in-situ DOM coincidence rates	59
9.1	ORCA online monitoring $z - t$	62
9.2	Trigger efficiency comparison MXShower vs. 2L2	63
9.3	Triggered pure noise rate for 3D triggers	64
9.4	Combined pure noise rate of the 3D triggers	65
9.5	Pure noise rate of the MXShower wrt. N_{hits} and D_{max}	66
9.6	MXShower effective volume ratios for different N_{hits}	66
9.7	MXShower effective volume evolution for extreme values of D_{max}	67
9.8	MXShower effective volume ratios for different N_{modules}	67
9.9	Trigger effective volumes for a scan of the MXShower D_{max}	69
9.10	Trigger efficiency with and without MXShower	70
9.11	Trigger effective volume evolution wrt. the LoI	70
9.12	Trigger effective volume new 23 m detector vs. LoI	71
9.13	ORCA-4/ORCA-6 mean optical rates (01/07/2019 – 01/03/2020)	72
9.14	PMT rate distribution for ORCA-6	73
9.15	Bioluminescence simulator baseline rate scenarios	73
9.16	Trigger rates for different bioluminescence simulator models	74
9.17	Efficiency loss from disabled channels	74
9.18	Efficiency loss from disabled PMTs/DOMs/DUs	75
9.19	ORCA-4/ORCA-6 high rate veto fractions (01/07/2019 – 01/03/2020)	76
9.20	HRV and broken channel induced loss in triggered neutrinos	76
9.21	ORCA trigger rate online monitor	77
9.22	Atmospheric muon trigger rate vs. number of DUs	77
9.23	Super-ORCA trigger effective volume ($\bar{\nu}_e^{\text{CC}}$, $\bar{\nu}_\mu^{\text{CC}}$) with different spacings	79
9.24	Super-ORCA trigger effective volume (10 m horizontal spacing)	79
10.1	Chart of reconstruction steps for Dusj (shower reconstruction)	81
10.2	Chart of reconstruction steps for JGandalf (track reconstruction)	81
10.3	Geometric containment for track events	83
10.4	Geometric coverage for shower events	85
10.5	Events remaining after subsequent event selection stages	86
11.1	Schematic representation of a Random Decision Forest	90
11.2	Five-fold cross validation scheme	92
11.3	Atmospheric muon classification result	95
11.4	Pure noise classification result	96
11.5	Track score as a function of Bjorken y for $\bar{\nu}_\mu^{\text{CC}}$	98

11.6	Results from hyperbolic tangent fits to the median track scores	99
11.7	Minimum muon energy needed for clear identification as track	100
11.8	Track-shower separability for the RDF classifier	101
11.9	Fractions of events classified as track/shower/middle vs. neutrino energy. . .	102
11.10	Track-shower classification of $\bar{\nu}_{\tau}^{\text{CC}}$ events	102
11.11	Effective volume of the 20 m ORCA detector at analysis stage, after EID and event selection	104
11.12	Energy resolution for 115 DU ORCA for tracks and showers	104
11.13	Energy resolution for 115 DU ORCA for the middle class	105
11.14	Angular resolution of $\bar{\nu}_{\mu}^{\text{CC}}$ and $\bar{\nu}_{e}^{\text{CC}}$ for 115 DU ORCA	105
11.15	Median angular resolution for 115 DU ORCA	106
12.1	Reconstructed event distribution in the analysis sample per EID class for $\bar{\nu}_{\tau}^{\text{CC}}$ and other flavours in the 20 m detector configuration	109
12.2	Statistical per-bin significance for the detected $\bar{\nu}_{\tau}$ signal	109
12.3	Detector effective mass derived from the ParamNMH parametrisation	112
12.4	One-year sensitivity to $\bar{\nu}_{\tau}$ appearance for 115 DU ORCA without systematics	118
12.5	One-year sensitivity to $\bar{\nu}_{\tau}$ appearance for 115 DU ORCA	119
12.6	Sensitivity to $\bar{\nu}_{\tau}^{\text{CC}}$ appearance vs. operation time for 115 DU ORCA	120
12.7	Sensitivity to exclude non-unitarity vs. operation time for 115 DU ORCA . .	121
12.8	Sensitivity to distinguish $\bar{\nu}_{\tau}$ CC from CC+NC scaling with 115 DU ORCA . .	122
12.9	Influence of systematics	123
12.10	Change of minimum when assuming the wrong neutrino mass ordering	124
12.11	Comparison of the classifier performance in terms of the separation power metric for the 7 DU sub-array	125
12.12	Fractions of events in the 7 DU analysis sample classified as track	126
12.13	Sensitivity to $\bar{\nu}_{\tau}$ appearance with a 7 DU sub-array of ORCA	126
14.1	Fermi Bubbles as seen in γ -rays by Fermi-LAT	132
14.2	Fermi Bubble templates observed by Fermi-LAT	133
14.3	Fermi Bubble low-latitude flux left and and right of the Galactic Centre	134
15.1	On- and off-zones in Galactic coordinates and ANTARES visibility	136
15.2	γ -ray fluxes and $E^{-2.18}/E^{-2}$ analysis spectra	136
15.3	Assumed γ -ray flux from the Fermi Bubbles	138
16.1	ANTARES hits and hit clusters	139
16.2	Long-term monitoring of the OM efficiencies	140
16.3	Quantities used in the TANTRA likelihood function	141
16.4	ANTARES resolutions for tracks and showers	142
16.5	Neutrino loss as function of neutrino energy vs. quantum efficiency	144
16.6	Neutrino loss as function of spectral index vs. quantum efficiency	145
16.7	Run quality: atm. μ dominated data–MC ratio after loose cut on Λ	147
17.1	Average (90% CL) signal upper limits as a function of the background count . .	150
17.2	Li and Ma significances evaluated for three off-zones	152
17.3	Events as a function of Λ in the off-zones	154

17.4	Cumulative distributions in E_{ANN} for the 2014/15 burn sample	155
17.5	Comparison of 2014/15 data and corresponding Monte Carlo in the off-zones for the reconstructed energy E_{ANN}	155
17.6	Event number differences between off-zones in 2014/15 tracks	157
17.7	On-/off-zone difference expected from Monte Carlo in the track analysis . . .	157
17.8	Energy distribution of events selected in the track analysis	159
17.9	Agreement between data and Monte Carlo simulation for the quality parameters in the shower analysis	161
17.10	Off-zone agreement between data and Monte Carlo for E_{shower}	162
17.11	MRF optimisation curves as a function of the cut in reconstructed shower energy	163
17.12	Off-zone agreement in shower energy for Monte Carlo, final selection	165
17.13	Event number differences between off-zones in 2008–2015 showers	166
17.14	On-/off-zone difference expected from Monte Carlo in the shower analysis .	166
17.15	Energy distribution of events selected in the shower analysis	167
17.16	Combined 90% CL upper limits on the neutrino flux from the Fermi Bubbles .	169
18.1	Possible definition of 18 off-regions for a small $10^\circ \times 6^\circ$ central search region.	170
18.2	MRF as function of signal and background events	172
18.3	Li and Ma significance for 18 off-zones	172

List of Tables

1.1	Fundamental particles of the Standard Model	5
8.1	Simulated event statistics for 115 DU setup with 23m average DU spacing. . .	60
8.2	Simulated event statistics for 7 DU setup with 23m average DU spacing. . . .	60
8.3	Simulated event statistics for 115 DU setup with 20m average DU spacing. . .	60
9.1	Optimised trigger parameters for ORCA (23 m / 20 m spacing)	65
9.2	Optimised MXShower trigger parameters for a SuperORCA detector.	78
10.1	Background rate after trigger and pre-selection for the 23 m ORCA detector .	87
11.1	Settings for the trained Random Decision Forests.	91
12.1	Values for the oscillation parameters used in the $\overleftrightarrow{\nu}_\tau$ appearance fit	114
12.2	Values for the fitted systematics used in the $\overleftrightarrow{\nu}_\tau$ appearance fit.	114
16.1	Livetime per year used for the analysis of the FB with tracks and showers. . .	148
17.1	Event pre-selection and final event selection in the FB track analysis	153
17.2	MRF optimisation result for the 2014/15 track analysis	156

17.3	List of selection cuts used in the Fermi Bubbles shower analysis	160
17.4	MRF optimisation result for the shower analysis	164
17.5	MRFs for the optimal shower cut with no / 50 TeV flux cut-offs	164
17.6	Expected number of signal events in the track and shower analysis	168
18.1	Estimated signal and background for the low-latitude analysis using 18 off-zones	171

Bibliography

- [1] **KM3NeT** Collaboration, S. Adrián-Martínez *et al.*, “Letter of Intent for KM3NeT 2.0” *J. Phys.* **G43** no. 8, (2016) 084001, [arXiv:1601.07459](#) [[astro-ph.IM](#)].
- [2] **KM3NeT** Collaboration, corresponding authors: S. Hallmann, J. Hofestädt, M. Perrin-Terrin, “Determining the Neutrino Mass Ordering and Oscillation Parameters with KM3NeT/ORCA.” Under review by the Collaboration., 2020.
- [3] M. de Jong and the KM3NeT Collaboration, “The JPP Software framework.” <https://git.km3net.de/common/jpp>.
- [4] J. Hofestädt, *Measuring the neutrino mass hierarchy with the future KM3NeT/ORCA detector*. PhD thesis, Friedrich-Alexander-Universität Erlangen-Nürnberg, 2017.
- [5] A. V. Akindinov, E. G. Anassontzis, G. Anton, *et al.*, “Letter of interest for a neutrino beam from Protvino to KM3NeT/ORCA,” *European Physical Journal C* **79** no. 9, (Sep, 2019) 758, [arXiv:1902.06083](#) [[physics.ins-det](#)].
- [6] J. Hofestädt, M. Bruchner, and T. Eberl, “Super-ORCA: Measuring the leptonic CP-phase with Atmospheric Neutrinos and Beam Neutrinos,” *arXiv e-prints* (2019), [arXiv:1907.12983](#) [[hep-ex](#)].
- [7] S. Geißelsöder, “Classification of events for the ANTARES neutrino detector,” Master’s thesis, Friedrich-Alexander-Universität Erlangen-Nürnberg, 2011.
- [8] KM3NeT Collaboration, “ParamNMH, tag v5.1.” <https://git.km3net.de/mperrinterrin/paramNMH.git>, 2020.
- [9] S. Hallmann and B. Strandberg, for the KM3NeT Collaboration, “Neutrino oscillation research with KM3NeT/ORCA,” *Proceedings of the 36th ICRC*, **PoS (ICRC2019) 1019** (2019).
- [10] L. Maderer, “Sensitivity to tau-neutrino appearance with the first seven strings of KM3NeT/ORCA,” Master’s thesis, Friedrich-Alexander-Universität Erlangen-Nürnberg, 2019.
- [11] **ANTARES** Collaboration, S. Adrian-Martinez *et al.*, “A Search for Neutrino Emission from the Fermi Bubbles with the ANTARES Telescope,” *Eur. Phys. J.* **C74** (2014) 2701, [arXiv:1308.5260](#) [[astro-ph.HE](#)].
- [12] S. Hallmann and T. Eberl for the ANTARES Collaboration, “Neutrinos from the Fermi Bubbles with ANTARES,” *Proceedings of the 35th ICRC*, **PoS (ICRC2017) 1001** (2017).

- [13] T. Eberl and S. Hallmann for the ANTARES Collaboration., “A Search for Neutrinos from the Fermi Bubbles with the ANTARES Telescope,” *Proceedings of the Neutrino 2016 Conference* (2016) .
- [14] W. Pauli, “Letter to the Group of "Radioactives"." 1930.
- [15] **Particle Data Group** Collaboration, M. Tanabashi *et al.*, “Review of Particle Physics,” *Phys. Rev. D* **98** (Aug, 2018) 030001.
- [16] J. Cowan, C. L., F. Reines, F. B. Harrison, H. W. Kruse, and A. D. McGuire, “Detection of the Free Neutrino: A Confirmation,” *Science* **124** no. 3212, (Jul, 1956) 103–104.
- [17] T. Schwetz-Mangold, “Neutrino Oscillations and Beyond Standard Model Physics.” Presentation, KIT GK Elementarteilchenphysik, 09, 2015.
- [18] S. F. King, “Neutrino Mass Models,” *Rept.Prog.Phys.* **67** (2004) 107–158, [arXiv:hep-ph/0310204v2](https://arxiv.org/abs/hep-ph/0310204v2).
- [19] I. Esteban, M. C. Gonzalez-Garcia, M. Maltoni, T. Schwetz, and A. Zhou, “The fate of hints: updated global analysis of three-flavor neutrino oscillations,” *arXiv e-prints* (2020) , [arXiv:2007.14792v1](https://arxiv.org/abs/2007.14792v1).
- [20] “KM3NeT homepage.” <https://www.km3net.org>. Accessed: 10/03/2020.
- [21] **ANTARES** Collaboration, M. Ageron *et al.*, “ANTARES: the first undersea neutrino telescope,” *NIM A* **656** (Nov., 2011) 11–38, [arXiv:1104.1607](https://arxiv.org/abs/1104.1607) [[astro-ph.IM](#)].
- [22] **IceCube** Collaboration, W. Y. Ma, “Physics Potential of the IceCube Upgrade,” *J. Phys. Conf. Ser.* **1468** no. 1, (2020) 012169.
- [23] **IceCube Gen2** Collaboration, M. Aartsen *et al.*, “IceCube-Gen2: The Window to the Extreme Universe,” [arXiv:2008.04323](https://arxiv.org/abs/2008.04323) [[astro-ph.HE](#)].
- [24] **Baikal-GVD** Collaboration, A. Avrorin *et al.*, “Neutrino Telescope in Lake Baikal: Present and Future,” *PoS ICRC2019* (2020) 1011, [arXiv:1908.05427](https://arxiv.org/abs/1908.05427) [[astro-ph.HE](#)].
- [25] **ATLAS** Collaboration, “Observation of a new particle in the search for the Standard Model Higgs boson with the ATLAS detector at the LHC,” *Phys. Lett. B* **716** (2012) 1–29, [arXiv:1207.7214v2](https://arxiv.org/abs/1207.7214v2).
- [26] **CMS** Collaboration, “Observation of a new boson at a mass of 125 GeV with the CMS experiment at the LHC,” *Phys. Lett. B* **716** no. 2012, (2012) 30, [1207.7235v2](https://arxiv.org/abs/1207.7235v2).
- [27] U. F. Katz and C. Spiering, “High-Energy Neutrino Astrophysics: Status and Perspectives,” *Prog. Part. Nucl. Phys.* **67** (2012) 651–704, [arXiv:1111.0507](https://arxiv.org/abs/1111.0507) [[astro-ph.HE](#)].
- [28] S. Hannestad, “Cosmological neutrinos,” *New J.Phys.* **6** (2004) 108, [arXiv:hep-ph/0404239v1](https://arxiv.org/abs/hep-ph/0404239v1).

Bibliography

- [29] T. Stanev, “GZK cutoff and associated neutrinos,” *Nuclear Physics B - Proceedings Supplements* **136** (2004) 103 – 110. CRIS 2004 Proceedings of the Cosmic Ray International Seminars: GZK and Surroundings.
- [30] A. L. Connolly and A. G. Viereg, “Radio Detection of High Energy Neutrinos,” [arXiv:1607.08232v1](https://arxiv.org/abs/1607.08232v1).
- [31] L. Köpke, “Improved Detection of Supernovae with the IceCube Observatory,” [arXiv:1704.03823v1](https://arxiv.org/abs/1704.03823v1).
- [32] M. Colomer Molla, A. Coleiro, D. Dornic, V. Kulikovskiy, and M. Lincetto for the KM3NeT Collaboration, “Offline performance studies and first real-time results on Core-Collapse Supernova neutrino searches with the KM3NeT neutrino detectors,” *Proceedings of the 36th ICRC, PoS (ICRC2019)* **857** (2020) .
- [33] **IceCube** Collaboration, “Evidence for High-Energy Extraterrestrial Neutrinos at the IceCube Detector,” *Science* **342** no. 6161, (2013) .
- [34] A. Fedynitch, “MCEq_classic repository.” https://github.com/afedynitch/MCEq_classic. Accessed: 03/04/2020.
- [35] A. Fedynitch, R. Engel, T. K. Gaisser, F. Riehn, and T. Stanev, “Calculation of conventional and prompt lepton fluxes at very high energy,” in *European Physical Journal Web of Conferences*, vol. 99 of *European Physical Journal Web of Conferences*, p. 08001. Aug., 2015. [arXiv:1503.00544](https://arxiv.org/abs/1503.00544) [hep-ph] .
- [36] F. Riehn, H. P. Dembinski, R. Engel, A. Fedynitch, T. K. Gaisser, and T. Stanev, “The hadronic interaction model SIBYLL 2.3c and Feynman scaling,” *PoS ICRC2017 (2018)* **301**, [arXiv:1709.07227](https://arxiv.org/abs/1709.07227) [hep-ph]. [35,301(2017)].
- [37] A. Fedynitch, “MCEq repository.” <https://github.com/afedynitch/MCEq>. Accessed: 03/04/2020.
- [38] T. Heid, *Characterizing the diffuse neutrino flux with the future KM3NeT/ARCA detector*. PhD thesis, Friedrich-Alexander-Universität Erlangen-Nürnberg, ECAP, 2018.
- [39] A. Fedynitch, J. Becker Tjus, and P. Desiati, “Influence of hadronic interaction models and the cosmic ray spectrum on the high energy atmospheric muon and neutrino flux,” *Phys. Rev. D* **86** (Dec, 2012) 114024.
- [40] M. Honda *et al.*, “HKKM 2014 flux tables.” <http://www.icrr.u-tokyo.ac.jp/~mhonda/nflx2014/index.html>. Accessed: 10/06/2017.
- [41] M. Honda *et al.*, “Atmospheric neutrino flux calculation using the NRLMSISE-00 atmospheric model,” *Phys. Rev. D* **92** (2015) 023004, [arXiv:1502.03916](https://arxiv.org/abs/1502.03916).
- [42] R. Enberg, M. H. Reno, and I. Sarcevic, “Prompt neutrino fluxes from atmospheric charm,” *Phys.Rev.D* **78** (2008) 043005, [arXiv:0806.0418v2](https://arxiv.org/abs/0806.0418v2).

- [43] M. Bustamante, J. F. Beacom, and W. Winter, “Theoretically palatable flavor combinations of astrophysical neutrinos,” *Phys. Rev. Lett.* **115** (2015) 161302, [arXiv:1506.02645v4](#).
- [44] E. Fermi, “On the Origin of the Cosmic Radiation,” *Phys. Rev.* **75** (Apr, 1949) 1169–1174.
- [45] E. Fermi, “Galactic Magnetic Fields and the Origin of Cosmic Radiation.,” *ApJ* **119** (1954) 1.
- [46] **IceCube** Collaboration, “Neutrino emission from the direction of the blazar TXS 0506+056 prior to the IceCube-170922A alert,” *Science* **361** no. 6398, (2018) 147–151.
- [47] **IceCube** Collaboration, M. Aartsen *et al.*, “Multimessenger observations of a flaring blazar coincident with high-energy neutrino IceCube-170922A,” *Science* **361** no. 6398, (2018) .
- [48] A. M. Dziewonski and D. L. Anderson, “Preliminary reference Earth model,” *Phys. Earth and Planet. Int.* **25** no. 4, (1981) 297–356.
- [49] D. Bailey, *Monte Carlo tools and analysis methods for understanding the ANTARES experiment and predicting its sensitivity to dark matter*. PhD thesis, Oxford U., 2002.
- [50] S. Schael *et al.*, “Precision electroweak measurements on the Z resonance,” *Phys. Rept.* **427** (2006) 257–454, [arXiv:hep-ex/0509008](#) [hep-ex].
- [51] **Super-Kamiokande** Collaboration, Y. Fukuda *et al.*, “Evidence for Oscillation of Atmospheric Neutrinos,” *Phys. Rev. Lett.* **81** (Aug, 1998) 1562–1567.
- [52] **SNO** Collaboration, Q. R. Ahmad *et al.*, “Measurement of the rate of $\nu_e + d \rightarrow p + p + e^-$ interactions produced by 8B solar neutrinos at the Sudbury Neutrino Observatory,” *Phys. Rev. Lett.* **87** (2001) 071301, [arXiv:nucl-ex/0106015](#) [nucl-ex].
- [53] Q. R. Ahmad *et al.*, “Direct evidence for neutrino flavor transformation from neutral current interactions in the Sudbury Neutrino Observatory,” *Phys. Rev. Lett.* **89** (2002) 011301, [arXiv:nucl-ex/0204008](#) [nucl-ex].
- [54] C. Giunti and C. W. Kim, *Fundamentals of Neutrino Physics and Astrophysics*. Oxford University Press, 2007.
- [55] N. Schmitz, *Neutrinophysik*. Teubner, Stuttgart, 1997.
- [56] S. Hallmann (Bachelor thesis, Friedrich-Alexander-Universität Erlangen-Nürnberg), “Sensitivity of ORCA to the neutrino mass hierarchy,” 2013.
- [57] Z. Maki, M. Nakagawa, and S. Sakata, “Remarks on the Unified Model of Elementary Particles,” *Progress of Theoretical Physics* **28** no. 5, (11, 1962) 870–880.
- [58] B. Pontecorvo, “Neutrino Experiments and the Problem of Conservation of Leptonic Charge,” *Sov. Phys. JETP* **26** (1968) 984–988.

Bibliography

- [59] I. Esteban, M. C. Gonzalez-Garcia, A. Hernandez-Cabezudo, M. Maltoni, and T. Schwetz, “Global analysis of three-flavour neutrino oscillations: synergies and tensions in the determination of θ_{23} , δ_{CP} , and the mass ordering,” *JHEP* **01** (2019) 106, [arXiv:1811.05487v1](#).
- [60] L. Wolfenstein, “Neutrino oscillations in matter,” *Phys. Rev. D* **17** (1978) 2369–2374.
- [61] S. Mikheev and A. Y. Smirnov, “Resonance Amplification of Oscillations in Matter and Spectroscopy of Solar Neutrinos,” *Sov.J.Nucl.Phys.* **42** (1985) 913–917.
- [62] J. Coelho, “OscProb Neutrino Oscillation Calculator.”
<https://github.com/joaoabcoelho/OscProb>.
- [63] P. Huber, M. Lindner, and W. Winter, “Simulation of long-baseline neutrino oscillation experiments with GLOBES,” *Comput.Phys.Commun.* **167** (2005) 195, [arXiv:hep-ph/0407333v1](#).
- [64] M. Spurio and T. Chiarusi, “High-energy astrophysics with neutrino telescopes,” *Eur. Phys. J. C* **65** (2010) 649–701.
- [65] **KM3NeT** Collaboration, S. Adrián-Martínez *et al.*, “Intrinsic limits on resolutions in muon- and electron-neutrino charged-current events in the KM3NeT/ORCA detector,” *JHEP* **05** (2017) 008, [arXiv:1612.05621](#) [[physics.ins-det](#)].
- [66] J. M. Conrad, M. H. Shaevitz, and T. Bolton, “Precision Measurements with High Energy Neutrino Beams,” *Rev.Mod.Phys.* **70** (1998) 1341–1392, [arXiv:hep-ex/9707015v1](#).
- [67] J. A. Formaggio and G. P. Zeller, “From eV to EeV: Neutrino cross sections across energy scales,” *Rev. Mod. Phys.* **84** (2012) 1307–1341.
- [68] P. Marmier and E. Sheldon, *Physics of Nuclei and Particles*. Academic Press, New York, 1969.
- [69] J. Jelley, *Cherenkov Radiation and its Applications*. Pergamon Press, London/New York, 1958.
- [70] P. A. Čerenkov, “Visible Radiation Produced by Electrons Moving in a Medium with Velocities Exceeding that of Light,” *Phys. Rev.* **52** (Aug, 1937) 378–379.
- [71] R. C. Smith and K. S. Baker, “Optical properties of the clearest natural waters (200–800 nm),” *Appl. Opt.* **20** no. 2, (Jan, 1981) 177–184.
- [72] G. Riccobene, A. Capone, and the NEMO collaboration, “Deep seawater inherent optical properties in the Southern Ionian Sea,” [astro-ph/0603701v1](#).
- [73] **ANTARES** Collaboration, J. A. Aguilar *et al.*, “Transmission of light in deep sea water at the site of the ANTARES Neutrino Telescope,” *Astropart. Phys.* **23** (2005) 131–155, [arXiv:astro-ph/0412126](#) [[astro-ph](#)].

- [74] I. Salvadori, *Study of atmospheric neutrino oscillations with the ANTARES neutrino telescope*. PhD thesis, Aix Marseille Université, 2018. [tel-02265258](#).
- [75] C. James and J. Hofestädt, “Ice and water optical properties,” *KM3NeT Internal Note* (2015). KM3NeT_SIM_2015_001.
- [76] J. Reubelt, *Hardware studies, in-situ prototype calibration and data analysis of the novel multi-PMT digital optical module for the KM3NeT neutrino telescope*. PhD thesis, Friedrich-Alexander-Universität Erlangen-Nürnberg, 2018.
- [77] S. H. Haddock, M. A. Moline, and J. F. Case, “Bioluminescence in the Sea,” *Annual Review of Marine Science* **2** no. 1, (2010) 443–493.
- [78] T. Kahlke and K. D. Umbers, “Bioluminescence,” *Current Biology* **26** no. 8, (2016) R313 – R314.
- [79] S. Cecchini and M. Sioli, “Cosmic Ray Muon Physics,” [arXiv:hep-ex/0002052v1](#).
- [80] ANTARES Collaboration, A. Albert *et al.*, “Measuring the atmospheric neutrino oscillation parameters and constraining the 3+1 neutrino model with ten years of ANTARES data,” *JHEP* **06** (2019) 113, [arXiv:1812.08650 \[hep-ex\]](#).
- [81] T. Kajita, “Nobel Lecture: Discovery of atmospheric neutrino oscillations,” *Rev. Mod. Phys.* **88** (Jul, 2016) 030501.
- [82] J. N. Bahcall and M. Pinsonneault, “Standard solar models, with and without helium diffusion and the solar neutrino problem,” *Rev. Mod. Phys.* **64** (1992) 885–926.
- [83] Daya Bay Collaboration, F. P. An *et al.*, “Observation of electron-antineutrino disappearance at Daya Bay,” *Phys. Rev. Lett.* **108** (2012) 171803, [arXiv:1203.1669v2](#).
- [84] T2K Collaboration, K. Abe *et al.*, “Measurement of neutrino and antineutrino oscillations by the T2K experiment including a new additional sample of ν_e interactions at the far detector,” *Phys. Rev. D* **96** (Nov, 2017) 092006.
- [85] RENO Collaboration, J. H. Choi *et al.*, “Observation of Energy and Baseline Dependent Reactor Antineutrino Disappearance in the RENO Experiment,” *Phys. Rev. Lett.* **116** (2016) 211801.
- [86] E. K. Akhmedov, S. Razzaque, and A. Y. Smirnov, “Mass hierarchy, 2-3 mixing and CP-phase with Huge Atmospheric Neutrino Detectors,” *JHEP* **02** (2013) 082, [arXiv:1205.7071v6](#).
- [87] P. F. de Salas, D. V. Forero, C. A. Ternes, M. Tortola, and J. W. F. Valle, “Status of neutrino oscillations 2018: first hint for normal mass ordering and improved CP sensitivity,” *Physics Letters B* **782** (2018) 633–640, [arXiv:1708.01186v2](#).
- [88] F. Capozzi, E. Lisi, A. Marrone, and A. Palazzo, “Current unknowns in the three neutrino framework,” *Progress in Particle and Nuclear Physics* **102** (2018) 48–72, [arXiv:1804.09678v1](#).

Bibliography

- [89] **DUNE** Collaboration, R. Acciarri *et al.*, “Long-Baseline Neutrino Facility (LBNF) and Deep Underground Neutrino Experiment (DUNE) Conceptual Design Report Volume 2: The Physics Program for DUNE at LBNF,” *arXiv e-prints* (2015), [arXiv:1512.06148](https://arxiv.org/abs/1512.06148) [physics.ins-det].
- [90] S. Parke and M. Ross-Lonergan, “Unitarity and the three flavor neutrino mixing matrix,” *Phys. Rev. D* **93** (Jun, 2016) 113009.
- [91] C. Andreopoulos *et al.*, “The GENIE Neutrino Monte Carlo Generator: Physics and User Manual,” [arXiv:1510.05494](https://arxiv.org/abs/1510.05494) [hep-ph].
- [92] Y. S. Jeong and M. H. Reno, “Tau neutrino and antineutrino cross sections,” *Phys. Rev. D* **82** no. 3, (Aug., 2010) 033010, [arXiv:1007.1966](https://arxiv.org/abs/1007.1966) [hep-ph].
- [93] K. Kuzmin, V. Lyubushkin, and V. Naumov, “Fine-tuning parameters to describe the total charged-current neutrino-nucleon cross section,” *Phys. Atom. Nucl.* **69** (2006) 1857–1871.
- [94] C. H. Albright and C. Jarlskog, “Neutrino production of M^+ and E^+ heavy leptons, 1,” *Nucl. Phys. B* **84** (1974) 467–492. 41 p. <http://cds.cern.ch/record/414953>.
- [95] S. Alekhin, W. Altmannshofer, T. Asaka, *et al.*, “A facility to search for hidden particles at the CERN SPS: the SHiP physics case,” *Reports on Progress in Physics* **79** no. 12, (2016) 124201.
- [96] L. Alvarez Ruso, “Neutrino interactions with matter for oscillation experiments: the ν_τ case.” Talk at the H2020 Oscillation Physics Workshop in Valencia (2018).
- [97] **DONuT** Collaboration, K. Kodama, N. Ushida, C. Andreopoulos, *et al.*, “Observation of tau neutrino interactions,” *Physics Letters B* **504** no. 3, (Apr, 2001) 218–224.
- [98] **DONuT** Collaboration, K. Kodama *et al.*, “Final tau-neutrino results from the DONuT experiment,” *Phys. Rev. D* **78** (Sep, 2008) 052002.
- [99] CERN, “CNGS overview page.” <https://proj-cngs.web.cern.ch>. Accessed: April, 2020.
- [100] **OPERA** Collaboration, N. Agafonova *et al.*, “Discovery of τ Neutrino Appearance in the CNGS Neutrino Beam with the OPERA Experiment,” *Phys. Rev. Lett.* **115** (Sep, 2015) 121802.
- [101] R. Baldy *et al.*, “The CERN Neutrino beam to Gran Sasso (NGS),” *Report: CERN-SL-99-034-DI, INFN-AE-99-05* (1999).
- [102] A. de Gouvêa, K. J. Kelly, G. V. Stenico, and P. Pasquini, “Physics with Beam Tau-Neutrino Appearance at DUNE,” *Phys. Rev. D* **100** (2019) 016004, [arXiv:1904.07265v1](https://arxiv.org/abs/1904.07265).
- [103] “LBNE Fluxes: Engineered Optimized 3 Horn Design & TauOptimized.” <http://home.fnal.gov/~ljf26/DUNEFluxes/>. Accessed: 04/10/2019.

- [104] **Super-Kamiokande** Collaboration, Z. Li *et al.*, “A Measurement of the Tau Neutrino Cross Section in Atmospheric Neutrino Oscillations with Super-Kamiokande,” *Phys. Rev. D* **98** (Sep, 2018) 052006.
- [105] **Super-Kamiokande** Collaboration, K. Abe *et al.*, “Evidence for the Appearance of Atmospheric Tau Neutrinos in Super-Kamiokande,” *Phys. Rev. Lett.* **110** (2013) 181802, [arXiv:1206.0328v2](#).
- [106] **IceCube** Collaboration, M. G. Aartsen *et al.*, “Measurement of atmospheric tau neutrino appearance with IceCube DeepCore,” *Phys. Rev. D* **99** (Feb, 2019) 032007.
- [107] **OPERA** Collaboration, N. Agafonova *et al.*, “Final Results of the OPERA Experiment on ν_τ Appearance in the CNGS Neutrino Beam,” *Phys. Rev. Lett.* **120** (May, 2018) 211801.
- [108] L. Classen, C. Dorn, A. Kappes, *et al.*, “A multi-PMT Optical Module for the IceCube Upgrade,” *Proceedings of the 36th ICRC PoS (ICRC2019)* **885** (2019), [arXiv:1908.10802 \[astro-ph.HE\]](#).
- [109] C. Distefano on behalf of the ANTARES and KM3NeT Collaborations, “gSeaGen: A GENIE-based code for neutrino telescopes,” vol. 116 of *European Physical Journal Web of Conferences*, p. 08001. 2016. [arXiv:1602.00501 \[astro-ph.IM\]](#).
- [110] C. Andreopoulos *et al.*, “The GENIE Neutrino Monte Carlo Generator,” *Nucl. Instrum. Meth. A* **614** (2010) 87–104, [arXiv:0905.2517 \[hep-ph\]](#).
- [111] T. Sjöstrand, S. Mrenna, and P. Skands, “PYTHIA 6.4 physics and manual,” *JHEP* **2006** no. 5, (2006) 026, [arXiv:hep-ph/0603175 \[hep-ph\]](#).
- [112] M. Chruszcz, T. Przedzinski, Z. Was, and J. Zaremba, “TAUOLA of tau lepton decays– framework for hadronic currents, matrix elements and anomalous decays,” *arXiv e-prints* (2016), [arXiv:1609.04617 \[hep-ph\]](#).
- [113] S. Iyer Dutta, M. H. Reno, I. Sarcevic, and D. Seckel, “Propagation of muons and taus at high energies,” *Phys. Rev. D* **63** (Apr, 2001) 094020.
- [114] A. G. Tsirigotis, A. Leisos, and S. E. Tzamarias, “HOU reconstruction & simulation (HOURS): A complete simulation and reconstruction package for very large volume underwater neutrino telescopes,” *Nucl. Instrum. Meth. A* **626** (2011) 185–187.
- [115] A. Capone *et al.*, “Measurements of light transmission in deep sea with the AC9 transmissometer,” *Nucl. Instrum. Meth. A* **487** (2002) 423–434, [arXiv:astro-ph/0109005 \[astro-ph\]](#).
- [116] G. Carminati *et al.*, “MUPAGE: a fast atmospheric MUon GEnerator for neutrino telescopes based on PArametric formulas,” [arXiv:0907.5563v1](#).
- [117] **MACRO** Collaboration, “MACRO, a large-area detector at the Gran Sasso Laboratory,” *Il Nuovo Cimento C* **9** no. 2, (Mar, 1986) 281–292.

Bibliography

- [118] G. Giacomelli and A. Margiotta, “The MACRO Experiment at Gran Sasso,” *arXiv e-prints* (2007), [arXiv:0707.1691](https://arxiv.org/abs/0707.1691) [hep-ex].
- [119] M. Jongen (Nikhef), April, 2017. Private communication; KM3NeT Analysis E-log 178.
- [120] **KM3NeT** Collaboration, M. Ageron *et al.*, “Dependence of atmospheric muon flux on seawater depth measured with the first KM3NeT detection units: The KM3NeT Collaboration,” *Eur. Phys. J. C* **80** no. 2, (2020) 99, [arXiv:1906.02704](https://arxiv.org/abs/1906.02704) [physics.ins-det].
- [121] KM3NeT Collaboration. ORCA online monitoring page.
- [122] M. Bruchner, “Sensitivity Studies for the ORCA and Super-ORCA Neutrino Detectors,” Master’s thesis, Friedrich-Alexander-Universität Erlangen-Nürnberg, 2018.
- [123] L. Quinn, *Determining the Neutrino Mass Hierarchy with KM3NeT/ORCA*. PhD thesis, Aix-Marseille Université, Centre de Physique des Particules de Marseille, 2018.
- [124] **KM3NeT** Collaboration, S. Aiello *et al.*, “Event reconstruction for KM3NeT/ORCA using convolutional neural networks,” *JINST* **15** no. 10, (2020) P10005, [arXiv:2004.08254](https://arxiv.org/abs/2004.08254) [astro-ph.IM].
- [125] M. Moser, *Sensitivity studies on Tau Neutrino Appearance in KM3NeT/ORCA using Deep Learning Techniques*. PhD thesis, Friedrich-Alexander-Universität Erlangen-Nürnberg, 2020.
- [126] M. Volkert, “A muon veto for the measurement of the downgoing neutrino flux with KM3NeT/ORCA,” Master’s thesis, Friedrich-Alexander-Universität Erlangen-Nürnberg, 2017. ECAP-2017-007.
- [127] L. Breiman, “Random Forests,” *Machine Learning* **45** no. 1, (Oct, 2001) 5–32.
- [128] **ANTARES** Collaboration, J. Schnabel on behalf of the ANTARES Collaboration *Nucl. Instrum. Methods Phys. Res., Sect. A* **725** (2013) 106.
- [129] **ANTARES** Collaboration, A. Albert *et al.*, “Model-independent search for neutrino sources with the ANTARES neutrino telescope,” *Astroparticle Physics* **114** (2020) 35 – 47.
- [130] M. Moser, S. Reck, *et al.*, “OrcaNet repository.” <https://git.km3net.de/ml/OrcaNet>. Accessed: 15/04/2020.
- [131] Z. Zhou, *Ensemble Methods: Foundations and Algorithms*. Chapman & Hall/CRC data mining and knowledge discovery series. CRC Press, 2012.
- [132] L. Kuncheva, *Combining Pattern Classifiers: Methods and Algorithms*. Wiley, 2004.
- [133] L. Maderer, Feb., 2020. Private communication. Cross-checked against implementation in the sklearn package.

- [134] S. Bourret, *Neutrino oscillations and Earth tomography with KM3NeT-ORCA*. PhD thesis, Université Sorbonne Paris Cité, 2018.
- [135] L. Nauta (Nikhef), Jan., 2019. Private communication.
- [136] **IceCube** Collaboration, M. G. Aartsen *et al.*, “Measurement of Atmospheric Neutrino Oscillations at 6-56 GeV with IceCube DeepCore,” *Phys. Rev. Lett.* **120** (2018) 071801, [arXiv:1707.07081v4](#).
- [137] R. Brun and F. Rademakers, “ROOT: An object oriented data analysis framework,” *Nucl. Instrum. Meth. A* **389** (1997) 81–86.
- [138] M. Perrin-Terrin (CPPM), Oct., 2019. Private communication. KM3NeT Analysis elog entry 542.
- [139] G. Cowan, K. Cranmer, E. Gross, and O. Vitells, “Asymptotic formulae for likelihood-based tests of new physics,” *Eur.Phys.J.C* **71** (2011) 1554, [arXiv:1007.1727v3](#).
- [140] G. Barr, T. Gaisser, S. Robbins, and T. Stanev, “Uncertainties in Atmospheric Neutrino Fluxes,” *Phys. Rev. D* **74** (2006) 094009, [arXiv:astro-ph/0611266](#).
- [141] B. Strandberg (Nikhef) and S. Hallmann, May, 2019. KM3NeT Analysis E-log entries 468 and 469.
- [142] J. Hofestädt, R. Coniglione, A. Sinopoulou, E. Tzamariudaki, and D. Zaborov, “Atmospheric Neutrinos Detected with the First KM3NeT Detection Units of ARCA and ORCA,” in *36th International Cosmic Ray Conference (ICRC2019)*, vol. 36 of *International Cosmic Ray Conference*, p. 910. July, 2019.
- [143] D. Stravopoulos and J. Hofestädt, “Detection of the atmospheric neutrino flux with the first detection units of KM3NeT/ORCA,” 2020.
- [144] G. Dobler, D. P. Finkbeiner, I. Cholis, T. Slatyer, and N. Weiner, “The FERMI Haze: a Gamma-Ray Counterpart to the Microwave Haze,” *ApJ* **717** (2010) 825–842, [arXiv:0910.4583 \[astro-ph.HE\]](#).
- [145] M. Su, T. Slatyer, and D. Finkbeiner, “Giant Gamma-ray Bubbles from Fermi-LAT: AGN Activity or Bipolar Galactic Wind?” *ApJ* **724** (2010) 1044, [arXiv:1005.5480 \[astro-ph.HE\]](#).
- [146] E. Carretti, R. Crocker, L. Staveley-Smith, M. Haverkorn, C. Purcell, B. Gaensler, G. Bernardi, M. Kesteven, and S. Poppi, “Giant Magnetized Outflows from the Centre of the Milky Way,” *Nature* **493** (2013) 66, [arXiv:1301.0512 \[astro-ph.GA\]](#).
- [147] G. Dobler, “A Last Look at the Microwave Haze/Bubbles with WMAP,” *Astrophys. J.* **750** (2012) 17, [arXiv:1109.4418 \[astro-ph.GA\]](#).
- [148] S. Snowden, R. Egger, M. Freyberg, D. McCammon, P. Plucinsky, W. Sanders, J. Schmitt, J. Truemper, and W. Voges, “ROSAT Survey Diffuse X-Ray Background Maps. II.,” *Astrophys. J.* **485** (1997) 125.

Bibliography

- [149] Nasa's Goddard Space Flight Center, 2015. Figure published on the web, http://www.nasa.gov/mission_pages/GLAST/news/new-structure.html.
- [150] P. Mertsch and S. Sarkar, "Fermi gamma-ray 'bubbles' from stochastic acceleration of electrons," *Phys. Rev. Lett.* **107** (2011) 091101, [arXiv:1104.3585](https://arxiv.org/abs/1104.3585) [astro-ph.HE].
- [151] G. Dobler, I. Cholis, and N. Weiner, "The Fermi Gamma-Ray Haze from Dark Matter Annihilations and Anisotropic Diffusion," *ApJ* **741** (2011) 25, [arXiv:1102.5095](https://arxiv.org/abs/1102.5095) [astro-ph.HE].
- [152] H. Y. K. Yang and M. Ruzkowski, "The Spatially Uniform Spectrum of the Fermi Bubbles: The Leptonic Active Galactic Nucleus Jet Scenario," *Astrophys. J.* **850** no. 1, (2017) 2, [arXiv:1706.05025](https://arxiv.org/abs/1706.05025) [astro-ph.HE].
- [153] R. Crocker and F. Aharonian, "The Fermi Bubbles: Giant, Multi-Billion-Year-Old Reservoirs of Galactic Center Cosmic Rays," *Phys. Rev. Lett.* **106** (2011) 101102, [arXiv:1008.2658](https://arxiv.org/abs/1008.2658) [astro-ph.GA].
- [154] S. Thoudam, "Fermi bubble γ -rays as a result of diffusive injection of Galactic cosmic rays," *ApJ, Letters* **778** (2013) L20, [arXiv:1304.6972](https://arxiv.org/abs/1304.6972) [astro-ph.HE].
- [155] B. C. Lacki, "The Fermi Bubbles as Starburst Wind Termination Shocks," *Monthly Notices of the RAS* **444** (2014) L39, [arXiv:1304.6137](https://arxiv.org/abs/1304.6137) [astro-ph.HE].
- [156] F. Guo and W. G. Mathews, "The Fermi Bubbles. I. Possible Evidence for Recent AGN Jet Activity in the Galaxy," *Astrophys. J.* **756** (2012) 181, [arXiv:1103.0055](https://arxiv.org/abs/1103.0055) [astro-ph.HE].
- [157] K. Cheng, D. Chernyshov, V. Dogiel, C. Ko, and W. Ip, "Origin of the Fermi Bubble," *Astrophys. J. Lett.* **731** (2011) L17, [arXiv:1103.1002](https://arxiv.org/abs/1103.1002) [astro-ph.HE].
- [158] **Fermi-LAT** Collaboration, M. Ackermann *et al.*, "The Spectrum and Morphology of the *Fermi* Bubbles," *Astrophys. J.* **793** no. 1, (2014) 64, [arXiv:1407.7905](https://arxiv.org/abs/1407.7905) [astro-ph.HE].
- [159] M. Ackermann *et al.*, "The Fermi Galactic Center GeV Excess and Implications for Dark Matter," *Astrophys. J.* **840** no. 1, (2017) 43, [arXiv:1704.03910](https://arxiv.org/abs/1704.03910) [astro-ph.HE].
- [160] L. Herold and D. Malyshev, "Hard and bright gamma-ray emission at the base of the Fermi bubbles," [1904.01454v2](https://arxiv.org/abs/1904.01454v2).
- [161] S. Hallmann, "Search for a Neutrino Signal from the Fermi Bubbles with the ANTARES Telescope," Master's thesis, Friedrich-Alexander-Universität Erlangen-Nürnberg, 2015.
- [162] F. L. Villante and F. Vissani, "How precisely neutrino emission from supernova remnants can be constrained by gamma ray observations?" *Phys. Rev. D* **78** (2008) 103007, [arXiv:0807.4151](https://arxiv.org/abs/0807.4151).

- [163] S. R. Kelner, F. A. Aharonian, and V. V. Bugayov, “Energy spectra of gamma rays, electrons, and neutrinos produced at proton-proton interactions in the very high energy regime,” *Phys. Rev. D* **74** no. 3, (2006) 034018.
- [164] **HAWC** Collaboration, H. Solares, “Search for a very high-energy gamma-ray signal in the northern Fermi bubble region with HAWC,” *AIP Conf. Proc.* **1792** no. 1, (2017) 040006.
- [165] B. Bakker, “Trigger studies for the Antares and KM3NeT neutrino telescopes,” Master’s thesis, University of Amsterdam, 2011.
- [166] **ANTARES** Collaboration, A. Albert *et al.*, “Long-term monitoring of the ANTARES optical module efficiencies using ^{40}K decays in sea water,” *Eur. Phys. J. C* **78** no. 8, (2018) 669, [arXiv:1805.08675](#) [astro-ph.IM].
- [167] A. J. Heijboer, *Track Reconstruction and Point Source Searches with ANTARES*. PhD thesis, NIKHEF, Amsterdam, 2004.
- [168] T. Michael, *Light at the End of the Shower*. PhD thesis, NIKHEF, Amsterdam, 2016.
- [169] T. Michael on behalf of the ANTARES Collaboration, “Neutrino Point Source Search including CascadeEvents with the ANTARES Neutrino Telescope,” *Proceedings of the 34th ICRC PoS (ICRC2015)* **1078** (2015).
- [170] **ANTARES** Collaboration, A. Albert *et al.*, “An algorithm for the reconstruction of neutrino-induced showers in the ANTARES neutrino telescope,” *Astron. J.* **154** no. 6, (2017) 275, [arXiv:1708.03649](#) [astro-ph.IM].
- [171] J. Barrios Martí, *Search for cosmic sources in neutrino telescopes and time calibration in the ANTARES neutrino telescope*. PhD thesis, Universitat de Valencis, CSIC-UV, 2018.
- [172] G. De Bonis, “GENHEN release v7r1 (... and some anticipations on the next release),” *ANTARES Internal Note* (2014). ANTARES-SOFT-2014-001.
- [173] **ANTARES** Collaboration, A. Albert *et al.*, “First all-flavor neutrino pointlike source search with the ANTARES neutrino telescope,” *Phys. Rev. D* **96** no. 8, (2017) 082001, [arXiv:1706.01857](#) [astro-ph.HE].
- [174] **ANTARES** Collaboration, A. Albert *et al.*, “An algorithm for the reconstruction of high-energy neutrino-induced particle showers and its application to the ANTARES neutrino telescope,” *Eur. Phys. J. C* **77** no. 6, (2017) 419, [arXiv:1703.02432](#) [astro-ph.HE].
- [175] V. Kulikovskiy, *Neutrino astrophysics with the ANTARES telescope*. PhD thesis, Genoa U., 2014.
- [176] G. J. Feldman and R. D. Cousins, “A Unified Approach to the Classical Statistical Analysis of Small Signals,” *Phys. Rev. D* **57** (1998) 3873, [arXiv:physics/9711021](#).
- [177] T.-P. Li and Y.-Q. Ma, “Analysis methods for results in gamma-ray astronomy,” *ApJ* **272** (1983) 317.

Bibliography

- [178] D. Malyshev (ECAP), Dec., 2017. Private communication.
- [179] **CTA Consortium** Collaboration, A. Viana *et al.*, “The Cherenkov Telescope Array view of the Galactic Center region,” *PoS ICRC2019* (2020) 817, [arXiv:1908.06162](#) [[astro-ph.HE](#)].
- [180] K. Fang, M. Su, T. Linden, and K. Murase, “IceCube and HAWC constraints on very-high-energy emission from the Fermi bubbles,” *Phys. Rev. D* **96** no. 12, (2017) 123007, [arXiv:1704.03869](#) [[astro-ph.HE](#)].
- [181] N. Sherf, U. Keshet, and I. Gurwich, “IceCube constraints on the Fermi Bubbles,” *Astrophys. J.* **847** no. 2, (2017) 95, [arXiv:1705.06665](#) [[astro-ph.HE](#)].
- [182] KM3NeT Collaboration, S. Adrian-Martinez *et al.*, “Detection potential of the KM3NeT detector for high-energy neutrinos from the Fermi bubbles,” *ApJ* **42** (2013) 7.